A dissertation submitted for the degree of
Doctor of Science

Properties of Quantum Vacuum Based on Nonlinear Quantum Electrodynamics and its Application to X-ray Polarimetry

非線形量子電気力学に基づく量子論的真空の性質とその X 線偏光観測への応用

February 2018

Akihiro YATABE

矢田部 彰宏

Properties of Quantum Vacuum Based on Nonlinear Quantum Electrodynamics and its Application to X-ray Polarimetry

非線形量子電気力学に基づく量子論的真空の性質とその X 線偏光観測への応用

February 2018

Waseda University
Graduate School of Advanced Science and Engineering
Department of Pure and Applied Physics,
Research on Theoretical Astrophysics

Akihiro YATABE

矢田部 彰宏

Abstract

The properties of the vacuum in the quantum theory are different from those in the classical one. In the quantum vacuum, particles repeat generation and annihilation persistently. Under sufficiently strong electromagnetic fields, the generated charged particles, such as a pair of electron and positron, can be observed. The refractive indices of the vacuum change by the external electromagnetic fields and the vacuum shows the birefringence, which is the phenomenon that the refractive index of the eigenmode is different from each other. Such phenomena are thought to occur when the strength of electromagnetic fields is more than or of the same order of that of the so-called critical field, which is about 4×10^{13}G for magnetic fields. The physics dealing the behavior of electrons and photons in the external such strong electromagnetic fields is called nonlinear quantum electrodynamics (QED) or strong-field QED. In this research, the vacuum polarization, which is one of the fundamental processes particular to nonlinear QED, is mainly treated.

To verify quantum electrodynamics by experiments, the electromagnetic field, the strength of which is the same order of the critical field, is necessary. In fact, the validation of the theory has been tried by the high-field laser experiments. The required strength to the nonlinear QED cannot be obtained in the experiments, so the phenomena predicted from nonlinear QED, which is caused by the interaction with the external electromagnetic fields, are not observed until now. However, the progress in the technology of the high-field laser experiments is fast and it is thought that physical processes specific in nonlinear QED will occur in the experiments in the near future.

In this research, I first calculate the vacuum polarization in external monochromatic plane-wave electromagnetic fields. I take into account spatial and temporal variations of the external fields. I develop a perturbation theory to calculate the induced electromagnetic current that appears in the Maxwell equations, based on Schwinger's proper-time method. Then, I combine it with the so-called gradient expansion to handle the variation of external fields perturbatively. The crossed field, which is the long wavelength limit of the electromagnetic plane wave, is considered. The eigenmodes and the refractive indices as the eigenvalues associated with the eigenmodes are computed numerically for the probe photon propagating in some particular directions. In so doing, no limitation is imposed on the field strength and the photon energy unlike previous studies. It is shown that the real part of the refractive index becomes less than unity for strong fields, the phenomenon that has been known to occur for high-energy probe photons. I then evaluate numerically the lowest-order corrections to the crossed-field resulting from the field variations in space and time. It is demonstrated that the corrections occur mainly in the

imaginary part of the refractive index.

The nonlinear QED also important in the astronomical objects called magnetars, where the strong magnetic fields exist. It is known that explosive radiation of transient phenomena called bursts and flares is observed in the energy range of X-ray and gamma ray. It is also thought that they are caused by magnetars' strong magnetic fields. Other than the transient phenomena, magnetars are observed by their persistent emission mainly in X-ray. The persistent emission consists of the thermal component radiated from the star surface and the non-thermal one emitted from the magnetosphere, which are observed in the soft X-ray and in the energy range higher than it, respectively. The thermal radiation propagates through the magnetosphere and are affected by the vacuum polarization therein. In fact, the vacuum polarization is important for the polarization of photons, so it may be a clue for the validation of the nonlinear QED when the polarization of the thermal radiation is observed.

In this research, I systematically calculated the polarization in soft X-rays emitted from magnetized neutron stars, which are expected to be observed by the next-generation X-ray satellites. Magnetars are one of the targets for these observations, since thermal radiations are normally observed in the soft X-ray band and they are thought to be linearly polarized because of different opacities for two polarization modes of photons in the magnetized atmosphere of neutron star as well as owing to the dielectric properties of the vacuum in strong magnetic fields. I computed polarization fractions in addition to the polarization angles, paying an appropriate attention to the mode conversion, which is possible conversion of photon's polarization modes in the atmosphere, and systematically changing magnetic field strengths, radii of the emission region, temperature, mass and radii of neutron stars. It is found that the mode conversion may affect both the polarization angle and the polarization fraction and produce discontinuities in the polarization angle as a function of photon energy, one of the important observables. I confirm that the mode conversion cannot be ignored indeed when the magnetic field is relatively weak $B \sim 10^{13}$G. My results indicate that strongly magnetized ($B \gtrsim 10^{14}$G) neutron stars are suitable to detect polarizations but not-so-strongly magnetized ($B \sim 10^{13}$G) ones will be the ones to confirm the mode conversion.

Contents

1 Introduction

1.1 Quantum Vacuum

Our understandings of the physics in the microscopic scale was revolutionized a lot by the quantum theory. It also changed the picture of the vacuum. Although the vacuum is the state that there is nothing in the classical theory, particles and antiparticles exist even in the vacuum in the quantum theory. More precisely, in the quantum vacuum, creation and annihilation of the particles and antiparticles, which 1is drawn by the vacuum bubble diagram of the Feynman diagram (Figure 1.1), occur repeatedly. The causes are the uncertainty principle,

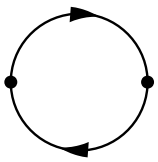

Figure 1.1: Vacuum bubble diagram. This diagram shows the creation and annihilation of an electron and a positron.

$$\Delta E \Delta t \gtrsim \hbar \tag{1.1}$$

which describes that the processes that break the energy conservation are allowed in a very short timescale. This timescale is too short for the observation and processes that the particles are created and annihilated from the vacuum cannot be observed. Such particles which exist in the short timescale predicted in the quantum theory is called “virtual” particles.

The situation changes when electromagnetic fields are added and the properties of the vacuum differ from the ordinary vacuum without the external fields. When we consider an electron and positron pair as virtual particles and electric field as the external field, an electron and a positron are accelerated in the opposite direction. If these particles are separated by a sufficient distance, these particles are not be annihilated and then observed. This process is seen as an electron-positron pair creation (Figure 1.2). This process is studied by Heisenberg and Euler (1936);

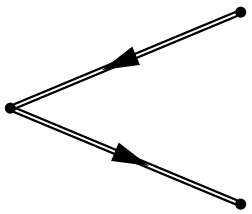

Figure 1.2: Electron-positron pair creation. The double solid line means the electron or positron in the external electromagnetic field.

Schwinger (1951). It is also known that the pair creation is suppressed exponentially with decreasing electric field strength. It is also noted that the pair creation occurs by the external strong magnetic fields. This is important in astrophysics, e.g., near neutron stars.

It is also predicted that the quantum vacuum in the external electromagnetic fields shows particular phenomena when a photon as a probe enters such a vacuum. Here let us consider a magnetic field, in which the pair creation does not expose itself, as an external field. In the classical theory, charged particles experience the Lorentz force in magnetic fields and rotate around magnetic field lines. This situation also holds for the quantum theory and orbits of electrons' motion are parallel with each other, which is also true for those of positrons'. Therefore, the arranged motion of virtual particles makes anisotropy in the vacuum and it causes the birefringence, which is the phenomenon that the refractive index depends on polarization of photons and the refractive index of one polarization mode is different from that of the other polarization mode. This is called the vacuum polarization (Figure 1.3).

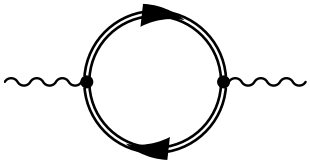

Figure 1.3: Vacuum polarization in the external electromagnetic field. This phenomenon causes the vacuum birefringence.

There have been many theoretical studies of the quantum vacuum in the external electromagnetic fields including Heisenberg and Euler (1936) for a long time. For these processes by the quantum vacuum in the external strong electromagnetic fields, interactions between the external fields and photons are important and they must not be treated as perturbations. So, the perturbation theory in quantum electrodynamics (QED), which is often used to investigate behaviors of photons and electrons, cannot be applied to physical phenomena considered here. Instead, nonlinear quantum electrodynamics (nonlinear QED) treats physical processes of electrons and photons in the external strong electromagnetic fields.

The criterion of the electromagnetic field strength that nonlinear QED becomes important is called the critical field. It is about 4×10^{13}G for magnetic field, which is the field strength at which the electron cyclotron energy equals to the rest mass energy of an electron. Attempts to validate nonlinear QED have been done in the terrestrial experiments utilizing the high-intensity laser facilities. The development of the experimental technology in the high-intensity laser is so fast that the validation of nonlinear QED is thought to be possible in the near future, though the field strength of the laser is less then the critical value.

As described above, the strong electromagnetic field such that nonlinear QED is important is not obtained in the terrestrial experiments so far. However, there are some celestial objects called neutron stars, in which nonlinear QED has to be considered. A neutron star is one of the final stages of the evolution of stars. Although they usually have dipole magnetic fields of $\sim 10^{12}$G, they are observed in various forms and some of them have extremely strong magnetic fields of $\sim 10^{14-15}$G, which are called magnetars. Therefore, there are some systems with strong magnetic fields, in which particular physical processes to nonlinear QED occur, and nonlinear QED may be verified by the observation of magnetars.

It is also pointed out that there may exist extremely strong electromagnetic fields in the heavy ion collision, which is a topic in nuclear physics, and in the early universe. Therefore, understanding nonlinear QED contributes to various subjects and disciplines as well as magnetars. Thus, the properties of the quantum vacuum have been theoretically studied in nonlinear QED for a long time, however, nonlinear QED can be still tackled as new problems by reason of the recent advances in the experiments and observations.

1.2 Theoretical Basics

In this section, I briefly show the birefringence of the vacuum and explain the behavior of the eigenmodes of the plane electromagnetic wave in the strongly magnetized plasma. Note that the electromagnetic units are different for these parts. I use the Heaviside-Lorentz system with the natural unit in the former part (Section 1.2.1) and the cgs Gauss unit in the latter part (Section 1.2.2).

1.2.1 Proper-time Method and Effective Lagrangian

The effective action for the electromagnetic fields, which contains the quantum correction of the 1-loop level, is known to contain the electron propagator. The expres-

sion is

$$\Gamma^{(1)} = -i \int d^4x \, \mathrm{tr} \ln \left(i \not{\partial} - e \not{A} - m \right), \tag{1.2}$$

where A_μ is the external electromagnetic field and m is the electron mass in this section. The slash / means the contraction with the gamma matrix, e.g., $\not{\partial} = \gamma^\mu \partial_\mu$ and the term $(i \not{\partial} - e \not{A} - m)$ is the inverse of the propagator. The Lagrangian is

$$\mathcal{L}^{(1)}(x) = -i \, \mathrm{tr} \ln \left(i \not{\partial} - e \not{A} - m \right). \tag{1.3}$$

The Lagrangian is related to the propagator, and the way to derive the propagator is similar that to calculate the effective Lagrangian. Here, the expression of the electron propagator in the electromagnetic external fields is derived by the Schwinger proper-time method (Schwinger, 1951). The propagator is expressed as

$$G(x, y) = \frac{1}{i \not{\partial}_x - e \not{A}(x) - m}. \tag{1.4}$$

In the proper-time method, the propagator is written by the operator $\hat{G}$ as

$$G(x, y) = \langle x | \hat{G} | y \rangle. \tag{1.5}$$

Operator $\hat{G}$ is shown in the integral of the proper-time s, which is introduced in this method and the proper-time in this method is not the proper time appearing in the relativity. The integral form is

$$\begin{aligned} \hat{G} &= \frac{1}{\gamma^\mu \hat{\Pi}_\mu - m} \\ &= -\frac{\gamma^\mu \hat{\Pi}_\mu + m}{m^2 - (\gamma^\mu \hat{\Pi}_\mu)^2} \\ &= \left(-\gamma^\mu \hat{\Pi}_\mu - m \right) i \int_0^\infty ds \exp \left[-i \left(m^2 - \left(\gamma^\mu \hat{\Pi}_\mu \right)^2 - i\varepsilon \right) s \right], \end{aligned} \tag{1.6}$$

where $\hat{\Pi}_\mu = i\partial_\mu - eA_\mu$ and ε in the integration is the small positive real value introduced to converge the integration. The propagator is then expressed as

$$\begin{aligned} &G(x, y) \\ &= i \int_0^\infty ds e^{-im^2 s - \varepsilon s} \left[\langle x | - \gamma^\mu \hat{\Pi}_\mu e^{-i(-(\gamma^\mu \hat{\Pi}_\mu)^2) s} | y \rangle - \langle x | m e^{-i(-(\gamma^\mu \hat{\Pi}_\mu)^2) s} | y \rangle \right]. \end{aligned} \tag{1.7}$$

The exponential function $U(s) \equiv e^{-i(-(\gamma^\mu \hat{\Pi}_\mu)^2) s}$ can be seen as the evolution operator of the proper-time s, , and $H \equiv -(\gamma^\mu \hat{\Pi}_\mu)^2$ is considered as the Hamiltonian. In this notation, the necessary components to calculate the propagator are

$$\begin{aligned} \langle x | e^{-i(-(\gamma^\mu \hat{\Pi}_\mu)^2) s} | y \rangle &= \langle x | U(s) | y \rangle \\ &= \langle x(s) | y(0) \rangle, \end{aligned} \tag{1.8}$$

$$\begin{aligned} \langle x | - \gamma^\mu \hat{\Pi}_\mu e^{-i(-(\gamma^\mu \hat{\Pi}_\mu)^2) s} | y \rangle &= \langle x | U(s) U^{-1}(s) (-\gamma^\mu \hat{\Pi}_\mu) U(s) | y \rangle \\ &= \langle x(s) | - \gamma^\mu \hat{\Pi}_\mu(s) | y(0) \rangle. \end{aligned} \tag{1.9}$$

Then, the propagator is written as follows:

$$G(x,y) = i\int_0^\infty e^{-im^2 s}\langle x(s)|\left(-\gamma^\mu\hat{\Pi}_\mu(s) - m\right)|y(0)\rangle. \tag{1.10}$$

These consist of the transformation amplitude $\langle x(s)|y(0)\rangle$ and the operator $\hat{\Pi}_\mu(s)$. The transformation amplitude evolves by the differential equation

$$i\partial_s\langle x(s)|y(0)\rangle = \langle x(s)| - (\gamma^\mu\hat{\Pi}_\mu(s))^2|y(0)\rangle, \tag{1.11}$$

and the operators evolves by the Heisenberg equations

$$\begin{aligned}\frac{d\hat{x}_\mu(s)}{ds} &= -i\left[\hat{x}_\mu(s), -(\gamma_\nu\hat{\Pi}^\nu(s))^2\right] \\ &= 2\hat{\Pi}_\mu(s), &(1.12)\\ \frac{d\hat{\Pi}_\mu(s)}{ds} &= -i\left[\hat{\Pi}_\mu(s), -(\gamma_\nu\hat{\Pi}^\nu(s))^2\right] \\ &= 2eF_\mu{}^\nu\hat{\Pi}_\nu(s) + e^{iHs}ie\frac{\partial F_\mu{}^\nu}{\partial x^\nu}e^{-iHs} + e^{iHs}\frac{1}{2}e\sigma^{\nu\lambda}\frac{\partial F_{\nu\lambda}}{\partial x^\mu}e^{-iHs}, &(1.13)\end{aligned}$$

where Equation (1.12) is necessary to express $\hat{\Pi}_\mu$ with $\hat{x}_\mu$, which satisfies

$$\hat{x}^\mu(s)|x(s)\rangle = x^\mu|x(s)\rangle, \tag{1.14}$$
$$\hat{x}^\mu(0)|x(0)\rangle = x^\mu|x(0)\rangle, \tag{1.15}$$

for the evaluation. Note that Equation (1.13) contains the derivative of the field written in the proper-time in the second and third terms, which make the evaluation possible only in the limited cases such as the constant and homogeneous electromagnetic field.

The expression of the Lagrangian is

$$\mathcal{L}^{(1)}(x) = i\int_0^\infty ds\frac{1}{s}e^{-im^2 s-\varepsilon s}\mathrm{tr}\langle x(s)|x(0)\rangle. \tag{1.16}$$

This is evaluated after one gets the transformation amplitude $< x(s)|x(0) >$. This Lagrangian is known as the Euler-Heisenberg Lagrangian. The birefringence of the vacuum can be understood with the lowest order of the correction term:

$$\mathcal{L}^{(1)}(x) \simeq \frac{2\alpha^2}{45m^4}\left\{\left(\mathbf{E}^2 - \mathbf{B}^2\right)^2 + 7\left(\mathbf{E}\cdot\mathbf{B}\right)^2\right\}. \tag{1.17}$$

The Lagrangian of the electromagnetic field is

$$\begin{aligned}\mathcal{L} &= \frac{1}{2}\left(\mathbf{E}^2 - \mathbf{B}^2\right) \\ &\quad + \frac{2\alpha^2}{45m^4}\left\{\left(\mathbf{E}^2 - \mathbf{B}^2\right)^2 + 7\left(\mathbf{E}\cdot\mathbf{B}\right)^2\right\}, &(1.18)\end{aligned}$$

in this case. When the external magnetic field, of which the strength is B, exists, the dielectric tensor and the inverse of the magnetic permeability tensor are

$$\epsilon_{ij} = \delta_{ij}(1-2\delta) + 7\delta b_i b_j, \tag{1.19}$$
$$\mu_{ij}^{-1} = \delta_{ij}(1-2\delta) - 4\delta b_i b_j, \tag{1.20}$$

where δ is

$$\delta = \frac{\alpha}{45\pi}\left(\frac{B}{B_Q}\right)^2 \simeq 5\times 10^{-5}\left(\frac{B}{B_Q}\right)^2 \tag{1.21}$$

and b_i is the direction of the external field. Note also that the variation of the dielectric and magnetic the inverse of the permeability can be seen as linear perturbation when one assume that δ is small.

When the plane electromagnetic wave propagates in z-direction, the external magnetic field is on $z-x$ plane and the angle between the external field and z-axis is θ, the refractive indices are

$$N_x = 1 + \frac{7\alpha}{90\pi}\left(\frac{B}{B_Q}\right)^2 \sin^2\theta, \tag{1.22}$$

$$N_y = 1 + \frac{2\alpha}{45\pi}\left(\frac{B}{B_Q}\right)^2 \sin^2\theta, \tag{1.23}$$

for the eigenmodes, which have the polarization parallel to x- and y-directions, respectively. It is known that the refractive indices are different for each polarization mode.

1.2.2 Eigenmodes in Strongly Magnetized Plasma

Neutron stars are endowed with strong magnetic field and the birefringence of the vacuum is expected therein. There may be also the plasma in the atmosphere near the surface of the star. In such a case, the polarization eigenmodes are affected by both the dielectric property of the birefringent vacuum and that of the plasma. Here I explain the polarization eigenmodes with considering the both effects.

Gas plasma generally contains electrons and ions, however, I do not take into account the collective motion of electrons and ions but the motion of electrons in the magnetic field here. This assumption is justified when the frequency of the electromagnetic wave concerned ω is much higher than the electron's plasma frequency

$$\omega_{pe} = \left(\frac{4\pi n_e e^2}{m_e}\right)^{1/2}, \tag{1.24}$$

where n_e is the number density of electrons and m_e is the electron mass and the ion's cyclotron frequency

$$\omega_{ci} = \frac{eB}{m_i c}, \tag{1.25}$$

where m_i is the ion mass. The thermal effect can be also ignored because the electron's cyclotron energy

$$\hbar\omega_{ce} = \frac{\hbar eB}{m_e c} = 11.6\left(\frac{B}{10^{12}\mathrm{G}}\right)\mathrm{keV}, \tag{1.26}$$

where ω_{ce} is the electron's cyclotron frequency, is much higher than the temperature of the neutron star surface radiating the persistent emission.

The electric flux density $\boldsymbol{D}$ in the magnetized plasma without the quantum correction of the vacuum is expressed as

$$\boldsymbol{D} = \left(1 - \frac{\omega_{pe}^2}{\omega^2 - \omega_{ce}^2}\right)\boldsymbol{E} + \frac{\omega_{pe}^2 \boldsymbol{\omega}_{ce}(\boldsymbol{\omega}_{ce}\cdot\boldsymbol{E})}{(\omega^2-\omega_{ce}^2)\omega^2} + i\frac{\omega_{pe}^2(\boldsymbol{\omega}_{ce}\times\boldsymbol{E})}{(\omega^2-\omega_{ce}^2)\omega}, \tag{1.27}$$

where $\boldsymbol{\omega}_{ce} = -e\boldsymbol{B}/m_e c$. The variation of the dielectric tensor $4\pi\alpha_{ij}^{(p)}$ for the system that the magnetic field is along z-axis is

$$4\pi\alpha_{ij}^{(p)} = \begin{pmatrix} S & iD & 0 \\ -iD & S & 0 \\ 0 & 0 & P \end{pmatrix}_{ij}, \tag{1.28}$$

where

$$\begin{aligned} &S = -\frac{v}{1-u},\ D = -\frac{vu^{1/2}}{1-u},\ P = -v, \\ &v = \left(\frac{\omega_{pe}}{\omega}\right)^2,\ u = \left(\frac{\omega_{ce}}{\omega}\right)^2,\ u^{1/2} = \frac{\omega_{ce}}{\omega}. \end{aligned} \tag{1.29}$$

The magnetic permeability of the plasma is usually same as that of the normal vacuum.

The eigenmodes of the plane electromagnetic waves and the corresponding refractive indices are evaluated by solving the equation

$$\varepsilon\frac{\partial^2\boldsymbol{E}}{\partial t^2} = -c^2\left[\nabla\times\mu^{-1}\left(\nabla\times\boldsymbol{E}\right)\right], \tag{1.30}$$

which is derived from the macroscopic Maxwell equations. The dielectric tensor and the inverse of the magnetic permeability tensor are obtained from Equations (1.19), (1.20) and (1.28). As the previous section, let us consider the plane electromagnetic wave propagating in z-direction. The external magnetic field is on $z-x$ plane and the angle between the magnetic field and z-axis is θ. In this case, there is also the longitudinal component of the polarization

$$E_z = -\varepsilon_{zz}^{-1}(\varepsilon_{zx}E_x + \varepsilon_{zy}E_y). \tag{1.31}$$

The equation of the transverse components is

$$\begin{pmatrix} \eta_{xx} - N^2 & \eta_{xy} \\ \eta_{yx} & \eta_{yy} - N^2\rho \end{pmatrix}\begin{pmatrix} E_x \\ E_y \end{pmatrix} = 0, \tag{1.32}$$

where

$$\eta_{xx} = (1-2\delta)^{-1}\left(\varepsilon_{xx} - \varepsilon_{xz}\varepsilon_{zz}^{-1}\varepsilon_{zx}\right), \tag{1.33}$$
$$\eta_{xy} = (1-2\delta)^{-1}\left(\varepsilon_{xy} - \varepsilon_{xz}\varepsilon_{zz}^{-1}\varepsilon_{zy}\right), \tag{1.34}$$
$$\eta_{yx} = (1-2\delta)^{-1}\left(\varepsilon_{yx} - \varepsilon_{yz}\varepsilon_{zz}^{-1}\varepsilon_{zx}\right), \tag{1.35}$$
$$\eta_{yy} = (1-2\delta)^{-1}\left(\varepsilon_{yy} - \varepsilon_{yz}\varepsilon_{zz}^{-1}\varepsilon_{zy}\right), \tag{1.36}$$
$$\rho = 1 - 4\delta a^{-1}\sin^2\theta, \tag{1.37}$$

which are expressed as

$$\eta_{xx} = (1-2\delta)^{-1}(S\sin^2\theta + P\cos^2\theta)^{-1}SP, \tag{1.38}$$
$$\eta_{yy} = (1-2\delta)^{-1}(S\sin^2\theta + P\cos^2\theta)^{-1}\left\{SP\cos^2\theta + (S^2-D^2)\sin^2\theta\right\}, \tag{1.39}$$
$$\eta_{xy} = -\eta_{yx} = (1-2\delta)^{-1}(S\sin^2\theta + P\cos^2\theta)^{-1}iDP\cos\theta, \tag{1.40}$$

in the system concerned. The refractive index $N = k_0/|\boldsymbol{k}|$ is obtained when

$$\det\begin{pmatrix} \eta_{xx}-N^2 & \eta_{xy} \\ \eta_{yx} & \eta_{yy}-N^2\rho \end{pmatrix} = 0. \tag{1.41}$$

The refractive indices for each polarization are

$$\begin{aligned} N_{1,2}^2 &= \frac{1}{2}(\eta_{xx}+\rho^{-1}\eta_{yy}) \pm \frac{1}{2}\sqrt{(\eta_{xx}-\rho^{-1}\eta_{yy})^2 + 4\rho^{-1}|\eta_{xy}|^2} \\ &= \left\{2(1-2\delta)(S\sin^2\theta + P\cos^2\theta)\right\}^{-1} \\ &\quad \times\Bigg[SP + \rho^{-1}(SP\cos^2\theta + (S^2-D^2)\sin^2\theta) \\ &\quad \pm\sqrt{\left\{SP - \rho^{-1}(SP\cos^2\theta + (S^2-P^2)\sin^2\theta)\right\}^2 + 4\rho^{-1}D^2P^2\cos^2\theta}\Bigg]. \end{aligned} \tag{1.42}$$

The polarization vector of the eigennmode can be obtained by the refractive index. Here, the transverse components, i.e., x and y components, are considered and the polarization vector is assumed to be

$$\mathbf{e}_{1,2}^t = C(i\alpha_{x_{1,2}}, 1), \tag{1.43}$$

where C is the normalization factor. x component is expressed as

$$\begin{aligned} \alpha_x &= \frac{N^2\rho - \eta_{yy}}{i\eta_{yx}} \\ &= \rho^{1/2}\left(\frac{\rho\eta_{xx}-\eta_{yy}}{2i\eta_{yx}\rho^{1/2}}\right)\left[1 \pm \left\{1 + \left(\frac{2i\eta_{yx}\rho^{1/2}}{\rho\eta_{xx}-\eta_{yy}}\right)^2\right\}^{1/2}\right] \\ &= \rho^{1/2}b\left[1 \pm (1+b^{-2})^{1/2}\right], \end{aligned} \tag{1.44}$$

where

$$b \equiv \frac{\rho\eta_{xx}-\eta_{yy}}{2i\eta_{yx}\rho^{1/2}} \tag{1.45}$$

is the ellipticity parameter. To the first order of δ and v, one gets

$$\begin{aligned} b &\simeq \left(1 + \frac{3\delta(1-u)}{uv}\right)\frac{u^{1/2}\sin^2\theta}{2\cos\theta(1-2\delta\sin^2\theta)(1+5\delta-v)} \\ &\simeq \left(1 + \frac{3\delta(1-u)}{uv}\right)\frac{u^{1/2}\sin 2\theta}{2\cos\theta(1-v)}. \end{aligned} \tag{1.46}$$

Here,

$$b_0 = \frac{u^{1/2} \sin 2\theta}{2 \cos\theta (1 - v)} \tag{1.47}$$

is the ellipticity parameter in case without taking into account the vacuum polarization. In contrast, when the vacuum polarization is considered, the ellipticity parameter b can be written as

$$b = b_0(1 + V), \tag{1.48}$$

where Vb_0 is the correction by nonlinear QED. The polarization vector changes by the balance of δ and v. The most drastically change occurs at

$$v = 3\delta \left(1 - \frac{1}{u}\right), \tag{1.49}$$

at which $1 + V$ equals zero. In Figure 1.4, the ellipticity parameter is plotted for the

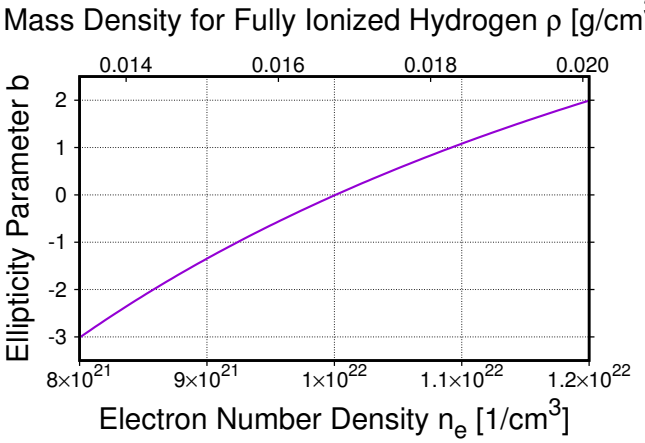

Figure 1.4: Ellipticity parameter around the vacuum resonance point. The lower horizontal axis shows the electron number density of the plasma and the vertical axis shows the ellipticity parameter of the polarization. The parameters are $B = 10^{12}$G, $\theta = 45°$ and $\hbar\omega = 3$keV. The vacuum resonance occurs at $b = 0$, which corresponds to the electron number density of $n_e = 10^{22}\,1/\mathrm{cm}^2$. The upper horizontal axis shows the plasma mass density in the case that the plasma consists of the fully ionized hydrogen.

different plasma density around the vacuum resonance. It is known from this figure that the ellipticity parameter b increases as the plasma density increases. The eigenmodes in the magnetized plasma is generally elliptically polarized, however, they are circularly polarized at the vacuum resonance point. The direction of the major axis also changes by 90° at the vacuum resonance, which is shown in Figure 1.5. So, the extraordinary mode (E-mode), of which the polarization is perpendicular to the plane determined by the photon momentum and the magnetic field, in the plasma-dominant regime corresponds the ordinary mode (O-mode), of which the polarization is parallel to the plane defined above, in the vacuum-dominant regime and vice versa.

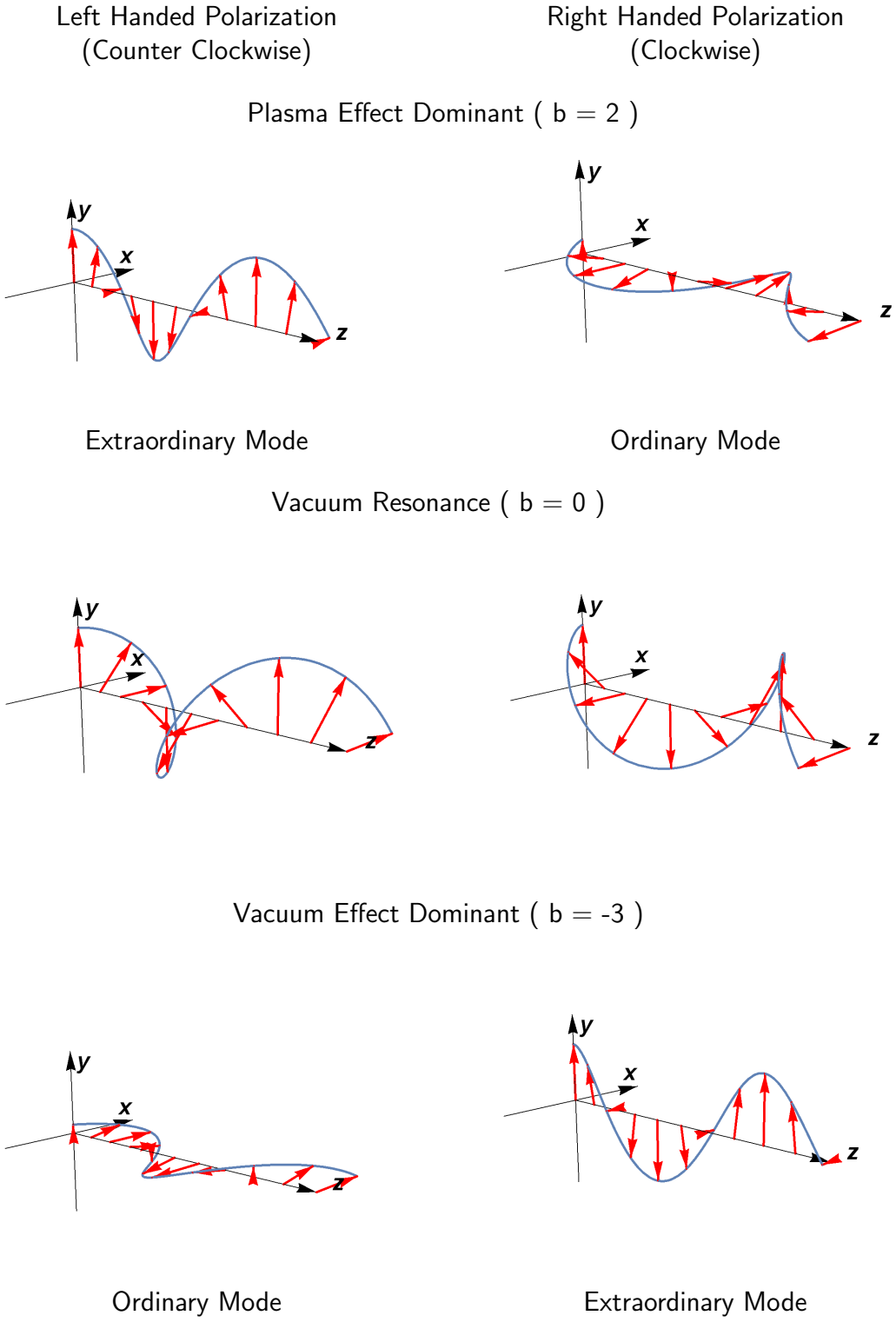

Figure 1.5: Behaviors of the polarization of the left handed and the right handed elliptical polarization. The polarization vectors are shown by red allows and the trajectories are shown by the blue lines. The electromagnetic wave propagates in the z-direction. The direction of the magnetic field is on $z - x$ plane. The left panels show the case of the left handed polarization and the right ones exhibit the right handed polarization. The top, middle and bottom panels are the cases for $b = 2$, $b = 0$ and $b = -3$. In the case of $b = 2$, the dielectric effect by the plasma is dominant. On the other hand, the vacuum effect is dominant in the case of $b = -3$. At $b = 0$, the vacuum resonance occurs and the eigenmodes are the circular polarization.

1.3 Application and Validation

1.3.1 Laser Experiments

Laser experiments are tools to obtain the strong electromagnetic fields. The laser was first realized using ruby in 1960 (Maiman, 1960). Just after being invented, the second harmonic generation, which is one of the specific phenomena of the nonlinear optics, was confirmed by Franken et al. (1961).[1] Further phenomena peculiar to the nonlinear optics were not seen until the chirped pulse amplification (CPA) (Strickland and Mourou, 1985) was developed and incorporated in the experiments. This is a method to obtain the high power laser pulse, in which the optical laser pulse is stretched and then amplified before the compression of the pulse. As the laser intensity increased (Tajima and Mourou, 2002; Mourou and Tajima, 2012), the changes of the electron's dynamics in the atoms and an electron reaching the relativistic regime were observed (Di Piazza et al., 2012). The current highest intensity of laser is $2 \times 10^{22}\mathrm{W/cm^2}$, which is reached by the *HERCULES 300 TW laser* (Yanovsky et al., 2008). A variety of the plans of high field laser facilities including the GEKKO EXA and the Extreme Light Infrastructure are now progressing.

Although the nonlinear QED phenomenon of the vacuum has not been validated yet, there are many theoretical studies for the test of the quantum properties of the vacuum. The photon-photon scattering is one of the specific processes in the quantum regime and it has been researched for a long time in order to be detected in the terrestrial experiments. The lowest order process is the fourth-order process.

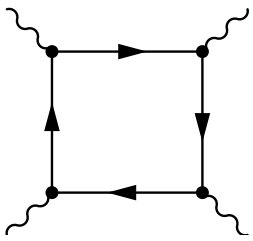

Figure 1.6: Feynman diagram of the lowest order of the photon-photon scattering.

The total cross section of this process is determined by the momenta of the two photons, which collide with each other, and it is known that the cross section is very small (Berestetskii et al.). When the third auxiliary laser in addition to the two colliding lasers is applied, the cross section of the photon-photon scattering increases (Varfolomeev, 1966), and they also suggested the the experimental setup.

The polarization of the photon in the external laser field has been also considered as a tool to verify the nonlinearity of the vacuum. The rotation of the plane of the polarization were considered in the experimental setups (Heinzl et al., 2006; di Piazza et al., 2006). The probe photon is assumed to be emitted from the X-ray free electron laser and it passes through the standing wave of the laser fields. The birefringence of the vacuum causes the rotation of the plane of the polarization.

[1] In this paper, the evidence of the second harmonic generation, which is a small spot in a photograph, is not shown. It is said that one of the journal technician erased it (Haroche, 2008).

The birefringence was also considered in the plasma. Di Piazza et al. (2007) took into account that the laser propagates through the medium consisting of the cold collisional electron and proton plasma. They calculated the refractive index for the laser photons and estimated the difference of the phase of the circularly polarized laser which had passed through the region with different plasma densities in the experimental setup they considered.

Other nonlinear phenomena of the vacuum have been also researched. The nonlinear behavior of the laser in the waveguides is studied by Brodin et al. (2001). In certain setups, a electromagnetic wave mode which has different frequency with that of the incident laser is induced. Monden and Kodama (2011) investigated the dependence of the angular aperture of the focused laser on the dielectric properties of the vacuum. They showed that the emission of the photons induced by the nonlinearity of the vacuum is strongly enhanced as the angular aperture increases.

The X-ray free electron laser (XFEL) produces coherent and ultrashort X-ray pulses, which are linearly polarized. Circular polarization in the XFEL was also realized in the SPring-8 Angstrom Compact Free-Electron Laser (SACLA) by the X-ray phase retarder made of diamond crystals and measured by fine powders of $CoPt_3$ and the silicon PIN diodes (Suzuki et al., 2014). The X-ray magnetic circular dichroism effect is utilized to measure the circular polarization (Maruyama et al., 1995).

1.3.2 Emission from Neutron Star

The existence of a neutron star was theoretically predicted by Baade and Zwicky (1934). In contrast, the first evidence of its existence was obtained after more than 30 years since then. In 1967, the radio pulses with constant time intervals were discovered (Hewish et al., 1968). The source of the pulses was thought to be originated from the star rotation because of their precise timing. From the short period of the pulse, the star was turned out to be a neutron star theoretically because it is not destroyed by the centrifugal force.

As the observational results of neutron stars were obtained, it was found that the period, which is the pulse interval, gets longer with time. This is explained by the rotating vector model, in which the radiation of a neutron star is caused by rotating magnetic dipole. The rotating vector model fits the energy balance of the expected dipole radiation and the emission from the Crab nebula well. One of the main energy source of the emission is the rotation energy. Radio pulsars are thought to be rotationally powered like the Crab.

The dipole magnetic field strength is estimated from the period P and the derivative of it $\dot{P}$ in this picture as

$$\begin{aligned} B_p &= \left(\frac{3Ic^3P\dot{P}}{8\pi^2R^6}\right)^{1/2} \\ &\simeq 1.0\times10^{12}\,\mathrm{G} \\ &\quad\times\left(\frac{I}{10^{45}\,\mathrm{g\,cm^2}}\right)^{1/2}\left(\frac{10^6\,\mathrm{cm}}{R}\right)^3\left(\frac{P}{10\,\mathrm{ms}}\right)^{1/2}\left(\frac{\dot{P}}{10^{-13}\,\mathrm{s/s}}\right)^{1/2}, \end{aligned} \tag{1.50}$$

where I is the inertial moment of the neutron star and R is the star radius, and neutron stars roughly takes B_p as 10^{12}G. Assuming the dipole magnetic field is constant, the age of a neutron star can be estimated as

$$\tau = \frac{P}{2\dot{P}} \simeq 1600\,\mathrm{yrs}\left(\frac{P}{10\,\mathrm{ms}}\right)\left(\frac{10^{-13}\,\mathrm{s/s}}{\dot{P}}\right), \tag{1.51}$$

which is known as the characteristic age. The spin periods and the period derivatives of the known pulsars are shown in Figure 1.7, which is called the P-Pdot diagram. The spin period (P) is exhibited in the horizontal axis and the period derivative ($\dot{P}$) is presented in the vertical axis. The lines of constant dipole magnetic fields (Equation (1.50)) and those of the characteristic age (Equation (1.51)) are also shown.

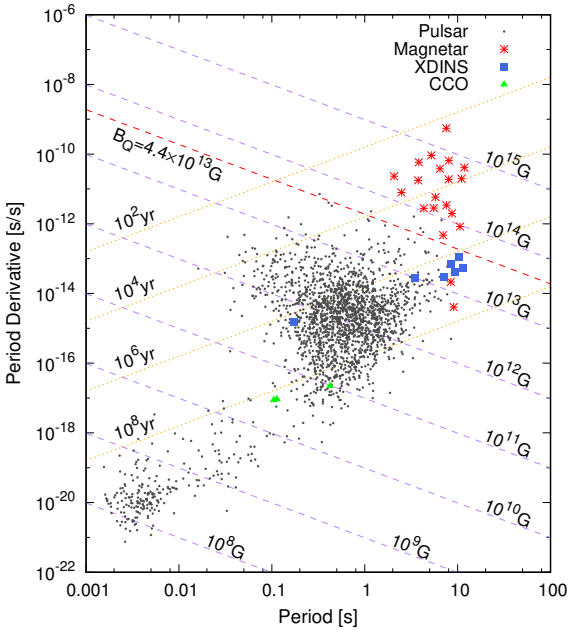

Figure 1.7: P-Pdot diagram. The data is taken from the ATNF Pulsar Catalogue (`http://www.atnf.csiro.au/research/pulsar/psrcat/`) (Manchester et al., 2005).

The development of observation has increased the number of pulsars. Some neutron stars are known to have extremely strong magnetic field of $\sim 10^{14-15}$G, which are called magnetars. Magnetars are characterized by the fact that their X-ray luminosity is higher than the spin-down luminosity and also by their burst activities. Although the source of the burst activities has not been understood, it is thought that the energy source is their strong magnetic field. Magnetars' dipole magnetic field is usually higher than the quantum critical field $B_Q = 4.4 \times 10^{13}$G. There are also magnetars whose magnetic field is weaker than the critical value. One of such objects, SGR 0418+5729 shows the absorption line in their spectrum (Tiengo et al., 2013). Although the dipole magnetic field of this magnetar is 6×10^{12}G, there is local magnetic field of $> 10^{14}$G on the surface if the absorption feature comes

from the proton cyclotron absorption. The existence of the toroidal magnetic field of $\sim 10^{16}$G is hinted in the modulation of the period of 4U 0142+61 (Makishima et al., 2014). Thus, it is observationally suggested that there are magnetic fields such as the toroidal component, other than the dipole component in magnetars.

Recently, the magnetar-like behavior by neutron stars which are not classified as mangetars is observed. The object 1E 161348-5055, which is known as a central compact object (CCO) in the supernova remnant (SNR) RCW 103 shows a magnetar-like outburst (Rea et al., 2016), and that by a high-field radio pulsar PSR J1119-6127 is also observed (Archibald et al., 2016).

The light curve, the spectrum and the image of the neutron star and its PWN have given us a lot of information about them. The polarization is another observational quantity. The polarization properties of neutron stars' emission are obtained only in the radio frequency in most cases. The emissions from radio pulsars, which are discovered by their radio pulses, have strong linear polarizations. The polarization angle swings like an S shape around the pulse, which is interpreted by the rotating vector model. On the other hand, this situation changes for higher photon energies. In the optical, although the observation technique is developed, neutron stars are dim in this energy range. The polarizations of a few neutron stars, e.g., the Crab pulsar, are observed.

In contrast, the observation of polarization is difficult in the energy ranges of X-ray and gamma ray. Historically, the X-ray polarimetry satellite $OSO-8$ observed the Crab pulsar in 2.6 keV and 5.2 keV for the first time. Although the polarization of the pulsar wind nebula (PWN) around the pulsar is observed (Weisskopf et al., 1978), the polarization of the pulsar itself was not obtained but for the upper limits (Silver et al., 1978). The polarization of the Crab pulsar itself was first observed by $INTEGRAL/SPI$ (Dean et al., 2008). The off-pulse component of the light curve of the Crab pulsar in from 0.1MeV to 1MeV was measured. An off-pulse component was also observed by another instrument of $INTEGRAL$, $IBIS$ (Forot et al., 2008).

The instruments explained above are satellite-borne. The polarization properties of the Crab pulsar are also observed by the balloon-borne instruments. *PoGOLite Pathfinder* and *PoGO+* are the balloon-borne instruments and observe the polarization of the high energy emission from the Crab pulsar (Chauvin et al., 2016, 2017). *PoGO+* measured the two pulse components of the emission of the Crab pulsar. It first obtained the polarization properties of the component of the second pulse counted from the off-pulse component. Recently, *AstroSat* detected the phase-resolved polarization properties. The polarization for the Crab pulsar and its PWN was measured. The polarization properties of the Crab pulsar is summarized in Table 1.1.

Although the polarization of the high energy emission has been observed for $\gtrsim$ 20keV except the observation by $OSO-8$ until now, the polarimetry of the soft X-ray will be done in the near future. Multiple projects, $IXPE$, $XIPE$ and $eXTP$, are planned and the energy range of the observation is $\lesssim$ 10keV. $IXPE$ is decided to be launched.

Table 1.1: Observed polarization properties of the Crab pulsar and nebula in the high energy emission. PA and PF are the polarization angle and the polarization fraction, respectively.

Instrument	Energy	PA	PF	Notes
$OSO-8$	2.6 keV	$156°.4 \pm 1°.4$	$19.2\% \pm 1.0\%$	PWN
	5.2 keV	$152°.6 \pm 4°.0$	$19.5\% \pm 2.8\%$	PWN
$INTEGRAL/SPI$	0.1-1.0 MeV	$123° \pm 11°$	$46\% \pm 10\%$	Pulsar, off-pulse
$INTEGRAL/IBIS$	200-800 keV	$120°.6 \pm 8°.5$	$> 72\%$	Pulsar, off-pulse
	200-800 keV	$100° \pm 11°$	$47\%^{+19\%}_{-13\%}$	Pulsar, phase-averaged
PoGOLite Pathfinder	20-120 keV	$149°.2 \pm 16°.0$	$18.4\%\pm^{+9.8\%}_{-10.6\%}$	Pulsar, phase-averaged
PoGO+	20-160 keV	$137° \pm 15°$	$17.4\%\pm^{+8.6\%}_{-9.3\%}$	Pulsar, off-pulse
	20-160 keV	$86° \pm 18°$	$33.5\%\pm^{+18.6\%}_{-22.3\%}$	Pulsar, P2
	20-160 keV	$131°.3 \pm 6°.8$	$20.9\% \pm 5.0\%$	Pulsar, phase-averaged
AstroSat CZT Imager	100-380 keV	$143°.5 \pm 2°.8$	$32.7 \pm 5.8\%$	Pulsar+PWN, total

The references are (Weisskopf et al., 1978) for OSO-8, (Dean et al., 2008) for *INTEGRAL/SPI*, (Forot et al., 2008) for *INTEGRAL/IBIS*, (Chauvin et al., 2016) for *PoGOLite Pathfinder*, (Chauvin et al., 2017) for *PoGO+* and (Vadawale et al., 2017) for *AstroSat CZT Imager*. Note also that *AstroSat CZT Imager* observed the phase-resolved polarization properties.

The emission of the soft X-ray corresponds to the thermal radiation from magnetars. It is thought to be emitted from the magnetars' surfaces and the polarization properties of the thermal component contain the information of the physical properties of the surface. The radiation from the surface may be also influenced by the vacuum birefringence of their magnetic fields (Heyl and Shaviv, 2002) and it may cause strongly polarized emission from magnetars. This is peculiar to nonlinear QED and if the strongly polarized emission is observed by the future polarimetry, it would be the evidence to the validation of nonlinear QED.

Recently, the polarization of RX J1856.5-3754, which is labeled as an X-ray dim isolated neutron star (XDINS), was observed in the optical wavelength (Mignani et al., 2017). The emission of XDINSs consists only of the surface thermal radiation and the strength of their magnetic fields are $\sim 10^{13}$G. The phase-averaged polarization fraction of RX J1856.5-3754 is $16.43\% \pm 5.26\%$ and the nonlinear QED effect is necessary to explain this value (Mignani et al., 2017). This is a strong hint to verify nonlinear QED.

There is another interesting topic in this observation, the surface properties of XDINSs. There are two possible states on the surface of XDINSs. One is the gas atmosphere state, which is like other neutron stars. The gas atmosphere on neutron stars consists of hydrogen plasma, which accretes from the interstellar medium. When the surface is hot enough to cause the nuclear burning, helium and carbon are contained in the gas atmosphere (Potekhin, 2014). The other state is the so-called condensed state. The strong magnetic field and low temperature of XDINSs stabilize the molecular chain of the elongated atoms and atoms do not become the gas state. In the former case, the radiation from the gas atmosphere is scattered in the plasma. The opacity differs for each polarization eigenmode and the opacity of the one mode is suppressed in the strong magnetic field. Thus, the surface radiation

is polarized in this case. In contrast, in the case of the condensed state, the surface emission directly escape from the condensed surface and it is not scattered by the plasma. Then, the polarization properties are determined on the surface and the surface emission is not so strongly polarized in this case.

In the optical observation of RX J1856.5-3754, the polarization fraction can be explained by the both surface models. So, its surface state could not be determined. The different surface models give a different feature. González Caniulef et al. (2016) calculated the polarization in the soft X-ray energy range ($0.12 - 0.39$keV) for the gas atmosphere and the condensed surface. They found that the strongly polarized emission is measured in the case of the gas atmosphere and that weakly polarized one is observed in the case of the condensed surface. Thus, we will understand which model is right when the polarization of the energy range of $\lesssim 0.1$keV is observed.

1.4 Main Topics of this Thesis

In this thesis, I first focus on the vacuum polarization, which is an elementary process in nonlinear QED. I derive the expression of the vacuum polarization in the external plane wave and estimate the refractive index for the probe photon quantitatively. I do not assume the plane wave can be seen as the locally constant electromagnetic field but consider the variation of the external field. The vacuum polarization is calculated by the induced electromagnetic current, which is derived from the effective Lagrangian, instead of the calculation of the Feynman diagrams with the electron propagator in the external field. I compute the refractive index of the probe photon by solving the equation. Then, I focus on how the vacuum polarization is manifested in the X-ray polarimetry of neutron stars. I discuss the influence of the strong magnetic field around neutron stars on their surface radiation. The strong magnetic field affects the polarization of the surface radiation. I also take into account the conversion of the polarization mode, which may occur near the neutron star surface if the dielectric property induced from the plasma of the gas atmosphere as well as that caused by the vacuum polarization. I compute systematically the observed polarization of the surface radiation from neutron stars for various parameters such as the magnetic field of the neutron star.

This thesis is organized as follows: the vacuum polarization in the external plane wave field is investigated in Chapter 2. The refractive index of the probe photon is computed with taking into account the variation of the external field. The crossed field, which can be regarded as the long-wavelength limit of the plane wave, is also considered as the external field. In chapter 3, the polarization properties of the surface radiation from neutron stars are systematically computed. The vacuum polarization is important for the conversion of the polarization mode and for the evolution of the polarization around the neutron star. I conclude this thesis in Chapter 4.

2
QED Vacuum Polarization

2.1 Introduction

In the quantum vacuum, virtual particles and anti-particles are produced and annihilated repeatedly in very short times as intuitively represented by bubble Feynman diagrams. When an external field is applied, even these virtual particles are affected, leading to modifications of the property of quantum vacuum. One of the interesting consequences is a deviation of the refractive index from unity accompanied by a birefringence, i.e., distinct refractive indices for different polarization modes of photon[1]. It is a purely quantum effect that becomes remarkable when the strength of the external field approaches or even exceeds the critical value, $f_c = m^2/e$ with m and e being the electron mass and the elementary charge in this chapter, respectively, whereas, the deviation of the refractive index from unity is proportional to the field-strength squared for much weaker fields. Note also that I use the Heaviside-Lorentz unit with the natural unit ($c = \hbar = 1$) in this chapter. Photon splitting, which is another phenomenon in external fields, has been also considered (Affleck and Kruglyak, 1987).

Such strong electromagnetic fields are not unrealistic these days. In fact, the astronomical objects called magnetars are a subclass of neutron stars, which are believed to have dipole magnetic fields of $\sim 10^{14-15}$G (Olausen and Kaspi, 2014)[2]. Although the origin of such strong magnetic fields is still unknown, they are supposed to have implications for various activities of magnetars such as giant flares and X-ray emissions (Mereghetti, 2008). In fact, their strong magnetic fields are thought to affect the polarization properties of surface emissions from neutron stars by the quantum effect (Heyl and Shaviv, 2002; Taverna et al., 2015). This phe-

[1]Interestingly, this does not occur for the nonlinear electrodynamics theory by Born and Infeld (Bialynicki-Birula, 1983).

[2]The online catalog of magnetars is found at (`http://www.physics.mcgill.ca/~pulsar/magnetar/main.html`).

nomenon may have indeed been detected in a recent optical polarimetric observation (Mignani et al., 2017). The quantum correction may also play an important role through the so-called resonant mode conversions (Mészáros and Ventura, 1979; Lai and Ho, 2003a). On the other hand, the progress in the high-field laser is very fast. Although the highest intensity realized so far by Hercules laser at CUOS (Yanovsky et al., 2008) is still sub-critical ($2 \times 10^{22}\mathrm{W/cm^2}$) for the moment, I may justifiably expect that the laser intensity will reach the critical value in not-so-far a future. Some theoretical studies on the vacuum polarization are meant for the experimental setups in the high-field laser (Heinzl et al., 2006; Dinu et al., 2014b,a; Karbstein and Shaisultanov, 2015; King and Heinzl, 2016).

The study of the vacuum polarization in strong-field QED has a long history. It was pioneered by Toll (1952). He studied in his dissertation the polarization of vacuum in stationary and homogeneous magnetic fields in detail and many authors followed with different methods, both analytic and numerical (Baier and Breitenlohner, 1967a; Brezin and Itzykson, 1971; Adler, 1971; Tsai and Erber, 1974, 1975; Kohri and Yamada, 2002; Shore, 2007; Hattori and Itakura, 2013a,b; Ishikawa et al., 2013; Karbstein, 2013), and obtained the refractive indices. The vacuum polarization for mixtures of constant electric and magnetic fields was also investigated (Bialynicka-Birula and Bialynicki-Birula, 1970; Batalin and Shabad, 1971; Urrutia, 1978; Artimovich, 1990; Dittrich and Gies, 2000; Schubert, 2000). Note that such fields can be brought to either a purely magnetic or a purely electric field by an appropriate Lorentz transformation, with so-called crossed fields being an exception.

In Toll (1952), the polarization in the crossed field was also discussed. The crossed field may be regarded as a long wavelength limit of electromagnetic waves, having mutually orthogonal electric and magnetic fields of the same amplitude. Toll first calculated the imaginary part of the refractive index from the amplitude of pair creations and then evaluated the real part of refractive index via the Kramers-Kronig relation. Although there was no limitation to the probe-photon energy, the external-field strength was restricted to small values (weak-field limit) because he ignored the modification of the dispersion relation of the probe photon. Baier and Breitenlohner (1967b) obtained the refractive index for the crossed field in two different ways: they first employed the polarization tensor that had been inferred in Baier and Breitenlohner (1967a) from the 1-loop calculation for the external magnetic fields, and utilized in the second method the expansion of the Euler-Heisenberg Lagrangian to the lowest order of field strength. Note that both approaches are valid only for weak fields or low-energy probe photons.

The expression of the polarization tensor to the full order of field strength for the external crossed field was obtained from the 1-loop calculation with the electron propagator derived either with Schwinger's proper-time method (Narozhnyĭ, 1969) or with Volkov's solution (Ritus, 1972). In Narozhnyĭ (1969), the general expressions for the dispersion relations and the refractive indices of the two eigenmodes were obtained. Note, however, that the refractive indices were evaluated only in the limit of the weak-field and strong-field[3]. On the other hand, another expression

[3]Although these limits are referred to as "weak-field limit" and "strong-field limit" in the literature, they may be better called "weak-field or low-energy limit" and "strong-field and high-

of polarization tensor was obtained and its asymptotic limit was derived in Ritus (1972) although the refractive index was not considered.

The evaluation of the refractive index based on the polarization tensor of Ritus (1972) was attempted by Heinzl and Schröder (2006) in two different ways: the first one is based on the hypothesized expression of the polarization tensor in the so-called large-order expansion with respect to the probe-photon energy; in the evaluation of the real part of the refractive index, the external crossed field was taken into account only to the lowest order of the field strength in each term of the expansion and the imaginary part was estimated from the hypothesized integral representation; in the second approach, the polarization tensor was expanded with respect to the product of the external-field strength and the probe-photon energy, and the refractive index was evaluated; the imaginary part was calculated consistently to the leading order and the anomalous dispersion for high-energy probe photons, which had been demonstrated by Toll (1952), was confirmed. Note that in these evaluations of the refractive index in the crossed field, the modification of the dispersion relation for the probe photon was again ignored as in Toll (1952) and hence the results cannot be applied to super-critical fields.

It should be now clear that the vacuum polarization and the refractive index have not been fully evaluated for supra-critical field strengths even in the crossed field. One of my goals is hence to do just that.

It is understandable, on the other hand, that the evaluation of the refractive index in the external electromagnetic plane-wave is more involved because of its non-uniformity. In fact, the refractive index has not been obtained except for some limiting cases. The polarization tensor and the refractive index in the external plane-wave were first discussed by Becker and Mitter (1975). They derived the polarization tensor in momentum space from the 1-loop calculation with the electron propagator obtained by Mitter (1975), which is actually Volkov's propagator represented in momentum space. Although the formulation is complete, the integrations were performed only for circularly polarized plane-waves as the background. The refractive indices were then evaluated at very high energies ($\gg m$) of the probe photon.

Baĭer et al. (1975) calculated scattering amplitudes of a probe photon again by the circularly-polarized external plane-wave to the 1-loop order, employing the electron propagator expressed with the proper-time integral. The general expression of the dispersion relation was obtained but evaluated only in the weak-field and low-energy limit. The refractive indices for the eigenmodes of probe photons were also calculated in this limit alone. Affleck (1988) treated this problem by expanding the Euler-Heisenberg Lagrangian to the lowest order of the field strength, assuming that the external field varies slowly in time and space. The refractive index was evaluated only in the weak-field limit again. Recently, yet another representation of the polarization tensor in the external plane-wave was obtained from the calculation of the 1-loop diagram with Volkov's electron propagator (Meuren et al., 2013). Only the expression of the polarization tensor was obtained, however, and no attempt was made to evaluate it in this study.

In their paper, Dinu et al. (2014b) employed the light front field theory, one of the

energy limit", respectively. See Figure 2.2 for the actual parameter region.

most mathematically sophisticated formulations, to derive the amplitude of photon-photon scatterings, from which the refractive index integrated over the photon path was obtained. They calculated it for a wide range of the probe-photon energy and field strength. Although they gave the expression for the local refractive index, it was not evaluated. The eigenmodes of probe photons were not calculated, either.

In this chapter, I also derive the expression of the polarization tensor and the refractive index for the external electromagnetic plane-wave, developing a perturbation theory for the induced electromagnetic current based on the proper-time method. It is similar to Adler's formulation (Adler, 1971) but is more general, based on the interaction picture, or Furry's picture, and not restricted to a particular field configuration. Combining it with the so-called gradient expansion, I calculate the lowest-order correction from temporal and spatial field variations to the induced electromagnetic current, and hence to the vacuum polarization tensor also, for the crossed fields. This is nothing but the WKB approximation and, as such, may be applicable not only to the electromagnetic wave but also to any slowly-varying background electromagnetic fields. I then evaluate numerically the refractive indices for eigenmodes of the Maxwell equations with the modification of the dispersion relation being fully taken into account. Note that unlike Dinu et al. (2014b) my results are not integrated over the photon path but local, being obtained at each point in the plane wave.

The chapter is organized as follows: I first review Schwinger's proper time method briefly and then outline the perturbation theory based on the Furry picture to obtain the induced electromagnetic current to the linear order of the field strength of the probe photon in Section 2.2. This is not a new stuff. I then apply it to the plane-wave background in Section 2.3; in so doing, I also appeal to the so-called gradient expansion of the background electromagnetic wave around the crossed field. Technical details are given in Sections 2.6 - 2.10. Numerical evaluations are performed both for the crossed fields and for the first-order corrections in Section 2.4; I summarize the results and conclude this chapter in Section 2.5.

2.2 Perturbation Theory in Proper-Time Method

In this section, I briefly summarize Schwinger's proper-time method and outline its perturbation theory, which will be applied to monochromatic plane-waves in the next section.

2.2.1 Schwinger's Proper-Time Method

The effective action of electromagnetic fields is represented as

$$\Gamma = \Gamma_{\rm cl} + \Gamma_{\rm q}, \tag{2.1}$$

where $\Gamma_{\rm cl}$ is the classical action and $\Gamma_{\rm q}$ is the quantum correction, which satisfies the following relation:

$$\frac{\delta\Gamma_{\rm q}}{\delta A_\mu} \equiv \langle j^\mu(x)\rangle = ie\,{\rm tr}[\gamma^\mu G(x,x)]. \tag{2.2}$$

Then, the vacuum Maxwell equation is modified as

$$-\Box A_\mu + \partial^\nu \partial_\mu A_\nu - \langle j_\mu \rangle = 0. \tag{2.3}$$

Although there is no electromagnetic current generated by real charged particles in the vacuum, $\langle j_\mu \rangle$ defined in this way is referred to as the induced electromagnetic current (Dittrich and Gies, 2000). This term can be written with the electron propagator $G(x, y)$ (Schwinger, 1951) with tr in Equation (2.2) being the trace, or the diagonal sum on spinor indices; γ^μ's are the gamma matrices. In this chapter, the Greek indices run over 0 through 3 and the Minkowski metric is assumed to be $\eta = \mathrm{diag}(+, -, -, -)$.

The electron propagator G in the external electromagnetic field is different from the ordinary one in the vacuum and the modification by the external field, the strength of which is close to or even exceeds the critical value f_c, cannot be treated perturbatively. The proper-time method is a powerful tool to handle such situations. The electron propagator satisfies the Dirac equation in the external electromagnetic field A^μ:

$$(i\gamma^\mu \partial_\mu - e\gamma^\mu A_\mu(x) - m)G(x, y) = \delta^4(x - y). \tag{2.4}$$

It is supposed in the proper-time method that there exists an operator $\hat{G}$, the x-representation of which gives the propagator as $\langle x|\hat{G}|y\rangle = G(x, y)$. Then Equation (2.4) can be cast into the following equation for the operators:

$$(\gamma^\mu \hat{\Pi}_\mu - m)\hat{G} = \hat{\mathbf{1}}, \tag{2.5}$$

where $\hat{\mathbf{1}}$ is the unit operator and $\hat{\Pi}_\mu = i\partial_\mu - eA_\mu$. Here I used $\delta^4(x - y) = \langle x|y\rangle$. From this equation, the operator $\hat{G}$ is formally solved as

$$\hat{G} = \frac{\hat{\mathbf{1}}}{\gamma^\mu \hat{\Pi}_\mu - m}, \tag{2.6}$$

which can be cast into the following integral form:

$$\hat{G} = i(-\gamma^\mu \hat{\Pi}_\mu - m) \int_0^\infty ds \exp\left[-i(m^2 - (\gamma^\mu \hat{\Pi}_\mu)^2 - i\varepsilon)s\right]. \tag{2.7}$$

In the above expression, the parameter s is called the proper-time and $-i\varepsilon$ is introduced to make the integration convergent as usual and will be dropped hereafter for brevity. The electron propagator, being an x-representation of this operator, is obtained as

$$G(x, y) = i \int_0^\infty ds e^{-im^2 s} \left[\langle x| - \gamma^\mu \hat{\Pi}_\mu e^{-i(-(\gamma^\nu \hat{\Pi}_\nu)^2)s}|y\rangle - \langle x|m e^{-i(-(\gamma^\mu \hat{\Pi}_\mu)^2)s}|y\rangle\right]. \tag{2.8}$$

Here I had better comment on the boundary condition for the electron propagator, or the causal Green function, in the electromagnetic wave. This issue may be addressed most conveniently for finite wave trains in the so-called light front formulation (e.g. Kogut and Soper (1970); Neville and Rohrlich (1971)), in which double null coordinates are employed. This is because the asymptotic states in the remote

past and future (in the null-coordinate sense) are unambiguously defined (Neville and Rohrlich, 1971), which is crucially important particularly when one calculates S-matrix elements (Dinu et al., 2014b; Neville and Rohrlich, 1971); it is also important that the translational symmetry is manifest in one of the null coordinates. Then the causal Green function is obtained in the usual way, i.e., by the appropriate linear combination of the homogeneous Green functions with positive- and negative-energies according to the time ordering in the null coordinate (Kogut and Soper, 1970; Neville and Rohrlich, 1971). On the other hand, it is a well-known fact that the Dirac equation can be solved in a closed form for an arbitrary plane wave (Volkov, 1935; Mitter, 1975). It is then possible to construct the same causal Green function with these Volkov solutions (Ritus, 1972; Mitter, 1975). According to Ritus (1972), all that is needed is a well-known $-i\epsilon$ prescription, i.e., the introduction of an infinitesimal negative imaginary mass. It was pointed out by Mitter (1975) then that this is equivalent to the same prescription in the proper-time method of Schwinger, that is, the formulation I adopt in this chapter (see Equation (2.7)). In this sense, the propagator I employ in this chapter is the causal Green function thus obtained in the limit of the infinite wave train. As will become clear later (see Equation (2.38) in Section 2.3), since I employ the gradient expansion in the local approximation, the distinction between the finite or infinite wave train will not be important in my formulation.

Returning to Equation (2.8) and interpreting the operator $e^{-i(-(\gamma^\mu\hat{\Pi}_\mu)^2)s}$ as the evolution operator in the proper-time, one can reduce the original field-theoretic problem to the one in quantum mechanics for the Hamiltonian $H = -(\gamma^\mu\hat{\Pi}_\mu)^2$. Then the transformation amplitude is given as

$$\begin{aligned}\langle x|e^{-i(-(\gamma^\mu\hat{\Pi}_\mu)^2)s}|y\rangle &= \langle x|e^{-iHs}|y\rangle \\ &= \langle x(s)|y(0)\rangle. \end{aligned} \tag{2.9}$$

Here the state $|x(s)\rangle$ is defined as the eigenstate for the operator $\hat{x}$ in the Heisenberg picture:

$$|x(s)\rangle \equiv e^{iHs}|x\rangle. \tag{2.10}$$

The Hamiltonian H is expressed as

$$H = -\hat{\Pi}^2 + \frac{1}{2}e\sigma^{\mu\nu}F_{\mu\nu}, \tag{2.11}$$

where I used the Clifford algebra for the gamma matrices $\{\gamma^\mu,\gamma^\nu\} = 2\eta^{\mu\nu}$ and the commutation relation $[\Pi^\mu,\Pi^\nu] = -ieF^{\mu\nu}$ to obtain $\hat{\Pi}^2 = \hat{\Pi}_\mu\hat{\Pi}^\mu$ and $\sigma^{\mu\nu} = \frac{i}{2}[\gamma^\mu,\gamma^\nu]$; A_μ and $F_{\mu\nu}$ are the vector potential and the field tensor for the external electromagnetic field, respectively. The proper-time evolutions of the operators $\hat{x}$ and $\hat{\Pi}$ are given by the Heisenberg equations:

$$\frac{d\hat{x}^\mu(s)}{ds} = 2\hat{\Pi}^\mu(s), \tag{2.12}$$

$$\frac{d\hat{\Pi}^\mu(s)}{ds} = 2eF^\mu{}_\nu\hat{\Pi}^\nu(s) + e^{iHs}ie\frac{\partial F^\mu{}_\nu}{\partial x_\nu}e^{-iHs} + e^{iHs}\frac{1}{2}e\sigma^{\nu\lambda}\frac{\partial F_{\nu\lambda}}{\partial x_\mu}e^{-iHs}. \tag{2.13}$$

Then, the induced electromagnetic current $\langle j^\mu \rangle$ in Equation (2.2) is represented as follows (Adler, 1971):

$$\begin{aligned}\langle j^\mu(x)\rangle &= \frac{e}{2}\int_0^\infty ds\, e^{-im^2 s}\mathrm{tr}\Big[\langle x(s)|\hat{\Pi}^\mu(s)+\hat{\Pi}^\mu(0)|x(0)\rangle \\ &\qquad -i\sigma^{\mu\nu}\langle x(s)|\hat{\Pi}_\nu(s)-\hat{\Pi}_\nu(0)|x(0)\rangle\Big]. \end{aligned} \tag{2.14}$$

Note that this is equivalent to the 1-loop approximation with the external field being fully taken into account.

In order to obtain the refractive index of the vacuum in the presence of an external electromagnetic field, I have to consider a probe photon in addition to the background electromagnetic field and apply Equation (2.3) to the amplitude of the probe photon. In so doing, the induced electromagnetic current $\langle j_\mu \rangle$ needs to be evaluated to the linear order of the amplitude of the probe photon and the perturbation theory is required at this point (Dittrich and Gies, 2000). The Heisenberg equations given above can be solved analytically for some limited cases such as time-independent homogeneous electric or magnetic fields and single electromagnetic plane-waves (Schwinger, 1951). I will employ the latter as an unperturbed solution in the perturbative calculations in Section 2.3. It is stressed that calculating the effective action for a given plane-wave background and taking its derivative with respective to the field strength is not sufficient for the evaluation of the refractive index, since the probe photon in general has a different wavelength and propagates in a different direction from those of the background electromagnetic wave. I hence need to take these differences fully into account in the perturbative calculations of the induced electromagnetic current. This was essentially done by Becker and Mitter (1975) in a different framework, i.e., performing 1-loop calculations in momentum space. In this chapter I assume that the background wave has a long wavelength and calculate the refractive index locally in the sense of the WKB-approximation. In so doing, I appeal to the gradient expansion of the background plane wave as explained in Section 2.3.

2.2.2 Outline of Perturbation Theory

I now consider the perturbation theory in the proper-time method. The purpose is to evaluate the induced electromagnetic current Equation (2.14) up to the linear order of the amplitude of the probe photon, which is supposed to propagate in an external electromagnetic field. It is then plugged into Equation (2.3) to derive the refractive indices. The Heisenberg equations (2.12), (2.13) can be analytically solved for a single monochromatic electromagnetic plane-wave (Schwinger, 1951). The calculation of the first order corrections to this solution is the main achievement in this chapter. As explained in the next section, I employ further the gradient expansion of the background electromagnetic wave, which in turn enables us to obtain the refractive indices locally in the WKB sense. In this section, I give the outline of the generic part of this perturbation theory, which is not limited to the plane-wave background. I will then proceed to its application to the monochromatic plane-wave background in the next section.

In the perturbation theory, the external electromagnetic fields are divided into two pieces: the background A^μ and the perturbation b^μ. The corresponding field strengths are denoted by $F_{\mu\nu}$ and $g_{\mu\nu}$, respectively. I take the latter into account only to the first order. Then, the Hamiltonian given in Equation (2.11) can be written as

$$\begin{aligned} H &= -\left(i\partial_\mu - eA_\mu(\hat{x}) - eb_\mu(\hat{x})\right)^2 + \frac{1}{2}e\sigma^{\mu\nu}\left(F_{\mu\nu}(\hat{x}) + g_{\mu\nu}(\hat{x})\right) \\ &= H^{(0)} + \delta H. \end{aligned} \tag{2.15}$$

In this expression, $H^{(0)}$ is the unperturbed Hamiltonian, for which I assume that the proper-time evolution is known, preferably analytically as in the time-independent homogeneous electric or magnetic fields and the single plane-wave. δH is the perturbation to the Hamiltonian. It is evaluated to the first order of b_μ and expressed with $\delta\Pi_\mu = -eb_\mu$ as

$$\delta H = -\hat{\Pi}_\mu^{(0)}\delta\hat{\Pi}^\mu - \delta\hat{\Pi}^\mu\hat{\Pi}_\mu^{(0)} + \frac{1}{2}e\sigma^{\mu\nu}g_{\mu\nu}. \tag{2.16}$$

In the proper-time method, the amplitudes of operators such as $\langle x(s)|\hat{\Pi}_\mu(s)|x(0)\rangle$ are evaluated very frequently and in the perturbation theory they need to be calculated with perturbations to both the operators and the states being properly taken into account. In so doing, I employ the interaction picture, which is also referred to as the Furry picture (Neville and Rohrlich, 1971) in the current case, rather than making full use of the properties of particular field configurations as in Adler (1971). The relation between the operator in the Heisenberg picture $\hat{A}_H(u)$ and that in the interaction picture $\hat{A}_I(u)$ is then given by the transformation: $\hat{A}_H(u) = U^{-1}(u)\hat{A}_I(u)U(u)$, where the operator $U(u)$ is written as $U(u) = e^{iH^{(0)}u}e^{-iHu}$. It also satisfies the following equation: $i\frac{\partial}{\partial u}U(u) = \delta H_I(u)U(u)$. Here the perturbation Hamiltonian in the interaction picture δH_I is given as $\delta H_I(u) \equiv e^{iH^{(0)}u}\delta H e^{-iH^{(0)}u}$. The equation of $U(u)$ can be solved iteratively as

$$\begin{aligned} U(u) &= 1 + (-i)\int_0^u du_1 \delta H_I(u_1) \\ &\quad + (-i)^2 \int_0^u du_1 \int_0^{u_1} du_2 \delta H_I(u_1)\delta H_I(u_2) + \cdots \\ &\quad + (-i)^n \int_0^u du_1 \cdots \int_0^{u_{n-1}} du_n \delta H_I(u_1)\cdots\delta H_I(u_n) \\ &\quad + \cdots . \end{aligned} \tag{2.17}$$

Note that the right hand side of this equation includes only unperturbed quantities, since the operators obey the free Heisenberg equations in the interaction picture.

The transformation amplitude $\langle x(s)|x(0)\rangle$ is also expressed with the unperturbed operators and states as

$$\langle x(s)|x(0)\rangle \simeq \langle x^{(0)}(s)|\left[1 - i\int_0^s du \delta H_I(u)\right]|x(0)\rangle. \tag{2.18}$$

In this expression, the index (0) attached to the state indicates its proper-time evolution by $H^{(0)}$:

$$|x^{(0)}(s)\rangle = e^{iH^{(0)}s}|x(0)\rangle. \tag{2.19}$$

Since I assume that the interaction and Heisenberg pictures are coincident with each other at $u = 0$, I have

$$|x^{(0)}(0)\rangle = |x(0)\rangle. \tag{2.20}$$

The operators $\hat{\Pi}(u)$ and the states $|x(u)\rangle$ at an arbitrary proper-time u are expressed with the unperturbed counterparts $\hat{\Pi}^{(0)}$, $\hat{x}^{(0)}$ and $|x^{(0)}\rangle$ via the operator $U(u)$ given in Equation (2.17) in a similar way.

The amplitudes that appear in Equation (2.14) for $\langle j^\mu(x)\rangle$ can be represented as

$$\langle x(s)|\hat{\Pi}^\mu(s)|x(0)\rangle = \langle x^{(0)}(s)|\hat{\Pi}^\mu_I(s)U(s)|x(0)\rangle, \tag{2.21}$$
$$\langle x(s)|\hat{\Pi}^\mu(0)|x(0)\rangle = \langle x^{(0)}(s)|U(s)\hat{\Pi}^\mu_I(0)|x(0)\rangle, \tag{2.22}$$

with the operators and states in the interaction picture. The calculations of these amplitudes are accomplished by the permutations of operators $\hat{x}(s)$ and $\hat{x}(0)$ with the employment of their commutation relations so that $\hat{x}(s)$ should sit always to the left of $\hat{x}(0)$.

2.3 Application to Single Plane-Waves

In this section, I apply the perturbation theory outlined above to the calculation of the induced electromagnetic current in the monochromatic plane-wave. It is stressed that the distinction between the electromagnetic wave train having a finite or infinite length is not important in my calculations, since they employ only local information of the electromagnetic wave in the background thanks to the gradient expansion. I first summarize the well-known results for the unperturbed background (Schwinger, 1951). The plane wave is represented as

$$F_{\mu\nu} = f_{\mu\nu}F(\Omega\xi), \tag{2.23}$$

with $f_{\mu\nu}$ being a constant tensor that sets the typical amplitude of the wave and $F(\Omega\xi)$ being an arbitrary function of $\Omega\xi = \Omega n_\mu x^\mu$; Ω is a frequency of the wave and n^μ is a null vector that specifies the direction of wave propagation. The Heisenberg equations are written in this case as

$$\frac{d\hat{x}^\mu(s)}{ds} = 2\hat{\Pi}^\mu(s), \tag{2.24}$$
$$\frac{d\hat{\Pi}^\mu(s)}{ds} = 2eF^\mu{}_\nu(s)\hat{\Pi}^\nu(s) + \frac{e}{2}n^\mu f_{\nu\lambda}\sigma^{\nu\lambda}\frac{dF(\Omega\xi(s))}{d\xi(s)}. \tag{2.25}$$

Note that the phase $\xi(s) = n_\mu\hat{x}^\mu(s)$ in these equations is an operator and a function of the proper time s. The term that contains $\partial^\nu F^\mu{}_\nu$ vanishes in the equation of $\hat{\Pi}$

because it is written as $\partial_\nu F_\mu{}^\nu = f_\mu{}^\nu n_\nu [dF(\Omega\xi(s))/d\xi(s)]$ and the following relation $f_\mu{}^\nu n_\nu = 0$ holds for the plane-wave.

To solve these equations, one introduces

$$C^\mu = f^\mu{}_\nu \hat{\Pi}^\nu(s) - ef^2 n^\mu A(\Omega\xi(s)), \tag{2.26}$$

which one can show is a constant of motion. In this expression, $f^2 = f_{\mu\nu}f^\nu{}_\lambda / n_\mu n_\lambda$ is the amplitude squared of the plane-wave and $A(\Omega\xi(s))$ is defined as a quantity that satisfies the following relation: $F(\Omega\xi(s)) = dA(\Omega\xi(s))/d\xi(s)$. Then, the operators $\hat{\Pi}^\mu(s)$ and $\hat{\Pi}^\mu(0)$ are obtained as follows:

$$\begin{aligned}
\hat{\Pi}^\mu(s) = & \frac{\hat{x}^\mu(s) - \hat{x}^\mu(0)}{2s} \\
& + \frac{s}{\xi(s) - \xi(0)} \left[2C^\mu eA(\Omega\xi(s)) + n^\mu e^2 f^2 A^2(\Omega\xi(s)) + \frac{1}{2} e\sigma^{\nu\lambda} f_{\nu\lambda} n^\mu F(\Omega\xi(s)) \right] \\
& - \frac{s}{(\xi(s) - \xi(0))^2} \int_{\xi(0)}^{\xi(s)} d\xi(u) \Bigg[2C^\mu eA(\Omega\xi(u)) + n^\mu e^2 f^2 A^2(\Omega\xi(u)) \\
& \qquad + \frac{1}{2} e\sigma^{\nu\lambda} f_{\nu\lambda} n^\mu F(\Omega\xi(u)) \Bigg],
\end{aligned} \tag{2.27}$$

$$\begin{aligned}
\hat{\Pi}^\mu(0) = & \frac{\hat{x}^\mu(s) - \hat{x}^\mu(0)}{2s} \\
& + \frac{s}{\xi(s) - \xi(0)} \left[2C^\mu eA(\Omega\xi(0)) + n^\mu e^2 f^2 A^2(\Omega\xi(0)) + \frac{1}{2} e\sigma^{\nu\lambda} f_{\nu\lambda} n^\mu F(\Omega\xi(0)) \right] \\
& - \frac{s}{(\xi(s) - \xi(0))^2} \int_{\xi(0)}^{\xi(s)} d\xi(u) \Bigg[2C^\mu eA(\Omega\xi(u)) + n^\mu e^2 f^2 A^2(\Omega\xi(u)) \\
& \qquad + \frac{1}{2} e\sigma_{\nu\lambda} f^{\nu\lambda} n^\mu F(\Omega\xi(u)) \Bigg].
\end{aligned} \tag{2.28}$$

C^μ is also expressed as

$$C^\mu = \frac{f^\mu{}_\nu (\hat{x}^\nu(s) - \hat{x}^\nu(0))}{2s} - \frac{1}{\xi(s) - \xi(0)} \int_{\xi(0)}^{\xi(s)} d\xi(u) n^\mu f^2 eA(\Omega\xi(u)). \tag{2.29}$$

The amplitude $\langle x'(s) | x''(0) \rangle$ is given, on the other hand, as

$$\begin{aligned}
& \langle x'(s) | x''(0) \rangle \\
& = \frac{1}{i(4\pi)^2} \exp\left[- \int_{x''}^{x'} dx_\mu eA^\mu(x) \right] \\
& \times \frac{1}{s^2} \exp\Bigg\{ -\frac{i}{4s}(x' - x'')^2 + \frac{if^2 s}{(\xi' - \xi'')^2} \left[\int_{\xi''}^{\xi'} eA(\Omega\xi) d\xi \right]^2 \\
& \qquad - \frac{is}{\xi' - \xi''} \int_{\xi''}^{\xi'} d\xi \left[e^2 f^2 A^2(\Omega\xi) + \frac{1}{2} e\sigma_{\rho\lambda} f^{\rho\lambda} F(\Omega\xi) \right] \Bigg\}.
\end{aligned} \tag{2.30}$$

To derive the induced electromagnetic current $\langle j^\mu \rangle$, I use the amplitude $\langle x(s)|x(0)\rangle$, which is immediately obtained from the above equation as

$$\begin{aligned} & \langle x(s)|x(0)\rangle \\ = & \frac{1}{i(4\pi)^2 s^2} \exp\left[-\frac{i}{2} e\sigma^{\alpha\beta} f_{\alpha\beta} F(\Omega\xi) s\right] \\ = & \frac{1}{i(4\pi)^2 s^2}\left(\mathbf{1} - \frac{ies}{2} F(\Omega\xi)\sigma^{\alpha\beta} f_{\alpha\beta}\right). \end{aligned} \tag{2.31}$$

I then find from Equations (2.27) through (2.30) that $\langle j^\mu \rangle$ in Equation (2.14) is vanishing as pointed out first by Schwinger in his seminal paper (Schwinger, 1951). This situation changes, however, if another plane wave is added.

In this chapter, I consider the propagation of a probe photon through the external monochromatic plane-wave with the former being treated as a perturbation to the latter as usual. I have in mind its application to high-field lasers. Since the wavelengths of these lasers are close to optical wavelengths, I assume in the following that the wavelength of the unperturbed monochromatic plane-wave is much longer than the electron's Compton wavelength, or $\Omega_0/m \ll 1$ for the wave frequency Ω_0. It may be then sufficient to consider temporal and spatial variations of the unperturbed plane-wave to the first order of Ω_0. This is equivalent to the so-called gradient expansion of the unperturbed field to the first order, which can be expressed generically as $F_{\mu\nu} \simeq f_{\mu\nu}(1 + \Omega\xi)$. In fact, the plane-wave field given as $F_{\mu\nu} = f_{0\mu\nu}\sin(\Omega_0 n_\alpha x^\alpha)$ is Taylor-expanded at a spacetime point x_0^μ as $f_{0\mu\nu}\sin(\Omega_0 n_\alpha x_0^\alpha)(1+\cos(\Omega_0 n_\beta x_0^\beta)\Omega_0 n_\gamma(x^\gamma - x_0^\gamma))$ to the first order. This can be recast into $F_{\mu\nu} \simeq f_{\mu\nu}(1 + \Omega n_\alpha x^\alpha)$ after shifting coordinates by x_0^α and employing the local amplitude and the gradient of the background field at x^α as $f_{\mu\nu} = f_{0\mu\nu}\sin(\Omega_0 n_\alpha x_0^\alpha)$ and $\Omega = \cos(\Omega_0 n_\beta x_0^\beta)\Omega_0$, respectively. Note that the above assumption on Ω_0 implies $\Omega/m \ll 1$.

Gusynin and Shovkovy (1999) developed a covariant formulation to derive the gradient expansion of the QED effective Lagrangian, employing the world-line formalism under the Fock-Schwinger gauge. Although their method is systematic and elegant indeed, the results obtained in their paper cannot be applied to the problem of my current interest, since the actual calculations were done only for the following field configurations: $F_{\mu\nu} = \Phi(x_\alpha) f_{\mu\nu}$, where $\Phi(x_\alpha)$ is an arbitrary slowly-varying function of x_α while $f_{\mu\nu}$ is a constant tensor; the former gives a field variation in space and time and the latter specifies a field configuration. Although it appears quite generic, it does not include the configurations of my concern, i.e., those consisting of two electromagnetic waves propagating in different directions, unfortunately. Note that if the background and probe plane-waves are both traveling in the same direction and having the identical polarization, then one may regard the sum of their amplitudes as Φ and apply the gradient expansion of Gusynin and Shovkovy (1999) to them; in this case, however, Schwinger (1951) already showed that there is no quantum correction to the effective Lagrangian.

In my method, the probe photon, which is also treated as a classical electromagnetic wave, is assumed to be monochromatic locally. Strictly speaking, it has neither a constant amplitude nor a constant frequency because the external field changes temporally and spatially. As long as the wavelength of the external field is much

longer than that of the probe photon, which I assume in the following, the above assumption that the probe field can be regarded as monochromatic locally may be justified. I need to elaborate on this issue a bit further, though. As Becker and Mitter (1975) developed, the polarization tensor $\Pi^{\mu\nu}(x_1, x_2)$ depends not only on the difference of the two coordinates $x_1 - x_2$ but also on each of them separately and, as a result, its Fourier transform has two momenta corresponding to these coordinates. If the electromagnetic wave in the background is monochromatic, then the Floquet theorem dictates that the difference between them should be equal to some multiple of the wave vector of the electromagnetic wave in the background (Zel'Dovich, 1967). It follows then that eigenmodes of the probe photon are not diagonal in momentum in general. In fact, they should satisfy the following Maxwell equation:

$$\Box_{x_1} b^\mu(x_1, x_2) - \partial^\nu_{x_1}\partial^\mu_{x_1} b_\nu(x_1, x_2) = \int dx' \Pi^{\mu\nu}(x_1, x') b_\nu(x', x_2) \tag{2.32}$$

Becker and Mitter (1975) Fourier-transformed this equation and attempted to solve it in momentum space. Although they showed analytically that the momenta of probe-photon were indeed mixed in the expected way, they ignored the mixing in actual evaluations of the refractive index, since the effect is of higher order in the coupling constant.

I take another approach in this chapter. Assuming, as mentioned above, that the electromagnetic wave in the background varies slowly in time and space and hence the probe photon can "see" the local field strength and its gradient alone, I expand the above equation in the small gradient. In so doing, I employ the Wigner representations of variables:

$$\Pi^{\mu\nu}(x_1 - x_2 : X) = \int \frac{d^4p}{(2\pi)^4} \tilde{\Pi}^{\mu\nu}(p, X) e^{ip(x_1 - x_2)}, \tag{2.33}$$

$$b^\mu(x_1 - x_2 : X) = \int \frac{d^4p}{(2\pi)^4} \tilde{b}^\mu(p, X) e^{ip(x_1 - x_2)}, \tag{2.34}$$

where $X = (x_1 + x_2)/2$ is the center-of-mass coordinates and $\Pi^{\mu\nu}$ and b^μ are regarded in these equations as functions of the relative coordinates $x_1 - x_2$ and X instead of x_1 and x_2. Inserting these expressions into the right hand side of Equation (2.32) and Fourier-transforming it with respective to the relative coordinates $x_1 - x_2$, I obtain

$$\begin{aligned}
&\int d^4(x_1 - x_2) \int d^4x' \Pi^{\mu\nu}(x_1, x') b_\nu(x', x_2) e^{-ip(x_1 - x_2)} \\
&= \int d^4(x_1 - x_2) \int d^4x' \Pi^{\mu\nu}(x_1 - x' : X + (x' - x_2)/2) \\
&\qquad\qquad \times b_\nu(x' - x_2 : X + (x' - X_1)/2) e^{-ip(x_1 - x_2)} \\
&= \tilde{\Pi}^{\mu\nu}(p, X) \exp\left(-\frac{1}{2}\partial^\Pi_p \partial^b_X\right) \exp\left(\frac{1}{2}\partial^b_p \partial^\Pi_X\right) \tilde{b}_\nu(p, X) \\
&\sim \tilde{\Pi}^{\mu\nu}(p, X) \tilde{b}_\nu(p, X),
\end{aligned} \tag{2.35}$$

in which ∂^Π_p is a partial derivative with respective to p acting on $\tilde{\Pi}$; other ∂'s should be interpreted in similar ways; the juxtapositions of two ∂'s stand for four-dimensional contractions; the last expression is the approximation to the lowest

order with respective to the gradient in X, which is justified by my assumption. In deriving the third line of the above equations, I employ the following relations:

$$\Pi^{\mu\nu}(x_1 - x' : X + (x' - x_2)/2) = \exp\left(\frac{x' - x_2}{2}\partial_X^{\Pi}\right)\Pi^{\mu\nu}(x_1 - x' : X), \quad (2.36)$$

$$b^{\mu}(x' - x_2 : X + (x' - x_1)/2) = \exp\left(\frac{x' - x_1}{2}\partial_X^{b}\right)b^{\mu}(x' - x_2 : X). \quad (2.37)$$

Fourier-transforming the left hand side of Equation (2.32) also with respective to the relative coordinates $x_1 - x_2$, I obtain finally the "local" Maxwell equation as follows:

$$-p^2\tilde{b}^{\mu}(p, X) + p^{\nu}p^{\mu}\tilde{b}_{\nu}(p, X) = \tilde{\Pi}^{\mu\nu}(p, X)\tilde{b}_{\nu}(p, X). \quad (2.38)$$

Note that I also ignore the derivative with respect to X in the kinetic part of the Maxwell equation, which is again valid under the current assumption. I then consider the dispersion relation for the probe photon in the point-wise fashion, plugging the polarization tensor obtained locally this way. This is nothing but the WKB approximation for the propagation of probe photon. Note that the momentum of the probe photon is hence not the one in the asymptotic states (Dinu et al., 2014b) but the local one defined at each point in the background electromagnetic wave. It should be also stressed that the derived refractive index is a local quantity. Although such a quantity may not be easy to detect in experiments, this is regardless the main accomplishment in this chapter.

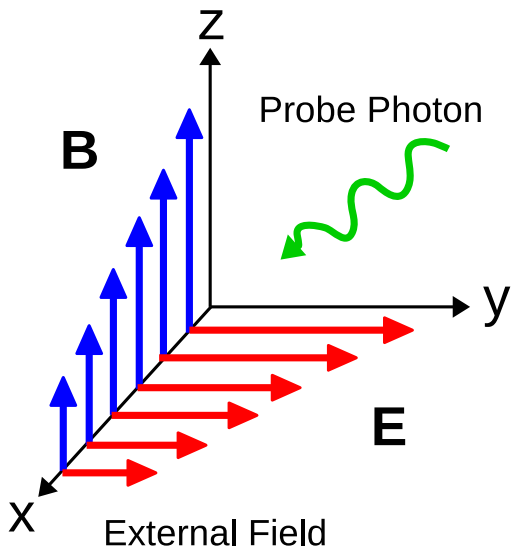

Figure 2.1: Schematic picture of the system considered in this chapter. The external field consists of a non-uniform electric and magnetic fields denoted by **E** and **B**, respectively, and the probe photon.

I now proceed to the actual calculations. The induced electromagnetic current

is written as

$$\langle j^\mu \rangle = \frac{e}{2}\int_0^\infty ds e^{-im^2 s}\mathrm{tr}\left[\langle x(s)|\hat{\Pi}^\mu(s)U(s) + U(s)\hat{\Pi}^\mu(0)|x(0)\rangle \right. \\ \left. -i\sigma^{\mu\nu}\langle x(s)|\hat{\Pi}_\nu(s)U(s) - U(s)\hat{\Pi}_\nu(0)|x(0)\rangle\right]. \quad (2.39)$$

In this expression, I drop for brevity the superscript $^{(0)}$, which means the unperturbed states, and the subscript $_I$, which stands for the operators in the interaction picture. I use these notations in the following.

The proper-time evolution operator $U(s)$ is given as

$$\begin{aligned} U(s) &= 1 - i\int_0^s du \delta H(u) \\ &= 1 - i\int_0^s du \left\{ e\hat{\Pi}^\alpha(u) b_\alpha \exp\left[-ik_\delta \hat{x}^\delta(u)\right] \right. \\ &\quad \left. + eb_\alpha \exp\left[-ik_\delta \hat{x}^\delta(u)\right]\hat{\Pi}^\alpha(u) + \frac{1}{2}e\sigma^{\alpha\beta}(u) g_{\alpha\beta}\exp\left[-ik_\delta \hat{x}^\delta(u)\right]\right\} \quad (2.40) \end{aligned}$$

for the present case. Note that $\sigma^{\alpha\beta}(u)$ is a proper-time-dependent operator in the interaction picture, which is defined as

$$\sigma^{\alpha\beta}(u) = e^{iHu}\sigma^{\alpha\beta}e^{-iHu}. \quad (2.41)$$

The explicit expression of $\sigma^{\alpha\beta}(u)$ can be easily obtained to the first order of perturbation for the current Hamiltonian evaluated at $u = 0$ [4] as $H = -\hat{\Pi}^2(0) + \frac{1}{2}e\sigma^{\mu\nu}F_{\mu\nu}(0)$:

$$\sigma^{\alpha\beta}(u) \simeq \left[1 + \frac{i}{2}eu(\sigma f)\left(1 + \Omega\xi(0)\right)\right]\sigma^{\alpha\beta}\left[1 - \frac{i}{2}eu(\sigma f)\left(1 + \Omega\xi(0)\right)\right], \quad (2.42)$$

where I employ the abbreviation $(\sigma f) \equiv \sigma^{\mu\nu}f_{\mu\nu}$. Note that although $\xi(0)$ does not have a spinor structure and commutes with $(\sigma g) \equiv \sigma^{\alpha\beta}g_{\alpha\beta}$, $\xi(s)$ may have a nontrivial spinor structure induced by the proper-time evolution.

The amplitudes of $\langle x(s)|\hat{\Pi}^\mu(s)U(s)|x(0)\rangle$ and $\langle x(s)|U(s)\hat{\Pi}^\mu(0)|x(0)\rangle$ can now be expressed with the unperturbed operators and states. The calculations are involved,

[4] The Hamiltonian is proper-time-independent and can be evaluated at any time.

though, and given in Section 2.6. The final expressions are given as

$$\begin{aligned}
&\langle x(s)|\hat{\Pi}^{\mu}(s)U(s)|x(0)\rangle \\
= \;&\langle x(s)|\hat{\Pi}^{\mu}(s)|x(0)\rangle \\
&-i\int_0^s du\langle x(s)|2eb_{\alpha}\hat{\Pi}^{\mu}(s)\hat{\Pi}^{\alpha}(u)\exp\left[-ik_{\delta}\hat{x}^{\delta}(u)\right]|x(0)\rangle \\
&-i\int_0^s du\langle x(s)|-eb_{\alpha}k^{\alpha}\hat{\Pi}^{\mu}(s)\exp\left[-ik_{\delta}\hat{x}^{\delta}(u)\right]|x(0)\rangle \\
&+\int_0^s du\langle x(s)|\hat{\Pi}^{\mu}(s)\exp\left[-ik_{\delta}\hat{x}^{\delta}(u)\right]|x(0)\rangle \\
&\times\left(-\frac{ie}{2}\right)\left[(\sigma g)+\frac{ieu}{2}\left\{(\sigma f)(\sigma g)-(\sigma g)(\sigma f)\right\}+\frac{e^2u^2}{4}(\sigma f)(\sigma g)(\sigma f)\right] \\
&+\int_0^s du\langle x(s)|\hat{\Pi}^{\mu}(s)\exp\left[-ik_{\delta}\hat{x}^{\delta}(u)\right]|x(0)\rangle \\
&\times\left(-\frac{ie}{2}\right)\left[\frac{ieu}{2}\left\{(\sigma f)(\sigma g)-(\sigma g)(\sigma f)\right\}(\Omega\xi)+\frac{e^2u^2}{2}(\sigma f)(\sigma g)(\sigma f)(\Omega\xi)\right],
\end{aligned} \tag{2.43}$$

$$\begin{aligned}
&\langle x(s)|U(s)\hat{\Pi}^{\mu}(0)|x(0)\rangle \\
= \;&\langle x(s)|\hat{\Pi}^{\mu}(0)|x(0)\rangle \\
&-i\int_0^s du\langle x(s)|2eb_{\alpha}\hat{\Pi}^{\alpha}(u)\exp\left[-ik_{\delta}\hat{x}^{\delta}(u)\right]\hat{\Pi}^{\mu}(0)|x(0)\rangle \\
&-i\int_0^s du\langle x(s)|-eb_{\alpha}k^{\alpha}\exp\left[-ik_{\delta}\hat{x}^{\delta}(u)\right]\hat{\Pi}^{\mu}(0)|x(0)\rangle \\
&+\int_0^s du\langle x(s)|\exp\left[-ik_{\delta}\hat{x}^{\delta}(u)\right]\hat{\Pi}^{\mu}(0)|x(0)\rangle \\
&\times\left(-\frac{ie}{2}\right)\left[(\sigma g)+\frac{ieu}{2}\left\{(\sigma f)(\sigma g)-(\sigma g)(\sigma f)\right\}+\frac{e^2u^2}{4}(\sigma f)(\sigma g)(\sigma f)\right] \\
&+\int_0^s du\langle x(s)|\exp\left[-ik_{\delta}\hat{x}^{\delta}(u)\right]\hat{\Pi}^{\mu}(0)|x(0)\rangle \\
&\times\left(-\frac{ie}{2}\right)\left[\frac{ieu}{2}\left\{(\sigma f)(\sigma g)-(\sigma g)(\sigma f)\right\}(\Omega\xi)+\frac{e^2u^2}{2}(\sigma f)(\sigma g)(\sigma f)(\Omega\xi)\right] \\
&+\int_0^s du\langle x(s)|\exp\left[-ik_{\delta}\hat{x}^{\delta}(u)\right]|x(0)\rangle \\
&\times\left(-\frac{ie}{2}\right)(-in^{\mu})\left[\frac{ieu}{2}\left\{(\sigma f)(\sigma g)-(\sigma g)(\sigma f)\right\}\Omega+\frac{e^2u^2}{2}(\sigma f)(\sigma g)(\sigma f)\Omega\right].
\end{aligned} \tag{2.44}$$

Then the induced electromagnetic current can be calculated by inserting these amplitudes in Equation (2.39). The operators $\hat{\Pi}^{\mu}(s)$, $\hat{\Pi}^{\mu}(0)$, $\hat{\Pi}^{\mu}(u)$ and $\exp[-ik_{\alpha}\hat{x}^{\alpha}(u)]$ that appear in these expressions can be written in terms of the operators $\hat{x}^{\mu}(s)$ and $\hat{x}^{\mu}(0)$ as given in Equations (2.85), (2.86), (2.88) and (2.95). Since the operators $\hat{x}^{\mu}(s)$ and $\hat{x}^{\mu}(0)$ do not commute with each other, I need to permute them with the

help of the commutation relations for these operators so that all $\hat{x}^\mu(s)$ should sit to the left of all $\hat{x}^\mu(0)$. The details are given in Section 2.7. Note that the commutators such as $[\hat{x}^\mu(s), \hat{x}^\nu(0)]$ are operators and hence I need to calculate commutation relations like $[\hat{x}^\mu(s), [\hat{x}^\nu(s), \hat{x}^\lambda(0)]]$. After these permutations, various amplitudes can be easily obtained from the following relations:

$$\langle x(s)|\hat{x}^\mu(s) = x^\mu\langle x(s)|, \tag{2.45}$$
$$\langle x(s)|\xi(s) = \xi\langle x(s)|, \tag{2.46}$$
$$\hat{x}^\mu(0)|x(0)\rangle = x^\mu|x(0)\rangle, \tag{2.47}$$
$$\xi(0)|x(0)\rangle = \xi|x(0)\rangle. \tag{2.48}$$

In deriving Equations (2.42) - (2.44), I consider only the neighborhood of the coordinate origin, the linear size of which is much shorter than the wavelength of the background plane-wave but larger than the wavelength of the probe photon. As mentioned earlier, however, the origin is arbitrary and one can shift the coordinates so that the point of interest should coincide with the origin. Hence the results are actually applicable to any point. More discussions on this point will be found in Section 2.8. Note also that Furry's theorem dictates that the number of external fields that appear in the expression of the induced electromagnetic current should be even, the details of which can be found in Section 2.9.

After all these considerations and calculations, the induced electromagnetic current is given to the lowest order of the perturbation and Ω. The details are presented in Section 2.10. Since the induced electromagnetic current $\langle j_\mu\rangle$ is vanishing in the absence of the probe photon, it is generated by its presence and is should be proportional to it:

$$\langle j_\mu(x)\rangle = \Pi_\mu{}^\nu(k,x)b_\nu(k,x)\exp(-ik_\alpha x^\alpha). \tag{2.49}$$

Note that I employ the local approximation here again.

In this expression, the probe photon is given as $b_\nu\exp(-ik_\alpha x^\alpha)$ and the proportionality coefficient $\Pi_\mu{}^\nu$ is nothing but the polarization tensor at each point. Following Ritus (1972), I decompose the polarization tensor so obtained as

$$\Pi_\mu{}^\nu \;=\; \int_0^\infty ds\int_0^s du\,\left[\Pi_1(fk)_\mu(fk)^\nu + \Pi_2(\tilde{f}k)_\mu(\tilde{f}k)^\nu + \Pi_3 G_\mu G^\nu\right], \tag{2.50}$$

with three mutually orthogonal vectors

$$(fk)_\mu = f_\mu{}^\nu k_\nu,\ (\tilde{f}k)_\mu = \tilde{f}_\mu{}^\nu k_\nu,\ G_\mu = \frac{k_\alpha k^\alpha}{k_\beta f^\beta{}_\gamma f^\gamma{}_\delta k^\delta} f_\mu{}^\nu f_\nu{}^\lambda k_\lambda, \tag{2.51}$$

where $\tilde{f}^{\mu\nu} = \varepsilon^{\mu\nu\rho\sigma}f_{\rho\sigma}/2$ is the dual tensor of $f^{\mu\nu}$. Here $\varepsilon^{\mu\nu\rho\sigma}$ is the Levi-Civita antisymmetric symbol, which satisfies $\varepsilon^{0123} = 1$. The following abbreviations $(kk) = k_\mu k^\mu$ and $(kffk) = k_\mu f^\mu{}_\nu f^\nu{}_\lambda k^\lambda$ are also used (Ritus, 1972). Then the coefficients

are given as follows:

$$
\begin{aligned}
\Pi_1 &= \frac{e^2 e^{-im^2 s}}{72\pi^2 s^3 (kffk)} \exp\left[i\left(u - \frac{u^2}{s}\right)(kk)\right] \\
&\times \left(-1 + \exp\left[\frac{i(s-u)^2 u^2 e^2 (kffk)}{3s}\right]\right)(-18i - 9s(kk)) \\
&+ \frac{e^2 e^{-im^2 s}}{72\pi^2 s^3} \exp\left[i\left(u - \frac{u^2}{s}\right)(kk) + \frac{i(s-u)^2 u^2 e^2 (kffk)}{3s}\right] \\
&\times e^2 \left(-\frac{18}{s}\right) u(s^3 - 3s^2 u + 4su^2 - 2u^3) \\
&+ \frac{e^2 e^{-im^2 s}}{72\pi^2 s^3} \exp\left[i\left(u - \frac{u^2}{s}\right)(kk) + \frac{i(s-u)^2 u^2 e^2 (kffk)}{3s}\right] \\
&\times \left[\left(\frac{2}{s^2} e^2 (\Omega kn)(s-u)u(6s^4 + 22s^3 u - 79s^2 u^2 + 78su^3 - 36u^4)\right)\right. \\
&+ \left(-\frac{4i}{s^2}\right) e^4 (kffk)(\Omega kn)(s-u)^3 u^2 (3s^4 - 7s^3 u + 5s^2 u^2 + 4su^3 - 6u^4) \\
&\left. + (-2i)\, e^2 (\Omega kn)(kk)(s-u)^2 u(3s^2 - su - 3u^2)\right], \qquad (2.52)
\end{aligned}
$$

$$
\begin{aligned}
\Pi_2 &= \frac{e^2 e^{-im^2 s}}{72\pi^2 s^3 (kffk)} \exp\left[i\left(u - \frac{u^2}{s}\right)(kk)\right] \\
&\times \left(-1 + \exp\left[\frac{i(s-u)^2 u^2 e^2 (kffk)}{3s}\right]\right)(-18i - 9s(kk)) \\
&+ \frac{e^2 e^{-im^2 s}}{72\pi^2 s^3} \exp\left[i\left(u - \frac{u^2}{s}\right)(kk) + \frac{i(s-u)^2 u^2 e^2 (kffk)}{3s}\right] e^2 (-18) su(s-u) \\
&+ \frac{e^2 e^{-im^2 s}}{72\pi^2 s^3} \exp\left[i\left(u - \frac{u^2}{s}\right)(kk) + \frac{i(s-u)^2 u^2 e^2 (kffk)}{3s}\right] \\
&\times \left[\left(\frac{2}{s} e^2 (\Omega kn)(s-u)u(6s^3 + 4s^2 u - 7su^2 + 6u^3)\right)\right. \\
&+ (-2i)\, e^2 (\Omega kn)(kk)(s-u)^2 u(3s^2 - su - 3u^2) \\
&\left. + (-4i)\, e^4 (kffk)(\Omega kn)(s-u)^3 u^2 (3s^2 - su - 3u^2)\right], \qquad (2.53)
\end{aligned}
$$

$$
\begin{aligned}
\Pi_3 &= \frac{e^2 e^{-im^2 s}}{72\pi^2 s^4 (kk)} \exp\left[i\left(u - \frac{u^2}{s}\right)(kk)\right] \\
&\times \left(-1 + \exp\left[\frac{i(s-u)^2 u^2 e^2 (kffk)}{3s}\right]\right)(-6is + (-3s^2 + 16su - 16u^2)(kk)) \\
&+ \frac{e^4 (kffk) e^{-im^2 s}}{324\pi^2 s^4 (kk)^2} \exp\left[i\left(u - \frac{u^2}{s}\right)(kk) + \frac{i(s-u)^2 u^2 e^2 (kffk)}{3s}\right] \\
&\times \big[3i(s^3 - 6s^2 u + 6su^2) - 2u^2 (s^2 - 3su + 2u^2)^2 e^2 (kffk) \\
&\qquad\qquad -12(s-2u)^2 (s-u)u(kk)\big] \\
&- \frac{ie^2 e^{-im^2 s}}{27(kk)^2 \pi^2 s^4} \exp\left[i\left(u - \frac{u^2}{s}\right)(kk) + \frac{i(s-u)^2 u^2 e^2 (kffk)}{3s}\right] \\
&\times (\Omega kn) e^2 (kffk)(s-u)u(s^2 - 5su + 5u^2) \\
&- \frac{e^2 e^{-im^2 s}}{972(kk)^2 \pi^2 s^5} \exp\left[i\left(u - \frac{u^2}{s}\right)(kk) + \frac{i(s-u)^2 u^2 e^2 (kffk)}{3s}\right] \\
&\times (\Omega kn) e^2 (kffk)(s-u)^2 u \\
&\qquad \times \big[2e^2 (kffk)(3s^5 - 19s^4 u + 6s^3 u^2 + 87s^2 u^3 - 138su^4 + 60u^5) \\
&\qquad\quad -9(6s^3 + 9s^2 u - 46su^2 + 40u^3)(kk)\big] \\
&- \frac{ie^2 e^{-im^2 s}}{2916(kk)^2 \pi^2 s^5} \exp\left[i\left(u - \frac{u^2}{s}\right)(kk) + \frac{i(s-u)^2 u^2 e^2 (kffk)}{3s}\right] \\
&\times (\Omega kn) e^2 (kffk)(s-u)^2 u(3s^2 - su - 3u^2) \\
&\times \big[4e^4 (kffk)^2 u^2 (s^2 - 3su + 2u^2)^2 + 24e^2 (kffk)(kk)(s-2u)^2 (s-u)u \\
&\qquad +9(3s^2 - 16su + 16u^2)(kk)^2\big], \qquad (2.54)
\end{aligned}
$$

where $(\Omega kn) = \Omega k_\mu n^\mu$ is the inner product of the momentum vectors of the external plane-wave and the probe photon. The refractive indices for physical modes are related to Π_1 and Π_2.

The proper-time integration in Equation (2.50) or its pre-decomposition form, Equation (2.167), has to be done numerically. The original form is not convenient for this purpose and I rotate the integral path by $-\pi/3$ in the complex plane so that the integral could converge exponentially as s goes to infinity. Note that the rotation angle is arbitrary as long as it is in the range of $(0, -\pi/3]$. The refractive index is then obtained by solving the Maxwell equation reduced in the following form:

$$A_\mu{}^\nu(k) b_\nu = 0, \qquad (2.55)$$

with $A_\mu{}^\nu = -(kk)\delta_\mu{}^\nu + k_\mu k^\nu + \Pi_\mu{}^\nu$. The probe photon is hence described as a non-trivial solution of this homogeneous equation and its dispersion relation is obtained from the relation $\det A = 0$. Note that not all of them are physical. Unphysical modes are easily eliminated, however, by calculating the electric and magnetic field strengths, which are gauge-invariant. It is then found that only two of them associated with Π_1 and Π_2 are physical as expected. Note that the four momenta of the probe photon thus obtained are no longer null in accordance with the refractive indices different from unity. The polarization vectors are also obtained simultaneously.

Table 2.1: Eigenmodes of the probe photons with different 4-momenta

probe momentum k_μ	eigenmode	mode name
$(k_0, k_1, 0, 0)$	$(0, 0, 1, 0)_\mu$	x2 mode
	$(0, 0, 0, 1)_\mu$	x3 mode
$(k_0, 0, k_2, 0)$	$(k_2, -k_2, k_0, 0)_\mu$	y1 mode
	$(0, 0, 0, 1)_\mu$	y3 mode
$(k_0, 0, 0, k_3)$	$(k_3, -k_3, 0, k_0)_\mu$	z1 mode
	$(0, 0, 1, 0)_\mu$	z2 mode
$(k_0, \frac{k_i}{\sqrt{3}}, \frac{k_i}{\sqrt{3}}, \frac{k_i}{\sqrt{3}})$	$(A, B, 1, 0)_\mu$	s2 mode [5]
	$(A, B, 0, 1)_\mu$	s3 mode

[5] A, B are constants written with k_0 and k_i.

In the next section, I show the results of some numerical evaluations. As representative cases, I consider four propagating directions of the probe photon as summarized in Table 2.1. Since the background plane-wave is assumed to have a definite propagation direction (x-direction) and linear polarization (y-direction), these four directions are not equivalent. For each propagation direction, there are two physical eigenmodes, as mentioned above, which are in general different from each other, having distinctive dispersion relations, i.e., the background is birefringent.

2.4 Results

In this section, I numerically evaluate the refractive index N, which is defined as $N = |\boldsymbol{k}|/k_0$. Firstly, the crossed fields are considered and then the first order correction δN in the gradient expansion is calculated for the plane-wave field. The eigenmodes of the probe photon depend on the propagation direction as already mentioned. The refractive index is complex in general with the real part representing the phase velocity of the probe photon divided by the light speed and the imaginary part indicating the decay, possibly via electron-positron pair creations. Since the deviation of the refractive index from unity is usually much smaller than unity, only the deviations are shown in the following: $\mathrm{Re}[N-1]$ and $\mathrm{Im}[N]$.

Note that for all cases considered in this chapter, the refractive indices, both real and imaginary parts, of the y1 and z2 modes are identical and so are those of the y3 and z1 modes. Although the exact reason for this phenomenon is not known to us for the moment, the following should be mentioned: the polarization tensor $\Pi^{\mu\nu}$ is expressed as the sum of three contributions proportional to $(fk)^\mu(fk)^\nu$, $(\tilde{f}k)^\mu(\tilde{f}k)^\nu$ and $G^\mu G^\nu$ given as Equation (2.50); each pair of the modes that have the identical refractive index are actually eigenmodes of either $(fk)^\mu(fk)^\nu$ or $(\tilde{f}k)^\mu(\tilde{f}k)^\nu$. I will show these degenerate modes with the same color in figures hereafter.

2.4.1 Crossed Fields

As mentioned in Section 2.1, the vacuum polarization in the crossed fields was already obtained by many authors. The refractive index was also evaluated both analytically and numerically (Toll, 1952; Baier and Breitenlohner, 1967b; Narozhnyĭ, 1969; Ritus, 1972; Heinzl and Schröder, 2006). The regions in the plane of the field strength f and the probe-photon energy k_0 that have been investigated in these papers are summarized in Figure 2.2. It is apparent from the figure that there is

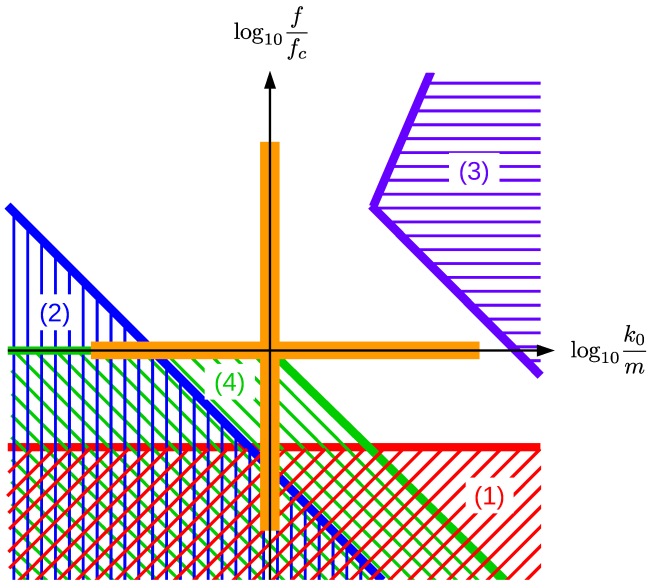

Figure 2.2: Regions in the plane of the strength of external crossed fields and the probe-photon energy that have been already explored. Each region is labeled as follows: region (1) is the weak-field limit $f/f_c \ll 1$ (Toll, 1952); region (2) is for the weak-field or low-energy limit $e^2 k_\mu f^\mu{}_\nu f^{\nu\lambda} k_\lambda / m^6 \ll 1$ (Baier and Breitenlohner, 1967b; Narozhnyĭ, 1969; Ritus, 1972); region (3) corresponds to the strong-field and high-energy limit $1 \ll e^2 k_\mu f^\mu{}_\nu f^{\nu\lambda} k_\lambda / m^6 \ll (k_0/m)^6 \times \alpha^{-3}$ studied in Narozhnyĭ (1969), where $\alpha = e^2/4\pi$ is the fine-structure constant; region (4) is the region that satisfies $(f/f_c) \lesssim 1$ and $(f/f_c) \times (k_0/m) \lesssim 1$ explored in Heinzl and Schröder (2006). The orange lines indicate the regions, in which the refractive indices are computed numerically in this chapter. Note that my method can treat the whole region in this figure in principle.

still an unexplored region, which is unshaded. And that is the target of this chapter. The parameter ranges I adopted in this chapter are displayed in orange in the same figure: I first calculate the refractive index for the external field of the critical value to validate my formulation by comparing my results with those in the previous studies; then I vary the strength of the external field.

The polarization tensor $\Pi_\mu{}^\nu$ in the crossed field is obtained by simply taking the limit of $\Omega \to 0$ in Equation (2.50). Setting the strength of the external field to the critical value $f/f_c = 1$, I compute the refractive indices for the range of

$0.01 \leq k_0/m \leq 1000$[6]. Note that the low-energy regime ($k_0/m \lesssim 1$) has been investigated already as shown in Figure 2.2. The real part $\mathrm{Re}[N-1]$ is shown in Figure 2.3 with colors indicating different modes of the probe photon.

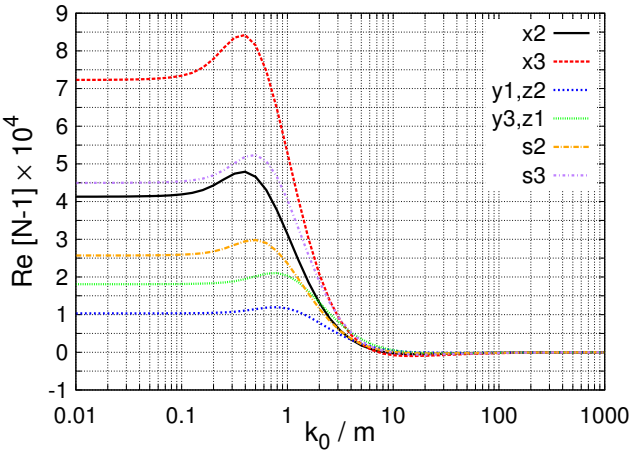

Figure 2.3: Plot of $\mathrm{Re}[N-1]$ as a function of the probe-photon energy in the crossed field. Here N is a refractive index. I set $f/f_c = 1$. Colors specify different modes.

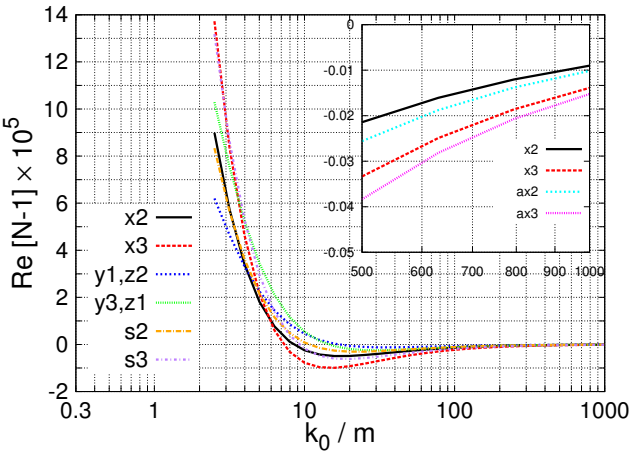

Figure 2.4: Same as Figure 2.3 but for high energies alone on a different vertical scale. The inset zooms into the high-energy range of $500 \leq k_0/m \leq 1000$ and asymptotic formulae are also shown as ax2 and ax3 for the x2 and x3 modes, respectively.

It is found that the deviation of the refractive index from unity is of the order of 10^{-4}. As k_0/m gets smaller, the refractive index approaches the values in the

[6]Shore studied the refractive index of super-critical magnetic fields for a wider range of the photon energy Shore (2007). The results are similar to mine for the crossed field.

weak-field or low-energy limit (region (2) in Figure 2.2), which are written as

$$N_{\rm x2} \simeq 1 + \frac{2\alpha}{45\pi}\frac{\kappa^2 m^2}{k_0^2}, \tag{2.56}$$

$$N_{\rm x3} \simeq 1 + \frac{7\alpha}{90\pi}\frac{\kappa^2 m^2}{k_0^2}, \tag{2.57}$$

for the x2 and x3 modes, respectively, where $\kappa^2 = e^2 k_\mu f^\mu{}_\nu f^{\nu\lambda} k_\lambda / m^6 = e^2 f^2 (k_0 + k_1)^2/m^6$ is the product of the probe photon energy and the field strength normalized by the critical value. Then the typical value of $N_{\rm x2} - 1$ can be estimated as

$$N_{\rm x2} - 1 \simeq \frac{8\alpha}{45\pi}\left(\frac{f}{f_c}\right)^2 \sim 4.1 \times 10^{-4}\left(\frac{I}{4.6 \times 10^{29}{\rm W/cm^2}}\right), \tag{2.58}$$

where $I = f^2/4\pi$ is the intensity of the plane wave. The results are hence in agreement with what was already published in Baier and Breitenlohner (1967b); Narozhnyĭ (1969); Ritus (1972); Heinzl and Schröder (2006). The refractive indices depend on the propagation direction of the probe photon: the modulus $|{\rm Re}[N-1]|$ is larger for the photon propagating in the opposite direction to the background plane-wave (the x mode) than those going perpendicularly (the y/z modes); the s mode that propagates obliquely lies normally in between although the modulus is greater for the s3 mode than for the x2 mode. The photons polarized in the z-direction have larger moduli in general except the z mode, which propagates in this direction, has a greater modulus when it is polarized in the x-direction. These trends are also true for other results obtained below in this chapter.

As k_0/m becomes larger than ~ 10, all the refractive indices for different propagation directions appear to converge to unity, which is consistent with Toll (1952); Heinzl and Schröder (2006). This is more apparent in Figure 2.4, which zooms into the region of $3 \lesssim k_0/m \leq 1000$. It is also seen in the same figure that ${\rm Re}[N-1]$ is negative and the modulus $|{\rm Re}[N-1]|$ decreases for $k_0/m \gtrsim 10$. This trend is consistent with the high-energy limits given in Narozhnyĭ (1969) (region (3) in Figure 2.2), which are written as

$$N_{\rm x2} \simeq 1 - \frac{\sqrt{3}\alpha m^2}{14\pi^2 k_0^2}(3\kappa)^{2/3}\Gamma^4\left(\frac{2}{3}\right)\left(1 - i\sqrt{3}\right), \tag{2.59}$$

$$N_{\rm x3} \simeq 1 - \frac{3\sqrt{3}\alpha m^2}{28\pi^2 k_0^2}(3\kappa)^{2/3}\Gamma^4\left(\frac{2}{3}\right)\left(1 - i\sqrt{3}\right), \tag{2.60}$$

for the x2 and x3 modes, respectively. In my formulation, these results are reproduced by putting $e^{-im^2 s}$ to unity and setting $(kk) = k_0^2 - k_1^2$ equal to zero in Equations (2.52), (2.53) and (2.54) for the polarization tensor $\Pi_\mu{}^\nu$ or Equations (2.225) and (2.227) for the induced electromagnetic current $\langle j_\mu \rangle$. Note, however, that my numerical results for ${\rm Re}[N-1]$ are not yet settled to the asymptotic limits with deviations of $\sim 10\%$ still remaining at $k_0/m \sim 1000$. In this figure, the high energy limits for the x2 and x3 modes are displayed as the lines labeled as ax2 and ax3, respectively. The imaginary parts, on the other hand, have already reached the asymptotic limits at $k_0/m \sim 1000$ (see below).

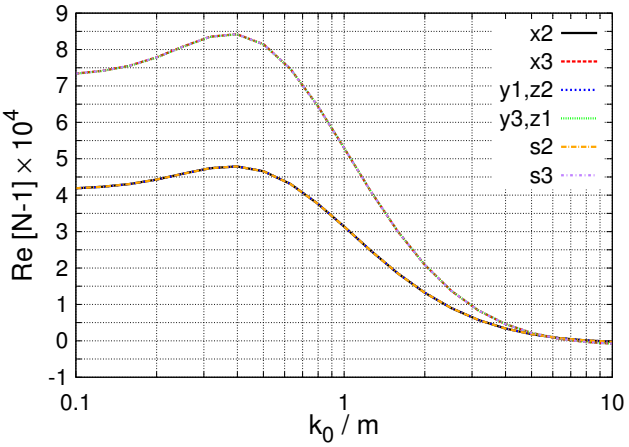

Figure 2.5: Same figure as Figure 2.3 but for $f_{\rm rd} = f_c$ in the energy range of $0.1 \leq k_0/m \leq 10$ for all the modes.

Toll (1952) pointed out that unless the Poynting vectors of the probe photon and the external field are parallel to each other, an appropriate Lorentz transformation makes them anti-parallel and, as a result, the refractive index depends only on the reduced field strength $f_{\rm rd}$

$$f_{\rm rd} = f \sin^2\left(\frac{\theta}{2}\right) \tag{2.61}$$

as long as the field strength is not much larger than the critical value. Here θ is the angle between the Poynting vectors of the probe photon and the external field. I hence redraw Figure 2.3 as Figure 2.5 in the range of $0.1 \leq k_0/m \leq 10$ after adjusting the external-field strength so that $f_{\rm rd} = f_c$ for all the modes. As expected, the x3, s3, y3 and z1 modes become identical, which is also true for the x2, s2, y1 and z2 modes. The relation also holds for the imaginary part. It is important that these relations are obtained as a result of separate calculations for different propagation directions in my formulation, the fact that guarantees the correctness of my calculations.

The imaginary part of the refractive index Im$[N]$ is shown in Figure 2.6 for the same case. It is found that the imaginary part is non-vanishing down to $k_0 = 0$ although it diminishes very rapidly for $k_0/m \lesssim 0.1$. It is also seen that Im$[N]$ for each photon mode reaches its maximum at $k_0/m \sim 1$ and it decreases monotonically for higher energies. These behaviors are also consistent with the known limits (Narozhnyĭ, 1969). In fact, as mentioned above, they are already settled to the asymptotic values at $k_0/m \sim 1000$ as shown in the inset of the figure. The imaginary parts Im$[N]$ for different modes follow the general trend mentioned earlier for $|{\rm Re}[N-1]|$ with the x3 mode being the largest and the y1/z2 being the smallest except around $k_0/m \sim 1$, where some crossings occur.

The imaginary part of the refractive index in the weak-field or low-energy (region (2) in Figure 2.2) was considered in Ritus (1972); Heinzl and Schröder (2006). Although I cannot obtain the analytic expression, I try to compute the imaginary

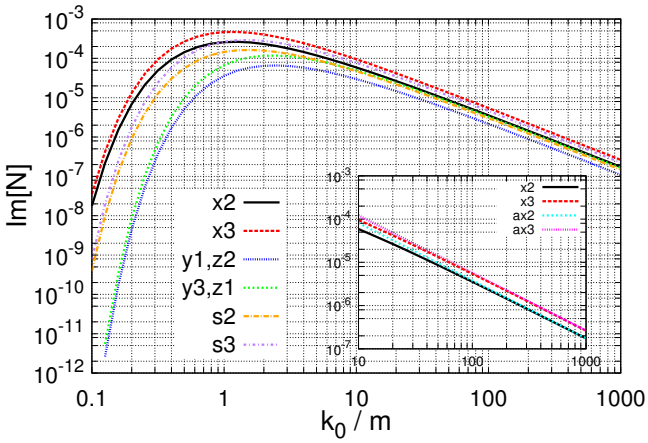

Figure 2.6: Same as Figure 2.3 but for the imaginary part of refractive index Im[N]. The inset shows the behavior in the high-energy regime as in Figure 2.4. The lines labeled as ax2 and ax3 show the high-energy limit expressed as Equations (2.59) and (2.60), respectively.

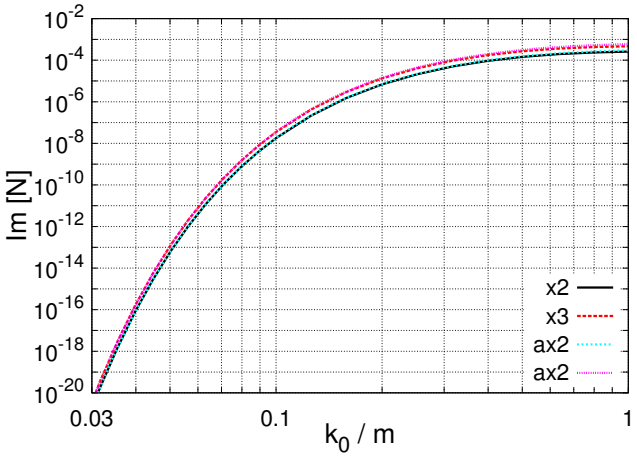

Figure 2.7: Same as Figure 2.6 but for the low-energy range. The lines labeled as ax2 and ax3 show the weak-field or low-energy limits expressed as Equations (2.62) and (2.63), respectively.

part numerically in this regime. The results are displayed in Figure 2.7 for the x2 and x3 modes in the range of $0.03 \lesssim k_0/m \leq 1$. The lines labeled as ax2 and ax3 are the results obtained in Ritus (1972), which are expressed as

$$\mathrm{Im}[N_{\mathrm{x2}}] \simeq \frac{1}{8}\sqrt{\frac{3}{2}}\frac{\alpha\epsilon}{\nu}e^{-\frac{4}{3\epsilon\nu}}, \tag{2.62}$$

$$\mathrm{Im}[N_{\mathrm{x3}}] \simeq \frac{1}{4}\sqrt{\frac{3}{2}}\frac{\alpha\epsilon}{\nu}e^{-\frac{4}{3\epsilon\nu}}, \tag{2.63}$$

where $\epsilon = f/f_c$ and $\nu = k_0/m$. It is found that the imaginary parts $\mathrm{Im}[N]$ are better approximated in this regime by Equations (2.62) and (2.63) rather than by

$$\mathrm{Im}[N_{\mathrm{x2}}] \simeq \frac{4\alpha\epsilon^2}{45}\frac{4}{3\epsilon\nu}e^{-\frac{4}{3\epsilon\nu}}, \tag{2.64}$$

$$\mathrm{Im}[N_{\mathrm{x3}}] \simeq \frac{7\alpha\epsilon^2}{45}\frac{4}{3\epsilon\nu}e^{-\frac{4}{3\epsilon\nu}}, \tag{2.65}$$

obtained in Heinzl and Schröder (2006).

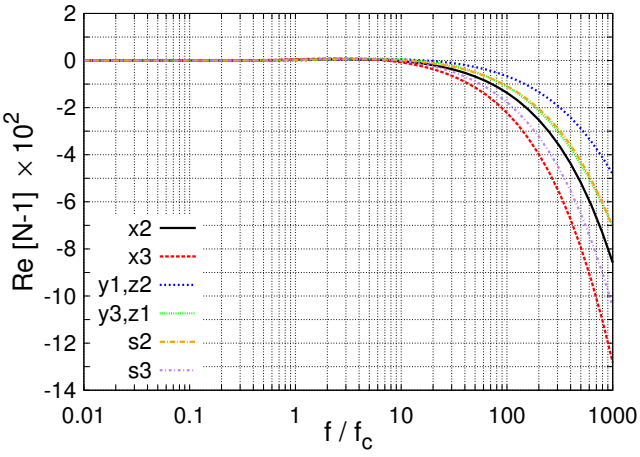

Figure 2.8: Plot of $\mathrm{Re}[N-1]$ as a function of the field strength. I assume $k_0/m = 1$ this time.

Next I show the dependence of the refractive index on the external-field strength, setting $k_0/m = 1$. This has never been published in the literature before. In Figure 2.8, $\mathrm{Re}[N-1]$ is shown as a function of f/f_c in the range of $0.01 \leq f/f_c \leq 1000$. Figure 2.9 zooms in to the range of $0.01 \leq f/f_c \leq 3$, setting the vertical axis in the logarithmic scale. The quadratic behavior observed for $0.01 \leq f/f_c \lesssim 0.5$ is in accord with the weak-field or low-energy limits (Narozhnyĭ, 1969), which are given as ax2 and ax3 for the x2 and x3 modes in the inset of this figure, respectively. $\mathrm{Re}[N-1]$ is negative at $f/f_c \gtrsim 10$, which is consistent with the earlier findings. The modulus $|\mathrm{Re}[N-1]|$ is an increasing function of f at $f/f_c \gtrsim 10$.

The imaginary part $\mathrm{Im}[N]$ is shown in Figure 2.10. It increases monotonically with the external-field strength. The slopes are steeper at $f/f_c \lesssim 0.5$, which is consistent with the analytic expression in the weak-field or low-energy limit of

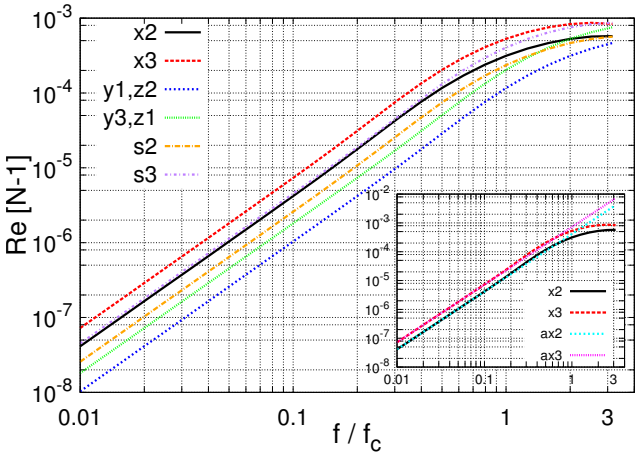

Figure 2.9: Same as Figure 2.8 but for weak fields. The inset shows the comparison between my numerical results and asymptotic expressions, Equations (2.56) and (2.57), labeled as ax2 and ax3 for the x2 and x3 modes, respectively, in the weak-field or low-energy limits.

Im[N] (Ritus, 1972; Heinzl and Schröder, 2006). The inset of this figure shows the comparison of my numerical results with the asymptotic limits, Equations (2.62) and (2.63), labeled as ax2 and ax3 for the x2 and x3 modes, respectively. They almost coincide with each other at $f/f_c \lesssim 0.5$. Note, on the other hand, that the behavior of the imaginary part at high field-strengths has not been reported in the literature.

2.4.2 Plane-Wave

I next consider the "local" refractive index for the plane wave field, which is also original in this chapter. I evaluate numerically the polarization tensor is given in Equations (2.50), (2.52) - (2.54) and solve the Maxwell equation, Equation (2.55), obtained in the gradient expansion. Since my formulation is based on the perturbation theory, it is natural to express the refractive index in the plane wave as $N+\delta N$, where N is the refractive index for the crossed field and δN is the correction from the temporal and spatial non-uniformities. As mentioned for the crossed field, the refractive indices for the y1 and z2 modes are identical to each other. In fact, the relevant components of the Maxwell equations, Equation (2.55), are the same for these modes. This is also true for the y3 and z1 modes.

It is found that the correction δN starts indeed with the linear order of Ω/m for both the real and imaginary part. It is then written as

$$\delta N = (C_{\rm Re} + iC_{\rm Im}) \times \Omega/m + O((\Omega/m)^2) \tag{2.66}$$

and the numerical values of the coefficients $C_{\rm Re}$ and $C_{\rm Im}$ are given for $k_0/m = 1$ and $f/f_c = 1$ in Table 2.2. The temporal and spatial variations are found to mainly affect the imaginary part: $|{\rm Im}[\delta N]| > |{\rm Re}[\delta N]|$ from these results. It is also seen that Im[δN] is larger for the photons propagating in the opposite direction

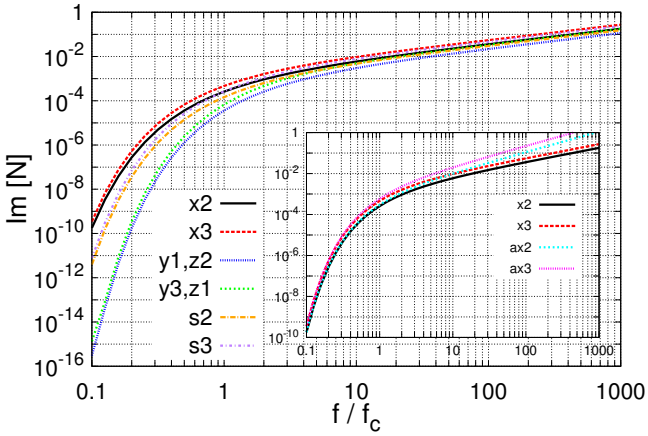

Figure 2.10: Same figure as Figure 2.8 but for the imaginary part of refractive index Im$[N]$. The inset shows the comparison between my numerical results and the asymptotic expressions in the weak-field or low-energy limits, Equations (2.62) and (2.63), labeled as ax2 and ax3 for the x2 and x3 modes, respectively.

Table 2.2: Proportionality coefficients in the correction δN from temporal and spatial non-uniformities [7]

mode	C_{Re}	C_{Im}
x2	-1.30×10^{-3}	3.16×10^{-3}
x3	-3.08×10^{-3}	5.17×10^{-3}
y1,z2	1.42×10^{-4}	4.35×10^{-4}
y3,z1	1.83×10^{-4}	8.28×10^{-4}
s2	-3.10×10^{-4}	1.79×10^{-3}
s3	-9.69×10^{-4}	3.11×10^{-3}

[7] $k_0/m = 1$ and $f/f_c = 1$.

to the external plane-wave (x-direction) as in the crossed field limit. The real parts Re$[\delta N]$ are negative for photons other than those propagating perpendicularly to the external plane-wave. The modulus $|\mathrm{Re}[N + \delta N]|$ is hence reduced for these modes by the field variation.

I next present the dependence on k_0/m of δN for $f/f_c = 1$, $\Omega/m = 10^{-3}$ in Figures 2.11 and 2.12. The real part Re$[\delta N]$ is exhibited in Figure 2.11. It is seen that the real part can be both positive and negative: it tends to be negative at higher values of k_0/m although the range depends on the mode; in fact, the values of the photon energy, above which δN gets positive, are smaller for the photons propagating oppositely to the external plane-wave. Re$[\delta N]$ is much smaller than Re$[N - 1]$ for the crossed field at $0.1 \leq k_0/m \leq 1$ and decreases very rapidly like Im$[N]$ for the crossed field.

The imaginary part Im$[\delta N]$ is shown in Figure 2.12 for the probe-photon energies of $0.03 \leq k_0/m \leq 1$. The inset indicates the comparison for the x2 and x3 modes

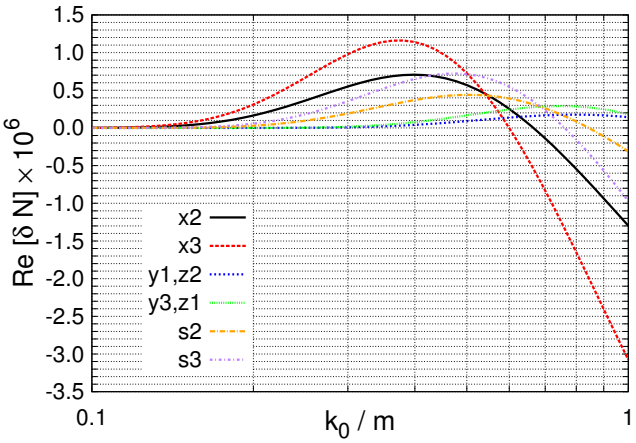

Figure 2.11: Plot of the correction to the real part of the refractive index for the crossed field from the temporal and spatial variations in the plane-wave field. The field strength is set to the critical value, i.e., $f/f_c = 1$ and the frequency of the external wave field is chosen as $\Omega/m = 10^{-3}$.

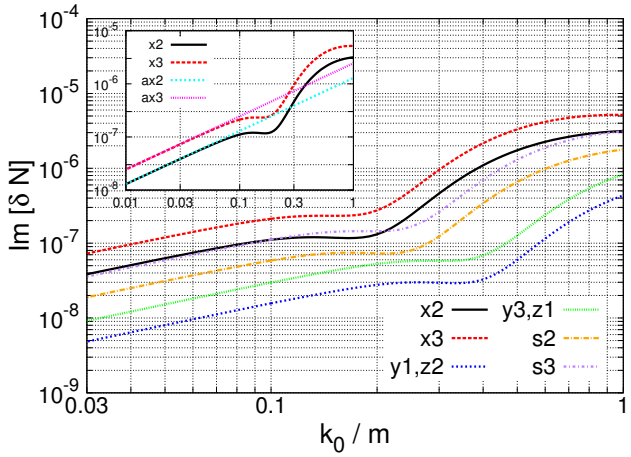

Figure 2.12: Same as Figure 2.11 but for Im$[\delta N]$. The inset shows the comparison for the x2 and x3 modes between the asymptotic limits (Equations (2.67) and (2.68) labeled as ax2 and ax3) and the numerically computed results.

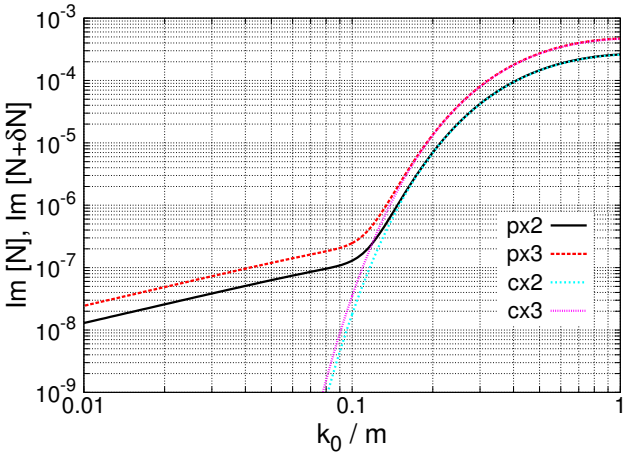

Figure 2.13: Comparison for the x2 and x3 modes of $\mathrm{Im}[N+\delta N]$ labeled as px2 and px3, respectively, and $\mathrm{Im}[N]$ labeled as cx2 and cx3, respectively, as a function of the probe-photon energy, k_0/m. Here I set $f/f_c = 1$ as in the previous two figures.

between the numerically computed results of $\mathrm{Im}[\delta N]$ and the asymptotic values in the weak-field or low-energy limits. The expressions of $\mathrm{Im}[\delta N]$ in this regime are given from Equations (2.52) and (2.53) as

$$\mathrm{Im}[\delta N_{\mathrm{x2}}] \simeq \frac{263\alpha}{3780\pi}\left(\frac{\Omega k_\mu n^\mu}{m^2}\right)\frac{\kappa^2 m^2}{k_0^2}, \tag{2.67}$$

$$\mathrm{Im}[\delta N_{\mathrm{x3}}] \simeq \frac{71\alpha}{540\pi}\left(\frac{\Omega k_\mu n^\mu}{m^2}\right)\frac{\kappa^2 m^2}{k_0^2}, \tag{2.68}$$

where $\Omega k_\mu n^\mu/m^2 = \Omega(k_0+k_1)/m^2$ is the product of the momentum of the external plane-wave and that of the probe photon normalized by the electron mass and is a representative term in the gradient expansion $F_{\mu\nu} \sim f_{\mu\nu}(1+\Omega\xi)$, being proportional to Ω with the proportional factor $k_\mu n^\mu$ originating from the commutation relation of ξ that accompanies Ω; $\kappa^2 = e^2 k_\mu f^\mu{}_\nu f^{\nu\lambda} k_\lambda/m^6 = e^2 f^2 (k_0+k_1)^2/m^6$ as previously defined in Equation (2.56). Equations (2.67) and (2.68) are convenient for the evaluation of the typical value of $\mathrm{Im}[\delta N]$:

$$\begin{aligned}\mathrm{Im}[\delta N] &\sim \alpha\left(\frac{\Omega}{m}\right)\left(\frac{k_0}{m}\right)\left(\frac{f}{f_c}\right)^2 \\ &\sim 7\times 10^{-6}\left(\frac{\Omega}{0.5\mathrm{keV}}\right)\left(\frac{k_0}{510\mathrm{keV}}\right)\left(\frac{I}{4.6\times 10^{29}\mathrm{W/cm^2}}\right),\end{aligned} \tag{2.69}$$

where I is the intensity of the external electromagnetic wave. It is found from the inset that $\mathrm{Im}[\delta N]$ is well approximated for $\Omega/m = 10^{-3}$ by the asymptotic expressions at $k_0/m \leq 0.03$ for $f/f_c = 1$. There occurs a dent at $k_0/m \simeq 0.2$ and $\mathrm{Im}[\delta N]$ rises more rapidly with k_0/m at larger energies, where $\mathrm{Im}[N]$ of the crossed field also becomes substantial. The location of the dent depends on the propagation direction of the probe photon, with the x (y/z) mode having the smallest (largest) value of k_0/m at the dent, respectively.

Since the imaginary part of the refractive index declines rapidly below these energies for the crossed field, it is dominated by the first-order correction $\mathrm{Im}[\delta N]$ from the temporal and spatial variations in the plane-wave at these low energies. In fact, the latter is commonly more than 10 times larger than the former $\mathrm{Im}[\delta N] \gtrsim 10 \times \mathrm{Im}[N]$ at $k_0/m \lesssim 0.1$. See also Figure 2.13, where I plot $\mathrm{Im}[N + \delta N]$ and $\mathrm{Im}[N]$ as a function of k_0/m. This is especially the case of the probe photons propagating transversally to the background plane-wave. In accordance with the trend for the crossed field, the x (y/z) modes have largest (smallest) moduli $|\mathrm{Im}[\delta N]|$ and s modes come in between in general.

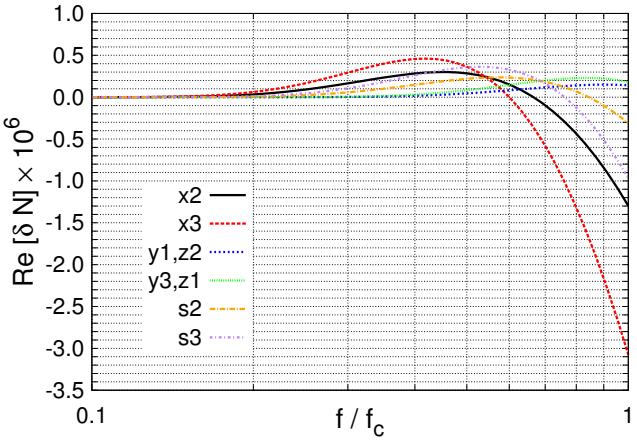

Figure 2.14: $\mathrm{Re}[\delta N]$ for the external plane-wave field of the frequency of $\Omega/m = 10^{-3}$. The probe-photon energy is chosen as $k_0/m = 1$.

Finally, I look into the dependence of δN on the field strength in the range of $f/f_c \leq 1$. The real and imaginary parts of δN are shown in Figures 2.14 and 2.15, respectively. The probe-photon energy is set to $k_0/m = 1$ and the frequency of the external field assumed to be $\Omega/m = 10^{-3}$ again, though the results scale with the latter linearly. It is evident that the results are quite similar to those shown in Figures 2.11 and 2.12: the real part, $\mathrm{Re}[\delta N]$, has a hump at $f/f_c \sim 0.5$ whereas the imaginary part, $\mathrm{Im}[\delta N]$, is quadratic in f/f_c at weak fields and becomes dominant over the crossed-field contribution, $\mathrm{Im}[N]$, at $f/f_c \lesssim 0.1$; the order in the magnitudes of $\mathrm{Im}[\delta N]$ for different modes is the same as that in Figure 2.11; $\mathrm{Re}[\delta N]$ is negative at a certain range of f/f_c, which depends on the mode, occurring for stronger fields for the mode propagating transversally to the background plane-field. The reason for these behaviors is the following: although δN depends not only on the product of k_0/m and $(f/f_c)^2$ but also on $k^\mu k_\mu/m^2$, the latter dependence is minuscule in the regime I consider here. As a result, the dependence of the refractive index on k_0/m can be translated into that of f/f_c. In fact, the numerical results for $\mathrm{Im}[\delta N]$ are well-approximated by the same asymptotic formulae, Equations (2.67) and (2.68), in the weak-field regime $f/f_c \lesssim 0.1$, which can be seen in the inset of Figure 2.15; $\mathrm{Im}[\delta N]$ has a dent at $f/f_c \sim 0.2$ and changes its behavior at larger field-strengths, where the crossed-field contribution, $\mathrm{Im}[N]$, becomes large, overwhelming $\mathrm{Im}[\delta N]$. See also Figure 2.16, where I plot $\mathrm{Im}[N + \delta N]$ and $\mathrm{Im}[N]$ as a function of f/f_c.

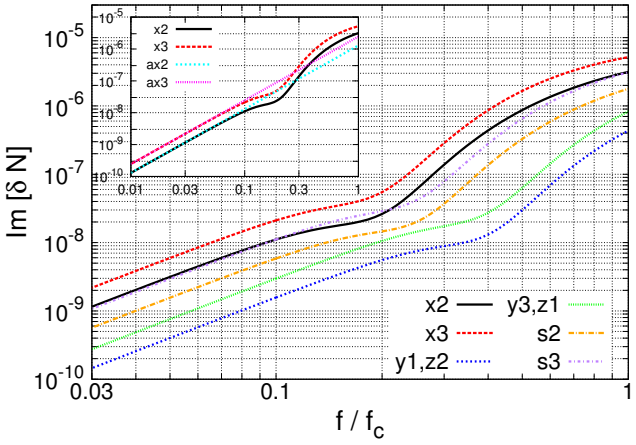

Figure 2.15: Same figure as Figure 2.14 but for Im$[\delta N]$. The inset shows the comparison for the x2 and x3 modes between the asymptotic limits (Equations (2.67) and (2.68)) labeled as ax2 and ax3, respectively, and the numerically computed results for the x2 and x3 modes labeled as x2 and x3, respectively.

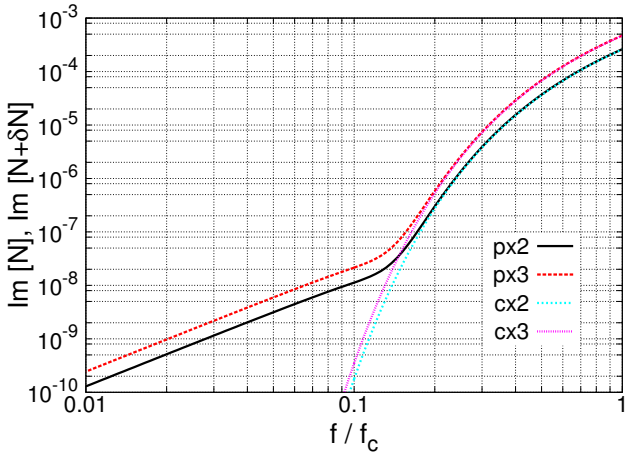

Figure 2.16: Same as Figure 2.13 but as a function of field strength, f/f_c. Here k_0/m is set to 1 as in the previous two figures.

2.5 Summary and Discussion

In this chapter I have developed a perturbation theory adapted to Schwinger's proper-time method to calculate the induced electromagnetic current, which should be plugged into the Maxwell equations to obtain the refractive indices, for the external, linearly polarized plane-waves, considering them as the unperturbed states and regarding a probe photon as the perturbation to them. Although this is nothing new and indeed was already employed previously (Adler, 1971), my formulation is based on the interaction picture, a familiar tool in quantum mechanics and referred to also as the Furry picture in strong-field QED, rather than utilizing the properties of particular electromagnetic fields from the beginning. Moreover, assuming that the wavelength of the external plane-wave is much longer than the Compton wavelength of electron and employing the gradient expansion, I have evaluated locally the polarization tensor via the induced electromagnetic current to the lowest order of the spatial and temporal variations of the external fields, which is the main achievement in this chapter. It has been shown that the vacuum polarization is given locally by the field strength and its gradient of the external plane-waves at each point. I have then considered the dispersion relations for the probe photons propagating in various directions and derived the local refractive indices.

I have first evaluated them for the crossed fields, which are the long-wavelength limit of the plane-waves. In so doing, the field strength and the energy of the probe photon are not limited but are allowed to take any values. Note that even for the crossed field not all the parameter regime has been investigated and I have explored those portions unconsidered so far. I have shown that the refractive index is larger for the photons propagating oppositely to the external field than for those propagating perpendicularly. I have also confirmed some limiting cases that were already known in the literature analytically or numerically (Baier and Breitenlohner, 1967b; Narozhnyĭ, 1969; Ritus, 1972; Heinzl and Schröder, 2006), particularly the behavior in the weak external fields demonstrated in Toll (1952). Note, however, that the assumption of a fixed classical background field becomes rather questionable at field strengths near or, in particular, above the critical field strength, since the back reactions to the background field from pair creations should be then taken into account. This issue is certainly much beyond the scope of this chapter and in spite of this conceptual problem I think that the results in such very strong fields are still useful to understand the scale and qualitative behavior of the corrections from the field gradient.

I have then proceeded to the evaluation of the refractive index for the plane-wave to the lowest order of the temporal and spatial variations of the background field. The local correction δN to the refractive index for the crossed field N has been numerically evaluated for the first time. I have demonstrated that the modulus of its imaginary part is larger than that of the real part, i.e., the field variations mainly affect the imaginary part of the refractive index. Note that the refractive index I have obtained in this chapter is local, depending on the local field-strength and its gradient, and is meaningful in the sense of the WKB approximation. This is in contrast to the refractive index averaged over the photon path in Dinu et al. (2014b).

In the optical laser experiments ($\Omega/m \sim 10^{-6}$), the refractive index may be approximated very well by that for the crossed field. The correction from the field variations is typically $|\delta N| \sim 10^{-5} \times \mathrm{Re}[N-1]$. The weak-field limit may be also justified, since the current maximum laser-intensity $\sim 2.0 \times 10^{22}\mathrm{W/cm^2}$ is still much lower than the critical value, $4.6 \times 10^{29}\mathrm{W/cm^2}$. Then the numerical results given in Figure 2.9 are applicable: $\mathrm{Re}[N-1] \sim 10^{-4} \times (f/f_c)^2$ for the probe photon with $k_0/m = 1$, which corresponds to $\sim 10^{-8}$ at $\sim 10^{25}\mathrm{W/cm^2}$, the power expected for future laser facilities such as ELI. Note that how to observe the local refractive index in the electromagnetic wave is a different issue and the averaged one will be better suited for experiments (Dinu et al., 2014b).

Unlike for the optical laser, the field variations may not be ignored for X-ray lasers with $\Omega/m \simeq 10^{-2}$. I find from Figure 2.9 and Table 2.2 that the refractive index for the crossed field and the first-order correction to it are $|N-1| \sim 10^{-4}$ and $|\delta N| \sim 10^{-5}$, respectively, for the probe photon with $k_0/m = 1$ propagating oppositely to the external fields with the critical field strength. It may be more interesting that the imaginary part of the first-order correction, $\mathrm{Im}[\delta N]$, becomes larger than that for the crossed field $\mathrm{Im}[N]$ at $f/f_c \lesssim 0.1$ for $k_0/m = 1$ or at $k_0/m \lesssim 0.1$ for $f/f_c = 1$. It should be noted, however, that the suppression is much relaxed by the presence of the temporal and spatial variations in the background plane-field. This is because the imaginary part of the refractive index is exponentially suppressed for the crossed-field while it is suppressed only by powers for the plane-wave.

Very strong electromagnetic fields and their temporal and/or spatial variations may be also important for some astronomical phenomena. For example, burst activities called giant flares and short bursts have been observed in magnetars, i.e., strongly magnetized neutron stars (Olausen and Kaspi, 2014). Although the energy source of these activities is thought to be the magnetic fields of magnetars, the mechanism of bursts is not understood yet. In the analysis of the properties of the emissions from these bursts, the results obtained in this chapter may be useful.

As for the burst mechanism, one interesting model related with the strong field variation was proposed by some authors (Heyl and Hernquist, 1998, 1999, 2005), in which they considered shock formations in electromagnetic waves propagating in strong magnetic fields around the magnetar. The shock dissipation may produce a fireball of electrons and positrons via pair creations. Their discussion is based on the Rankine-Hugoniot-type jump condition and the Euler-Heisenberg Lagrangian, which is certainly not able to treat the close vicinity of the shock wave, since the shock is essentially a discontinuity. Note, however, that my result in this chapter is not very helpful for this problem, either, since the field variation is very rapid and has quite short wavelengths and, moreover, finite amplitudes of waves are essential for shock formation while my method is limited to the linear level. It is hence needed to extend the formulation to accommodate these nonlinear effects somehow, which will be a future task.

2.6 Detailed Derivations

I begin with the following transformation amplitudes: $\langle x^{(0)}(s)|\hat{\Pi}^{\mu}_{I}(s)U(s)|x(0)\rangle$, $\langle x^{(0)}(s)|U(s)\hat{\Pi}^{\mu}_{I}(0)|x(0)\rangle$. They are written as

$$\begin{aligned}
&\langle x(s)|\hat{\Pi}^{\mu}(s)U(s)|x(0)\rangle \\
&= \langle x(s)|\hat{\Pi}^{\mu}(s)\left[1-i\int_0^s du\Big\{e\hat{\Pi}^{\alpha}(u)b_{\alpha}\exp\left[-ik_{\delta}\hat{x}^{\delta}(u)\right]\right. \\
&\quad \left.+eb_{\alpha}\exp\left[-ik_{\delta}\hat{x}^{\delta}(u)\right]\hat{\Pi}^{\alpha}(u)+\frac{1}{2}e\sigma^{\alpha\beta}(u)g_{\alpha\beta}(u)\Big\}\right]|x(0)\rangle, \qquad (2.70)
\end{aligned}$$

$$\begin{aligned}
&\langle x(s)|U(s)\hat{\Pi}^{\mu}(0)|x(0)\rangle \\
&= \langle x(s)|\left[1-i\int_0^s du\Big\{e\hat{\Pi}^{\alpha}(u)b_{\alpha}\exp\left[-ik_{\delta}\hat{x}^{\delta}(u)\right]\right. \\
&\quad \left.+eb_{\alpha}\exp\left[-ik_{\delta}\hat{x}^{\delta}(u)\right]\hat{\Pi}^{\alpha}(u)+\frac{1}{2}e\sigma^{\alpha\beta}(u)g_{\alpha\beta}(u)\Big\}\right]\hat{\Pi}^{\mu}(0)|x(0)\rangle \qquad (2.71)
\end{aligned}$$

with the proper-time evolution operator given in Equation (2.40). In this expression, $g_{\alpha\beta}(u)=g_{\alpha\beta}\exp\left[-ik_{\delta}\hat{x}^{\delta}(u)\right]$. I rearrange the first two terms in the integrand as

$$\begin{aligned}
&\hat{\Pi}^{\mu}(s)\left(e\hat{\Pi}^{\alpha}(u)b_{\alpha}\exp\left[-ik_{\delta}\hat{x}^{\delta}(u)\right]+eb_{\alpha}\exp\left[-ik_{\delta}\hat{x}^{\delta}(u)\right]\hat{\Pi}^{\alpha}(u)\right) \\
&=2eb_{\alpha}\hat{\Pi}^{\mu}(s)\hat{\Pi}^{\alpha}(u)\exp\left[-ik_{\delta}\hat{x}^{\delta}(u)\right]-eb_{\alpha}k^{\alpha}\hat{\Pi}^{\mu}(s)\exp\left[-ik_{\delta}\hat{x}^{\delta}(u)\right], \qquad (2.72) \\
&\left(e\hat{\Pi}^{\alpha}(u)b_{\alpha}\exp\left[-ik_{\delta}\hat{x}^{\delta}(u)\right]+eb_{\alpha}\exp\left[-ik_{\delta}\hat{x}^{\delta}(u)\right]\hat{\Pi}^{\alpha}(u)\right)\hat{\Pi}^{\mu}(0) \\
&=2eb_{\alpha}\hat{\Pi}^{\alpha}(u)\exp\left[-ik_{\delta}\hat{x}^{\delta}(u)\right]\hat{\Pi}^{\mu}(0)-eb_{\alpha}k^{\alpha}\exp\left[-ik_{\delta}\hat{x}^{\delta}(u)\right]\hat{\Pi}^{\mu}(0), \qquad (2.73)
\end{aligned}$$

using by the following relation

$$\begin{aligned}
\exp\left[-ik_{\delta}\hat{x}^{\delta}(u)\right]\hat{\Pi}_{\alpha}(u) &= \left\{\hat{\Pi}_{\alpha}(u)+\left[-ik_{\delta}\hat{x}^{\delta}(u),\hat{\Pi}_{\alpha}(u)\right]\right\}\exp\left[-ik_{\delta}\hat{x}^{\delta}(u)\right] \\
&= \hat{\Pi}_{\alpha}(u)\exp\left[-ik_{\delta}\hat{x}^{\delta}(u)\right]-k_{\alpha}\exp\left[-ik_{\delta}\hat{x}^{\delta}(u)\right], \qquad (2.74)
\end{aligned}$$

which is obtained from Equations (2.98) and (2.151). The calculations of the remaining terms in the integrand, $\langle x(s)|\hat{\Pi}^{\mu}(s)\left(-i\int_0^s du\frac{1}{2}e\sigma^{\alpha\beta}(u)g_{\alpha\beta}(u)\right)|x(0)\rangle$ and $\langle x(s)|\left(-i\int_0^s du\frac{1}{2}e\sigma^{\alpha\beta}(u)g_{\alpha\beta}(u)\right)\hat{\Pi}^{\mu}(0)|x(0)\rangle$ proceed as follows:

$$\begin{aligned}
&\langle x(s)|\hat{\Pi}^{\mu}(s)\int_0^s du\left(-\frac{ie}{2}\right)\sigma^{\alpha\beta}(u)g_{\alpha\beta}(u)|x(0)\rangle \\
&\simeq \langle x(s)|\int_0^s du\hat{\Pi}^{\mu}(s)\exp\left[-ik_{\delta}\hat{x}^{\delta}(u)\right] \\
&\quad\times\left(-\frac{ie}{2}\right)\left[(\sigma g)+\frac{ieu}{2}\left\{(\sigma f)(\sigma g)-(\sigma g)(\sigma f)\right\}+\frac{e^2u^2}{4}(\sigma f)(\sigma g)(\sigma f)\right]|x(0)\rangle \\
&\quad+\langle x(s)|\int_0^s du\hat{\Pi}^{\mu}(s)\exp\left[-ik_{\delta}\hat{x}^{\delta}(u)\right]\left(-\frac{ie}{2}\right) \\
&\quad\times\left[\frac{ieu}{2}\left\{(\sigma f)(\sigma g)-(\sigma g)(\sigma f)\right\}(\Omega\xi(0))+\frac{e^2u^2}{2}(\sigma f)(\sigma g)(\sigma f)(\Omega\xi(0))\right]|x(0)\rangle,
\end{aligned} \qquad (2.75)$$

$$
\begin{aligned}
& \langle x(s)| \int_0^s du \left(-\frac{ie}{2}\right) g_{\alpha\beta}(u)\sigma^{\alpha\beta}(u)\hat{\Pi}^\mu(0)|x(0)\rangle \\
\simeq\ & \langle x(s)| \int_0^s du \left(-\frac{ie}{2}\right) \exp\left[-ik_\delta \hat{x}^\delta(u)\right] \hat{\Pi}^\mu(0) \\
& \times \left[(\sigma g) + \frac{ieu}{2}\left\{(\sigma f)(\sigma g) - (\sigma g)(\sigma f)\right\} + \frac{e^2u^2}{4}(\sigma f)(\sigma g)(\sigma f)\right]|x(0)\rangle \\
& + \langle x(s)| \int_0^s du \left(-\frac{ie}{2}\right) \exp\left[-ik_\delta \hat{x}^\delta(u)\right] \hat{\Pi}^\mu(0) \\
& \times \left[\frac{ieu}{2}\left\{(\sigma f)(\sigma g) - (\sigma g)(\sigma f)\right\}(\Omega\xi(0)) + \frac{e^2u^2}{2}(\sigma f)(\sigma g)(\sigma f)(\Omega\xi(0))\right]|x(0)\rangle \\
& + \langle x(s)| \int_0^s du \left(-\frac{ie}{2}\right) \exp\left[-ik_\delta \hat{x}^\delta(u)\right] (-in^\mu) \\
& \times \left[\frac{ieu}{2}\left\{(\sigma f)(\sigma g) - (\sigma g)(\sigma f)\right\}\Omega + \frac{e^2u^2}{2}(\sigma f)(\sigma g)(\sigma f)\Omega\right]|x(0)\rangle. \qquad (2.76)
\end{aligned}
$$

On the second lines in the above equations, I employed the expansion of $\sigma^{\alpha\beta}(u)$ given in Equation (2.42). The resultant expressions with Equations (2.72), (2.73) give Equations (2.43) and (2.44). Note that all operators in these expressions, i.e., $\hat{\Pi}^\mu(s)$, $\hat{\Pi}^\mu(0)$, $\hat{\Pi}^\mu(u)$ and $\hat{x}^\mu(u)$, are defined in the interaction picture.

Remaining are the evaluations of the transformation amplitudes such as

$$
\begin{aligned}
\langle x(s)|\hat{\Pi}^\mu(s)|x(0)\rangle, & \qquad (2.77)\\
\langle x(s)|\hat{\Pi}^\mu(0)|x(0)\rangle, & \qquad (2.78)\\
\langle x(s)|\exp\left[-ik_\delta \hat{x}^\delta(u)\right]|x(0)\rangle, & \qquad (2.79)\\
\langle x(s)|\hat{\Pi}^\alpha(u)\exp\left[-ik_\delta \hat{x}^\delta(u)\right]|x(0)\rangle, & \qquad (2.80)\\
\langle x(s)|\hat{\Pi}^\mu(s)\exp\left[-ik_\delta \hat{x}^\delta(u)\right]|x(0)\rangle, & \qquad (2.81)\\
\langle x(s)|\exp\left[-ik_\delta \hat{x}^\delta(u)\right]\hat{\Pi}^\mu(0)|x(0)\rangle, & \qquad (2.82)\\
\langle x(s)|\hat{\Pi}^\mu(s)\hat{\Pi}^\alpha(u)\exp\left[-ik_\delta \hat{x}^\delta(u)\right]|x(0)\rangle, & \qquad (2.83)\\
\langle x(s)|\hat{\Pi}^\alpha(u)\exp\left[-ik_\delta \hat{x}^\delta(u)\right]\hat{\Pi}^\mu(0)|x(0)\rangle. & \qquad (2.84)
\end{aligned}
$$

Each operator in these amplitudes can be represented with $\hat{x}^\mu(s)$ and $\hat{x}^\mu(0)$. For example, $\hat{\Pi}^\mu(s)$ and $\hat{\Pi}^\mu(0)$ are derived from Equations (2.27) and (2.28) to the lowest order of Ω as

$$
\begin{aligned}
& \hat{\Pi}^\mu(s) \\
& = \frac{\hat{x}^\mu(s) - \hat{x}^\mu(0)}{2s} + \frac{e}{2}f^\mu{}_\nu(\hat{x}^\nu(s) - \hat{x}^\nu(0)) \\
& + \Omega\frac{e}{2}f^\mu{}_\nu(\hat{x}^\nu(s) - \hat{x}^\nu(0))\left(\frac{2}{3}\xi(s) + \frac{1}{3}\xi(0)\right) + n^\mu e^2 f^2 s\left(\frac{1}{6}\xi(s) - \frac{1}{6}\xi(0)\right) \\
& + \Omega n^\mu e^2 f^2 s\left(\frac{1}{4}\xi^2(s) - \frac{1}{6}\xi(s)\xi(0) - \frac{1}{12}\xi^2(0)\right) + \frac{1}{4}\Omega e s n^\mu(\sigma f), \qquad (2.85)
\end{aligned}
$$

$$
\begin{aligned}
&\hat{\Pi}^{\mu}(0)\\
&=\frac{\hat{x}^{\mu}(s)-\hat{x}^{\mu}(0)}{2s}-\frac{e}{2}f^{\mu}{}_{\nu}(\hat{x}^{\nu}(s)-\hat{x}^{\nu}(0))\\
&+\Omega\frac{e}{2}f^{\mu}{}_{\nu}(\hat{x}^{\nu}(s)-\hat{x}^{\nu}(0))\left(-\frac{1}{3}\xi(s)-\frac{2}{3}\xi(0)\right)+n^{\mu}e^{2}f^{2}s\left(\frac{1}{6}\xi(s)-\frac{1}{6}\xi(0)\right)\\
&+\Omega n^{\mu}e^{2}f^{2}s\left(\frac{1}{12}\xi^{2}(s)+\frac{1}{6}\xi(s)\xi(0)-\frac{1}{4}\xi^{2}(0)\right)-\frac{1}{4}\Omega esn^{\mu}(\sigma f). \qquad (2.86)
\end{aligned}
$$

Using the fact that the left hand side (and hence the right hand side also) of Equation (2.86) is independent of s, I obtain the operator $\hat{x}^{\mu}(u)$ in terms of $\hat{x}^{\mu}(s)$ and $\hat{x}^{\mu}(0)$ as

$$
\begin{aligned}
&\hat{x}^{\mu}(u)\\
&=\hat{x}^{\mu}(0)+\frac{u}{s}(\hat{x}^{\mu}(s)-\hat{x}^{\mu}(0))\\
&+ef^{\mu}{}_{\nu}(\hat{x}^{\nu}(s)-\hat{x}^{\nu}(0))\\
&\qquad\times\left[-u+\frac{u^{2}}{s}+\Omega\left\{\left(-\frac{u}{3}+\frac{1}{3}\frac{u^{3}}{s^{2}}\right)\xi(s)+\left(-\frac{2}{3}u+\frac{u^{2}}{s}-\frac{1}{3}\frac{u^{3}}{s^{2}}\right)\xi(0)\right\}\right]\\
&+n^{\mu}e^{2}f^{2}\left\{\left(\frac{su}{3}-u^{2}+\frac{2}{3}\frac{u^{3}}{s}\right)\xi(s)+\left(-\frac{su}{3}+u^{2}-\frac{2}{3}\frac{u^{3}}{s}\right)\xi(0)\right\}\\
&+\Omega n^{\mu}e^{2}f^{2}\left\{\left(\frac{su}{6}-\frac{1}{3}u^{2}-\frac{1}{3}\frac{u^{3}}{s}+\frac{1}{2}\frac{u^{4}}{s^{2}}\right)\xi^{2}(s)\right.\\
&\quad\left.+\left(\frac{su}{3}-\frac{4}{3}u^{2}+2\frac{u^{3}}{s}-\frac{u^{4}}{s^{2}}\right)\xi(s)\xi(0)+\left(-\frac{su}{2}+\frac{5}{3}u^{2}-\frac{5}{3}\frac{u^{3}}{s}+\frac{1}{2}\frac{u^{4}}{s^{2}}\right)\xi^{2}(0)\right\}\\
&+\frac{1}{2}\Omega e\sigma^{\nu\lambda}f_{\nu\lambda}n^{\mu}\left(u^{2}-su\right). \qquad (2.87)
\end{aligned}
$$

Replacing s with u in Equation (2.85) and plugging Equation (2.87) into Equation (2.85), I can express $\hat{\Pi}^{\mu}(u)$ as

$$
\begin{aligned}
&\hat{\Pi}^{\mu}(u)\\
&=\frac{\hat{x}^{\mu}(s)-\hat{x}^{\mu}(0)}{2s}\\
&+ef^{\mu}{}_{\nu}(\hat{x}^{\nu}(s)-\hat{x}^{\nu}(0))\\
&\qquad\times\left[-\frac{1}{2}+\frac{u}{s}+\Omega\left\{\left(\frac{1}{2}\left(\frac{u}{s}\right)^{2}-\frac{1}{6}\right)\xi(s)+\left(-\frac{1}{2}\left(\frac{u}{s}\right)^{2}+\frac{u}{s}-\frac{1}{3}\right)\xi(0)\right\}\right]\\
&+n^{\mu}e^{2}f^{2}s\left[\left\{\frac{1}{6}-\frac{u}{s}+\left(\frac{u}{s}\right)^{2}\right\}\xi(s)+\left\{-\frac{1}{6}+\frac{u}{s}-\left(\frac{u}{s}\right)^{2}\right\}\xi(0)\right]\\
&+\Omega n^{\mu}e^{2}f^{2}s\left[\left\{\frac{1}{12}-\frac{1}{3}\left(\frac{u}{s}\right)-\frac{1}{2}\left(\frac{u}{s}\right)^{2}+\left(\frac{u}{s}\right)^{3}\right\}\xi^{2}(s)\right.\\
&\left.+\left\{\frac{1}{6}-\frac{4}{3}\frac{u}{s}+3\left(\frac{u}{s}\right)^{2}-2\left(\frac{u}{s}\right)^{3}\right\}\xi(s)\xi(0)+\left\{-\frac{1}{4}+\frac{5}{3}\frac{u}{s}-\frac{5}{2}\left(\frac{u}{s}\right)^{2}+\left(\frac{u}{s}\right)^{3}\right\}\xi^{2}(0)\right]\\
&+\Omega e\sigma^{\nu\lambda}f_{\nu\lambda}n^{\mu}s\left(-\frac{1}{4}+\frac{1}{2}\frac{u}{s}\right). \qquad (2.88)
\end{aligned}
$$

It is now easy to evaluate the amplitudes in Equations (2.77) and (2.78), which appear in the induced electromagnetic current as $\mathrm{tr}\left(\langle x(s)|\hat{\Pi}^{\mu}(s)+\hat{\Pi}^{\mu}(0)|x(0)\rangle\right)$ and $\mathrm{tr}\left(\sigma^{\mu\nu}\langle x(s)|\hat{\Pi}^{\mu}(s)-\hat{\Pi}^{\mu}(0)|x(0)\rangle\right)$. They are given as

$$\mathrm{tr}\left(\langle x(s)|\hat{\Pi}^{\mu}(s)+\hat{\Pi}^{\mu}(0)|x(0)\rangle\right) \simeq \mathrm{tr}\left(\langle x(s)|0|x(0)\rangle\right)=0, \tag{2.89}$$

$$\mathrm{tr}\left(\sigma^{\mu\nu}\langle x(s)|\hat{\Pi}_{\nu}(s)-\hat{\Pi}_{\nu}(0)|x(0)\rangle\right) \simeq \mathrm{tr}\left[\sigma^{\mu\nu}n_{\nu}(\sigma f)\right]\frac{1}{i(4\pi)^2 s}\frac{e}{2}\Omega=0, \tag{2.90}$$

where I used the following relation

$$\langle x(s)|x(0)\rangle=\frac{1}{i(4\pi)^2 s^2}\left(\mathbf{1}-\frac{ies}{2}(\sigma f)(1+\Omega\xi)\right), \tag{2.91}$$

which is derived from Equation (2.31). There is hence no contribution to the induced electromagnetic current from $\langle x(s)|\hat{\Pi}^{\mu}(s)|x(0)\rangle$ and $\langle x(s)|\hat{\Pi}^{\mu}(0)|x(0)\rangle$.

The amplitude given in Equation (2.79) is calculated to the linear order of Ω by using the Zassenhaus formula:

$$\begin{aligned} e^{X+\Omega Y} &\simeq e^{X}e^{\Omega Y}e^{-\frac{1}{2}[X,\Omega Y]}e^{\frac{1}{6}(2[\Omega Y,[X,\Omega Y]]+[X,[X,\Omega Y]])} \\ &\simeq e^{X}(1+\Omega Y)(1-\frac{1}{2}[X,\Omega Y])\left(1+\frac{1}{6}(2[\Omega Y,[X,\Omega Y]]+[X,[X,\Omega Y]])\right) \\ &\simeq e^{X}+e^{X}\Omega Y+e^{X}\left(-\frac{1}{2}\left[X,\Omega Y\right]\right)+e^{X}\frac{1}{6}\left[X,[X,\Omega Y]\right]. \end{aligned} \tag{2.92}$$

In this expression, X stands collectively for the terms that do not include Ω in the argument of the exponential function in Equation (2.80) whereas ΩY represents those terms that depend on Ω. The commutation relations in this equation are evaluated as follows:

$$\begin{aligned} &[X,\Omega Y] \\ &=i\Omega(k\cdot n)^2e^2f^2\left(-\frac{4}{3}su^2+\frac{10}{3}u^3-2\frac{u^4}{s}\right)\xi(s) \\ &\quad+i\Omega(k\cdot n)^2e^2f^2\left(-\frac{2}{3}s^2u+\frac{10}{3}su^2-\frac{14}{3}u^3+2\frac{u^4}{s}\right)\xi(0) \\ &\quad+i\Omega(k\cdot n)ek_{\beta}f^{\beta}{}_{\nu}\left[\hat{x}^{\nu}(s)-\hat{x}^{\nu}(0)\right]\left(-\frac{2}{3}su+2u^2-\frac{4}{3}\frac{u^3}{s}\right), \end{aligned} \tag{2.93}$$

$$[X,[X,\Omega Y]]=i\Omega(k\cdot n)^3e^2f^2\left(\frac{4}{3}s^3u-\frac{16}{3}s^2u^2+8su^3-4u^4\right). \tag{2.94}$$

Putting these results together, I obtain the explicit expression of the exponential

operator suited for the calculation of the amplitude as

$$
\begin{aligned}
&e^{-ik_\alpha \hat{x}^\alpha(u)} \\
&= \exp\left\{-ik_\alpha\left[\frac{u}{s}\hat{x}^\alpha(s) + ef^\alpha{}_\beta\hat{x}^\beta(s)\left(-u+\frac{u^2}{s}\right) + n^\alpha e^2 f^2\left(\frac{su}{3}-u^2+\frac{2}{3}\frac{u^3}{s}\right)\xi(s)\right]\right\} \\
&\times\left(1+\Omega\left\{iek_\alpha f^\alpha{}_\beta\left[\hat{x}^\beta(s)-\hat{x}^\beta(0)\right]\left[\left(\frac{u}{3}-\frac{1}{3}\frac{u^3}{s^2}\right)\xi(s)+\left(\frac{2}{3}u-\frac{u^2}{s}+\frac{1}{3}\frac{u^3}{s^2}\right)\xi(0)\right]\right.\right. \\
&+i(k\cdot n)e^2f^2\left[\left(-\frac{su}{6}+\frac{1}{3}u^2+\frac{1}{3}\frac{u^3}{s}-\frac{1}{2}\frac{u^4}{s^2}\right)\xi^2(s)\right. \\
&\quad\left.+\left(-\frac{su}{3}+\frac{4}{3}u^2-2\frac{u^3}{s}+\frac{u^4}{s^2}\right)\xi(s)\xi(0)+\left(\frac{su}{2}-\frac{5}{3}u^2+\frac{5}{3}\frac{u^3}{s}-\frac{1}{2}\frac{u^4}{s^2}\right)\xi^2(0)\right] \\
&+ie(k\cdot n)k_\alpha f^\alpha{}_\beta\left[\hat{x}^\beta(s)-\hat{x}^\beta(0)\right]\left(-\frac{2}{3}u^2+\frac{4}{3}\frac{u^3}{s}-\frac{2}{3}\frac{u^4}{s^2}\right) \\
&+i(k\cdot n)^2e^2f^2\xi(s)\left(\frac{1}{3}su^2-2u^3+3\frac{u^4}{s}-\frac{4}{3}\frac{u^5}{s^2}\right) \\
&+i(k\cdot n)^2e^2f^2\xi(0)\left(-su^2+\frac{10}{3}u^3-\frac{11}{3}\frac{u^4}{s}+\frac{4}{3}\frac{u^5}{s^2}\right) \\
&+i(k\cdot n)^3e^2f^2\left(-\frac{2}{3}s^3u+\frac{14}{9}s^2u^2-\frac{4}{9}su^3-\frac{10}{9}u^4+\frac{2}{3}\frac{u^5}{s}\right) \\
&\left.\left.+ie(\sigma f)(k\cdot n)\left(\frac{1}{2}su-\frac{1}{2}u^2\right)\right\}\right) \\
&\times\exp\left\{-ik_\mu\left[\left(1-\frac{u}{s}\right)\hat{x}^\mu(0)+ef^\mu{}_\nu\hat{x}^\nu(0)\left(u-\frac{u^2}{s}\right)\right.\right. \\
&\qquad\left.\left.+n^\mu e^2f^2\left(-\frac{su}{3}+u^2-\frac{2}{3}\frac{u^3}{s}\right)\xi(0)\right]\right\} \\
&\times\exp\left[i(k)^2\left(u-\frac{u^2}{s}\right)+i(k\cdot n)^2e^2f^2\left(-\frac{1}{3}su^2+\frac{2}{3}u^3-\frac{1}{3}\frac{u^4}{s}\right)\right]. \qquad (2.95)
\end{aligned}
$$

The transformation amplitude is then given as

$$
\begin{aligned}
&\langle x(s)|\exp\left[-ik_\mu\hat{x}^\mu(u)\right]|x(0)\rangle \\
&=\langle x(s)|x(0)\rangle\exp\left(-ik_\mu x^\mu\right) \\
&\times\exp\left[i(k)^2\left(u-\frac{u^2}{s}\right)+i(k\cdot n)^2e^2f^2\left(-\frac{1}{3}su^2+\frac{2}{3}u^3-\frac{1}{3}\frac{u^4}{s}\right)\right] \\
&\times\left\{1+\Omega\left[i(k\cdot n)^2e^2f^2\xi\left(-\frac{2}{3}su^2+\frac{4}{3}u^3-\frac{2}{3}\frac{u^4}{s}\right)\right.\right. \\
&\qquad+i(k\cdot n)^3e^2f^2\left(-\frac{2}{3}s^3u+\frac{14}{9}s^2u^2-\frac{4}{9}su^3-\frac{10}{9}u^4+\frac{2}{3}\frac{u^5}{s}\right) \\
&\qquad\left.\left.+ie(\sigma f)(k\cdot n)\left(\frac{1}{2}su-\frac{1}{2}u^2\right)\right]\right\}. \qquad (2.96)
\end{aligned}
$$

I next calculate the amplitudes in Equations (2.80) - (2.82). The operators $\hat{\Pi}^\mu(u), \hat{\Pi}^\mu(s), \hat{\Pi}^\mu(0)$ are written in terms of $\hat{x}^\mu(s)$ and $\hat{x}^\mu(0)$ and the amplitude can

be calculated after re-arranging the order of operators. I first consider the rearrangement of $\hat{x}^\alpha(0)\exp\left[-ik_\mu\hat{x}^\mu(u)\right]$. Using the relations

$$Be^{-A} = e^{-A}B + e^{-A}\left[A,B\right] + \frac{1}{2}e^{-A}\left[A,\left[A,B\right]\right], \tag{2.97}$$

$$e^{A}B = Be^{A} + \left[A,B\right]e^{A} + \frac{1}{2}\left[A,\left[A,B\right]\right]e^{A}, \tag{2.98}$$

which are derived from Hadamard's lemma

$$e^{A}Be^{-A} = B + \left[A,B\right] + \frac{1}{2}\left[A,\left[A,B\right]\right], \tag{2.99}$$

one can obtain

$$\begin{aligned}
&\hat{x}^\alpha(0)\exp\left[-ik_\mu\hat{x}^\mu(u)\right]\\
=\;&\exp\left[-ik_\mu\hat{x}^\mu(u)\right]\\
&\times\Bigg[\hat{x}^\alpha(0) - 2uk^\alpha + 2e(f^{\alpha\mu}k_\mu)u^2 - \frac{4}{3}u^3n^\alpha(k\cdot n)e^2f^2\\
&\quad+\Omega e(f^{\alpha\mu}k_\mu)\left\{\frac{2}{3}\frac{u^3}{s}\xi(s) + \left(2u^2 - \frac{2}{3}\frac{u^3}{s}\right)\xi(0)\right\}\\
&\quad+\Omega en^\alpha k_\mu f^\mu{}_\nu\left(\hat{x}^\nu(s) - \hat{x}^\nu(0)\right)\left(-\frac{2}{3}\frac{u^3}{s}\right)\\
&\quad+\Omega n^\alpha(k\cdot n)e^2f^2\left\{\left(\frac{2}{3}u^3 - 2\frac{u^4}{s}\right)\xi(s) + \left(-\frac{10}{3}u^3 + 2\frac{u^4}{s}\right)\xi(0)\right\}\\
&\quad+\Omega e(f^{\alpha\mu}k_\mu)(k\cdot n)\left(-\frac{4}{3}u^3\right) + \Omega n^\alpha(k\cdot n)^2e^2f^2(2u^4)\Bigg],
\end{aligned} \tag{2.100}$$

which is still inappropriate for the calculation of the amplitudes because some $\hat{x}^\mu(s)$ are sitting to the right of $\exp\left[-ik_\delta\hat{x}^\delta(u)\right]$, which contains $\hat{x}^\mu(0)$. I hence have to rearrange further the terms that contain $\hat{x}^\mu(s)$ to obtain

$$\begin{aligned}
&\hat{x}^\alpha(0)\exp\left[-ik_\mu\hat{x}^\mu(u)\right]\\
=\;&\exp\left[-ik_\mu\hat{x}^\mu(u)\right]\left[\hat{x}^\alpha(0) + \Omega e(f^{\alpha\mu}k_\mu)\left(2u^2 - \frac{2}{3}\frac{u^3}{s}\right)\xi(0)\right.\\
&\quad\left.+\Omega en^\alpha k_\mu f^\mu{}_\nu\hat{x}^\nu(0)\frac{2}{3}\frac{u^3}{s} + \Omega n^\alpha(k\cdot n)e^2f^2\left(-\frac{10}{3}u^3 + 2\frac{u^4}{s}\right)\xi(0)\right]\\
&+\left[\Omega e(f^{\alpha\mu}k_\mu)\frac{2}{3}\frac{u^3}{s}\xi(s) + \Omega en^\alpha k_\mu f^\mu{}_\nu\hat{x}^\nu(s)\left(-\frac{2}{3}\frac{u^3}{s}\right)\right.\\
&\quad\left.+\Omega n^\alpha(k\cdot n)e^2f^2\left(\frac{2}{3}u^3 - 2\frac{u^4}{s}\right)\xi(s)\right]\exp\left[-ik_\mu\hat{x}^\mu(u)\right]\\
&+\exp\left[-ik_\mu\hat{x}^\mu(u)\right]\left[-2uk^\alpha + 2e(f^{\alpha\mu}k_\mu)u^2 - \frac{4}{3}u^3n^\alpha(k\cdot n)e^2f^2\right.\\
&\quad\left.+\Omega e(f^{\alpha\mu}k_\mu)(k\cdot n)\left(\frac{4}{3}\frac{u^4}{s} - \frac{8}{3}u^3\right) + \Omega n^\alpha(k\cdot n)^2e^2f^2\left(-\frac{8}{3}\frac{u^5}{s} + \frac{14}{3}u^4\right)\right].
\end{aligned} \tag{2.101}$$

This is the expression suitable for the calculation of the transformation amplitudes.

The re-arrangement of $\exp\left[-ik_\mu \hat{x}^\mu(u)\right] \hat{x}^\alpha(s)$ goes similarly: after the rearrangements it becomes as follows:

$$
\begin{aligned}
& \exp\left[-ik_\mu \hat{x}^\mu(u)\right] \hat{x}^\alpha(s) \\
= \; & \left[\hat{x}^\alpha(s) + \Omega e (f^{\alpha\mu} k_\mu) \left(-\frac{4}{3}s^2 + 2su - \frac{2}{3}\frac{u^3}{s}\right)\xi(s)\right. \\
& + \Omega e n^\alpha k_\mu f^\mu{}_\nu \hat{x}^\nu(s) \left(-\frac{2}{3}s^2 + 2su - 2u^2 + \frac{2}{3}\frac{u^3}{s}\right) \\
& \left. + \Omega n^\alpha (k\cdot n) e^2 f^2 \left(-\frac{4}{3}s^3 + 2s^2 u + 2su^2 - \frac{14}{3}u^3 + 2\frac{u^4}{s}\right)\xi(s)\right] \exp\left[-ik_\mu \hat{x}^\mu(u)\right] \\
& + \exp\left[-ik_\mu \hat{x}^\mu(u)\right] \left[\Omega e (f^{\alpha\mu} k_\mu) \left(-\frac{2}{3}s^2 + 2su - 2u^2 + \frac{2}{3}\frac{u^3}{s}\right)\xi(0)\right. \\
& + \Omega e n^\alpha k_\mu f^\mu{}_\nu \hat{x}^\nu(0) \left(\frac{2}{3}s^2 - 2su + 2u^2 - \frac{2}{3}\frac{u^3}{s}\right) \\
& \left. + \Omega n^\alpha (k\cdot n) e^2 f^2 \left(-\frac{4}{3}s^3 + 6s^2 u - 10su^2 + \frac{22}{3}u^3 - 2\frac{u^4}{s}\right)\xi(0)\right] \\
& + \exp\left[-ik_\mu \hat{x}^\mu(u)\right] \\
& \times \left[2(u-s)k^\alpha + 2ef^{\alpha\mu}k_\mu(-s^2 + 2su - u^2)\right. \\
& + n^\alpha (k\cdot n) e^2 f^2 \left(-\frac{4}{3}s^3 + 4s^2 u - 4su^2 + \frac{4}{3}u^3\right) \\
& + \Omega e (k\cdot n)(f^{\alpha\mu}k_\mu) \left(\frac{4}{3}s^3 - \frac{8}{3}s^2 u + \frac{8}{3}u^3 - \frac{4}{3}\frac{u^4}{s}\right) \\
& \left. + \Omega n^\alpha (k\cdot n)^2 e^2 f^2 \left(2s^4 - \frac{16}{3}s^3 u + \frac{4}{3}s^2 u^2 + 8su^3 - \frac{26}{3}u^4 + \frac{8}{3}\frac{u^5}{s}\right)\right]. \qquad (2.102)
\end{aligned}
$$

The amplitudes of these operators are then written as follows:

$$
\begin{aligned}
& \langle x(s)|\hat{x}^\mu(0) \exp\left[-ik_\delta \hat{x}^\delta(u)\right]|x(0)\rangle \\
& = \langle x(s)| \exp\left[-ik_\delta \hat{x}^\delta(u)\right]|x(0)\rangle \\
& \times \left[x^\mu + \Omega e f^{\mu\nu} k_\nu \xi 2u^2 + \Omega n^\mu (k\cdot n) e^2 f^2 \xi \left(-\frac{8}{3}u^3\right) - 2uk^\alpha + 2ef^{\mu\nu}k_\nu u^2\right. \\
& \quad - \frac{4}{3}u^3 n^\mu (k\cdot n) e^2 f^2 + \Omega e f^{\mu\nu} k_\nu (k\cdot n) \left(\frac{4}{3}\frac{u^4}{s} - \frac{8}{3}u^3\right) \\
& \quad \left. + \Omega n^\mu (k\cdot n)^2 e^2 f^2 \left(-\frac{8}{3}\frac{u^5}{s} + \frac{14}{3}u^4\right)\right], \qquad (2.103)
\end{aligned}
$$

$$
\begin{aligned}
&\langle x(s)|\exp\left[-ik_\delta\hat{x}^\delta(u)\right]\hat{x}^\mu(s)|x(0)\rangle \\
&=\langle x(s)|\exp\left[-ik_\delta\hat{x}^\delta(u)\right]|x(0)\rangle \\
&\times\Bigg[x^\mu+\Omega e f^{\mu\nu}k_\nu\xi(-2s^2+4su-2u^2) \\
&\quad+\Omega n^\mu(k\cdot n)e^2f^2\left(-\frac{8}{3}s^3+8s^2u-8su^2+\frac{8}{3}u^3\right)\xi \\
&\quad+2(u-s)k^\mu+2ef^{\mu\nu}k_\nu(-s^2+2su-u^2) \\
&\quad+n^\mu(k\cdot n)e^2f^2\left(-\frac{4}{3}s^3+4s^2u-4su^2+\frac{4}{3}u^3\right) \\
&\quad+\Omega e(k\cdot n)f^{\mu\nu}k_\nu\left(\frac{4}{3}s^3-\frac{8}{3}s^2u+\frac{8}{3}u^3-\frac{4}{3}\frac{u^4}{s}\right) \\
&\quad+\Omega n^\mu(k\cdot n)^2e^2f^2 \\
&\qquad\times\left(2s^4-\frac{16}{3}s^3u+\frac{4}{3}s^2u^2+8su^3-\frac{26}{3}u^4+\frac{8}{3}\frac{u^5}{s}\right)\Bigg], \qquad (2.104)
\end{aligned}
$$

The following relations, which are obtained in the similar way, are also needed to evaluate Equations (2.80) - (2.82).

$$
\begin{aligned}
&f^\beta{}_\alpha\hat{x}^\alpha(0)\exp\left[-ik_\mu\hat{x}^\mu(u)\right] \\
&=\exp\left[-ik_\mu\hat{x}^\mu(u)\right]\left[f^\beta{}_\alpha\hat{x}^\alpha(0)+\Omega n^\beta(k\cdot n)ef^2\left(2u^2-\frac{2}{3}\frac{u^3}{s}\right)\xi(0)\right] \\
&+\Omega n^\beta(k\cdot n)ef^2\left(\frac{2}{3}\frac{u^3}{s}\right)\xi(s)\exp\left[-ik_\mu\hat{x}^\mu(u)\right] \\
&+\exp\left[-ik_\mu\hat{x}^\mu(u)\right] \\
&\times\left[-2uf^\beta{}_\alpha k^\alpha+2n^\beta(k\cdot n)ef^2u^2+\Omega n^\beta(k\cdot n)^2ef^2\left(\frac{4}{3}\frac{u^4}{s}-\frac{8}{3}u^3\right)\right], \qquad (2.105) \\
&\xi(0)\exp\left[-ik_\mu\hat{x}^\mu(u)\right]=\exp\left[-ik_\mu\hat{x}^\mu(u)\right]\left[\xi(0)-2u(k\cdot n)\right], \qquad (2.106) \\
&\exp\left[-ik_\mu\hat{x}^\mu(u)\right]f^\beta{}_\alpha\hat{x}^\alpha(s) \\
&=\left[f^\beta{}_\alpha\hat{x}^\alpha(s)+\Omega n^\beta(k\cdot n)ef^2\left(-\frac{4}{3}s^2+2su-\frac{2}{3}\frac{u^3}{s}\right)\xi(s)\right]\exp\left[-ik_\mu\hat{x}^\mu(u)\right] \\
&+\exp\left[-ik_\mu\hat{x}^\mu(u)\right]\Omega n^\beta(k\cdot n)ef^2\left(-\frac{2}{3}s^2+2su-2u^2+\frac{2}{3}\frac{u^3}{s}\right)\xi(0) \\
&+\exp\left[-ik_\mu\hat{x}^\mu(u)\right]\Big[2(u-s)f^\beta{}_\alpha k^\alpha+2n^\beta(k\cdot n)ef^2(-s^2+2su-u^2) \\
&+\Omega n^\beta(k\cdot n)^2ef^2\left(\frac{4}{3}s^3-\frac{8}{3}s^2u+\frac{8}{3}u^3-\frac{4}{3}\frac{u^4}{s}\right)\Big], \qquad (2.107) \\
&\exp\left[-ik_\mu\hat{x}^\mu(u)\right]\xi(s)=\left[\xi(s)+2(u-s)(k\cdot n)\right]\exp\left[-ik_\mu\hat{x}^\mu(u)\right]. \qquad (2.108)
\end{aligned}
$$

They yield immediately the followings:

$$\begin{aligned}
&\langle x(s)|f^{\mu}{}_{\nu}\hat{x}^{\nu}(0)\exp\left[-ik_{\delta}\hat{x}^{\delta}(u)\right]|x(0)\rangle \\
&=\langle x(s)|\exp\left[-ik_{\delta}\hat{x}^{\delta}(u)\right]|x(0)\rangle\Bigg[f^{\mu}{}_{\nu}x^{\nu}+\Omega n^{\mu}(k\cdot n)ef^{2}\xi 2u^{2} \\
&-2uf^{\mu}{}_{\nu}k^{\nu}+2n^{\mu}(k\cdot n)ef^{2}u^{2}+\Omega n^{\mu}(k\cdot n)^{2}ef^{2}\left(\frac{4}{3}\frac{u^{4}}{s}-\frac{8}{3}u^{3}\right)\Bigg], \qquad (2.109)\\
&\langle x(s)|\xi(0)\exp\left[-ik_{\delta}\hat{x}^{\delta}(u)\right]|x(0)\rangle \\
&=\langle x(s)|\exp\left[-ik_{\delta}\hat{x}^{\delta}(u)\right]|x(0)\rangle\left[\xi-2u(k\cdot n)\right], \qquad (2.110)\\
&\langle x(s)|\exp\left[-ik_{\delta}\hat{x}^{\delta}(u)\right]f^{\mu}{}_{\nu}\hat{x}^{\nu}(s)|x(0)\rangle \\
&=\langle x(s)|\exp\left[-ik_{\delta}\hat{x}^{\delta}(u)\right]|x(0)\rangle\Bigg[f^{\mu}{}_{\nu}x^{\nu}+\Omega n^{\mu}(k\cdot n)ef^{2}\xi(-2s^{2}+4su-2u^{2}) \\
&+2(u-s)f^{\mu}{}_{\nu}k^{\nu}+2n^{\mu}(k\cdot n)ef^{2}(-s^{2}+2su-u^{2}) \\
&+\Omega n^{\mu}(k\cdot n)^{2}ef^{2}\left(\frac{4}{3}s^{3}-\frac{8}{3}s^{2}u+\frac{8}{3}u^{3}-\frac{4}{3}\frac{u^{4}}{s}\right)\Bigg], \qquad (2.111)\\
&\langle x(s)|\exp\left[-ik_{\delta}\hat{x}^{\delta}(u)\right]\xi(s)|x(0)\rangle \\
&=\langle x(s)|\exp\left[-ik_{\delta}\hat{x}^{\delta}(u)\right]|x(0)\rangle\left[\xi+2(u-s)(k\cdot n)\right]. \qquad (2.112)
\end{aligned}$$

Finally, the quadratic terms in x, e.g., $\langle x(s)|f^{\mu}{}_{\nu}\hat{x}^{\nu}(0)\xi(0)\exp\left[-ik_{\delta}\hat{x}^{\delta}(u)\right]|x(0)\rangle$, can be calculated as

$$\begin{aligned}
&\langle x(s)|f^{\mu}{}_{\nu}\hat{x}^{\nu}(0)\xi(0)\exp\left[-ik_{\delta}\hat{x}^{\delta}(u)\right]|x(0)\rangle \\
=\;&\langle x(s)|f^{\mu}{}_{\nu}\hat{x}^{\nu}(0)\exp\left[-ik_{\delta}\hat{x}^{\delta}(u)\right]\left[\xi(0)-2u(k\cdot n)\right]|x(0)\rangle \\
=\;&(\xi-2u(k\cdot n))\langle x(s)|f^{\mu}{}_{\nu}\hat{x}^{\nu}(0)\exp\left[-ik_{\delta}\hat{x}^{\delta}(u)\right]|x(0)\rangle. \qquad (2.113)
\end{aligned}$$

All results combined, $\hat{\Pi}^{\mu}(u)\exp\left[-ik_{\delta}\hat{x}^{\delta}(u)\right]$ is cast into

$$\begin{aligned}
&\hat{\Pi}^{\mu}(u)\exp\left[-ik_{\delta}\hat{x}^{\delta}(u)\right] \\
&=\Big(\text{rearranged terms of }\hat{\Pi}^{\mu}(u)\exp\left[-ik_{\delta}\hat{x}^{\delta}(u)\right]\Big) \\
&+\exp\left[-ik_{\delta}\hat{x}^{\delta}(u)\right] \\
&\times\Bigg[ef^{\mu\alpha}k_{\alpha}\left(-u+\frac{u^{2}}{s}\right)+(-\Omega)(k\cdot n)ef^{\mu\alpha}k_{\alpha}\left(-\frac{4}{3}u^{2}+\frac{8}{3}\frac{u^{3}}{s}-\frac{4}{3}\frac{u^{4}}{s^{2}}\right)+\frac{u}{s}k^{\mu} \\
&+n^{\mu}(k\cdot n)e^{2}f^{2}\left(\frac{1}{3}su-u^{2}+\frac{2}{3}\frac{u^{3}}{s}\right)+(-\Omega)n^{\mu}(k\cdot n)^{2}e^{2}f^{2}\left(su^{2}-4u^{3}+5\frac{u^{4}}{s}-2\frac{u^{5}}{s^{2}}\right)\Bigg]
\end{aligned}$$

(The expression continues to the next page.)

(The expression is continued.)

$$
\begin{aligned}
&+\exp\left[-ik_\delta\hat{x}^\delta(u)\right]\left[(-\Omega)ef^{\mu\alpha}k_\alpha\xi(0)\left(\frac{2}{3}u-\frac{u^2}{s}+\frac{2}{3}\frac{u^3}{s^2}\right)\right.\\
&+(-\Omega)n^\mu(k\cdot n)e^2f^2\xi(0)\left(-su+5u^2-\frac{22}{3}\frac{u^3}{s}+\frac{10}{3}\frac{u^4}{s^2}\right)\\
&\left.+(-\Omega)(k\cdot n)ef^\mu{}_\alpha\hat{x}^\alpha(0)\left(\frac{2}{3}u-2\frac{u^2}{s}+\frac{u^3}{s^2}\right)+(-\Omega)n^\mu ek_\alpha f^\alpha{}_\beta\hat{x}^\beta(0)\frac{1}{3}\frac{u^3}{s^2}\right]\\
&+\left[\xi(s)(-\Omega)ef^{\mu\alpha}k_\alpha\left(\frac{1}{3}u-\frac{2}{3}\frac{u^3}{s^2}\right)+(-\Omega)(k\cdot n)ef^\mu{}_\alpha\hat{x}^\alpha(s)\left(-\frac{2}{3}u+2\frac{u^2}{s}-\frac{u^3}{s^2}\right)\right.\\
&+(-\Omega)n^\mu ek_\alpha f^\alpha{}_\beta\hat{x}^\beta(s)\left(-\frac{1}{3}\frac{u^3}{s^2}\right)\\
&\left.+\xi(s)(-\Omega)n^\mu(k\cdot n)e^2f^2\left(\frac{1}{3}su-3u^2+6\frac{u^3}{s}-\frac{10}{3}\frac{u^4}{s^2}\right)\right]\exp\left[-ik_\delta\hat{x}^\delta(u)\right], \qquad (2.114)
\end{aligned}
$$

where the first term on the right hand side means that all $\hat{x}^\mu(s)$'s in the operator $\hat{\Pi}^\mu(u)$ have already been moved to the left of $\exp[-ik_\delta\hat{x}^\delta(u)]$ and all $\hat{x}^\mu(0)$'s to the right so that its amplitude could be expressed as the product of those of $\hat{\Pi}^\mu(u)$ and $\exp[-ik_\delta\hat{x}^\delta(u)]$. The corresponding amplitude is then given as

$$
\begin{aligned}
&\langle x(s)|\hat{\Pi}^\alpha(u)\exp\left[-ik_\mu\hat{x}^\mu(u)\right]|x(0)\rangle\\
&=\langle x(s)|\exp\left[-ik_\mu\hat{x}^\mu(u)\right]|x(0)\rangle\left[\frac{u}{s}k^\alpha+ef^{\alpha\beta}k_\beta\left(\frac{u^2}{s}-u\right)\right.\\
&\quad+n^\alpha(k\cdot n)e^2f^2\left(\frac{1}{3}su-u^2+\frac{2}{3}\frac{u^3}{s}\right)+\Omega ef^{\alpha\beta}k_\beta\xi\left(\frac{u^2}{s}-u\right)\\
&\quad+\Omega n^\alpha(k\cdot n)e^2f^2\xi\left(\frac{2}{3}su-2u^2+\frac{4}{3}\frac{u^3}{s}\right)+\Omega ef^{\alpha\beta}k_\beta(k\cdot n)\left(\frac{4}{3}u^2-\frac{8}{3}\frac{u^3}{s}+\frac{4}{3}\frac{u^4}{s^2}\right)\\
&\quad\left.+\Omega n^\alpha(k\cdot n)^2e^2f^2\left(-su^2+4u^3-5\frac{u^4}{s}+2\frac{u^5}{s^2}\right)+\Omega e(\sigma f)n^\alpha\left(-\frac{1}{4}s+\frac{1}{2}u\right)\right],
\end{aligned}
\qquad (2.115)
$$

since $\langle x(s)|\hat{\Pi}^\mu(u)|x(0)\rangle = \langle x(s)|x(0)\rangle\Omega e(\sigma f)n^\mu(-s/4+u/2)$. Similar expressions are obtained for $\hat{\Pi}^\mu(s)\exp\left[-ik_\delta\hat{x}^\delta(u)\right]$ and $\exp\left[-ik_\delta\hat{x}^\delta(u)\right]\hat{\Pi}^\mu(0)$, which are shown, respectively, as follows:

$$
\begin{aligned}
&\hat{\Pi}^\mu(s)\exp\left[-ik_\delta\hat{x}^\delta(u)\right]\\
&=\left(\text{rearranged terms of }\hat{\Pi}^\mu(s)\exp\left[-ik_\delta\hat{x}^\delta(u)\right]\right)\\
&+\exp\left[-ik_\delta\hat{x}^\delta(u)\right]\left[ef^{\mu\alpha}k_\alpha\left(u-\frac{u^2}{s}\right)+(-\Omega)(k\cdot n)ef^{\mu\alpha}k_\alpha\left(\frac{2}{3}u^2-\frac{4}{3}\frac{u^3}{s}+\frac{2}{3}\frac{u^4}{s^2}\right)\right.\\
&\quad+\frac{u}{s}k^\mu+n^\mu(k\cdot n)e^2f^2\left(\frac{1}{3}su-u^2+\frac{2}{3}\frac{u^3}{s}\right)\\
&\quad\left.+(-\Omega)(k\cdot n)^2n^\mu e^2f^2\left(\frac{1}{3}su^2-2u^3+3\frac{u^4}{s}-\frac{4}{3}\frac{u^5}{s^2}\right)\right]
\end{aligned}
$$

(The expression continues to the next page.)

(The expression is continued.)

$$
\begin{aligned}
&+\exp\left[-ik_\delta\hat{x}^\delta(u)\right]\left[(-\Omega)ef^{\mu\alpha}k_\alpha\xi(0)\left(-\frac{1}{3}u+\frac{u^2}{s}-\frac{1}{3}\frac{u^3}{s^2}\right)\right.\\
&\quad+(-\Omega)n^\mu(k\cdot n)e^2f^2\xi(0)\left(-\frac{1}{3}su+\frac{4}{3}u^2-2\frac{u^3}{s}+\frac{u^4}{s^2}\right)\\
&\quad\left.+(-\Omega)(k\cdot n)ef^\mu{}_\alpha\hat{x}^\alpha(0)\left(-\frac{1}{3}u\right)+(-\Omega)n^\mu ek_\alpha f^\alpha{}_\beta\hat{x}^\beta(0)\left(\frac{1}{3}\frac{u^3}{s^2}\right)\right]\\
&+\left[(-\Omega)n^\mu(k\cdot n)e^2f^2\xi(s)\left(-\frac{1}{3}su+\frac{2}{3}u^2+\frac{2}{3}\frac{u^3}{s}-\frac{u^4}{s^2}\right)\right.\\
&\quad+(-\Omega)ef^{\mu\alpha}k_\alpha\xi(s)\left(-\frac{2}{3}u+\frac{1}{3}\frac{u^3}{s^2}\right)+(-\Omega)(k\cdot n)ef^\mu{}_\alpha\hat{x}^\alpha(s)\left(\frac{1}{3}u\right)\\
&\quad\left.+(-\Omega)n^\mu ek_\alpha f^\alpha{}_\beta\hat{x}^\beta(s)\left(-\frac{1}{3}\frac{u^3}{s^2}\right)\right]\exp\left[-ik_\delta\hat{x}^\delta(u)\right], \qquad (2.116)
\end{aligned}
$$

$$
\begin{aligned}
&\exp\left[-ik_\delta\hat{x}^\delta(u)\right]\hat{\Pi}^\mu(0)\\
&=\left(\text{rearranged terms of }\hat{\Pi}^\mu(0)\exp\left[-ik_\delta\hat{x}^\delta(u)\right]\right)\\
&+\exp\left[-ik_\delta\hat{x}^\delta(u)\right]\left[ef^{\mu\alpha}k_\alpha\left(u-\frac{u^2}{s}\right)+(-\Omega)(k\cdot n)ef^{\mu\alpha}k_\alpha\left(\frac{2}{3}u^2-\frac{4}{3}\frac{u^3}{s}+\frac{2}{3}\frac{u^4}{s^2}\right)\right.\\
&\quad+k^\mu\left(\frac{u}{s}-1\right)+n^\mu(k\cdot n)e^2f^2\left(\frac{1}{3}su-u^2+\frac{2}{3}\frac{u^3}{s}\right)\\
&\quad\left.+(-\Omega)n^\mu(k\cdot n)^2e^2f^2\left(su^2-\frac{10}{3}u^3+\frac{11}{3}\frac{u^4}{s}-\frac{4}{3}\frac{u^5}{s^2}\right)\right]\\
&+\exp\left[-ik_\delta\hat{x}^\delta(u)\right]\left[(-\Omega)n^\mu(k\cdot n)e^2f^2\xi(0)\left(-su+\frac{10}{3}u^2-\frac{10}{3}\frac{u^3}{s}+\frac{u^4}{s^2}\right)\right.\\
&\quad+(-\Omega)ef^{\mu\alpha}k_\alpha\xi(0)\left(-\frac{1}{3}s-\frac{1}{3}u+\frac{u^2}{s}-\frac{1}{3}\frac{u^3}{s^2}\right)\\
&\quad+(-\Omega)(k\cdot n)ef^\mu{}_\alpha\hat{x}^\alpha(0)\left(\frac{1}{3}s-\frac{1}{3}u\right)\\
&\quad\left.+(-\Omega)n^\mu ek_\alpha f^\alpha{}_\beta\hat{x}^\beta(0)\left(-\frac{1}{3}s+u-\frac{u^2}{s}+\frac{1}{3}\frac{u^3}{s^2}\right)\right]\\
&+\left[(-\Omega)ef^{\mu\alpha}k_\alpha\xi(s)\left(\frac{1}{3}s-\frac{2}{3}u+\frac{1}{3}\frac{u^3}{s^2}\right)+(-\Omega)(k\cdot n)ef^\mu{}_\alpha\hat{x}^\alpha(s)\left(-\frac{1}{3}s+\frac{1}{3}u\right)\right.\\
&\quad+(-\Omega)n^\mu(k\cdot n)e^2f^2\xi(s)\left(\frac{1}{3}su-\frac{4}{3}u^2+2\frac{u^3}{s}-\frac{u^4}{s^2}\right)\\
&\quad\left.+(-\Omega)n^\mu ek_\alpha f^\alpha{}_\beta\hat{x}^\beta(s)\left(\frac{1}{3}s-u+\frac{u^2}{s}-\frac{1}{3}\frac{u^3}{s^2}\right)\right]\exp\left[-ik_\delta\hat{x}^\delta(u)\right], \qquad (2.117)
\end{aligned}
$$

and their amplitudes are then obtained as

$$\begin{aligned}
&\langle x(s)|\hat{\Pi}^{\mu}(s)\exp\left[-ik_{\alpha}\hat{x}^{\alpha}(u)\right]|x(0)\rangle \\
&=\langle x(s)|\exp\left[-ik_{\alpha}\hat{x}^{\alpha}(u)\right]|x(0)\rangle \\
&\quad\times\left[\Omega ef^{\mu\nu}k_{\nu}\xi\left(u-\frac{u^{2}}{s}\right)+\Omega n^{\mu}(k\cdot n)e^{2}f^{2}\xi\left(\frac{2}{3}su-2u^{2}+\frac{4}{3}\frac{u^{3}}{s}\right)\right. \\
&\quad+\left(u-\frac{u^{2}}{s}\right)ef^{\mu\nu}k_{\nu}+\left(\frac{1}{3}su-u^{2}+\frac{2}{3}\frac{u^{3}}{s}\right)n^{\mu}(k\cdot n)e^{2}f^{2}+\frac{u}{s}k^{\mu} \\
&\quad+\left(-\frac{2}{3}u^{2}+\frac{4}{3}\frac{u^{3}}{s}-\frac{2}{3}\frac{u^{4}}{s^{2}}\right)\Omega ef^{\mu\nu}k_{\nu}(k\cdot n) \\
&\quad\left.+\left(-\frac{1}{3}su^{2}+2u^{3}-3\frac{u^{4}}{s}+\frac{4}{3}\frac{u^{5}}{s^{2}}\right)\Omega n^{\mu}(k\cdot n)^{2}e^{2}f^{2}+\frac{1}{4}\Omega esn^{\mu}(\sigma f)\right],
\end{aligned} \tag{2.118}$$

$$\begin{aligned}
&\langle x(s)|\exp\left[-ik_{\alpha}\hat{x}^{\alpha}(u)\right]\hat{\Pi}^{\mu}(0)|x(0)\rangle \\
&=\langle x(s)|\exp\left[-ik_{\alpha}\hat{x}^{\alpha}(u)\right]|x(0)\rangle \\
&\times\left[\Omega ef^{\mu\nu}k_{\nu}\xi\left(u-\frac{u^{2}}{s}\right)+\Omega n^{\mu}(k\cdot n)e^{2}f^{2}\xi\left(\frac{2}{3}su-2u^{2}+\frac{4}{3}\frac{u^{3}}{s}\right)+\left(\frac{u}{s}-1\right)k^{\mu}\right. \\
&\quad+\left(u-\frac{u^{2}}{s}\right)ef^{\mu\nu}k_{\nu}+\left(\frac{1}{3}su-u^{2}+\frac{2}{3}\frac{u^{3}}{s}\right)n^{\mu}(k\cdot n)e^{2}f^{2} \\
&\quad+\Omega\left(-\frac{2}{3}u^{2}+\frac{4}{3}\frac{u^{3}}{s}-\frac{2}{3}\frac{u^{4}}{s^{2}}\right)ef^{\mu\nu}k_{\nu}(k\cdot n) \\
&\quad\left.+\Omega\left(-su^{2}+\frac{10}{3}u^{3}-\frac{11}{3}\frac{u^{4}}{s}+\frac{4}{3}\frac{u^{5}}{s^{2}}\right)n^{\mu}(k\cdot n)^{2}e^{2}f^{2}+\left(-\frac{1}{4}\right)\Omega esn^{\mu}(\sigma f)\right].
\end{aligned} \tag{2.119}$$

Finally, Equations (2.83) and (2.84) are calculated. I rewrite them in terms of $\langle x(s)|\exp\left[-ik_{\delta}\hat{x}^{\delta}(u)\right]|x(0)\rangle$ and $\langle x(s)|\hat{\Pi}^{\alpha}(u)\exp\left[-ik_{\delta}\hat{x}^{\delta}(u)\right]|x(0)\rangle$, which have been already evaluated. In so doing, the products of the operators such as $\hat{x}^{\mu}(0)\hat{\Pi}^{\alpha}(u)\times\exp\left[-ik_{\delta}\hat{x}^{\delta}(u)\right]$ in $\hat{\Pi}^{\mu}(s)\hat{\Pi}^{\alpha}(u)\exp\left[-ik_{\delta}\hat{x}^{\delta}(u)\right]$ and $\hat{\Pi}^{\alpha}(u)\exp\left[-ik_{\delta}\hat{x}^{\delta}(u)\right]\hat{x}^{\mu}(s)$ in $\hat{\Pi}^{\alpha}(u)\exp\left[-ik_{\delta}\hat{x}^{\delta}(u)\right]\hat{\Pi}^{\mu}(0)$ have to be rearranged. To accomplish it, I need the following commutation relations for $\hat{\Pi}^{\mu}(u)$, which are obtained from the results given in Section 2.7:

$$\begin{aligned}
&\left[\hat{x}^{\mu}(0),\hat{\Pi}^{\alpha}(u)\right] \\
&=-i\eta^{\mu\alpha}+2uief^{\mu\alpha}-2u^{2}in^{\mu}n^{\alpha}e^{2}f^{2}+\Omega ief^{\mu\alpha}\xi(s)\left(\frac{u^{2}}{s}\right) \\
&\quad+\Omega ief^{\mu\alpha}\xi(0)\left(2u-\frac{u^{2}}{s}\right)+\Omega in^{\mu}n^{\alpha}e^{2}f^{2}\xi(s)\left(u^{2}-4\frac{u^{3}}{s}\right) \\
&\quad+\Omega in^{\mu}n^{\alpha}e^{2}f^{2}\xi(0)\left(-5u^{2}+4\frac{u^{3}}{s}\right)+\Omega ien^{\mu}f^{\alpha}{}_{\beta}\left(\hat{x}^{\beta}(s)-\hat{x}^{\beta}(0)\right)\left(-\frac{u^{2}}{s}\right),
\end{aligned} \tag{2.120}$$

$$\left[ef^{\mu}{}_{\nu}\hat{x}^{\nu}(0),\hat{\Pi}^{\alpha}(u)\right]$$
$$=-ief^{\mu\alpha}+2uin^{\mu}n^{\alpha}e^{2}f^{2}+\Omega in^{\mu}n^{\alpha}e^{2}f^{2}\left[\frac{u^{2}}{s}\xi(s)+\left(2u-\frac{u^{2}}{s}\right)\xi(0)\right], \tag{2.121}$$

$$\left[\xi(0),\hat{\Pi}^{\alpha}(u)\right]=-in^{\alpha}, \tag{2.122}$$

$$\left[\hat{\Pi}^{\alpha}(u),\hat{x}^{\mu}(s)\right]=i\eta^{\alpha\mu}+(-2s+2u)ief^{\alpha\mu}+(2s^{2}-4su+2u^{2})in^{\alpha}n^{\mu}e^{2}f^{2}$$
$$+\Omega ief^{\alpha\mu}\xi(s)\left(\frac{u^{2}}{s}-s\right)+\Omega ief^{\alpha\mu}\xi(0)\left(-\frac{u^{2}}{s}+2u-s\right)$$
$$+\Omega in^{\alpha}n^{\mu}e^{2}f^{2}\xi(s)\left(s^{2}+2su-7u^{2}+4\frac{u^{3}}{s}\right)$$
$$+\Omega in^{\alpha}n^{\mu}e^{2}f^{2}\xi(0)\left(3s^{2}-10su+11u^{2}-4\frac{u^{3}}{s}\right)$$
$$+\Omega ien^{\mu}f^{\alpha}{}_{\beta}\left(\hat{x}^{\beta}(s)-\hat{x}^{\beta}(0)\right)\left(\frac{u^{2}}{s}-2u+s\right), \tag{2.123}$$

$$\left[\hat{\Pi}^{\alpha}(u),ef^{\mu}{}_{\nu}\hat{x}^{\nu}(s)\right]=-ief^{\alpha\mu}+(2s-2u)in^{\alpha}n^{\mu}e^{2}f^{2}$$
$$+\Omega in^{\alpha}n^{\mu}e^{2}f^{2}\xi(s)\left(-\frac{u^{2}}{s}+s\right)+\Omega in^{\alpha}n^{\mu}e^{2}f^{2}\xi(0)\left(\frac{u^{2}}{s}-2u+s\right), \tag{2.124}$$

$$\left[\hat{\Pi}^{\alpha}(u),\xi(s)\right]=in^{\alpha}. \tag{2.125}$$

The employment of these relations produces the following results:

$$\hat{x}^{\mu}(0)\hat{\Pi}^{\alpha}(u)\exp\left[-ik_{\beta}\hat{x}^{\beta}(u)\right]$$
$$=\left[\Omega ief^{\mu\alpha}\xi(s)\frac{u^{2}}{s}+\Omega in^{\mu}n^{\alpha}e^{2}f^{2}\xi(s)\left(u^{2}-4\frac{u^{3}}{s}\right)+\Omega ien^{\mu}f^{\alpha}{}_{\beta}\hat{x}^{\beta}(s)\left(-\frac{u^{2}}{s}\right)\right]$$
$$\times\exp\left[-ik_{\delta}\hat{x}^{\delta}(u)\right]$$
$$+\left[\Omega e(f^{\mu\nu}k_{\nu})\left(\frac{2}{3}\frac{u^{3}}{s}\right)\xi(s)+\Omega en^{\mu}k_{\rho}f^{\rho}{}_{\sigma}\hat{x}^{\sigma}(s)\left(-\frac{2}{3}\frac{u^{3}}{s}\right)\right.$$
$$\left.+\Omega n^{\mu}(k\cdot n)e^{2}f^{2}\left(\frac{2}{3}u^{3}-2\frac{u^{4}}{s}\right)\xi(s)\right]\hat{\Pi}^{\alpha}(u)\exp\left[-ik_{\delta}\hat{x}^{\delta}(u)\right]$$
$$+\hat{\Pi}^{\alpha}(u)\exp\left[-ik_{\beta}\hat{x}^{\beta}(u)\right]\left[\hat{x}^{\mu}(0)+\Omega ef^{\mu\nu}k_{\nu}\left(2u^{2}-\frac{2}{3}\frac{u^{3}}{s}\right)\xi(0)\right.$$
$$\left.+\Omega en^{\mu}k_{\alpha}f^{\alpha}{}_{\beta}\hat{x}^{\beta}(0)\left(\frac{2}{3}\frac{u^{3}}{s}\right)+\Omega n^{\mu}(k\cdot n)e^{2}f^{2}\left(-\frac{10}{3}u^{3}+2\frac{u^{4}}{s}\right)\xi(0)\right]$$
$$+\exp\left[-ik_{\delta}\hat{x}^{\delta}(u)\right]\left[\Omega ief^{\mu\alpha}\left(2u-\frac{u^{2}}{s}\right)\xi(0)\right.$$
$$\left.+\Omega in^{\mu}n^{\alpha}e^{2}f^{2}\left(-5u^{2}+4\frac{u^{3}}{s}\right)\xi(0)+\Omega\frac{u^{2}}{s}ien^{\mu}f^{\alpha}{}_{\beta}\hat{x}^{\beta}(0)\right]$$

(The expression continues to the next page.)

(The expression is continued.)

$$
\begin{aligned}
&+\hat{\Pi}^{\alpha}(u)\exp\left[-ik_{\delta}\hat{x}^{\delta}(u)\right]\left[-2uk^{\mu}+2ef^{\mu\nu}k_{\nu}u^{2}-\frac{4}{3}u^{3}n^{\mu}(k\cdot n)e^{2}f^{2}\right.\\
&\quad\left.+\Omega ef^{\mu\nu}k_{\nu}(k\cdot n)\left(\frac{4}{3}\frac{u^{4}}{s}-\frac{8}{3}u^{3}\right)+\Omega n^{\mu}(k\cdot n)^{2}e^{2}f^{2}\left(-\frac{8}{3}\frac{u^{5}}{s}+\frac{14}{3}u^{4}\right)\right]\\
&+\left[-i\eta^{\mu\alpha}+2uief^{\mu\alpha}-2u^{2}in^{\mu}n^{\alpha}e^{2}f^{2}+i\Omega en^{\alpha}f^{\mu\nu}k_{\nu}\left(\frac{2}{3}\frac{u^{3}}{s}\right)\right.\\
&\quad+i\Omega en^{\mu}f^{\alpha\beta}k_{\beta}\left(-\frac{4}{3}\frac{u^{3}}{s}\right)+i\Omega e(k\cdot n)f^{\mu\alpha}\left(-4u^{2}+2\frac{u^{3}}{s}\right)\\
&\quad\left.+i\Omega n^{\mu}n^{\alpha}(k\cdot n)e^{2}f^{2}\left(\frac{28}{3}u^{3}-\frac{20}{3}\frac{u^{4}}{s}\right)\right]\exp\left[-ik_{\delta}\hat{x}^{\delta}(u)\right], \qquad (2.126)
\end{aligned}
$$

$$
\begin{aligned}
&\hat{\Pi}^{\alpha}(u)\exp\left[-ik_{\delta}\hat{x}^{\delta}(u)\right]\hat{x}^{\mu}(s)\\
&=\left[\hat{x}^{\mu}(s)+\Omega ef^{\mu\nu}k_{\nu}\left(-\frac{4}{3}s^{2}+2su-\frac{2}{3}\frac{u^{3}}{s}\right)\xi(s)\right.\\
&\quad+\Omega en^{\mu}\left(-\frac{2}{3}s^{2}+2su-2u^{2}+\frac{2}{3}\frac{u^{3}}{s}\right)k_{\rho}f^{\rho}{}_{\sigma}\hat{x}^{\sigma}(s)\\
&\quad\left.+\Omega n^{\mu}(k\cdot n)e^{2}f^{2}\left(-\frac{4}{3}s^{3}+2s^{2}u+2su^{2}-\frac{14}{3}u^{3}+2\frac{u^{4}}{s}\right)\xi(s)\right]\\
&\quad\times\hat{\Pi}^{\alpha}(u)\exp\left[-ik_{\delta}\hat{x}^{\delta}(u)\right]\\
&+\left[\Omega ief^{\alpha\mu}\xi(s)\left(\frac{u^{2}}{s}-s\right)+\Omega in^{\alpha}n^{\mu}e^{2}f^{2}\xi(s)\left(s^{2}+2su-7u^{2}+4\frac{u^{3}}{s}\right)\right.\\
&\quad\left.+\Omega ien^{\mu}f^{\alpha}{}_{\beta}\hat{x}^{\beta}(s)\left(\frac{u^{2}}{s}-2u+s\right)\right]\exp\left[-ik_{\delta}\hat{x}^{\delta}(u)\right]\\
&+\hat{\Pi}^{\alpha}(u)\exp\left[-ik_{\delta}\hat{x}^{\delta}(u)\right]\left[\Omega ef^{\mu\nu}k_{\nu}\left(-\frac{2}{3}s^{2}+2su-2u^{2}+\frac{2}{3}\frac{u^{3}}{s}\right)\xi(0)\right.\\
&\quad+\Omega en^{\mu}k_{\rho}f^{\rho}{}_{\sigma}\hat{x}^{\sigma}(0)\left(\frac{2}{3}s^{2}-2su+2u^{2}-\frac{2}{3}\frac{u^{3}}{s}\right)\\
&\quad\left.+\Omega n^{\mu}(k\cdot n)e^{2}f^{2}\left(-\frac{4}{3}s^{3}+6s^{2}u-10su^{2}+\frac{22}{3}u^{3}-2\frac{u^{4}}{s}\right)\xi(0)\right]\\
&\quad+\exp\left[-ik_{\delta}\hat{x}^{\delta}(u)\right]\left[\Omega ief^{\alpha\mu}\xi(0)\left(-\frac{u^{2}}{s}+2u-s\right)\right.\\
&\qquad+\Omega in^{\alpha}n^{\mu}e^{2}f^{2}\xi(0)\left(3s^{2}-10su+11u^{2}-4\frac{u^{3}}{s}\right)\\
&\qquad\left.+\Omega ien^{\mu}f^{\alpha}{}_{\beta}\hat{x}^{\beta}(0)\left(-\frac{u^{2}}{s}+2u-s\right)\right]
\end{aligned}
$$

(The expression continues to the next page.)

(The expression is continued.)

$$
\begin{aligned}
&+\hat{\Pi}^{\alpha}(u)\exp\left[-ik_{\delta}\hat{x}^{\delta}(u)\right]\\
&\times\Bigg[2(u-s)k^{\mu}+2ef^{\mu\nu}k_{\nu}(-s^{2}+2su-u^{2})\\
&\quad+n^{\mu}(k\cdot n)e^{2}f^{2}\left(-\frac{4}{3}s^{3}+4s^{2}u-4su^{2}+\frac{4}{3}u^{3}\right)\\
&\quad+\Omega e(k\cdot n)f^{\mu\nu}k_{\nu}\left(\frac{4}{3}s^{3}-\frac{8}{3}s^{2}u+\frac{8}{3}u^{3}-\frac{4}{3}\frac{u^{4}}{s}\right)\\
&\quad+\Omega n^{\mu}(k\cdot n)^{2}e^{2}f^{2}\left(2s^{4}-\frac{16}{3}s^{3}u+\frac{4}{3}s^{2}u^{2}+8su^{3}-\frac{26}{3}u^{4}+\frac{8}{3}\frac{u^{5}}{s}\right)\Bigg]\\
&+\exp\left[-ik_{\delta}\hat{x}^{\delta}(u)\right]\\
&\times\Bigg[i\eta^{\alpha\mu}+(2u-2s)ief^{\alpha\mu}+(2s^{2}-4su+2u^{2})in^{\alpha}n^{\mu}e^{2}f^{2}\\
&\quad+\Omega ien^{\alpha}f^{\mu\nu}k_{\nu}\left(-\frac{4}{3}s^{2}+2su-\frac{2}{3}\frac{u^{3}}{s}\right)\\
&\quad+\Omega ien^{\mu}f^{\alpha\beta}k_{\beta}\left(\frac{2}{3}s^{2}-2u^{2}+\frac{4}{3}\frac{u^{3}}{s}\right)+\Omega ie(k\cdot n)f^{\alpha\mu}\left(2\frac{u^{3}}{s}-4u^{2}+2su\right)\\
&\quad+\Omega in^{\mu}n^{\alpha}(k\cdot n)e^{2}f^{2}\left(-\frac{8}{3}s^{3}+\frac{4}{3}s^{2}u+12su^{2}-\frac{52}{3}u^{3}+\frac{20}{3}\frac{u^{4}}{s}\right)\Bigg], \qquad (2.127)
\end{aligned}
$$

$$
\begin{aligned}
&f^{\mu}{}_{\nu}\hat{x}^{\nu}(0)\hat{\Pi}^{\alpha}(u)\exp\left[-ik_{\delta}\hat{x}^{\delta}(u)\right]\\
&=i\Omega n^{\mu}n^{\alpha}ef^{2}\xi(s)\exp\left[-ik_{\delta}\hat{x}^{\delta}(u)\right]\frac{u^{2}}{s}\\
&\quad+\Omega n^{\mu}(k\cdot n)ef^{2}\xi(s)\hat{\Pi}^{\alpha}(u)\exp\left[-ik_{\delta}\hat{x}^{\delta}(u)\right]\frac{2}{3}\frac{u^{3}}{s}\\
&\quad+\hat{\Pi}^{\alpha}(u)\exp\left[-ik_{\delta}\hat{x}^{\delta}(u)\right]\left[f^{\mu}{}_{\nu}\hat{x}^{\nu}(0)+\xi(0)\Omega n^{\mu}(k\cdot n)ef^{2}\left(2u^{2}-\frac{2}{3}\frac{u^{3}}{s}\right)\right]\\
&\quad+\exp\left[-ik_{\delta}\hat{x}^{\delta}(u)\right]\xi(0)i\Omega n^{\mu}n^{\alpha}ef^{2}\left(2u-\frac{u^{2}}{s}\right)\\
&\quad+\exp\left[-ik_{\delta}\hat{x}^{\delta}(u)\right]\left[-if^{\mu\alpha}+2uin^{\mu}n^{\alpha}ef^{2}+i\Omega n^{\mu}n^{\alpha}(k\cdot n)ef^{2}\left(-4u^{2}+\frac{8}{3}\frac{u^{3}}{s}\right)\right]\\
&\quad+\hat{\Pi}^{\alpha}(u)\exp\left[-ik_{\delta}\hat{x}^{\delta}(u)\right]\\
&\quad\times\left[-2uf^{\mu}{}_{\nu}k^{\nu}+2u^{2}n^{\mu}(k\cdot n)ef^{2}+\Omega n^{\mu}(k\cdot n)^{2}ef^{2}\left(\frac{4}{3}\frac{u^{4}}{s}-\frac{8}{3}u^{3}\right)\right], \qquad (2.128)
\end{aligned}
$$

$$
\begin{aligned}
&\hat{\Pi}^{\alpha}(u)\exp\left[-ik_{\delta}\hat{x}^{\delta}(u)\right]f^{\mu}{}_{\nu}\hat{x}^{\nu}(s)\\
&=\left[f^{\mu}{}_{\nu}\hat{x}^{\nu}(s)+\Omega n^{\mu}(k\cdot n)ef^{2}\left(-\frac{4}{3}s^{2}+2su-\frac{2}{3}\frac{u^{3}}{s}\right)\xi(s)\right]\hat{\Pi}^{\alpha}(u)\exp\left[-ik_{\delta}\hat{x}^{\delta}(u)\right]
\end{aligned}
$$

(The expression continues to the next page.)

(The expression is continued.)

$$
\begin{aligned}
&+i\Omega n^\mu n^\alpha e f^2 \left(s-\frac{u^2}{s}\right)\xi(s)\exp\left[-ik_\delta \hat{x}^\delta(u)\right]\\
&+\exp\left[-ik_\delta \hat{x}^\delta(u)\right] i\Omega n^\mu n^\alpha e f^2\left(\frac{u^2}{s}-2u+s\right)\xi(0)\\
&+\hat{\Pi}^\alpha(u)\exp\left[-ik_\delta \hat{x}^\delta(u)\right]\Omega n^\mu (k\cdot n) e f^2\left(-\frac{2}{3}s^2+2su-2u^2+\frac{2}{3}\frac{u^3}{s}\right)\xi(0)\\
&+\hat{\Pi}^\alpha(u)\exp\left[-ik_\delta \hat{x}^\delta(u)\right]\left[2(u-s)f^{\mu\nu}k_\nu+2n^\mu(k\cdot n)ef^2(-s^2+2su-u^2)\right.\\
&\quad\left.+\Omega n^\mu(k\cdot n)^2 e f^2\left(\frac{4}{3}s^3-\frac{8}{3}s^2u+\frac{8}{3}u^3-\frac{4}{3}\frac{u^4}{s}\right)\right]\\
&+\exp\left[-ik_\delta \hat{x}^\delta(u)\right]\\
&\quad\times\left[if^{\mu\alpha}+in^\mu n^\alpha e f^2(2s-2u)+i\Omega n^\mu n^\alpha (k\cdot n) e f^2\left(-\frac{4}{3}s^2+4u^2-\frac{8}{3}\frac{u^3}{s}\right)\right],
\end{aligned}
\tag{2.129}
$$

$$
\begin{aligned}
&\xi(0)\hat{\Pi}^\alpha(u)\exp\left[-ik_\delta \hat{x}^\delta(u)\right]\\
&=\hat{\Pi}^\alpha(u)\exp\left[-ik_\delta \hat{x}^\delta(u)\right]\xi(0)+\exp\left[-ik_\delta \hat{x}^\delta(u)\right](-in^\alpha)\\
&\quad+\hat{\Pi}^\alpha(u)\exp\left[-ik_\delta \hat{x}^\delta(u)\right](-2u(k\cdot n)),
\end{aligned}
\tag{2.130}
$$

$$
\begin{aligned}
&\hat{\Pi}^\alpha(u)\exp\left[-ik_\delta \hat{x}^\delta(u)\right]\xi(s)\\
&=\xi(s)\hat{\Pi}^\alpha(u)\exp\left[-ik_\delta \hat{x}^\delta(u)\right]+\hat{\Pi}^\alpha(u)\exp\left[-ik_\delta \hat{x}^\delta(u)\right]2(u-s)(k\cdot n)\\
&\quad+\exp\left[-ik_\delta \hat{x}^\delta(u)\right]in^\alpha.
\end{aligned}
\tag{2.131}
$$

The amplitudes of these operators are also obtained as follows:

$$
\begin{aligned}
&\langle x(s)|\hat{x}^\mu(0)\hat{\Pi}^\alpha(u)\exp\left[-ik_\delta \hat{x}^\delta(u)\right]|x(0)\rangle\\
&=\langle x(s)|\exp\left[-ik_\delta \hat{x}^\delta(u)\right]|x(0)\rangle\\
&\times\left[-i\eta^{\mu\alpha}+2uief^{\mu\alpha}-2u^2in^\mu n^\alpha e^2f^2+i\Omega e n^\alpha f^{\mu\nu}k_\nu\frac{2}{3}\frac{u^3}{s}+i\Omega e n^\mu f^{\alpha\beta}k_\beta\left(-\frac{4}{3}\frac{u^3}{s}\right)\right.\\
&\quad+i\Omega e(k\cdot n)f^{\mu\alpha}\left(-4u^2+2\frac{u^3}{s}\right)+i\Omega n^\mu n^\alpha(k\cdot n)e^2f^2\left(\frac{28}{3}u^3-\frac{20}{3}\frac{u^4}{s}\right)\\
&\quad\left.+i\Omega n^\mu n^\alpha e^2f^2\xi(-4u^2)+i\Omega e f^{\mu\alpha}\xi 2u\right]\\
&+\langle x(s)|\hat{\Pi}^\alpha(u)\exp\left[-ik_\delta \hat{x}^\delta(u)\right]|x(0)\rangle\\
&\times\left[x^\mu-2uk^\mu+2ef^{\mu\nu}k_\nu u^2-\frac{4}{3}u^3n^\mu(k\cdot n)e^2f^2+\Omega e f^{\mu\nu}k_\nu(k\cdot n)\left(\frac{4}{3}\frac{u^4}{s}-\frac{8}{3}u^3\right)\right.\\
&\quad+\Omega n^\mu(k\cdot n)^2e^2f^2\left(-\frac{8}{3}\frac{u^5}{s}+\frac{14}{3}u^4\right)+\Omega e f^{\mu\nu}k_\nu(2u^2)\xi\\
&\quad\left.+\Omega n^\mu(k\cdot n)e^2f^2\left(-\frac{8}{3}u^3\right)\xi\right],
\end{aligned}
\tag{2.132}
$$

$$
\begin{aligned}
&\langle x(s)|\hat{\Pi}^{\alpha}(u)\exp\left[-ik_{\delta}\hat{x}^{\delta}(u)\right]\hat{x}^{\mu}(s)|x(0)\rangle \\
&=\langle x(s)|\exp\left[-ik_{\delta}\hat{x}^{\delta}(u)\right]|x(0)\rangle \\
&\quad\times\Bigg[i\Omega ef^{\alpha\mu}\xi(2u-2s)+i\Omega n^{\alpha}n^{\mu}e^{2}f^{2}\xi(4s^{2}-8su+4u^{2})+i\eta^{\alpha\mu}+(2u-2s)ief^{\alpha\mu} \\
&\quad+(2s^{2}-4su+2u^{2})in^{\alpha}n^{\mu}e^{2}f^{2}+i\Omega en^{\alpha}f^{\mu\nu}k_{\nu}\left(-\frac{4}{3}s^{2}+2su-\frac{2}{3}\frac{u^{3}}{s}\right) \\
&\quad+i\Omega en^{\mu}f^{\alpha\beta}k_{\beta}\left(\frac{2}{3}s^{2}-2u^{2}+\frac{4}{3}\frac{u^{3}}{s}\right)+i\Omega e(k\cdot n)f^{\alpha\mu}\left(2\frac{u^{3}}{s}-4u^{2}+2su\right) \\
&\quad+i\Omega n^{\mu}n^{\alpha}(k\cdot n)e^{2}f^{2}\left(-\frac{8}{3}s^{3}+\frac{4}{3}s^{2}u+12su^{2}-\frac{52}{3}u^{3}+\frac{20}{3}\frac{u^{4}}{s}\right)\Bigg] \\
&+\langle x(s)|\hat{\Pi}^{\alpha}(u)\exp\left[-ik_{\delta}\hat{x}^{\delta}(u)\right]|x(0)\rangle \\
&\quad\times\Bigg[x^{\mu}+\Omega ef^{\mu\nu}k_{\nu}\xi(-2s^{2}+4su-2u^{2}) \\
&\quad+\Omega n^{\mu}(k\cdot n)e^{2}f^{2}\xi\left(-\frac{8}{3}s^{3}+8s^{2}u-8su^{2}+\frac{8}{3}u^{3}\right) \\
&\quad+2(u-s)k^{\mu}+2ef^{\mu\nu}k_{\nu}(-s^{2}+2su-u^{2}) \\
&\quad+n^{\mu}(k\cdot n)e^{2}f^{2}\left(-\frac{4}{3}s^{3}+4s^{2}u-4su^{2}+\frac{4}{3}u^{3}\right) \\
&\quad+\Omega e(k\cdot n)f^{\mu\nu}k_{\nu}\left(\frac{4}{3}s^{3}-\frac{8}{3}s^{2}u+\frac{8}{3}u^{3}-\frac{4}{3}\frac{u^{4}}{s}\right) \\
&\quad+\Omega n^{\mu}(k\cdot n)^{2}e^{2}f^{2}\left(2s^{4}-\frac{16}{3}s^{3}u+\frac{4}{3}s^{2}u^{2}+8su^{3}-\frac{26}{3}u^{4}+\frac{8}{3}\frac{u^{5}}{s}\right)\Bigg], \qquad (2.133)
\end{aligned}
$$

$$
\begin{aligned}
&\langle x(s)|f^{\mu}{}_{\nu}\hat{x}^{\nu}(0)\hat{\Pi}^{\alpha}(u)\exp\left[-ik_{\delta}\hat{x}^{\delta}(u)\right]|x(0)\rangle \\
&=\langle x(s)|\hat{\Pi}^{\alpha}(u)\exp\left[-ik_{\delta}\hat{x}^{\delta}(u)\right]|x(0)\rangle\Bigg[f^{\mu}{}_{\nu}x^{\nu}+\Omega n^{\mu}(k\cdot n)ef^{2}2u^{2}\xi \\
&\qquad-2uf^{\mu}{}_{\nu}k^{\nu}+2u^{2}n^{\mu}(k\cdot n)ef^{2}+\Omega n^{\mu}(k\cdot n)^{2}ef^{2}\left(\frac{4}{3}\frac{u^{4}}{s}-\frac{8}{3}u^{3}\right)\Bigg] \\
&+\langle x(s)|\exp\left[-ik_{\delta}\hat{x}^{\delta}(u)\right]|x(0)\rangle\Bigg[i\Omega n^{\mu}n^{\alpha}ef^{2}\xi 2u-if^{\mu\alpha} \\
&\qquad+2uin^{\mu}n^{\alpha}ef^{2}+i\Omega n^{\mu}n^{\alpha}(k\cdot n)ef^{2}\left(-4u^{2}+\frac{8}{3}\frac{u^{3}}{s}\right)\Bigg], \qquad (2.134)
\end{aligned}
$$

$$
\begin{aligned}
&\langle x(s)|\hat{\Pi}^{\alpha}(u)\exp\left[-ik_{\delta}\hat{x}^{\delta}(u)\right]f^{\mu}{}_{\nu}\hat{x}^{\nu}(s)|x(0)\rangle \\
&=\langle x(s)|\exp\left[-ik_{\delta}\hat{x}^{\delta}(u)\right]|x(0)\rangle\Bigg[i\Omega n^{\mu}n^{\alpha}ef^{2}(2s-2u)\xi+if^{\mu\alpha} \\
&\quad+in^{\mu}n^{\alpha}ef^{2}(2s-2u)+i\Omega n^{\mu}n^{\alpha}(k\cdot n)ef^{2}\left(-\frac{4}{3}s^{2}+4u^{2}-\frac{8}{3}\frac{u^{3}}{s}\right)\Bigg] \\
&+\langle x(s)|\hat{\Pi}^{\alpha}(u)\exp\left[-ik_{\delta}\hat{x}^{\delta}(u)\right]|x(0)\rangle\Bigg[f^{\mu}{}_{\nu}x^{\nu}+\Omega n^{\mu}(k\cdot n)ef^{2}(-2s^{2}+4su-2u^{2})\xi \\
&\qquad+2(u-s)f^{\mu\nu}k_{\nu}+2n^{\mu}(k\cdot n)ef^{2}(-s^{2}+2su-u^{2}) \\
&\qquad+\Omega n^{\mu}(k\cdot n)^{2}ef^{2}\left(\frac{4}{3}s^{3}-\frac{8}{3}s^{2}u+\frac{8}{3}u^{3}-\frac{4}{3}\frac{u^{4}}{s}\right)\Bigg], \qquad (2.135)
\end{aligned}
$$

$$\begin{aligned}
&\langle x(s)|\xi(0)\hat{\Pi}^{\alpha}(u)\exp\left[-ik_{\delta}\hat{x}^{\delta}(u)\right]|x(0)\rangle \\
&=\langle x(s)|\hat{\Pi}^{\alpha}(u)\exp\left[-ik_{\delta}\hat{x}^{\delta}(u)\right]|x(0)\rangle\left[\xi-2u(k\cdot n)\right] \\
&\quad+\langle x(s)|\exp\left[-ik_{\delta}\hat{x}^{\delta}(u)\right]|x(0)\rangle(-in^{\alpha}), \qquad (2.136)\\
&\langle x(s)|\hat{\Pi}^{\alpha}(u)\exp\left[-ik_{\delta}\hat{x}^{\delta}(u)\right]\xi(s)|x(0)\rangle \\
&=\langle x(s)|\hat{\Pi}^{\alpha}(u)\exp\left[-ik_{\delta}\hat{x}^{\delta}(u)\right]|x(0)\rangle\left[\xi+2(u-s)(k\cdot n)\right] \\
&\quad+\langle x(s)|\exp\left[-ik_{\delta}\hat{x}^{\delta}(u)\right]|x(0)\rangle in^{\alpha}. \qquad (2.137)
\end{aligned}$$

I am now ready to write down the amplitudes of the addition $\langle x(s)|\hat{\Pi}^{\mu}(s)\hat{\Pi}^{\alpha}(u)\times\exp\left[-ik_{\delta}\hat{x}^{\delta}(u)\right]+\hat{\Pi}^{\alpha}(u)\exp\left[-ik_{\delta}\hat{x}^{\delta}(u)\right]\hat{\Pi}^{\mu}(0)|x(0)\rangle$ and the subtraction $\langle x(s)|\hat{\Pi}^{\mu}(s)\times\hat{\Pi}^{\alpha}(u)\exp\left[-ik_{\delta}\hat{x}^{\delta}(u)\right]-\hat{\Pi}^{\alpha}(u)\exp\left[-ik_{\delta}\hat{x}^{\delta}(u)\right]\hat{\Pi}^{\mu}(0)|x(0)\rangle$, which appear in the induced electromagnetic current. The results are as follows:

$$\begin{aligned}
&\langle x(s)|\hat{\Pi}^{\mu}(s)\hat{\Pi}^{\alpha}(u)\exp\left[-ik_{\delta}\hat{x}^{\delta}(u)\right]+\hat{\Pi}^{\alpha}(u)\exp\left[-ik_{\delta}\hat{x}^{\delta}(u)\right]\hat{\Pi}^{\mu}(0)|x(0)\rangle \\
=\;&\langle x(s)|\exp\left[-ik_{\delta}\hat{x}^{\delta}(u)\right]|x(0)\rangle \\
&\times\left[ief^{\mu\alpha}\left(1-2\frac{u}{s}\right)+k^{\mu}k^{\alpha}\left(-\frac{u}{s}+2\frac{u^{2}}{s^{2}}\right)+ek^{\mu}f^{\alpha\beta}k_{\beta}\left(u-3\frac{u^{2}}{s}+2\frac{u^{3}}{s^{2}}\right)\right. \\
&+ef^{\mu\nu}k_{\nu}k^{\alpha}\left(2\frac{u^{2}}{s}-2\frac{u^{3}}{s^{2}}\right)+e^{2}f^{\mu\nu}k_{\nu}f^{\alpha\beta}k_{\beta}\left(-2u^{2}+4\frac{u^{3}}{s}-2\frac{u^{4}}{s^{2}}\right) \\
&+k^{\mu}n^{\alpha}(k\cdot n)e^{2}f^{2}\left(-\frac{1}{3}su+\frac{5}{3}u^{2}-\frac{8}{3}\frac{u^{3}}{s}+\frac{4}{3}\frac{u^{4}}{s^{2}}\right) \\
&+f^{\mu\nu}k_{\nu}n^{\alpha}(k\cdot n)e^{3}f^{2}\left(\frac{2}{3}su^{2}-\frac{8}{3}u^{3}+\frac{10}{3}\frac{u^{4}}{s}-\frac{4}{3}\frac{u^{5}}{s^{2}}\right) \\
&+n^{\mu}k^{\alpha}(k\cdot n)e^{2}f^{2}\left(\frac{2}{3}u^{2}-2\frac{u^{3}}{s}+\frac{4}{3}\frac{u^{4}}{s^{2}}\right) \\
&+n^{\mu}f^{\alpha\beta}k_{\beta}(k\cdot n)e^{3}f^{2}\left(-\frac{2}{3}su^{2}+\frac{8}{3}u^{3}-\frac{10}{3}\frac{u^{4}}{s}+\frac{4}{3}\frac{u^{5}}{s^{2}}\right) \\
&+in^{\mu}n^{\alpha}e^{2}f^{2}\left(\frac{1}{3}s-2u+2\frac{u^{2}}{s}\right) \\
&\left.+n^{\mu}n^{\alpha}(k\cdot n)^{2}e^{4}f^{4}\left(\frac{2}{9}s^{2}u^{2}-\frac{4}{3}su^{3}+\frac{26}{9}u^{4}-\frac{8}{3}\frac{u^{5}}{s}+\frac{8}{9}\frac{u^{6}}{s^{2}}\right)+i\eta^{\mu\alpha}\frac{1}{s}\right] \\
+\;&i\Omega\langle x(s)|\exp\left[-ik_{\delta}\hat{x}^{\delta}(u)\right]|x(0)\rangle \\
&\times\left[ef^{\mu\alpha}(k\cdot n)\left(\frac{1}{3}s-\frac{5}{3}u+4\frac{u^{2}}{s}-2\frac{u^{3}}{s^{2}}\right)+ef^{\mu\alpha}\xi\left(1-2\frac{u}{s}\right)\right. \\
&+ie(k\cdot n)k^{\mu}f^{\alpha\beta}k_{\beta}\left(\frac{4}{3}u^{2}-\frac{16}{3}\frac{u^{3}}{s}+\frac{20}{3}\frac{u^{4}}{s^{2}}-\frac{8}{3}\frac{u^{5}}{s^{3}}\right) \\
&\left.+ie\xi k^{\mu}f^{\alpha\beta}k_{\beta}\left(-u+3\frac{u^{2}}{s}-2\frac{u^{3}}{s^{2}}\right)\right.
\end{aligned}$$

(The expression continues to the next page.)

(The expression is continued.)

$$
\begin{aligned}
&+ie(k\cdot n)f^{\mu\nu}k_\nu k^\alpha\left(\frac{4}{3}\frac{u^3}{s}-\frac{8}{3}\frac{u^4}{s^2}+\frac{4}{3}\frac{u^5}{s^2}\right)+ie\xi f^{\mu\nu}k_\nu k^\alpha\left(-2\frac{u^2}{s}+2\frac{u^3}{s^2}\right)\\
&+ie^2(k\cdot n)f^{\mu\nu}k_\nu f^{\alpha\beta}k_\beta\left(-4u^3+12\frac{u^4}{s}-12\frac{u^5}{s^2}+4\frac{u^6}{s^3}\right)\\
&+ie^2\xi f^{\mu\nu}k_\nu f^{\alpha\beta}k_\beta\left(4u^2-8\frac{u^3}{s}+4\frac{u^4}{s^2}\right)\\
&+ik^\mu n^\alpha(k\cdot n)^2e^2f^2\left(-su^2+6u^3-13\frac{u^4}{s}+12\frac{u^5}{s^2}-4\frac{u^6}{s^3}\right)\\
&+ik^\mu n^\alpha\xi(k\cdot n)e^2f^2\left(\frac{2}{3}su-\frac{10}{3}u^2+\frac{16}{3}\frac{u^3}{s}-\frac{8}{3}\frac{u^4}{s^2}\right)\\
&+iek^\mu n^\alpha(\sigma f)\left(-\frac{1}{4}s+u-\frac{u^2}{s}\right)+ef^{\mu\nu}k_\nu n^\alpha\left(-\frac{1}{3}s+\frac{1}{3}u-\frac{2}{3}\frac{u^3}{s^2}\right)\\
&+if^{\mu\nu}k_\nu n^\alpha(k\cdot n)^2e^3f^2\left(\frac{22}{9}su^3-\frac{110}{9}u^4+22\frac{u^5}{s}-\frac{154}{9}\frac{u^6}{s^2}+\frac{44}{9}\frac{u^7}{s^3}\right)\\
&+if^{\mu\nu}k_\nu n^\alpha\xi(k\cdot n)e^3f^2\left(-2su^2+8u^3-10\frac{u^4}{s}+4\frac{u^5}{s^2}\right)\\
&+ie^2f^{\mu\nu}k_\nu n^\alpha(\sigma f)\left(\frac{1}{2}su-\frac{3}{2}u^2+\frac{u^3}{s}\right)\\
&+in^\mu k^\alpha(k\cdot n)^2e^2f^2\left(\frac{4}{3}u^3-\frac{16}{3}\frac{u^4}{s}+\frac{20}{3}\frac{u^5}{s^2}-\frac{8}{3}\frac{u^6}{s^3}\right)\\
&+in^\mu k^\alpha\xi(k\cdot n)e^2f^2\left(-\frac{4}{3}u^2+4\frac{u^3}{s}-\frac{8}{3}\frac{u^4}{s^2}\right)\\
&+en^\mu f^{\alpha\beta}k_\beta\left(\frac{1}{3}s-\frac{u^2}{s}+\frac{4}{3}\frac{u^3}{s^2}\right)\\
&+in^\mu f^{\alpha\beta}k_\beta(k\cdot n)^2e^3f^2\left(-\frac{20}{9}su^3+\frac{100}{9}u^4-20\frac{u^5}{s}+\frac{140}{9}\frac{u^6}{s^2}-\frac{40}{9}\frac{u^7}{s^3}\right)\\
&+in^\mu f^{\alpha\beta}k_\beta\xi(k\cdot n)e^3f^2\left(2su^2-8u^3+10\frac{u^4}{s}-4\frac{u^5}{s^2}\right)\\
&+n^\mu n^\alpha(k\cdot n)e^2f^2\left(-\frac{4}{3}su+8u^2-\frac{40}{3}\frac{u^3}{s}+\frac{20}{3}\frac{u^4}{s^2}\right)\\
&+in^\mu n^\alpha(k\cdot n)^3e^4f^4\left(\frac{10}{9}s^2u^3-\frac{70}{9}su^4+\frac{190}{9}u^5-\frac{250}{9}\frac{u^6}{s}+\frac{160}{9}\frac{u^7}{s^2}-\frac{40}{9}\frac{u^8}{s^3}\right)\\
&+n^\mu n^\alpha\xi e^2f^2\left(\frac{2}{3}s-4u+4\frac{u^2}{s}\right)\\
&+in^\mu n^\alpha\xi(k\cdot n)^2e^4f^4\left(-\frac{8}{9}s^2u^2+\frac{16}{3}su^3-\frac{104}{9}u^4+\frac{32}{3}\frac{u^5}{s}-\frac{32}{9}\frac{u^6}{s^2}\right)\\
&+in^\mu n^\alpha(k\cdot n)(\sigma f)e^3f^2\left(\frac{1}{6}s^2u-\frac{5}{6}su^2+\frac{4}{3}u^3-\frac{2}{3}\frac{u^4}{s}\right)\Bigg],
\end{aligned}
\tag{2.138}
$$

$$
\begin{aligned}
& \langle x(s)|\hat{\Pi}^{\mu}(s)\hat{\Pi}^{\alpha}(u)\exp\left[-ik_{\delta}\hat{x}^{\delta}(u)\right]-\hat{\Pi}^{\alpha}(u)\exp\left[-ik_{\delta}\hat{x}^{\delta}(u)\right]\hat{\Pi}^{\mu}(0)|x(0)\rangle \\
= \;& \langle x(s)|\exp\left[-ik_{\delta}\hat{x}^{\delta}(u)\right]|x(0)\rangle \\
& \times\left[k^{\mu}k^{\alpha}\frac{u}{s}+ek^{\mu}f^{\alpha\beta}k_{\beta}\left(-u+\frac{u^{2}}{s}\right)+k^{\mu}n^{\alpha}(k\cdot n)e^{2}f^{2}\left(\frac{1}{3}su-u^{2}+\frac{2}{3}\frac{u^{3}}{s}\right)\right] \\
+ \;& i\Omega\langle x(s)|\exp\left[-ik_{\delta}\hat{x}^{\delta}(u)\right]|x(0)\rangle \\
& \times\left[ef^{\mu\alpha}(k\cdot n)\left(-\frac{1}{3}s+u\right)+iek^{\mu}f^{\alpha\beta}k_{\beta}(k\cdot n)\left(-\frac{4}{3}u^{2}+\frac{8}{3}\frac{u^{3}}{s}-\frac{4}{3}\frac{u^{4}}{s^{2}}\right)\right. \\
& +ie\xi k^{\mu}f^{\alpha\beta}k_{\beta}\left(u-\frac{u^{2}}{s}\right)+ik^{\mu}n^{\alpha}(k\cdot n)^{2}e^{2}f^{2}\left(su^{2}-4u^{3}+5\frac{u^{4}}{s}-2\frac{u^{5}}{s^{2}}\right) \\
& +ik^{\mu}n^{\alpha}\xi(k\cdot n)e^{2}f^{2}\left(-\frac{2}{3}su+2u^{2}-\frac{4}{3}\frac{u^{3}}{s}\right)+ik^{\mu}n^{\alpha}e(\sigma f)\left(\frac{1}{4}s-\frac{1}{2}u\right) \\
& +ef^{\mu\nu}k_{\nu}n^{\alpha}\left(\frac{1}{3}s-u\right)+in^{\mu}k^{\alpha}(k\cdot n)^{2}e^{2}f^{2}\left(-\frac{2}{3}u^{3}+\frac{4}{3}\frac{u^{4}}{s}-\frac{2}{3}\frac{u^{5}}{s^{2}}\right) \\
& +in^{\mu}k^{\alpha}e(\sigma f)\left(-\frac{1}{2}u\right)+en^{\mu}f^{\alpha\beta}k_{\beta}\left(-\frac{1}{3}s+\frac{u^{2}}{s}\right) \\
& +in^{\mu}f^{\alpha\beta}k_{\beta}(k\cdot n)^{2}e^{3}f^{2}\left(\frac{2}{3}su^{3}-2u^{4}+2\frac{u^{5}}{s}-\frac{2}{3}\frac{u^{6}}{s^{2}}\right) \\
& +in^{\mu}f^{\alpha\beta}k_{\beta}e^{2}(\sigma f)\left(\frac{1}{2}su-\frac{1}{2}u^{2}\right)+n^{\mu}n^{\alpha}(k\cdot n)e^{2}f^{2}\left(\frac{2}{3}su-2u^{2}+\frac{4}{3}\frac{u^{3}}{s}\right) \\
& +in^{\mu}n^{\alpha}(k\cdot n)^{3}e^{4}f^{4}\left(-\frac{2}{9}s^{2}u^{3}+\frac{10}{9}su^{4}-2u^{5}+\frac{14}{9}\frac{u^{6}}{s}-\frac{4}{9}\frac{u^{7}}{s^{2}}\right) \\
& \left.+in^{\mu}n^{\alpha}e^{3}f^{2}(\sigma f)(k\cdot n)\left(-\frac{1}{6}s^{2}u+\frac{1}{2}su^{2}-\frac{1}{3}u^{3}\right)\right]. \qquad (2.139)
\end{aligned}
$$

2.7 Permutations of Operators

I give some technical details relevant for permutations of operators in this section. The basic commutation relations are those among $\hat{x}^{\mu}(s)$, $\hat{x}^{\mu}(u)$ and $\hat{x}^{\mu}(0)$. It is written as

$$
\begin{aligned}
& [\hat{x}^{\mu}(0),\hat{x}^{\alpha}(s)] \\
= \;& -2is\eta^{\mu\alpha}+2ies^{2}f^{\mu\alpha}-\frac{4}{3}in^{\mu}n^{\alpha}e^{2}f^{2}s^{3}+i\Omega es^{2}f^{\mu\alpha}\left(\frac{4}{3}\xi(s)+\frac{2}{3}\xi(0)\right) \\
& -\frac{2}{3}i\Omega es^{2}n^{\alpha}f^{\mu}{}_{\nu}[\hat{x}^{\nu}(s)-\hat{x}^{\nu}(0)]+i\Omega n^{\mu}n^{\alpha}e^{2}f^{2}s^{3}\left(-\frac{4}{3}\xi(s)-\frac{4}{3}\xi(0)\right) \qquad (2.140)
\end{aligned}
$$

for $\hat{x}^{\mu}(s)$ and $\hat{x}^{\alpha}(0)$. Its derivation is as follows. The canonical commutation relation is written as

$$
\left[\hat{x}^{\mu}(0),\hat{\Pi}^{\nu}(0)\right]=\left[\hat{x}^{\mu}(s),\hat{\Pi}^{\nu}(s)\right]=-i\eta^{\mu\nu} \qquad (2.141)
$$

and the expression of $\hat{x}^\mu(0)$ in terms of $\hat{\Pi}^\mu(s)$ is obtained from Equation (2.85) as

$$\begin{aligned}
&\hat{x}^\mu(0) \\
&= -2s\hat{\Pi}^\mu(s) + \hat{x}^\mu(s) + 2es^2 f^\mu{}_\nu \hat{\Pi}^\nu(s) + n^\mu e^2 f^2 s^2 \left(-\frac{2}{3}\xi(s) + \frac{2}{3}\xi(0)\right) \\
&+\Omega e s^2 f^\mu{}_\nu \hat{\Pi}^\nu(s) \left(\frac{4}{3}\xi(s) + \frac{2}{3}\xi(0)\right) + \Omega n^\mu e^2 f^2 s^2 \left(-\frac{5}{6}\xi^2(s) + \frac{1}{3}\xi(s)\xi(0) + \frac{1}{2}\xi^2(0)\right) \\
&+\frac{1}{2}\Omega e s^2 n^\mu (\sigma f). \qquad (2.142)
\end{aligned}$$

Let us first consider the commutation relation $[\xi(0), \hat{x}^\alpha(s)]$. From Equation (2.142), I obtain

$$\xi(0) = -2sn_\mu \hat{\Pi}^\mu(s) + \xi(s). \qquad (2.143)$$

I then easily derive the following relation:

$$\begin{aligned}
[\xi(0), \hat{x}^\alpha(s)] &= \left[-2sn_\mu \hat{\Pi}^\mu(s), \hat{x}^\alpha(s)\right] \\
&= -2sn_\mu i\eta^{\mu\alpha} \\
&= -2isn^\alpha. \qquad (2.144)
\end{aligned}$$

Combining Equations (2.141)-(2.144), I obtain Equation (2.140) easily.

The following commutation relations, which are frequently used, also follow immediately:

$$\begin{aligned}
&[\hat{x}^\alpha(0), f^\mu{}_\nu \hat{x}^\nu(s)] \\
&= 2isf^{\alpha\mu} - 2in^\alpha n^\mu e f^2 s^2 + i\Omega n^\alpha n^\mu e f^2 s^2 \left(-\frac{4}{3}\xi(s) - \frac{2}{3}\xi(0)\right), \qquad (2.145)
\end{aligned}$$

$$\begin{aligned}
&[\hat{x}^\alpha(s), f^\mu{}_\nu \hat{x}^\nu(0)] \\
&= -2isf^{\alpha\mu} - 2in^\alpha n^\mu e f^2 s^2 + i\Omega n^\alpha n^\mu e f^2 s^2 \left(-\frac{2}{3}\xi(s) - \frac{4}{3}\xi(0)\right), \qquad (2.146)
\end{aligned}$$

$$\left[f^\alpha{}_\beta \hat{x}^\beta(s), f^\mu{}_\nu \hat{x}^\nu(0)\right] = -2in^\alpha n^\mu f^2 s, \qquad (2.147)$$

$$[\xi(s), \xi(0)] = 0, \qquad (2.148)$$

$$[\hat{x}^\mu(0), \xi(s)] = -2isn^\mu, \qquad (2.149)$$

$$[\xi(0), \hat{x}^\mu(s)] = -2isn^\mu, \qquad (2.150)$$

$$\left[\hat{x}^\mu(s), \hat{\Pi}^\nu(s)\right] = \left[\hat{x}^\mu(0), \hat{\Pi}^\nu(0)\right] = \left[\hat{x}^\mu(u), \hat{\Pi}^\nu(u)\right] = -i\eta^{\mu\nu}. \qquad (2.151)$$

The commutation relations between $\hat{x}^\alpha(u)$ and $\hat{x}^\beta(0)$ or $\hat{x}^\beta(s)$ are derived by Equations (2.87) and (2.140) as

$$\begin{aligned}
&\left[\hat{x}^\alpha(u), \hat{x}^\beta(0)\right] \\
&= 2iu\eta^{\alpha\beta} + 2ieu^2 f^{\alpha\beta} + \frac{4}{3}in^\alpha n^\beta e^2 f^2 u^3 + i\Omega e f^{\alpha\beta} \left[\frac{2}{3}\frac{u^3}{s}\xi(s) + \left(2u^2 - \frac{2}{3}\frac{u^3}{s}\right)\xi(0)\right] \\
&+i\Omega e n^\beta f^\alpha{}_\nu [\hat{x}^\nu(s) - \hat{x}^\nu(0)] \left(\frac{2}{3}\frac{u^3}{s}\right) \\
&+i\Omega n^\alpha n^\beta e^2 f^2 \left[\left(-\frac{2}{3}u^3 + 2\frac{u^4}{s}\right)\xi(s) + \left(\frac{10}{3}u^3 - 2\frac{u^4}{s}\right)\xi(0)\right], \qquad (2.152)
\end{aligned}$$

$$
\begin{aligned}
&\left[\hat{x}^\alpha(s), \hat{x}^\beta(u)\right] \\
= \;& 2i(s-u)\eta^{\alpha\beta} + 2ie(s^2-2su+u^2)f^{\alpha\beta} + in^\alpha n^\beta e^2 f^2 \left(\frac{4}{3}s^3 - 4s^2u + 4su^2 - \frac{4}{3}u^3\right) \\
&+i\Omega e f^{\alpha\beta}\left[\left(\frac{4}{3}s^2 - 2su + \frac{2}{3}\frac{u^3}{s}\right)\xi(s) + \left(\frac{2}{3}s^2 - 2su + 2u^2 - \frac{2}{3}\frac{u^3}{s}\right)\xi(0)\right] \\
&+i\Omega e n^\alpha f^\beta{}_\nu [\hat{x}^\nu(s) - \hat{x}^\nu(0)]\left(\frac{2}{3}s^2 - 2su + 2u^2 - \frac{2}{3}\frac{u^3}{s}\right) \\
&+i\Omega n^\alpha n^\beta e^2 f^2 \left[\left(\frac{4}{3}s^3 - 2s^2u - 2su^2 + \frac{14}{3}u^3 - 2\frac{u^4}{s}\right)\xi(s)\right. \\
&\quad \left. + \left(\frac{4}{3}s^3 - 6s^2u + 10su^2 - \frac{22}{3}u^3 + 2\frac{u^4}{s}\right)\xi(0)\right]. \qquad (2.153)
\end{aligned}
$$

2.8 x-dependence of Transformation Amplitudes

Here I discuss the x-dependence of the results. Note that the calculations of the amplitudes in Equations (2.77) - (2.84) are calculated of x^μ in the neighborhood of each point under the assumption that the wavelength of the external wave field is much longer than the Compton wavelength of the electron. Then x appears explicitly only in the form of $\xi = n_\mu x^\mu$ and it turns out in addition that ξ occurs only as a combination of $f(0)(1+\Omega\xi)$. For example, the amplitude in Equation (2.79) is written as

$$
\begin{aligned}
&\langle x(s)| \exp\left[-ik_\mu \hat{x}^\mu(u)\right] |x(0)\rangle \\
&\simeq \langle x(s)|x(0)\rangle \times \exp\left(-ik_\mu x^\mu\right) \exp\left[i(k)^2\left(u - \frac{u^2}{s}\right)\right] \\
&\times \exp\left[i(k\cdot n)^2 e^2 f^2(0)(1+\Omega\xi)^2\left(-\frac{1}{3}su^2 + \frac{2}{3}u^3 - \frac{1}{3}\frac{u^4}{s}\right)\right] \\
&\times\left\{1 + \Omega\left[i(k\cdot n)^3 e^2 f^2(0)\left(-\frac{2}{3}s^3u + \frac{14}{9}s^2u^2 - \frac{4}{9}su^3 - \frac{10}{9}u^4 + \frac{2}{3}\frac{u^5}{s}\right)\right.\right. \\
&\left.\left. + ie(\sigma f(0))(k\cdot n)\left(\frac{1}{2}su - \frac{1}{2}u^2\right)\right]\right\} \qquad (2.154)
\end{aligned}
$$

and that in Equation (2.80) is given as

$$\begin{aligned}
&\langle x(s)|\hat{\Pi}^{\alpha}(u)\exp\left[-ik_{\mu}\hat{x}^{\mu}(u)\right]|x(0)\rangle \\
&\simeq \langle x(s)|\exp\left[-ik_{\mu}\hat{x}^{\mu}(u)\right]|x(0)\rangle \\
&\quad\times\left[\frac{u}{s}k^{\alpha}+ef^{\alpha\beta}(0)k_{\beta}(1+\Omega\xi)\left(\frac{u^2}{s}-u\right)\right. \\
&\quad+n^{\alpha}(k\cdot n)e^2f^2(0)(1+\Omega\xi)^2\left(\frac{1}{3}su-u^2+\frac{2}{3}\frac{u^3}{s}\right) \\
&\quad+\Omega ef^{\alpha\beta}(0)k_{\beta}(k\cdot n)\left(\frac{4}{3}u^2-\frac{8}{3}\frac{u^3}{s}+\frac{4}{3}\frac{u^4}{s^2}\right) \\
&\quad+\Omega n^{\alpha}(k\cdot n)^2e^2f^2(0)\left(-su^2+4u^3-5\frac{u^4}{s}+2\frac{u^5}{s^2}\right) \\
&\quad\left.+\Omega e(\sigma f(0))n^{\alpha}\left(-\frac{1}{4}s+\frac{1}{2}u\right)\right]. \qquad (2.155)
\end{aligned}$$

Note that the terms proportional to Ω in these equations are of higher order and that $f(0)$ in these terms can be replaced with $f(0)(1+\Omega\xi)$. Considering $f(0)(1+\Omega\xi)\approx f(x)$ in the same approximation, I may conclude that all the explicit x-dependence can be included in the amplitude of the external field and hence that the current term depends on the field strength f and its gradient Ω at each point. I can then assume that $x^{\mu}=0$ at any points and the terms that contain ξ disappear in my results.

2.9 Furry's Theorem in Proper-Time Method

It is well known as Furry's theorem in QED that all loop diagrams with an odd number of vertices vanish. The same reasoning applies to my theory and I find that the terms in the induced electromagnetic current that include odd numbers of the external electromagnetic fields should be dropped in my case. To understand this, I consider the charge conjugation of the electron propagator with the external electromagnetic fields.

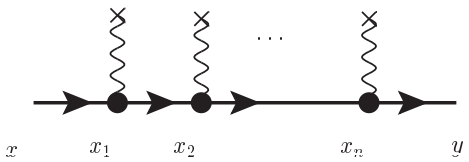

Figure 2.17: Electron propagator with external electromagnetic fields is shown.

The propagator with n external fields $S_{n,A}$ is represented as

$$S_{n,A}(y-x)=S(y-x_1)[-e\gamma^{\mu}A_{\mu}(x_1)]S(x_1-x_2)\cdots[-e\gamma^{\mu}A_{\mu}(x_n)]S(x_n-x), \qquad (2.156)$$

where $S(y-x)$ is the electron free propagator. Because the charge conjugation of

the free propagator is

$$\begin{aligned} S^c(y-x) &= \mathcal{C}S(y-x)\mathcal{C}^\dagger \\ &= CS^T(x-y)C^{-1}, \end{aligned} \tag{2.157}$$

where C is the matrix, which is $C = i\gamma^2\gamma^0$ for the Dirac representation and the charge conjugation of the electromagnetic field A_μ is

$$A^c_\mu = \mathcal{C}A_\mu\mathcal{C}^\dagger = -A_\mu, \tag{2.158}$$

the charge conjugation of $S_{n,A}(y-x)$ is

$$\begin{aligned} S^c_{n,A}(y-x) &= \mathcal{C}S_{n,A}(y-x)\mathcal{C}^\dagger \\ &= \mathcal{C}S(y-x_1)\mathcal{C}^\dagger\mathcal{C}[-e\gamma^\mu A_\mu(x_1)]\mathcal{C}^\dagger\cdots\mathcal{C}^\dagger\mathcal{C}S(x_n-x)\mathcal{C}^\dagger \\ &= CS^T(x_1-y)C^{-1}\left\{-e\gamma^\mu[-A_\mu(x_1)]\right\}C\cdots CS^T(x-x_n)\mathcal{C}^\dagger C^{-1} \\ &= CS^T(x_1-y)(-e)(-\gamma^{\mu T})[-A_\mu(x_1)]\cdots S^T(x-x_n)C^{-1} \\ &= C\left\{S(x-x_n)[-e\gamma^\mu A_\mu(x_1)]\cdots S(x_1-y)\right\}^T C^{-1} \\ &= CS^T_A(x-y)C^{-1}. \end{aligned} \tag{2.159}$$

Another expression of charge conjugation is

$$\begin{aligned} S^c_{n,A}(y-x) &= \mathcal{C}S_{n,A}(y-x)\mathcal{C}^\dagger \\ &= \mathcal{C}S(y-x_1)\mathcal{C}^\dagger\mathcal{C}(-e\gamma^\mu A_\mu(x_1))\cdots\mathcal{C}^\dagger\mathcal{C}S(x_n-x)\mathcal{C}^\dagger \\ &= S(y-x_1)(-e\gamma^\mu)(-A_\mu(x_1))\cdots S(x_n-x) \\ &= S_{n,-A}(y-x) \end{aligned} \tag{2.160}$$

because of the property of the electron propagator that it does not change by the charge conjugation $\mathcal{C}S\mathcal{C}^\dagger = S$. From Equation (2.160), I conclude that the sign of the propagator changes when the propagator contains odd numbers of electromagnetic fields

$$S^c_{\mathrm{odd},A}(y-x) = -S_{\mathrm{odd},A}(y-x) \tag{2.161}$$

and that the sign of the propagator does not change when the propagator contains even numbers of electromagnetic fields

$$S^c_{\mathrm{even},A}(y-x) = S_{\mathrm{even},A}(y-x). \tag{2.162}$$

As shown in Equation (2.2), the induced electromagnetic current is represented by the propagator

$$j^\mu(x) = \frac{\partial\mathcal{L}[A,a](x)}{\partial a_\mu} = ie\mathrm{tr}\left[\gamma^\mu G(x,x)\right]. \tag{2.163}$$

There are two ways to obtain the charge conjugation of the propagator. One is to extract the matrix C

$$\begin{aligned} j^{c\mu}_A(x) &= ie\mathrm{tr}\left[\gamma^\mu G^c_A(x,x)\right] = ie\mathrm{tr}\left[\gamma^\mu CG^T_A(x,x)C^{-1}\right] \\ &= ie\mathrm{tr}\left[-\gamma^{\mu T}G^T_A(x,x)\right] = -ie\mathrm{tr}\left[\gamma^{\mu T}G^T_A(x,x)\right] \\ &= -ie\mathrm{tr}\left[\gamma^\mu G_A(x,x)\right] = -j^\mu_A(x). \end{aligned} \tag{2.164}$$

The other is to change the sign of the electromagnetic field

$$\begin{aligned} j_A^{c\mu}(x) &= ie\mathrm{tr}\left[\gamma^\mu G_A^c(x,x)\right] = ie\mathrm{tr}\left[\gamma^\mu G_{-A}(x,x)\right] \\ &= j_{-A}^\mu(x). \end{aligned} \tag{2.165}$$

Comparing these two expression, I obtain

$$-j_A^\mu(x) = j_{-A}^\mu(x). \tag{2.166}$$

Thus, the induced electromagnetic current should contain only those terms with odd numbers of external electromagnetic fields. Since it is represented as $\langle j_\mu \rangle = \Pi_\mu{}^\nu b_\nu$ with the probe photon b_ν and the polarization tensor $\Pi_\mu{}^\nu$, the number of the external fields in $\Pi_\mu{}^\nu$ should be even.

2.10 Expression of the Induced Electromagnetic Current

The induced electromagnetic current $\langle j^\mu \rangle$ as given in Equation (2.39) is given as follows:

$$\langle j^\mu \rangle \simeq \frac{e}{2}\int_0^\infty ds \int_0^s du\; e^{-im^2 s}\Big[A^\mu + B^\mu + C^\mu + D^\mu + E^\mu + F^\mu + G^\mu + H^\mu\Big], \tag{2.167}$$

in which the terms $A^\mu, B^\mu, \cdots, H^\mu$ are expressed as follows:

$$\begin{aligned} A^\mu = \mathrm{tr}\Big[& ieb_\alpha k^\alpha \langle x(s)|\hat{\Pi}^\mu(s)\exp\left[-ik_\delta \hat{x}^\delta(u)\right] \\ & + \exp\left[-ik_\delta \hat{x}^\delta(u)\right]\hat{\Pi}^\mu(0)|x(0)\rangle\Big], \end{aligned} \tag{2.168}$$

$$\begin{aligned} B^\mu = \mathrm{tr}\Big[& \left(-\frac{ie}{2}\right)\langle x(s)|\hat{\Pi}^\mu(s)\exp\left[-ik_\delta \hat{x}^\delta(u)\right] \\ & + \exp\left[-ik_\delta \hat{x}^\delta(u)\right]\hat{\Pi}^\mu(0)|x(0)\rangle(\sigma g)\Big], \end{aligned} \tag{2.169}$$

$$\begin{aligned} C^\mu = \mathrm{tr}\Big[& (-2ie)b_\alpha \langle x(s)|\hat{\Pi}^\mu(s)\hat{\Pi}^\alpha(u)\exp\left[-ik_\delta \hat{x}^\delta(u)\right] \\ & + \hat{\Pi}^\alpha(u)\exp\left[-ik_\delta \hat{x}^\delta(u)\right]\hat{\Pi}^\mu(0)|x(0)\rangle\Big], \end{aligned} \tag{2.170}$$

$$\begin{aligned} D^\mu = \mathrm{tr}\Big[& (-2eb_\alpha)\sigma^{\mu\nu}\langle x(s)|\hat{\Pi}_\nu(s)\hat{\Pi}^\alpha(u)\exp\left[-ik_\delta \hat{x}^\delta(u)\right] \\ & - \hat{\Pi}^\alpha(u)\exp\left[-ik_\delta \hat{x}^\delta(u)\right]\hat{\Pi}_\nu(0)|x(0)\rangle\Big], \end{aligned} \tag{2.171}$$

$$\tag{2.172}$$

$$E^\mu = \mathrm{tr}\Bigg[\left(-\frac{e}{2}\right)\sigma^{\mu\nu}\langle x(s)|\hat{\Pi}_\nu(s)\exp\left[-ik_\delta\hat{x}^\delta(u)\right] - \exp\left[-ik_\delta\hat{x}^\delta(u)\right]\hat{\Pi}_\nu(0)|x(0)\rangle\left\{(\sigma g)+\frac{e^2u^2}{4}(\sigma f)(\sigma g)(\sigma f)\right\}\Bigg] \quad (2.173)$$

$$F^\mu = \mathrm{tr}\Bigg[\left(-\frac{ie^2u}{4}\right)\sigma^{\mu\nu}\langle x(s)|\hat{\Pi}_\nu(s)\exp\left[-ik_\delta\hat{x}^\delta(u)\right] - \exp\left[-ik_\delta\hat{x}^\delta(u)\right]\hat{\Pi}_\nu(0)|x(0)\rangle\left\{(\sigma f)(\sigma g)-(\sigma g)(\sigma f)\right\}\Bigg], \quad (2.174)$$

$$G^\mu = \mathrm{tr}\Bigg[\left(\frac{\Omega e^2u}{4}\right)\sigma^{\mu\nu}n_\nu\langle x(s)|\exp\left[-ik_\delta\hat{x}^\delta(u)\right]|x(0)\rangle \times\left\{(\sigma f)(\sigma g)-(\sigma g)(\sigma f)\right\}\Bigg], \quad (2.175)$$

$$H^\mu = \mathrm{tr}\Bigg[\left(-\frac{i\Omega e^3u^2}{4}\right)\sigma^{\mu\nu}n_\nu\langle x(s)|\exp\left[-ik_\delta\hat{x}^\delta(u)\right]|x(0)\rangle \times(\sigma f)(\sigma g)(\sigma f)\Bigg]. \quad (2.176)$$

They are further decomposed: e.g., A^μ is written as the sum of A_i^μ as $A^\mu=\sum_{i=1}^5 A_i^\mu$. The same notation is used for $B^\mu, C^\mu, \cdots, F^\mu$. All these components are explicitly written as follows:

$$A_1^\mu = K(u)ie(b\cdot k)k^\mu\left(2\frac{u}{s}-1\right)-c.t., \quad (2.177)$$

$$A_2^\mu = K(u)ie^3f^2(b\cdot k)(k\cdot n)n^\mu\left(\frac{2}{3}su-2u^2+\frac{4}{3}\frac{u^3}{s}\right), \quad (2.178)$$

$$A_3^\mu = K(u)i\Omega e^3f^2(b\cdot k)(k\cdot n)^2n^\mu\left(-\frac{4}{3}su^2+\frac{16}{3}u^3-\frac{20}{3}\frac{u^4}{s}+\frac{8}{3}\frac{u^5}{s^2}\right), \quad (2.179)$$

$$A_4^\mu = K(u)\Omega e^3f^2(b\cdot k)(k\cdot n)^3k^\mu \times\left(-\frac{2}{3}s^3u+\frac{26}{9}s^2u^2-\frac{32}{9}su^3-\frac{2}{9}u^4+\frac{26}{9}\frac{u^5}{s}-\frac{4}{3}\frac{u^6}{s^2}\right), \quad (2.180)$$

$$A_5^\mu = K(u)\Omega e^5f^4(b\cdot k)(k\cdot n)^4n^\mu \times\left(\frac{4}{9}s^4u^2-\frac{64}{27}s^3u^3+\frac{116}{27}s^2u^4-\frac{20}{9}su^5-\frac{56}{27}u^6+\frac{76}{27}\frac{u^7}{s}-\frac{8}{9}\frac{u^8}{s^2}\right), \quad (2.181)$$

$$B_1^\mu = \mathrm{tr}\left[(\sigma f)(\sigma g)\right]L(u)e^3f^{\mu\nu}k_\nu\left(-\frac{su}{2}+\frac{u^2}{2}\right), \quad (2.182)$$

$$B_2^\mu = \mathrm{tr}\left[(\sigma f)(\sigma g)\right]L(u)i\Omega e^5f^2(k\cdot n)^3f^{\mu\nu}k_\nu \times\left(\frac{1}{3}s^4u^2-\frac{10}{9}s^3u^3+s^2u^4+\frac{1}{3}su^5-\frac{8}{9}u^6+\frac{1}{3}\frac{u^7}{s}\right), \quad (2.183)$$

$$B_3^\mu = \mathrm{tr}\left[(\sigma f)(\sigma g)\right]L(u)\Omega e^3(k\cdot n)f^{\mu\nu}k_\nu\left(\frac{1}{2}su^2-u^3+\frac{1}{2}\frac{u^4}{s}\right), \quad (2.184)$$

$$B_4^\mu = \mathrm{tr}\left[(\sigma f)(\sigma g)\right]L(u)\Omega e^3(k\cdot n)f^{\mu\nu}k_\nu\left(\frac{1}{3}su^2-\frac{2}{3}u^3+\frac{1}{3}\frac{u^4}{s}\right), \quad (2.185)$$

$$C_1^\mu = K(u) ie (b\cdot k) k^\mu \left(2\frac{u}{s} - 4\frac{u^2}{s^2} \right) - c.t., \tag{2.186}$$

$$C_2^\mu = K(u) ie^3 (bfk) f^{\mu\nu} k_\nu \left(4u^2 - 8\frac{u^3}{s} + 4\frac{u^4}{s^2} \right), \tag{2.187}$$

$$C_3^\mu = K(u) ie^3 f^2 (b\cdot n)(k\cdot n) k^\mu \left(\frac{2}{3}su - \frac{10}{3}u^2 + \frac{16}{3}\frac{u^3}{s} - \frac{8}{3}\frac{u^4}{s^2} \right), \tag{2.188}$$

$$C_4^\mu = K(u) ie^3 f^2 (b\cdot k)(k\cdot n) n^\mu \left(-\frac{4}{3}u^2 + 4\frac{u^3}{s} - \frac{8}{3}\frac{u^4}{s^2} \right), \tag{2.189}$$

$$C_5^\mu = K(u) e^3 f^2 (b\cdot n) n^\mu \left(\frac{2}{3}s - 4u + 4\frac{u^2}{s} \right), \tag{2.190}$$

$$C_6^\mu = K(u) ie^5 f^4 (b\cdot n)(k\cdot n)^2 n^\mu \times \left(-\frac{4}{9}s^2u^2 + \frac{8}{3}su^3 - \frac{52}{9}u^4 + \frac{16}{3}\frac{u^5}{s} - \frac{16}{9}\frac{u^6}{s^2} \right), \tag{2.191}$$

$$C_7^\mu = K(u) eb^\mu \frac{2}{s} - c.t., \tag{2.192}$$

$$C_8^\mu = K(u) \Omega e^3 f^2 (b\cdot k)(k\cdot n)^3 k^\mu \times \left(\frac{4}{3}s^2u^2 - \frac{52}{9}su^3 + \frac{64}{9}u^4 + \frac{4}{9}\frac{u^5}{s} - \frac{52}{9}\frac{u^6}{s^2} + \frac{8}{3}\frac{u^7}{s^3} \right), \tag{2.193}$$

$$C_9^\mu = K(u) \Omega e^5 f^2 (bfk)(k\cdot n)^3 f^{\mu\nu} k_\nu \times \left(\frac{8}{3}s^3u^3 - \frac{104}{9}s^2u^4 + \frac{152}{9}su^5 - \frac{16}{3}u^6 - \frac{88}{9}\frac{u^7}{s} + \frac{88}{9}\frac{u^8}{s^2} - \frac{8}{3}\frac{u^9}{s^3} \right), \tag{2.194}$$

$$C_{10}^\mu = K(u) \Omega e^5 f^4 (b\cdot n)(k\cdot n)^4 k^\mu \left(\frac{4}{9}s^4u^2 - \frac{88}{27}s^3u^3 + \frac{244}{27}s^2u^4 - \frac{292}{27}su^5 + \frac{64}{27}u^6 + \frac{188}{27}\frac{u^7}{s} - \frac{176}{27}\frac{u^8}{s^2} + \frac{16}{9}\frac{u^9}{s^3} \right), \tag{2.195}$$

$$C_{11}^\mu = K(u) \Omega e^5 f^4 (b\cdot k)(k\cdot n)^4 n^\mu \left(-\frac{8}{9}s^3u^3 + \frac{128}{27}s^2u^4 - \frac{232}{27}su^5 + \frac{40}{9}u^6 + \frac{112}{27}\frac{u^7}{s} - \frac{152}{27}\frac{u^8}{s^2} + \frac{16}{9}\frac{u^9}{s^3} \right), \tag{2.196}$$

$$C_{12}^\mu = K(u) i\Omega e^5 f^4 (b\cdot n)(k\cdot n)^3 n^\mu \times \left(-\frac{4}{9}s^4u + \frac{100}{27}s^3u^2 - \frac{248}{27}s^2u^3 + \frac{196}{27}su^4 + \frac{28}{9}u^5 - \frac{64}{9}\frac{u^6}{s} + \frac{8}{3}\frac{u^7}{s^2} \right), \tag{2.197}$$

$$C_{13}^\mu = K(u) \Omega e^7 f^6 (b\cdot n)(k\cdot n)^5 n^\mu \left(-\frac{8}{27}s^5u^3 + \frac{200}{81}s^4u^4 - \frac{664}{81}s^3u^5 + \frac{1072}{81}s^2u^6 - \frac{712}{81}su^7 - \frac{248}{81}u^8 + \frac{728}{81}\frac{u^9}{s} - \frac{448}{81}\frac{u^{10}}{s^2} + \frac{32}{27}\frac{u^{11}}{s^3} \right), \tag{2.198}$$

$$C_{14}^\mu = K(u) i\Omega e^3 f^2 (k\cdot n)^3 b^\mu \times \left(-\frac{4}{3}s^2u + \frac{28}{9}su^2 - \frac{8}{9}u^3 - \frac{20}{9}\frac{u^4}{s} + \frac{4}{3}\frac{u^5}{s^2} \right), \tag{2.199}$$

$$\tag{2.200}$$

$$C_{15}^{\mu} = K(u) i\Omega e^3 (bfk)(k\cdot n) f^{\mu\nu} k_\nu \times \left(-8u^3 + 24\frac{u^4}{s} - 24\frac{u^5}{s^2} + 8\frac{u^6}{s^3}\right), \tag{2.201}$$

$$C_{16}^{\mu} = K(u) i\Omega e^3 f^2 (b\cdot n)(k\cdot n)^2 k^{\mu} \times \left(-2su^2 + 12u^3 - 26\frac{u^4}{s} + 24\frac{u^5}{s^2} - 8\frac{u^6}{s^3}\right), \tag{2.202}$$

$$C_{17}^{\mu} = K(u) i\Omega e^3 f^2 (b\cdot k)(k\cdot n)^2 n^{\mu} \times \left(\frac{8}{3}u^3 - \frac{32}{3}\frac{u^4}{s} + \frac{40}{3}\frac{u^5}{s^2} - \frac{16}{3}\frac{u^6}{s^3}\right), \tag{2.203}$$

$$C_{18}^{\mu} = K(u) \Omega e^3 f^2 (b\cdot n)(k\cdot n) n^{\mu} \times \left(-\frac{8}{3}su + 16u^2 - \frac{80}{3}\frac{u^3}{s} + \frac{40}{3}\frac{u^4}{s^2}\right), \tag{2.204}$$

$$C_{19}^{\mu} = K(u) i\Omega e^5 f^4 (b\cdot n)(k\cdot n)^3 n^{\mu} \times \left(\frac{20}{9}s^2u^3 - \frac{140}{9}su^4 + \frac{380}{9}u^5 - \frac{500}{9}\frac{u^6}{s} + \frac{320}{9}\frac{u^7}{s^2} - \frac{80}{9}\frac{u^8}{s^3}\right), \tag{2.205}$$

$$D_1^{\mu} = \mathrm{tr}\left[\sigma^{\mu\nu}(\sigma f)\right] L(u) i e^3 (bfk) k_\nu (-su + u^2), \tag{2.206}$$

$$D_2^{\mu} = \mathrm{tr}\left[\sigma^{\mu\nu}(\sigma f)\right] L(u) \Omega e^5 f^2 (bfk)(k\cdot n)^3 k_\nu \times \left(-\frac{2}{3}s^4u^2 + \frac{20}{9}s^3u^3 - 2s^2u^4 - \frac{2}{3}su^5 + \frac{16}{9}u^6 - \frac{2}{3}\frac{u^7}{s}\right), \tag{2.207}$$

$$D_3^{\mu} = \mathrm{tr}\left[\sigma^{\mu\nu}(\sigma f)\right] L(u) \Omega e^3 (k\cdot n) f_\nu{}^\alpha b_\alpha \left(\frac{1}{3}s^2 - su\right), \tag{2.208}$$

$$D_4^{\mu} = \mathrm{tr}\left[\sigma^{\mu\nu}(\sigma f)\right] L(u) i\Omega e^3 (bfk)(k\cdot n) k_\nu \left(\frac{4}{3}su^2 - \frac{8}{3}u^3 + \frac{4}{3}\frac{u^4}{s}\right), \tag{2.209}$$

$$D_5^{\mu} = \mathrm{tr}\left[\sigma^{\mu\nu}(\sigma f)\right] L(u) \Omega e^3 (b\cdot n) f_\nu{}^\lambda k_\lambda \left(-\frac{1}{3}s^2 + su\right), \tag{2.210}$$

$$D_6^{\mu} = \mathrm{tr}\left[\sigma^{\mu\nu}(\sigma f)\right] L(u) \Omega e^3 (bfk) n_\nu \left(\frac{1}{3}s^2 - u^2\right), \tag{2.211}$$

$$D_7^{\mu} = \mathrm{tr}\left[\sigma^{\mu\nu}(\sigma f)\right] L(u) i\Omega e^5 f^2 (bfk)(k\cdot n)^2 n_\nu \times \left(-\frac{2}{3}s^2u^3 + 2su^4 - 2u^5 + \frac{2}{3}\frac{u^6}{s}\right), \tag{2.212}$$

$$D_8^{\mu} = \mathrm{tr}\left[\sigma^{\mu\nu}(\sigma f)\right] L(u) i\Omega e^3 (bfk)(k\cdot n) k_\nu \left(su^2 - 2u^3 + \frac{u^4}{s}\right), \tag{2.213}$$

$$D_9^{\mu} = \mathrm{tr}\left[\sigma^{\mu\nu}(\sigma f)\right] L(u) \Omega e^3 (bfk) n_\nu (su - u^2), \tag{2.214}$$

$$E_1^{\mu} = \mathrm{tr}\left[\sigma^{\mu\nu}\left((\sigma g) + \frac{e^2u^2}{4}(\sigma f)(\sigma g)(\sigma f)\right)\right] L(u) \left(-\frac{e}{2}k_\nu\right) - c.t., \tag{2.215}$$

$$E_2^{\mu} = \mathrm{tr}\left[\sigma^{\mu\nu}\left((\sigma g) + \frac{e^2u^2}{4}(\sigma f)(\sigma g)(\sigma f)\right)\right] \times L(u) \Omega e^3 f^2 (k\cdot n)^2 n_\nu \left(-\frac{1}{3}su^2 + \frac{2}{3}u^3 - \frac{1}{3}\frac{u^4}{s}\right), \tag{2.216}$$

$$E_3^{\mu} = \mathrm{tr}\left[\sigma^{\mu\nu}\left((\sigma g) + \frac{e^2u^2}{4}(\sigma f)(\sigma g)(\sigma f)\right)\right] L(u) i\Omega e^3 f^2 (k\cdot n)^3 k_\nu \times \left(\frac{1}{3}s^3u - \frac{7}{9}s^2u^2 + \frac{2}{9}su^3 + \frac{5}{9}u^4 - \frac{1}{3}\frac{u^5}{s}\right), \tag{2.217}$$

$$F_1^\mu = \mathrm{tr}[\sigma^{\mu\nu}(\sigma f)(\sigma g)(\sigma f)]L(u)e^3 k_\nu \frac{su}{8}, \tag{2.218}$$

$$F_2^\mu = \mathrm{tr}[\sigma^{\mu\nu}(\sigma f)(\sigma g)(\sigma f)]L(u)i\Omega e^5 f^2 (k\cdot n)^3 n_\nu \times \left(-\frac{1}{12}s^4u^2 + \frac{7}{36}s^3u^3 - \frac{1}{18}s^2u^4 - \frac{5}{36}su^5 + \frac{1}{12}u^6\right), \tag{2.219}$$

$$F_3^\mu = \mathrm{tr}[\sigma^{\mu\nu}(\sigma f)(\sigma g)(\sigma f)] \times L(u)\Omega e^5 f^2 (k\cdot n)^2 k_\nu \left(\frac{1}{12}s^2u^3 - \frac{1}{6}su^4 + \frac{1}{12}u^5\right), \tag{2.220}$$

$$F_4^\mu = \mathrm{tr}[\sigma^{\mu\nu}(\sigma f)(\sigma g)(\sigma f)]L(u)\Omega e^3 (k\cdot n) k_\nu \left(-\frac{1}{8}su^2 + \frac{1}{8}u^3\right), \tag{2.221}$$

$$F_5^\mu = \mathrm{tr}[\sigma^{\mu\nu}(\sigma f)(\sigma g)(\sigma f)]L(u)i\Omega e^3 n_\nu \frac{su}{8}, \tag{2.222}$$

$$G^\mu = F_5^\mu, \tag{2.223}$$

$$H^\mu = \mathrm{tr}[\sigma^{\mu\nu}(\sigma f)(\sigma g)(\sigma f)]L(u)\left(-i\Omega e^3 n_\nu \frac{u^2}{4}\right), \tag{2.224}$$

where I employ the following abbreviations: $k\cdot n = k_\mu n^\mu$ and $bfk = b_\alpha f^{\alpha\beta}k_\beta$. In the above equations, $K(u)$ and $L(u)$ are defined as

$$K(u) = \frac{1}{4i\pi^2 s^2}\exp(-ikx) \times \exp\left\{i(k)^2\left(u - \frac{u^2}{s}\right) + i(k\cdot n)^2 e^2 f^2\left(-\frac{1}{3}su^2 + \frac{2}{3}u^3 - \frac{1}{3}\frac{u^4}{s}\right)\right\}, \tag{2.225}$$

$$L(u) = K(u)/4, \tag{2.226}$$

where $\exp(-ikx) = \exp(-ik_\mu x^\mu)$. The counter terms that originate from renormalization are denoted by *c.t.* in some equations. For the crossed-field, i.e., the long wavelength limit ($\Omega \to 0$) of the external plane-wave, the above expression is reduced to

$$\langle j^\mu\rangle|_{\Omega=0} \simeq \frac{e}{2}\int_0^\infty ds \int_0^s du\; e^{-im^2 s}\left[\sum_{i=1}^{2} A_i^\mu + B_1^\mu + \sum_{i=1}^{7} C_i^\mu + D_1^\mu + E_1^\mu + F_1^\mu\right]. \tag{2.227}$$

3

Polarization of Neutron Stars Emission

3.1 Introduction

X-ray polarimetry will be realized in the near future. In fact, the *Imaging X-ray Polarimetry Explorer (IXPE)* was recently selected as the next Small Explorer astrophysics mission of NASA recently and is planned to be launched in 2020 (Weisskopf et al., 2013). There are other satellite-borne X-ray polarimetry projects, such as the *X-ray Imaging Polarimetry Explorer (XIPE)* (Soffitta et al., 2016) and the *enhanced X-ray Timing and Polarimetry (eXTP)* (Zhang et al., 2016), which, if approved, will advance X-ray astronomy substantially.

Neutron stars are among the targets in some proposed observations in the soft X-ray band, $\sim$ a few keV. Thermal radiation has been detected from isolated neutron stars such as X-ray dim isolated neutron stars (XDINSs) and magnetars. The polarization of this thermal radiation, if observed, will provide us with an important clue to the physical properties of neutron stars near the surface, as well as the possible configurations of their magnetic fields.

Another aim of the polarimetry is the validation of strong-field quantum electrodynamics (QED), a quantum theory for electrons and photons in the supra-critical electromagnetic fields with strengths $\gtrsim 4.4 \times 10^{13}$G in the case of magnetic fields. The strong-field QED has been studied theoretically for a long time (Heisenberg and Euler, 1936; Schwinger, 1951; Dittrich and Gies, 2000): it predicts, for instance, that the vacuum becomes birefringent and a single photon may split into two photons in the presence of strong electromagnetic fields, both of which are absent in the ordinary vacuum and are of purely quantum origin. Although high-intensity laser is supposed to be a promising probe into QED in the strong-field regime (Heinzl et al., 2006; Zavattini et al., 2006, 2007; King and Heinzl, 2016), the currently attainable field strength is still much smaller than the critical one (Yanovsky et al., 2008), and the strong-field QED effects are yet to be observed in laser experiments. In contrast, some neutron stars are believed to possess very strong magnetic fields, which are

comparable to or stronger than the critical field (Mereghetti, 2008) and may hence be the only realistic possibility to study the strong-field QED for the moment. Recently, a hint of the vacuum polarization effect is obtained in the optical observation of polarizations in the thermal emissions from an XDINS (Mignani et al., 2017).

Photons emitted thermally from the surface of a magnetized neutron star propagate through its magnetosphere. They may be polarized in the atmosphere, and their polarization state will be further modified in the magnetosphere. It is well known that there are generally two elliptical polarization modes for photons propagating in magnetized plasmas (Mészáros, 1992). One is called the ordinary mode (O-mode), in which the major axis of the ellipse for the electric field of the photon is parallel to the $\boldsymbol{k}$-$\boldsymbol{B}$ plane, with $\boldsymbol{k}$ and $\boldsymbol{B}$ being the wave vector and the external magnetic field, respectively. The other mode is referred to as the extraordinary mode (E-mode), in which the ellipse is perpendicular to the $\boldsymbol{k}$-$\boldsymbol{B}$ plane. These situations are not changed if one takes into account the vacuum polarization. Note, however, that the helicities of these modes are changed as the plasma density varies. In fact, when the plasma is dominant, the O-mode is left-handed, whereas it becomes right-handed if the vacuum polarization is more important (Mészáros and Ventura, 1979; Lai and Ho, 2003b). Incidentally, the two modes are linearly polarized in the limit of the vanishing plasma density.

For ionized hydrogen atmospheres, which may cover the neutron star surface in a gas state, the opacity is different between the two modes (Lodenquai et al., 1974). In fact, it is lower for the E-mode than for the O-mode, because the scattering with electrons is suppressed for the former owing to gyration motions of electrons around magnetic field lines. The E-mode photons are hence emitted from deeper and hotter regions in the atmosphere than the O-mode photons and are dominant when they get out of the atmosphere. Then, the polarization vector of the surface emission is expected to be perpendicular to the $\boldsymbol{k}$-$\boldsymbol{B}$ plane. Such polarizations may be significantly reduced when integrated over the neutron star surface, however, since the magnetic field is not uniform on the surface and, as a result, the polarizations originated from different parts will cancel each other (Pavlov and Zavlin, 2000).

Note, in contrast, that the polarization changes adiabatically thereafter during the passage through the magnetosphere of the neutron star (Heyl and Shaviv, 2002). Although such evolutions of the polarization along the photon trajectories were computed and the light curves were obtained by Heyl et al. (2003), configurations of the neutron star considered in their paper were limited. Taverna et al. (2015) conducted more systematic study on the evolution of the polarization in the magnetosphere but with simplifications: they considered QED effects only for photons propagating in vacuo, assuming that all photons are emitted in one of the linearly polarized states. If propagation in a sufficiently dense medium is also considered, conversions of the polarization modes, which are one of the important effects caused by QED, become important. Lai and Ho (2003a) and van Adelsberg and Lai (2006) took into account both the mode conversion and the radiative transfer in the atmosphere to find the polarization properties. Unfortunately, they considered emissions from a small hot spot alone, which may not be applicable to some neutron stars.

Although it is not considered in this study, the resonant cyclotron scattering occurs in the magnetosphere if the density of charged particles is not low there, and

its effect on the polarization was discussed (Nobili et al., 2008; Fernández and Davis, 2011; Taverna et al., 2014). While I pay attention only to the persistent emission from neutron stars in this article, transient phenomena such as the bursts and flares of magnetars were investigated actively these days (Yang and Zhang, 2015; van Putten et al., 2016; Taverna and Turolla, 2017).

Once such polarization features are observed, possibly by the planned satellite-borne detectors, then I may be able to obtain new insights not only into the configuration of the magnetic fields of a neutron star and the thermodynamic state at the neutron star surface but also into the strong-field QED. In fact, Taverna et al. (2015) calculated the fraction and position angle of polarization for various configurations of a rotating magnetized neutron star, accounting for the vacuum polarization in the magnetosphere as well as geometrical effects. González Caniulef et al. (2016) applied the same method with realistic surface emission models to XDINSs and compared the results with observations (Mignani et al., 2017). They detected a possible imprint of the vacuum polarization in strong magnetic fields.

They considered two possibilities for the thermodynamic state of the neutron star surface, i.e., the normal gaseous state and the condensed state. It has been argued that the latter may occur via a phase transition at $T \lesssim 0.1$keV for neutron stars endowed with relatively strong magnetic fields, $B_p \gtrsim 10^{13}$G such as XDINSs (Turolla et al., 2004; Potekhin et al., 2012). The polarization properties of the thermal radiation from the bare surface in the condensed state are different from those from the gas atmosphere, and González Caniulef et al. (2016) and Mignani et al. (2017) claimed that they will be distinguished in polarimetric observations of the soft X-rays.

Although the dielectric effect of the vacuum polarization and resonant features in the radiative opacities at the vacuum resonance were considered in these papers, the mode conversion at the vacuum resonance was neglected. It may be irrelevant for photons with energies less than 1keV, which are dominant in the thermal emissions from XDINSs, but it cannot be neglected for photons with higher energies of $\sim$ a few keV, which may be radiated as a thermal component in magnetars.

The aim of this chapter is to study the polarizations of thermal radiation from isolated rotating magnetized neutron stars more systematically, taking the mode conversion at the vacuum resonance properly into account properly in the formulation of Taverna et al. (2015); I explore a large number of configurations systematically. Inhomogeneities on the neutron star surface, i.e., the possible existence of a hot spot, are also investigated.

The chapter is organized as follows. I describe my method in Section 3.2. In Section 3.3 I first make some comparisons with the previous study (Taverna et al., 2015) to validate my method and then show the main results, with a particular emphasis on the vacuum resonance and the hot-spot effects. Some discussions are also given in this section. I summarize this chapter in Section 3.4. Some supplementary discussions are given in Section 3.5. Note that the electromagnetic unit system is the cgs Gauss in this chapter.

3.2 Methods and Models

3.2.1 Theoretical Overview

I first summarize some theoretical basics on the behaviors of photons in strongly magnetized plasmas and vacuum and the polarization properties of thermal radiation in X-ray bands from magnetized rotating neutron stars. In the magnetosphere, it suffices to consider the vacuum polarization alone, whereas the contributions from magnetized plasmas also need to be taken into account in the neutron star atmosphere, in which photospheres are located in the case of my current interest.

X-ray photons have two elliptically polarized normal modes in the magnetized plasma, i.e., O-mode and E-mode. This is also true of the magnetized vacuum. As mentioned already, the O-mode has the electric field that traces the ellipse, the major axis of which is parallel to the $\boldsymbol{k}$-$\boldsymbol{B}$ plane, whereas for the E-mode, it is perpendicular to the plane. What is interesting is that the O-mode (E-mode) photons in the plasma-dominant regime have the same helicity as the E-mode (O-mode) photons in the vacuum-dominant regime. As a result of this property, when a photon propagates from the inner atmosphere of neutron star, where the plasma effect is dominant, through the outer part to the magnetosphere, where the vacuum polarization is dominant, the so-called mode conversion may occur from the O-mode photon to the E-mode and vice versa (Mészáros and Ventura, 1979).

This is also referred to as the vacuum resonance, since the conversion takes place at the resonance point, at which the plasma and vacuum polarizations become comparable to each other. This resonant mode conversion proceeds adiabatically if the following condition is satisfied:

$$E \gg E_{\rm ad} = 1.49 (f \tan\theta_B |1-u_i|)^{2/3} \left(\frac{5{\rm cm}}{H_\rho}\right)^{1/3} {\rm keV}, \tag{3.1}$$

where f is a factor of the order of unity and will be explained below separately; E is the photon energy; θ_B is the angle between $\boldsymbol{k}$ and $\boldsymbol{B}$; $u_i = (E_{ci}/E)^2$, with $E_{ci} = \hbar eB/m_p c$ being the cyclotron energy of the proton; and H_ρ is the density scale height, i.e., $H_\rho \simeq 2kT/(m_p g\cos\theta) = 19.1\, T_1/(g_{14}\cos\theta){\rm cm}$, for the ionized hydrogen atmosphere with a temperature $kT = 1\,{\rm keV}\, T_1$, a surface gravity $g = 10^{14}\,{\rm cm\ s^{-2}}\, g_{14}$, and the angle θ between $\boldsymbol{k}$ and the surface normal (Lai and Ho, 2002; Ho and Lai, 2003; Lai and Ho, 2003a,b).

The factor f in Equation (3.1) is expressed as $f = [3\delta/(q+m)]^{1/2}$, where $\delta = (\alpha/45\pi)b^2$, with $\alpha = 1/137$ being the fine structure constant and $b = B/B_Q$ being the field strength normalized with the critical field strength, given as $B_Q = m_e^2 c^3/e\hbar = 4.4\times10^{13}{\rm G}$. Parameters q and m are defined in the following formulae (Heyl and Hernquist, 1997b,a):

$$q = \int_0^\infty d\eta \frac{e^2 e^{-\eta}}{48 b\pi^2\eta^2 \sinh^2(b\eta)} \left\{6b\eta + (-3+2b^2\eta^2)\sinh(2b\eta)\right\}, \tag{3.2}$$

$$m = \int_0^\infty d\eta \frac{e^2 e^{-\eta}}{32 b\pi^2\eta^2 \sinh^2(b\eta)} \times \left\{-4b\eta + (1+8b^2\eta^2)\frac{\cosh(b\eta)}{\sinh(b\eta)} - \frac{\cosh(3b\eta)}{\sinh(b\eta)}\right\}, \tag{3.3}$$

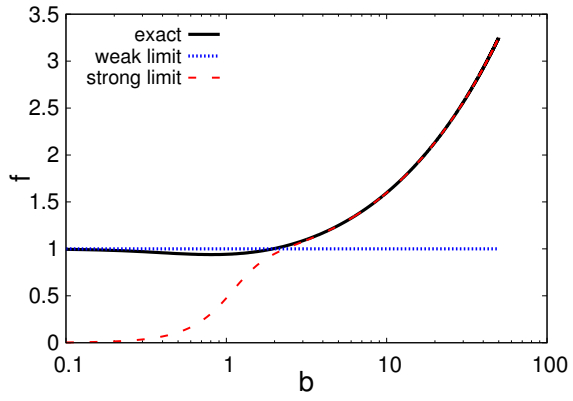

Figure 3.1: Comparison of the approximate expressions for f. The solid black line is the exact result, whereas the blue dotted line and the red dashed line show the results in the weak (Equations (3.4) and (3.5)) and strong limits (Equations (3.6) and (3.7)) limits, respectively.

the derivation of which is given in Section 3.5, but they can be well approximated as

$$q \simeq 7\delta, \tag{3.4}$$
$$m \simeq -4\delta, \tag{3.5}$$

for $B \ll B_Q$ and as

$$q \simeq -\frac{\alpha}{2\pi}\left[-\frac{2}{3}b + 1.272 - \frac{1}{b}(0.307 + \ln b) - \frac{0.7}{b^2}\right], \tag{3.6}$$
$$m \simeq -\frac{\alpha}{2\pi}\left[\frac{2}{3} + \frac{1}{b}(0.145 - \ln b) - \frac{1}{b^2}\right], \tag{3.7}$$

for $B \gtrsim B_Q$ (Lai and Ho, 2002). I compare these approximate expressions for f with the exact one in Figure 3.1. In my calculations, I employ Equations (3.4) and (3.5) for $b < 0.1$, whereas I adopt Equations (3.6) and (3.7) for $b \geq 50$. In between, I use the exact expressions (Equations (3.2) and (3.3)).

For $E \sim E_{\rm ad}$, the adiabatic approximation is no longer valid. The mode conversion occurs only partially, and its probability may be given approximately (Lai and Ho, 2003a) as

$$P_{\rm con} = 1 - \exp\left[-\left(\frac{\pi}{2}\right)\left(\frac{E}{E_{\rm ad}}\right)^3\right]. \tag{3.8}$$

The surface radiation of neutron stars is thought to be strongly polarized. This is because the opacity for the E-mode photon is smaller in magnetized plasma compared with that of the O-mode photon, $\kappa_E \sim (E/E_{ce})^2\kappa_O$, where $E_{ce} = \hbar eB/m_e c$ is the electron cyclotron energy (Lodenquai et al., 1974). The photosphere of the E-mode is hence located inside the photosphere of the O-mode; i.e., the E-mode photons are emitted from deeper and hotter regions in the atmosphere than the O-mode photons. As a result, emergent photons are dominated by the E-mode

photons. Since I focus on how the mode conversion affects the photon polarization, and solving the radiative transfer of photons in the atmosphere is outside the scope of this chapter, I assume for the sake of simplicity that photons are all in the E-mode at the top of the atmosphere in the absence of the mode conversion.

The mode conversion modifies the polarization produced in the surface radiation. It is the relative positions of the vacuum resonance point with respect to the photospheres that are relevant here. When the magnetic field is not so strong and satisfies the condition

$$B < B_l \simeq 4.9 \times 10^{13} \text{ G } f T_1^{-1/8} E_1^{-1/4} G^{-1/4}, \tag{3.9}$$

where $E = 1\text{keV}\ E_1$ and $G = 1 - e^{-E/kT}$, with E being the photon energy, the vacuum resonance point lies outside the photospheres for both the E- and O-modes. If the magnetic field is stronger, in contrast, and the following condition holds,

$$B_l < B < B_h \simeq 2.8 \times 10^{16} \text{ G } f^2 T_1^{-1/4} E_1^{-3/2} G^{-1/2}, \tag{3.10}$$

the vacuum resonance point is still located outside the E-mode photosphere but now lies inside the O-mode photosphere (Lai and Ho, 2003b). It follows, then, that when $B < B_l$, both the E- and O-modes photons experience mode conversion, and the O-mode, into which the originally dominant E-mode is converted, becomes predominant as long as the photon energy satisfies the adiabaticity condition: $E \gtrsim E_{\rm ad}$ (Lai and Ho, 2003a). If $B_l < B < B_h$ is met, in contrast, the E-mode photons emitted from their photosphere transform into the O-mode photons at the vacuum resonance point. Since this point is inside the O-mode photosphere, the O-mode photons thus converted cannot escape immediately and diffuse out until the O-mode photosphere is reached. The E-mode photons generated at the vacuum resonance point, in contrast, can escape as soon as they are produced, since matter is transparent for them there. This implies that the vacuum resonance point behaves as the effective E-mode photosphere, whereas the O-mode photosphere is essentially intact; as a result, the E-mode is dominant in this case (Lai and Ho, 2003b). In this chapter, I assume that all photons are initially emitted in the E-mode from their photosphere if $B < B_l$ and from the resonance point if $B > B_l$. I also explicitly take into account the mode conversion only for the former, although even in the case of $B > B_l$, the mode conversion occurs in the atmosphere between the photospheres of the two modes.

The polarization is further modified in the magnetosphere according to the equation

$$\frac{d}{dZ}\begin{pmatrix} A_X \\ A_Y \end{pmatrix} = \frac{ik_0\delta}{2}\begin{pmatrix} M & P \\ P & N \end{pmatrix}\begin{pmatrix} A_X \\ A_Y \end{pmatrix} \tag{3.11}$$

for photons propagating in the Z-direction, where $\boldsymbol{A} = (A_X, A_Y)$ are the X- and Y-components of the electric-field amplitude of the photon with an angular frequency ω, $k_0 = \omega/c$, $\delta = (\alpha/45\pi)b^2$. Here M, N, and P are given as $M = 7\hat{B}_X\hat{B}_X + 4\hat{B}_Y\hat{B}_Y$, $N = 4\hat{B}_X\hat{B}_X + 7\hat{B}_Y\hat{B}_Y$, and $P = 3\hat{B}_X\hat{B}_Y$, where $\hat{B}_X = \mathbf{B}\cdot\hat{\mathbf{e}}_X/|\mathbf{B}|$ and $\hat{B}_Y = \mathbf{B}\cdot\hat{\mathbf{e}}_Y/|\mathbf{B}|$ are the X- and Y-components of the unit vector aligned with the magnetic field, respectively. The above equation is the same as Equations (21) and (22) in

Fernández and Davis (2011), except that those authors assumed that the magnetic field lies in the X-Z plane, which is not assumed in this chapter for numerical convenience (see also Taverna et al. (2014, 2015)). Note that these expressions of M, N, and P are valid in the weak-field limit ($B \ll B_Q$), which is well satisfied in the magnetosphere in the present case. There are two length scales of relevance in these equations: one is the scaled wavelength of the photon, $l_A = 2/k_0\delta$, and the other is the scale height of the magnetic field in the direction of the wave vector, $l_B = |\boldsymbol{B}||\boldsymbol{k}|/|\boldsymbol{k}\cdot\nabla\boldsymbol{B}| \sim r$, where r is the radial distance. If the wavelength of the photon is short and/or the magnetic field is strong, satisfying $l_A \ll l_B$, then the polarization varies adiabatically as the direction of the external magnetic field changes slowly. If the opposite is true, $l_A \gg l_B$, in contrast, the polarization cannot follow the rapid change of the magnetic field and is unchanged. This means that the polarization is essentially fixed at the point corresponding to the so-called polarization-limiting radius, at which $l_A = l_B$ is satisfied.

This point is somewhat far from the surface if the magnetic field is strong, $B \sim 10^{14}$G and is given, for example, as

$$\frac{r_{pl}}{R_{\rm NS}} \simeq 74 \left(\frac{B_p}{10^{14}{\rm G}}\right)^{2/5} \left(\frac{E}{1{\rm keV}}\right)^{1/5} \left(\frac{R_{\rm NS}}{10{\rm km}}\right)^{1/5}, \tag{3.12}$$

on the symmetry axis of a dipolar magnetic field, where B_p is the field strength at the magnetic pole and $R_{\rm NS}$ is the radius of the neutron star. If one considers an imaginary surface that is formed by the polarization-limiting radii and referred to hereafter as the polarization-limiting surface, the photons reaching a distant observer should pass through a small patch on the surface. Since the magnetic field is fairly uniform on the patch, the superposition of radiation coming from different portions on the neutron star surface does not cancel the polarizations (Heyl and Shaviv, 2002).

Although the evolution of polarization in the magnetosphere is obtained by solving Equation (3.11) in principle, I use the adiabatic approximation; i.e., the polarization state follows the change in the eigenvectors of the matrix in Equation (3.11): $\mathbf{b}_E = (-\hat{B}_Y, \hat{B}_X)$ and $\mathbf{b}_O = (\hat{B}_X, \hat{B}_Y)$, which correspond to the E- and O-mode, respectively. It is true that the adiabaticity is violated near the limiting radius, but I ignore it for simplicity and apply the approximation down to the limiting radius, at which I evaluate the final polarization state (Taverna et al., 2015).

3.2.2 Method

I now explain the procedure to obtain the polarization angle and fraction of X-rays emitted from magnetars based on the picture just mentioned. I first specify the configuration of the magnetic field. In this chapter, I consider only dipole magnetic fields, although the formulation is applicable to other configurations as well. I introduce coordinates as shown in Figure 3.2. In this frame, an observer is assumed to be sitting at an infinite distance on the positive Z-axis. I assume without loss of generality that the spin axis of the magnetar ($\boldsymbol{\Omega}$) lies in the X-Z plane and that the angle between the Z-axis and the spin axis $\boldsymbol{\Omega}$ is γ. The magnetic dipole $\boldsymbol{d}$ is assumed to be tilted from the rotation axis by an angle η. Its rotation around $\boldsymbol{\Omega}$ is

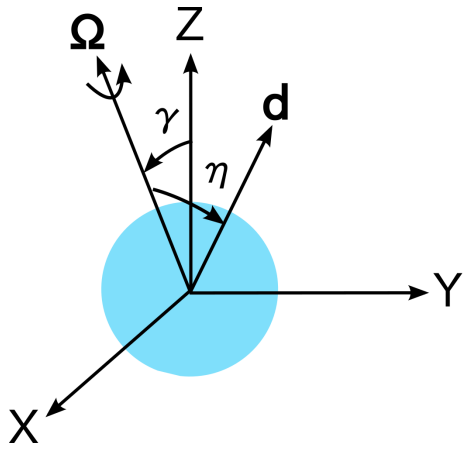

Figure 3.2: Configuration of a magnetar. The rotation axis and magnetic dipole are denoted by $\mathbf{\Omega}$ and $\mathbf{d}$, respectively. The angles that $\mathbf{\Omega}$ makes with the Z-axis and $\mathbf{d}$ are denoted by γ and η, respectively. The observer is assumed to be sitting at infinity on the Z-axis.

specified by another angle ψ, which is measured from the X-Z plane. The magnetic dipole moment $\boldsymbol{d}$ in this reference frame is expressed as

$$\boldsymbol{d} = R_Y(\gamma)R_Z(\psi)R_Y(\eta)\boldsymbol{d}_Z, \tag{3.13}$$

where

$$R_Y(\theta) = \begin{pmatrix} \cos\theta & 0 & \sin\theta \\ 0 & 1 & 0 \\ -\sin\theta & 0 & \cos\theta \end{pmatrix}, \; R_Z(\theta) = \begin{pmatrix} \cos\theta & -\sin\theta & 0 \\ \sin\theta & \cos\theta & 0 \\ 0 & 0 & 1 \end{pmatrix}$$

are rotational matrices around the Y- and Z-axes, respectively, and $\boldsymbol{d}_Z$ is defined as $\boldsymbol{d}_Z = B_p R_{\rm NS}^3(0, 0, 1/2)$.

The initial polarization is determined by the magnetic field at the photosphere. As explained earlier, if the condition $B > B_l$ is satisfied, I assume that the radiation is completely in the E-mode, though the mode conversion occurs inside the O-mode photosphere. If, in contrast, the surface magnetic field satisfies $B < B_l$, then the originally dominant E-mode is converted to a mixture of the O- and E-modes according to Equation (3.8). As a result, the radiation generally contains in general both polarized and unpolarized parts, and I consider the former alone in the following. The fraction of the polarized part is $|1 - 2P_{\rm con}|$.

As mentioned above, I employ the adiabatic approximation in solving Equation (3.11). Then, the solution is expressed as follows:

$$\mathbf{A}(\mathbf{r}) = A_E\mathbf{b}_E(\mathbf{r}) + A_O\mathbf{b}_O(\mathbf{r}), \tag{3.14}$$

in which $\mathbf{b}_E(\mathbf{r})$ and $\mathbf{b}_O(\mathbf{r})$ are the eigenvectors of the coefficient matrix in Equation (3.11) at point $\mathbf{r}$. Since the matrix depends on the magnetic field at each point on the photon trajectory, the eigenvectors also change along the path. Since I

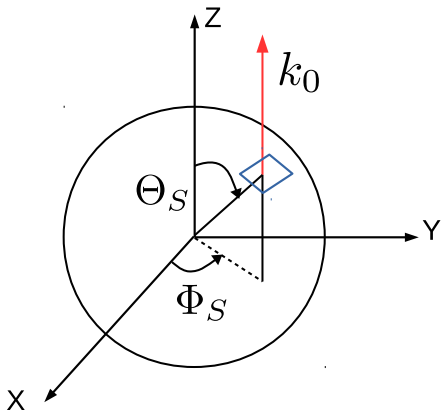

Figure 3.3: Emission (red arrow) from a patch (blue square) on the (effective) photosphere. The location of the patch is specified by the zenith and azimuth angles Θ_S and Φ_S. The observer is assumed to be located at infinity on the positive Z-axis.

assume in this chapter that the polarization state is finally fixed at the polarization-limiting radius, it is given by the coefficients A_E and A_O determined at the (effective) photosphere and the eigenvectors at the limiting radius. I neglect gravitational effects such as redshifts and ray bendings other than those on the scale height H_ρ of the atmosphere. Observed polarizations are the sum of individual polarizations obtained in the fashion described just now for emissions from different portions of the (effective) photosphere, which are specified by the zenith and azimuth angles, Θ_S and Φ_S, as shown in Figure 3.3 (Taverna et al., 2015).

To derive the polarization angle and fraction, I utilize the Stokes parameters, Q, U, and V, which describe the linear and circular polarizations. They are expressed as

$$Q = A_X^p A_X^{p*} - A_Y^p A_Y^{p*}, \tag{3.15}$$
$$U = A_X^p A_Y^{p*} + A_Y^p A_X^{p*}, \tag{3.16}$$
$$V = i(A_X^p A_Y^{p*} - A_Y^p A_X^{p*}), \tag{3.17}$$

where $\boldsymbol{A}^p = (A_X^p, A_Y^p)$ is the amplitude of the polarized component. The other Stokes parameter, I, is nothing but the intensity of the emission. The polarization angle and fraction are finally derived from the Stokes parameters as

$$\chi_p = \frac{1}{2}\arctan\left(\frac{U}{Q}\right), \tag{3.18}$$
$$\Pi_L = \frac{\sqrt{Q^2+U^2}}{I}. \tag{3.19}$$

Note that the Stokes parameters are additive quantities and are hence used in calculating the polarization properties of spatially and/or temporally integrated radiation. It should be also mentioned that I assume in this chapter that the E- and O-modes are completely uncorrelated with each other. In reality, however, circular

polarizations will be produced by the partial mode conversion and they are expected to be correlated (Lai and Ho, 2003a). They will also be produced if the magnetic field near the polarization-limiting radius changes rapidly and the polarization cannot catch up. Such situations may occur if the polarization-limiting surface is close to the neutron star (Heyl and Shaviv, 2002). Although the superposition of radiation emitted from different points on the neutron star surface will reduce the circular polarization in general, quantitative investigations are certainly interesting and will be conducted in the future.

3.3 Results and Discussions

3.3.1 Comparison with Previous Study

I now apply the formalism developed so far to concrete models. I begin with a comparison with the work by Taverna et al. (2015), in which they studied the polarization of the emissions from the surface of a neutron star with a mass and radius of $M = 1.4M_\odot$ and $R_{\rm NS} = 10$km, respectively. They assumed that the surface temperature is given as $T(\theta_{\rm NS}) = \max(T_p|\cos\theta_{\rm NS}|^{1/2}, T_e)$, where $T_p = 150$eV, $T_e = 100$eV, and $\theta_{\rm NS}$ is the zenith angle measured from the north pole of the core-centered dipole field (Greenstein and Hartke, 1983; Page, 1995); the surface emission was assumed to be in the E-mode initially. Ignoring the mode conversion entirely, they calculated the phase-resolved polarization fraction and angle, as well as the phase-averaged polarization fraction and semi-amplitude (defined to be half the range of variations in the polarization angle during a single rotation) for different field strengths. They also considered the ray bending and modifications of the dipole magnetic field by the strong gravity of the neutron star.

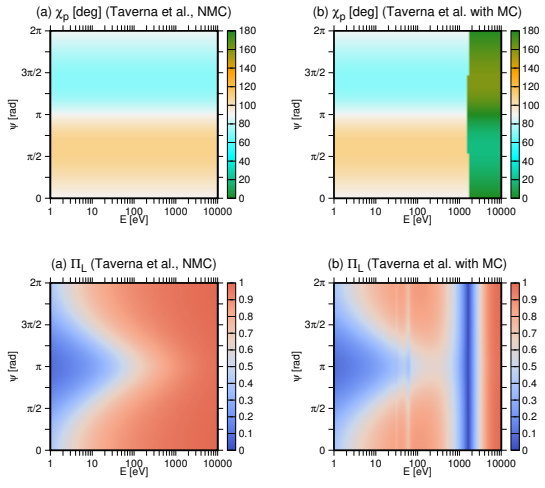

Figure 3.4: Phase-resolved polarization angles (upper panels) and fractions (lower panels) for the same condition as in Taverna et al. (2015), except for the relativistic ray bending and the modifications of the magnetic field by the strong gravity near the neutron star. (a) The mode conversion is ignored, as in Taverna et al. (2015). (b) The mode conversion is considered.

Let us start with the phase-resolved quantities. I apply my method to the same model with $B_p = 10^{13}$G, $\gamma = 15°$, and $\eta = 5°$. Note that χ, ξ, and γ in Taverna et al. (2015) correspond to γ, $-\eta$, and $-\psi$ in my notation. For comparison, I first neglect the mode conversion. The results are shown in the left panels of Figure 3.4. The upper and lower panels present the polarization angle χ_p and fraction Π_L, respectively, as color contours in the $E - \psi$ plane, which are to be compared with Figure 5 in Taverna et al. (2015). I find a good agreement between them.

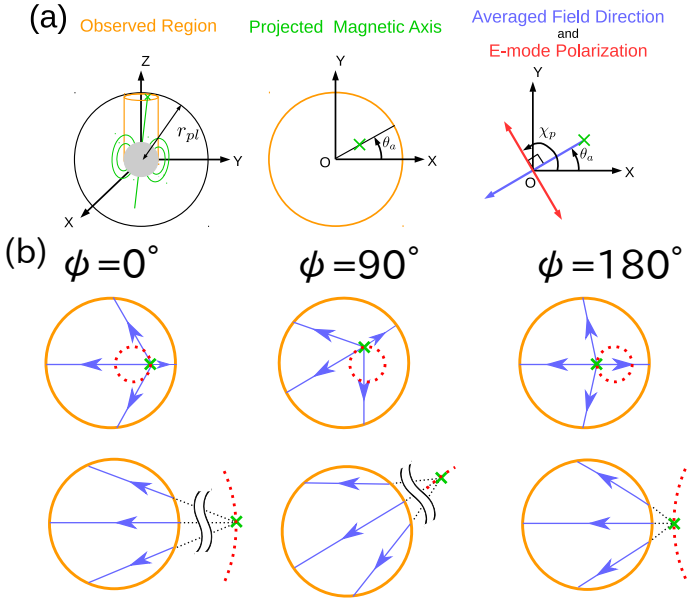

Figure 3.5: Schematic pictures to explain how the polarization is determined. (a) The left panel is a snapshot of the configuration of the neutron star considered in Figure 3.4. The central gray sphere is the neutron star, and the green arrow and curves are the star magnetic axis and some field lines, respectively. The orange cylinder is a bundle of light rays emitted from the neutron star parallel to the Z-axis; the outer sphere of radius r_{pl} is the polarization-limiting surface. The middle panel is a top view of the patch on the polarization-limiting surface cut out by the cylinder; the green cross is the point where the star magnetic axis meets the polarization-limiting surface, and θ_a is its angle from the X-axis. The right panel is the same as the middle one but for the average magnetic field (blue arrow) and polarization direction (red arrow); the polarization angle is denoted by χ_p. See the text for definitions. (b) The upper three panels show the projected magnetic field lines on the patch at different rotational phases; the green cross is again the magnetic north pole on the polarization-limiting surface. The red dotted circle indicates the locus of the magnetic north pole. The lower three panels show the case with larger r_{pl}, in which the magnetic north pole is located outside the observed patch.

The behavior of the polarization angle is understood from Figure 3.5 as follows. In the upper left panel, I draw a schematic picture of a snapshot of the neutron star I am considering now. The central gray sphere is the neutron star, with the green arrow and curves being the magnetic dipole and some field lines, respectively. The outer sphere with the radius r_{pl} is the polarization-limiting surface. Note that

the surface is not a sphere in general. Photons reaching the distant observer on the positive Z-axis should propagate in the cylinder drawn in orange.

It is the configuration of the projected magnetic field on the patch of the polarization-limiting surface cut out by this fictitious cylinder that finally determines the polarization angle. In the top middle panel, I schematically depict this patch as the orange circle and mark with the green cross the point at which the star magnetic axis meets the polarization-limiting surface. The angle of this point from the X-axis is denoted by θ_a. Note that, depending on the configuration of the neutron star and the radius of the polarization-limiting surface, the green cross may sit outside the orange circle, the radius of which is equal to that of the neutron star (see also the bottom panels).

The top right panel is the same as the top middle panel, except that the magnetic field averaged over the patch and the corresponding polarization direction are exhibited in blue and red, respectively, instead of the circle to indicate the patch. I find that the average magnetic field, which is defined to be the integral of the (projected) magnetic fields over the observed patch of the polarization-limiting surface divided by its area, is actually directed from the green cross to the origin of the patch from the symmetry of the projected magnetic fields around the green cross. In fact, the angle between the projection of the magnetic axis and the X-axis θ_a is given as $\theta_a = \arctan(d_2/d_1)$ from the magnetic dipole momentum expressed as $\boldsymbol{d} = (d_1, d_2, d_3)$; then, the orientation from the green cross to the origin on the patch is given by the angle $\theta_a + 180^\circ$ from the X-axis, which is found to be almost identical to the direction of the averaged magnetic field obtained numerically from the surface integral. In the case of $\gamma = 15^\circ$, $\eta = 5^\circ$, for example, I find $\theta_a + 180^\circ = 198.^\circ02$, whereas the numerically obtained value is $198.^\circ68$ for $\psi = \pi/2$; they are identical at $\psi = 0$. In the same figure, I assume that the photons are all in the E-mode and hence the polarization direction, which is specified by the electric field of the photon, is perpendicular to the (averaged) magnetic field. Then, the polarization angle is given as $\chi_p = \theta_a + 90^\circ \pmod{180^\circ}$.

In Figure 3.5 (b), I display some (projected) field lines on the observed patch at different rotational phases. As mentioned above, the location of the green cross, i.e., the (extension of the) magnetic north pole to the polarization-limiting surface, may be inside (upper panels) or outside (lower panels) the observed patch. It moves around on the surface, as indicated in red, owing to the rotation of the neutron star. The radius of the trajectory depends on the angles γ and η (see Figure 3.2), which I assume here to be $\gamma = 15^\circ$ and $\eta = 5^\circ$. In this case, it is not very large, and the polarization angle does not change much, as confirmed in the upper left panel of Figure 3.4.

Using the same figure, I can also understand the behavior of the polarization fractions shown in the lower left panel of Figure 3.4. In fact, it is clear from the upper panels of Figure 3.5 (b) that the polarization is somewhat canceled when averaged over the observed patch if the green cross, or the magnetic north pole, is located inside the patch. This happens if the magnetic field is weak and/or the photon energy is low, and, as a consequence, the polarization-limiting surface is rather close to the neutron star (see Equation (3.12)). Such cancellations do not occur if the polarization-limiting surface is distant from the neutron star and the

magnetic north pole sits outside the observed patch on the surface (see the bottom panels of Figure 3.5 (b)).

In the lower left panel of Figure 3.4, the polarization fraction is ~ 1 at high photon energies, since the polarization-limiting surface is far away from the neutron star and the magnetic north pole is always outside the observed patch during the entire rotation period. As the energy is decreased, this is no longer the case, and the pole enters the patch at some rotational phases near $\psi = \pi$. As a result, the cancellation occurs, and the polarization fraction is reduced there. At very low energies, the north pole stays inside the patch at all times, and the polarization fraction is always low accordingly.

This is the essential picture in the absence of the mode conversion. I now consider how it is modified by the mode conversion, using the same model.

In the right column of Fig. 3.4, the results with the mode conversion are displayed. The density scale height is set to $H_\rho \simeq 10.3 T_1/\cos\theta$ cm in this calculation. The upper and lower panels are for χ_p and Π_L, respectively. One can see that they are different from the previous ones for high-energy photons with $E \gtrsim 1$keV. The most remarkable is the abrupt change in the polarization angle χ_p by $\simeq 90^\circ$ at $E \simeq 2$keV, which indicates that the dominant polarization mode changes from the E-mode at low energies to the O-mode when the photon energy exceeds 2keV. At this energy, $E \sim E_{\rm ad}$ is satisfied. The adiabatic mode conversion occurs at the vacuum-resonance points above this energy, whereas the conversion is suppressed below it (Lai and Ho, 2003a).

The effects of the mode conversion on the polarization fraction are shown in the bottom right panel. It is remarkable that there is a blue strip at $E \simeq 2$keV, where the polarization fraction is very small. As mentioned above, this energy corresponds to the adiabatic energy given by Equation (3.1). The mode conversion occurs nonadiabatically below this energy, and both the E- and O-mode photons are emitted according to Equation (3.8). In the blue strip of the panel, in particular, both modes are almost equally mixed, and the polarization fraction becomes very small as observed. At much smaller energies, the mode conversion is essentially frozen, and the polarization fraction returns to the original value at emission.

One can recognize, however, that other vertical strips exist at $E \sim 30$eV and ~ 60eV, where the polarization fraction is somewhat reduced again. These energies are special, corresponding to the cyclotron energies of protons for the magnetic fields of 5×10^{12}G at the (magnetic) equator and 10^{13}G at the (magnetic) pole, respectively. Note that when the photon energy equals the proton cyclotron energy and $E_{\rm ad} = 0$, the completely adiabatic conversion occurs again for this particular energy of photons. As a result, the O-mode photons increase at this energy, reducing the polarization fraction. Note also that the magnetic pole and equator are the two main contributors to the surface emissions in the current configuration (see the explanations given later).

I next discuss the phase-averaged quantities. The semi-amplitudes and polarization fractions are shown in the upper and lower panels of Figure 3.6, respectively. Note that, rigorously speaking, the semi-amplitude is not a phase-averaged quantity, but I consider it here just for comparison. In this chapter, the semi-amplitude is defined as the quantity related to the total variation of the polarization angle during

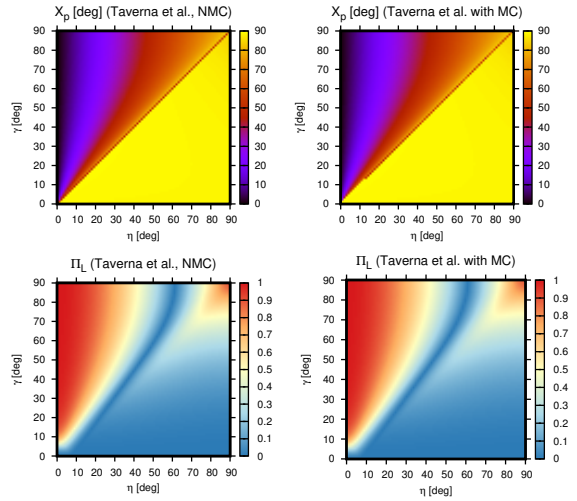

Figure 3.6: Semi-amplitudes of the polarization angle X_p (upper panels) and phase-averaged polarization fractions (lower panels) for different configurations of a rotating neutron star. The left and right columns correspond to the cases without and with the mode conversion, respectively. The photon energy is set to $E = 300\mathrm{eV}$.

the rotational period divided by four, which is expressed as

$$X_p = \frac{1}{4} \sup_P \left[\sum_{i=0}^{n_P - 1} \min\left((\Delta\chi_p)_i, 180^\circ - (\Delta\chi_p)_i \right) \right],$$
$$(\Delta\chi_p)_i = |\chi_p(\psi_{i+1}) - \chi_p(\psi_i)|, \tag{3.20}$$

where the supremum is taken over all possible partitions of the range $[0, 2\pi]$ for ψ. This definition coincides with that given in Taverna et al. (2015) in most cases but not always (see below). The photon energy is set to $E = 300\mathrm{eV}$ following Taverna et al. (2015). In the left column, the mode conversion is neglected on purpose for comparison with the previous work, whereas it is incorporated in the right column. The results without mode conversion are consistent with those in Taverna et al. (2015). The discontinuous suppression of the semi-amplitude on the diagonal line observed in my result (see the top left panel of Fig. 3.6) but absent in their result is mainly due to the fact that my definition of the semi-amplitude is not completely the same as theirs.

I explain this in more detail using Figure 3.7, which shows how the polarization angle changes with the rotational phase for different combinations of η and γ.

In the middle three panels of Figure 3.7 (a), I schematically draw the top views of the observed patch on the polarization-limiting surface for $\eta < \gamma$, $\eta = \gamma$, and $\eta > \gamma$. The green circles indicate the trajectories of the (extended) magnetic north pole on this surface. Note that they are not exact circles in general. In the bottom panels, I give the corresponding average magnetic fields (blue arrows) and polarization directions (red arrows), which are estimated from the relative locations of the magnetic north pole and the origin on the observed patch as explained earlier. Again, I assume that the photons are all in the E-mode. It is apparent from the middle panels and easily understood from the configurations that the coordinate

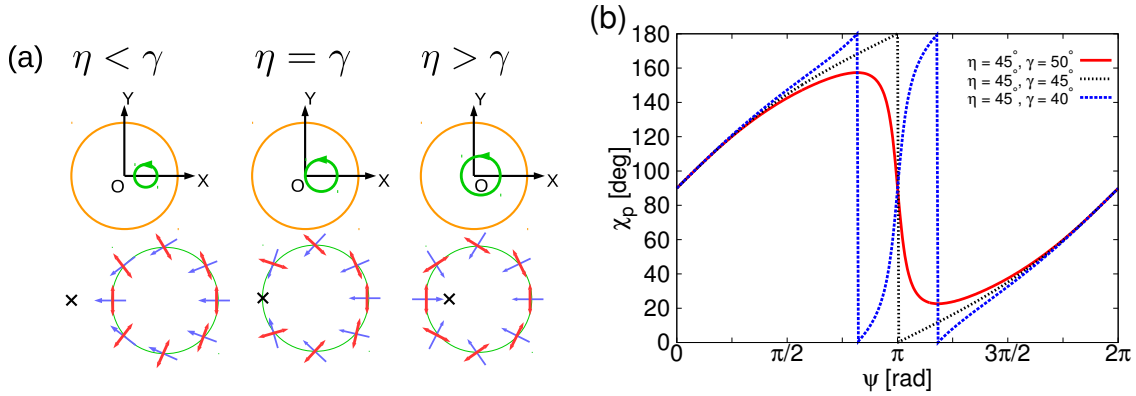

Figure 3.7: (a) Top views of the observed patches (orange circles) on the polarization-limiting surface in the middle row and the polarization directions (red arrows) at different rotational phases in the bottom row for $\eta < \gamma$ (left), $\eta = \gamma$ (center), $\eta > \gamma$ (right). The trajectories of the (extended) magnetic north pole are drawn in green. Blue arrows and black crosses in the bottom panels indicate the directions of the average magnetic fields at the different rotational phases and the position of the coordinate origin, respectively. (b) Polarization angles as functions of the rotational phase. The angle η is fixed to $\eta = 45°$, whereas the angle γ is changed: $\gamma = 40°, 45°, 50°$.

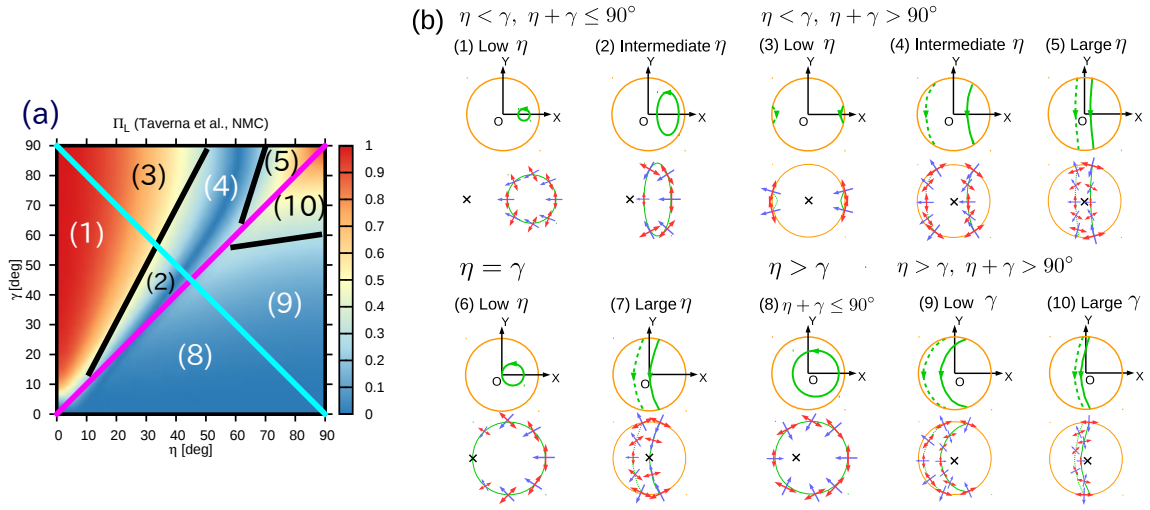

Figure 3.8: (a) Classification of configurations in the $\eta - \gamma$ plane. Ten cases are distinguished. Regions (6) and (7) are the lower ($< 45°$) and upper ($> 45°$) halves of the diagonal line of $\eta = \gamma$, shown in magenta. (b) Trajectories (green) of the (extended) magnetic north pole on the observed patch (orange) of the polarization-limiting surface and the corresponding directions of the average (projected) magnetic field (blue) and the polarization (red) of E-mode. The length of these arrows represents either the amplitude of the magnetic field or the polarization fraction. Note that the phase-averaged polarization fraction is not the average of the phase-resolved polarization fraction but is obtained from the Stokes parameters integrated over the entire rotational phase. The dashed lines are the trajectories of the south pole. The black crosses are the center of the observed patch.

origin is sitting outside, on, and inside the green circle for $\eta < \gamma$, $\eta = \gamma$, and $\eta > \gamma$, respectively. Then, it should be also be clear that the average magnetic fields and polarization angles behave as exhibited in the bottom panels.

In the case of $\eta < \gamma$ (left column), the average magnetic field is always directed leftward, or in the negative X-direction. As a result, the polarization angle is limited in a certain range less than π. This is confirmed in Figure 3.7 (b), in which I show the polarization angles as functions of the rotational phase for three combinations of η and γ. The red solid line for $\eta = 45°$ and $\gamma = 50°$ corresponds to the current case. The polarization angle changes continuously and is indeed limited between 23° and 157°. Note that χ_p changes more rapidly near $\psi = \pi$ as η approaches γ. In fact, it becomes discontinuous at $\eta = \gamma$, as demonstrated by the black dotted line in Figure 3.7 (b). In this case, the polarization angle changes by $|\Delta\chi_p| = 180°$ at $\psi = \pi$, indicating the reverse of the magnetic field direction there. This is indeed confirmed in the bottom center panel of Figure 3.7 (a). As a matter of fact, the average magnetic field vanishes at that point. Although $\eta = \gamma$ is a limit of $\eta < \gamma$, Equation (3.20) gives a discontinuity to the semi-amplitude at $\eta = \gamma$. The semi-amplitude defined in Taverna et al. (2015) is continuous, on the contrary. This is the reason for the apparent discrepancy I mentioned earlier.

When $\eta > \gamma$ is satisfied, in contrast, the direction of the average magnetic field changes continuously again and rotates by 360° in this case, as demonstrated in the bottom right panel of Figure 3.7 (a). As a result, the polarization direction also varies by the same amount continuously. This is confirmed as the blue dotted line in Figure 3.7 (b), although the polarization angle χ_p is given modulo 180° and looks discontinuous at two values of ψ. Note also that even in this case, χ_p changes rapidly around $\psi = \pi$.

Next, I shift my attention to the phase-averaged polarization fraction in the same model. It is calculated according to Equation (3.19) from the Stokes parameters integrated over the entire rotational phase. Note that it is not equal to the average of the phase-resolved polarization fractions. For the understanding of this quantity, it is not sufficient to distinguish the three cases, $\eta < \gamma$, $\eta = \gamma$, and $\eta > \gamma$, as for the semi-amplitude, but it is necessary to divide the cases further according to the values of η and γ. In fact, I distinguish 10 cases, as shown in Figure 3.8 (a). Note that regions (6) and (7) are the lower ($\eta < 45°$) and upper ($\eta > 45°$) halves of the diagonal line of $\eta = \gamma$, shown in magenta. The other diagonal line, $\eta + \gamma = 90°$, is shown in cyan.

I consider each regime in turn, referring to Figure 3.8(b). Region (1) is a regime with $\eta \ll \gamma$ and $\eta + \gamma < 90°$. As shown in the upper left panel of Figure 3.8 (b), the north pole is always inside the observed patch but is not very close to the origin. It does not move very much during a rotation, either. As a result, the average magnetic field is directed in the $-X$ direction, having similar amplitudes. This then leads to the facts that the phase-averaged polarization fraction is very high and that the polarization angle remains $\sim 90°$.

As η approaches γ, I enter region (2). The typical situation is displayed in the second panel from the left in the upper row of Figure 3.8 (b). In this case, the north pole still remains inside the observed patch but moves over a wider region. As a result, the polarization angle changes more widely with the rotational phase, leading

to the cancellation of polarizations. Note that the magnetic field averaged over the observed patch nearly vanishes when the north pole comes close to the origin.

I move on to the regimes still with $\eta < \gamma$ but with $\eta + \gamma > 90°$, i.e., regions (3)-(5). In these cases, not only the north pole but also the south pole comes into sight. If η is small, i.e., region (3), the rotation axis is almost perpendicular to the line of sight, and the typical situation is depicted in the third panel from the left in the upper row. It is evident that the polarization angle is nearly 90° at all phases, irrespective of which pole is visible. Since there is no cancellation in the averaging of the magnetic field over the observed patch, the phase-averaged polarization fraction is high. At intermediate η values in region (4), the variation of χ_p becomes large. In the fourth panel from the left in the upper row of the figure, it changes between $\chi_p \sim 45°$ and $\chi_p \sim 135°$. As a result, the phase-averaged polarization fraction is lowered by the cancellation. At even larger η values in region (5), the polarization angle does not change much again, lingering at $\chi_p \sim 0°$, and the phase-averaged polarization fraction returns to higher values.

I now consider the case of $\eta = \gamma$. In the case of low η values, the leftmost panel in the lower row of Figure 3.8(b) shows the typical situation. The polarization angle changes substantially, and the cancellation leads to low values of the phase-averaged polarization fraction. Although the variation of the polarization angle still exists at large η values, the cancellation is much reduced, and the phase-averaged polarization fraction becomes higher in region (7).

Finally, I look at the regions with $\eta > \gamma$. Region (8) corresponds to the one with $\eta + \gamma \leq 90°$. As demonstrated in the middle panel in the lower row of Figure 3.8 (b), the north pole goes around the origin in the observed patch, and, as a result, the polarization angle also rotates by 360°. The polarization is mostly canceled when averaged over the rotational phase in this case. Regions (9) and (10), where $\eta + \gamma > 90°$, are distinguished by the value of γ. For low values of γ, i.e., region (9), neither the north pole nor the south pole comes close to the origin and the polarizations are large at all phases, while the polarization angle changes by large amounts. The severe cancellation still occurs, and the phase-averaged polarization fraction remains low. At high γ values in region (10), in contrast, the polarization angle still varies by large amounts, but the polarization itself becomes very small when the poles come close to the origin, where $\chi_p \sim 90°$. When averaged over the rotational phase, this leads to higher polarization fractions where the phase-averaged polarization angle is either $\sim 0°$ or 180°, which are, in fact, almost the same.

I now consider the effect of the mode conversion on these phase-averaged quantities. The semi-amplitude is little affected for the case shown in Figure 3.6. This is simply because the polarization angle is not modified at the energy of 300eV in the figure, which is evident in the upper right panel of Figure 3.4. Then, the above discussion is not changed by the mode conversion. The polarization fraction, in contrast, tends to be reduced. It is particularly clear in regions (1) and (3). This is because the O-mode photons that are partially converted from the E-mode cancel the polarization. See the bottom right panel of Figure 3.4, in which the phase-resolved polarization fractions are shown for different photon energies. Since the energy of 300eV assumed in Figure 3.6 is a bit lower than $E \sim E_{\rm ad} \sim 1$keV, the adiabatic mode conversion at the resonance point is partially suppressed, leading to

the mixture of O- and E-mode photons just mentioned.

3.3.2 Phase-resolved Quantities for Various Configurations with Different Magnetic Field Strengths

It should be evident from the results given in the previous section that I need to study more systematically the phase-resolved polarization angle and fraction for various configurations of the rotating magnetized neutron star, different photon energies, and magnetic field strengths, based on the classification given in Figures 3.7 and 3.8. This is particularly true of the mode-conversion effects, since they are sensitive to the photon energy.

I should begin without the mode conversion, however. I can then assume that the photons are all in the E-mode. Although I vary it later, I set the strength of the magnetic field to $B_p = 10^{13}$G here. The parameters on the neutron star are fixed to $R_{\rm NS} = 10$km, $M_{\rm NS} = 1.4M_\odot$, and $T = 0.4$keV, though they are not relevant as long as the mode conversion and general relativistic effects are ignored.

The phase-resolved polarization angles are displayed as a function of the photon energy and rotational phase for 24 combinations of η and γ in Figure 3.9. It is clear at a glance that the results do not actually depend on the photon energy. Small glitches are just artifacts in drawing pictures. As explained in Figure 3.7, these cases can be understood by dividing them into the three regimes: $\eta < \gamma$, $\eta = \gamma$, and $\eta > \gamma$. In the first case, i.e., the upper left panels in Figure 3.9, the polarization angle oscillates around $\chi_p = 90^\circ$. It becomes $\chi_p = 90^\circ$ exactly when the rotational phase is 0, π, and 2π. The color maps in this case are hence rather featureless. In the case of $\eta = \gamma$, in contrast, the polarization angle changes by 180° during a single rotation. Note that the polarization angle has the mod (π) nature and that $\chi_p = 0^\circ$ and $\chi_p = 180^\circ$ are equivalent. Finally, for $\eta > \gamma$, the polarization angle varies by more than 180° in general (see cases (8), (9), and (10) in Figure 3.8), and, as a result, the polarization is mostly canceled, as is evident from Figure 3.8 (a). The color maps in this case (lower right panels in Figure 3.9) are characterized by the two horizontal bands shown in, e.g., green sharp boundaries. Note again that $\chi_p = 0^\circ$ and $\chi_p = 180^\circ$ are equivalent, which are shown in green. The polarization angle becomes 90° exactly at $\psi = 0$, π, and 2π.

The phase-resolved polarization fraction is mainly determined by the position of the (extended) north or south pole in the observed patch on the polarization-limiting surface. Various cases are summarized in Figure 3.10. As the photon energy increases, the radius of the polarization-limiting surface gets larger, and, as a result, the pole tends to be located outside the observed patch longer, which then leads to higher polarization fractions. During a single rotation, in contrast, the pole comes closest to the origin at the rotational phase of $\psi = \pi$, and the polarization fraction becomes minimum at that point. Note that in the case of $\gamma = 0^\circ$, which is an example of case (8) given in Figure 3.8 (b), the polarization fraction is not changed by rotation, since the curve drawn by the pole is a circle with its center located at the origin. For $\eta = \gamma$, in contrast, the pole comes to the origin at $\psi = \pi$, and the polarization fraction vanishes completely by the cancellation.

Having understood the variety of the polarization angle and fraction as functions

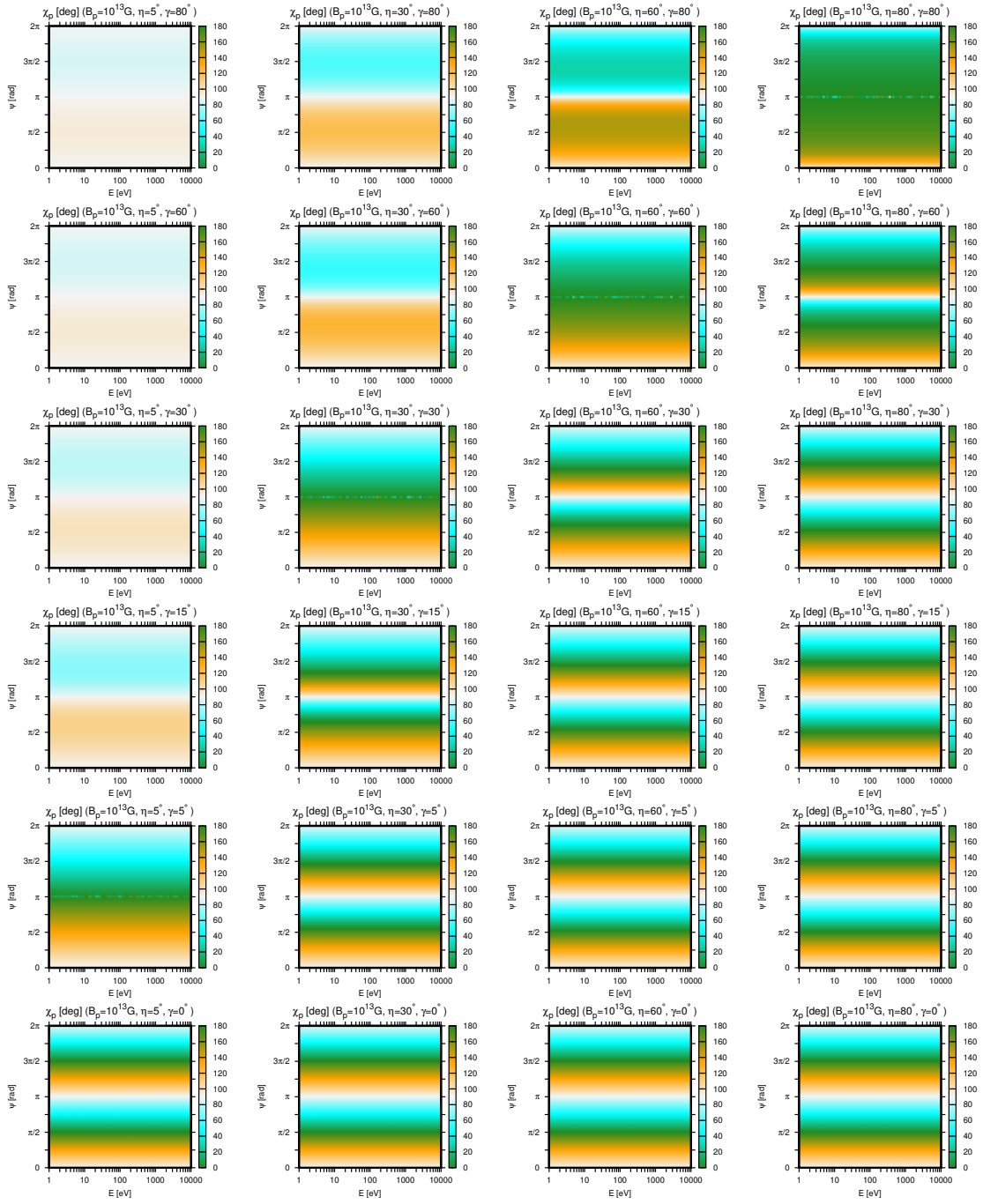

Figure 3.9: Phase-resolved polarization angles for different combinations of η and γ. The mode conversion is neglected in this figure. The magnetic field strength is fixed to $B_p = 10^{13}$G.

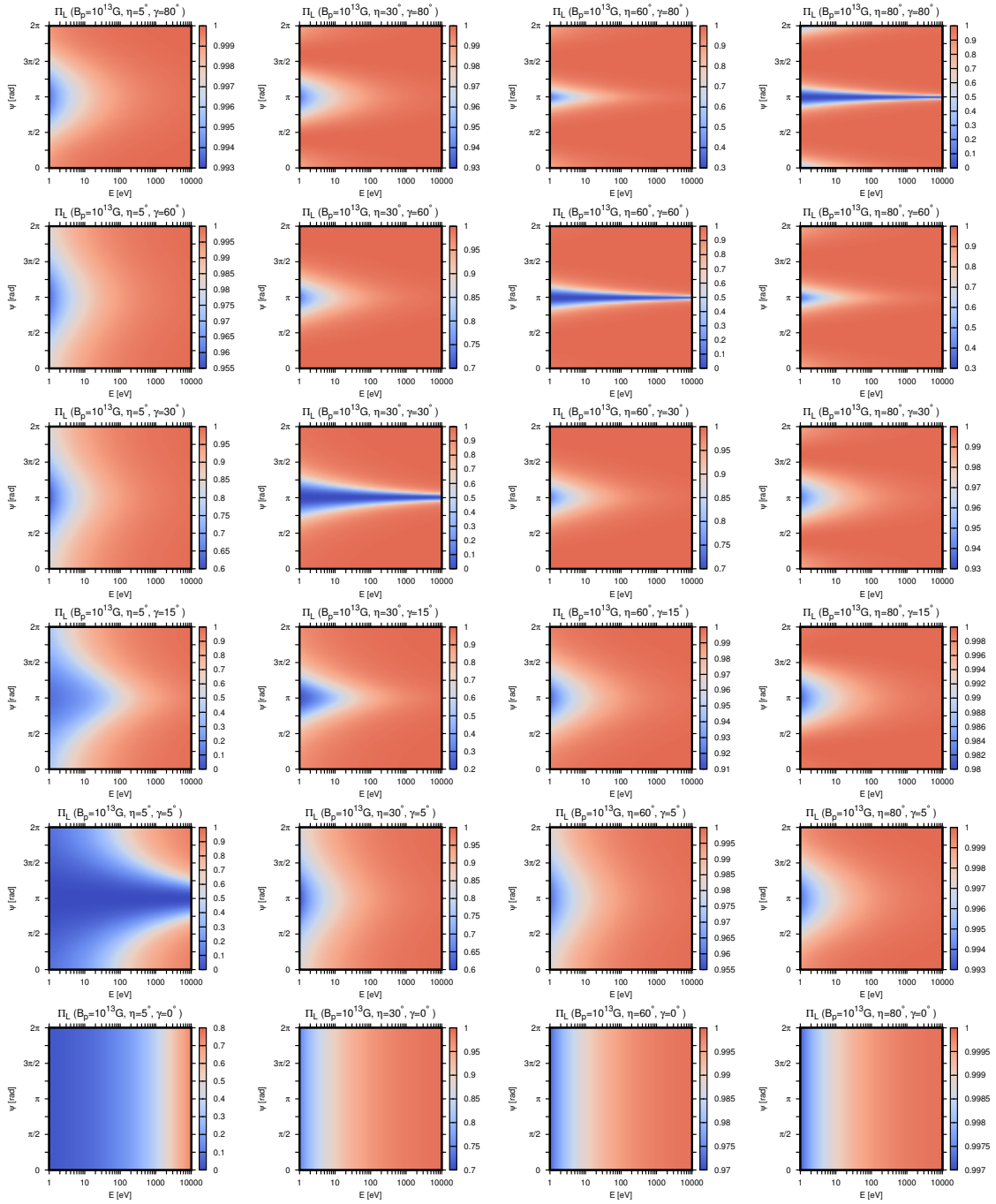

Figure 3.10: Same as Figure 3.9 but for the phase-resolved polarization fraction. Note the color scale in each panel.

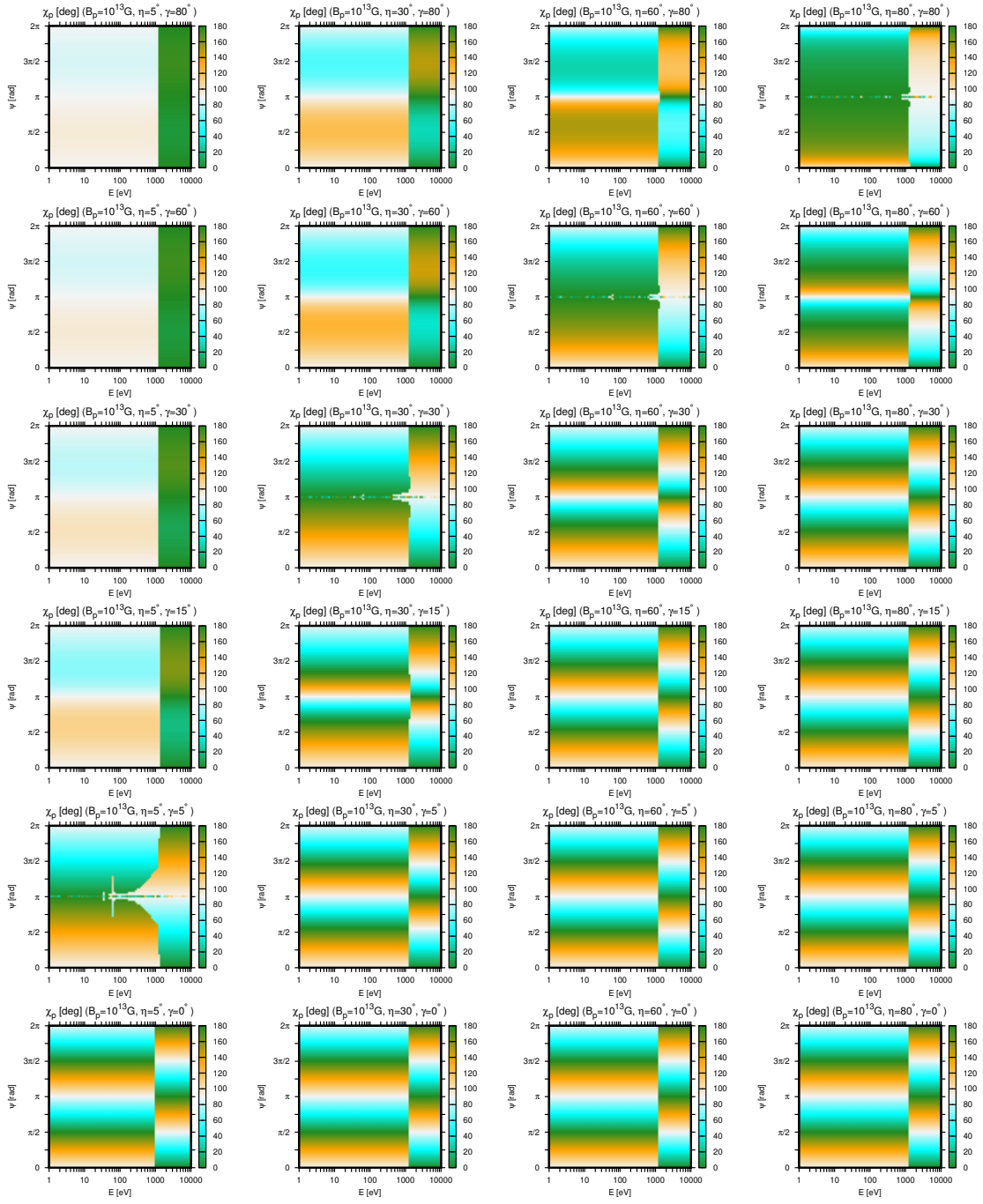

Figure 3.11: Same as Figure 3.9 but with the mode conversion taken into account.

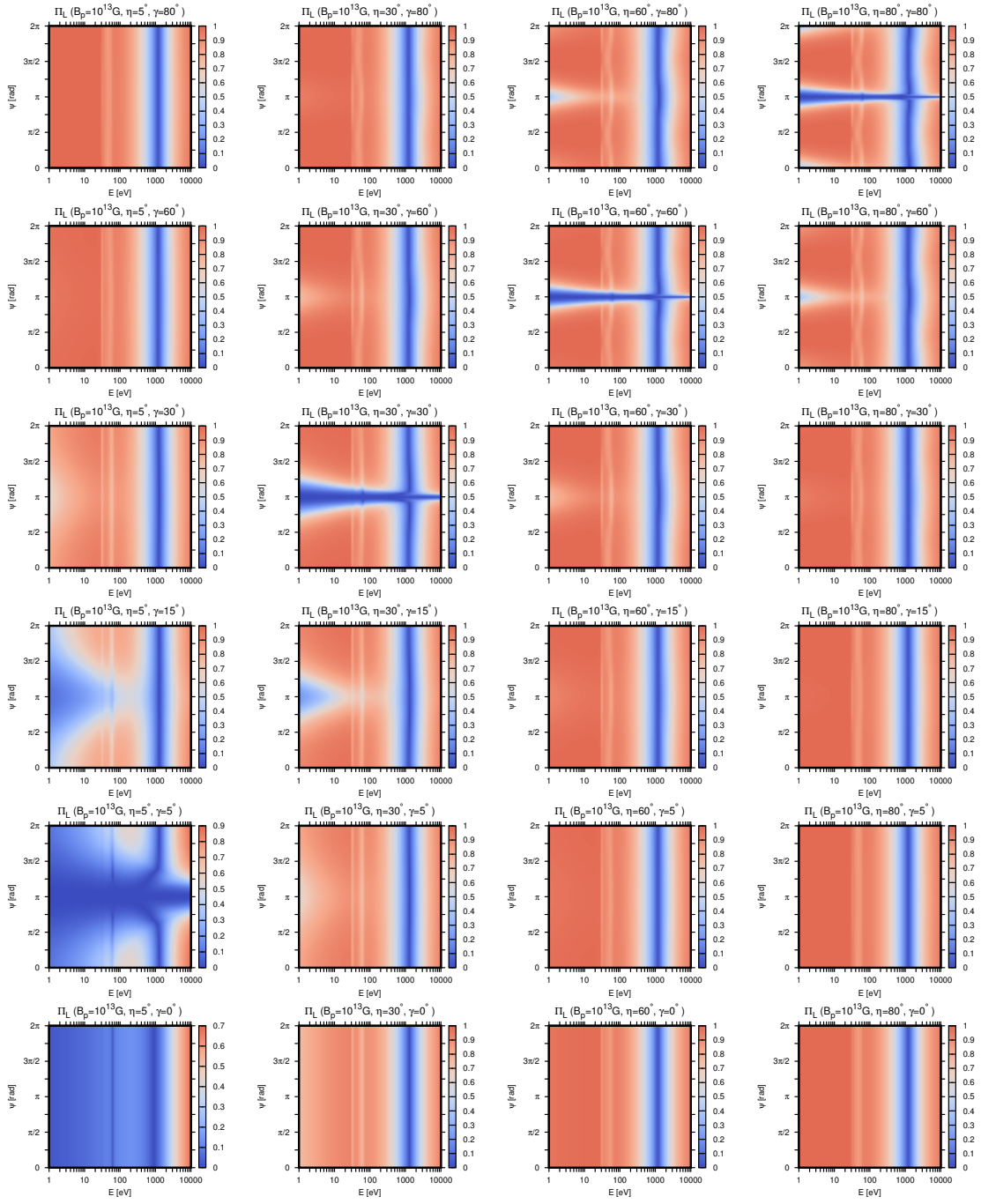

Figure 3.12: Same as Figure 3.11 but for the polarization fraction.

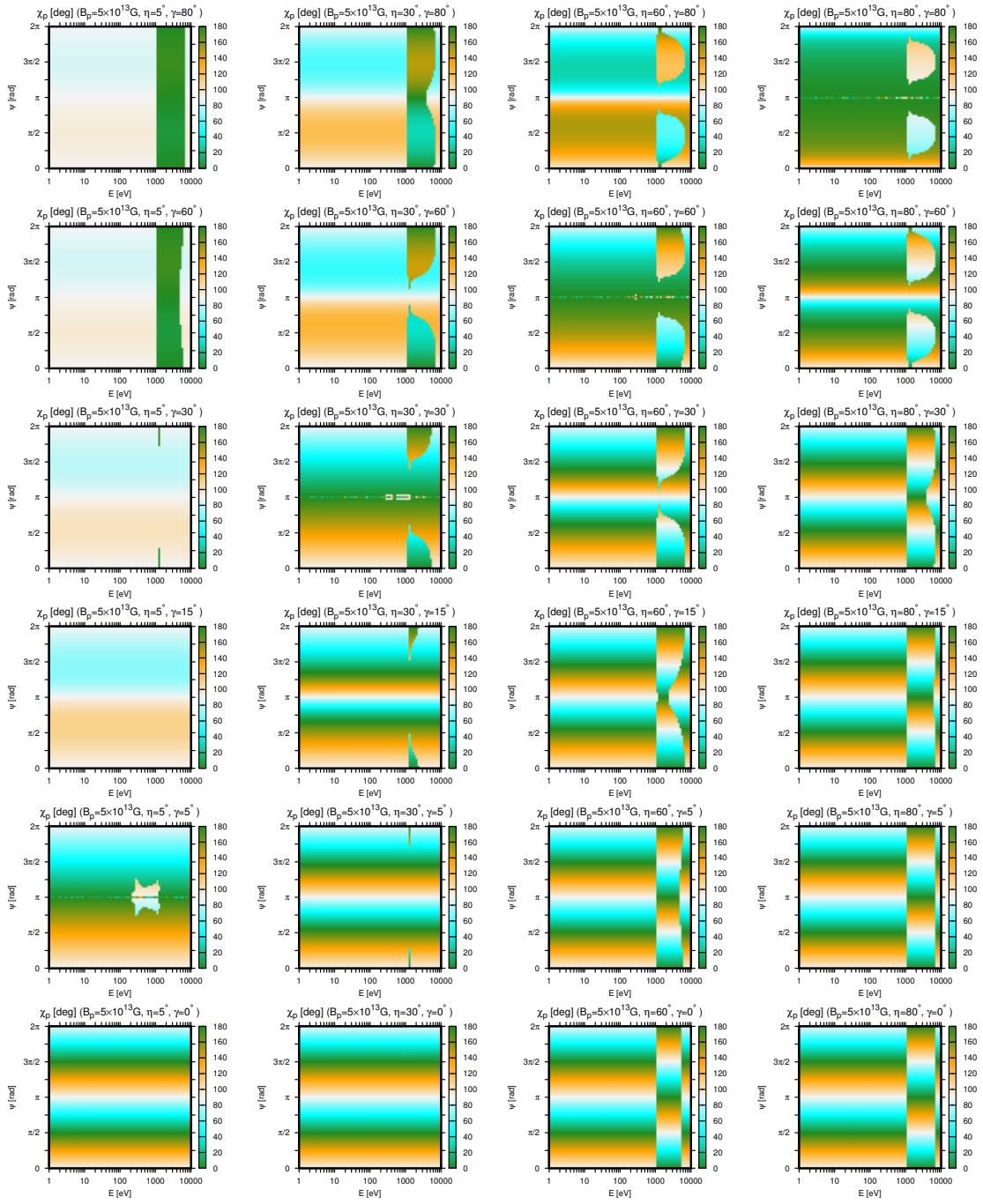

Figure 3.13: Same as Figure 3.11 but for $B_p = 5 \times 10^{13}$G.

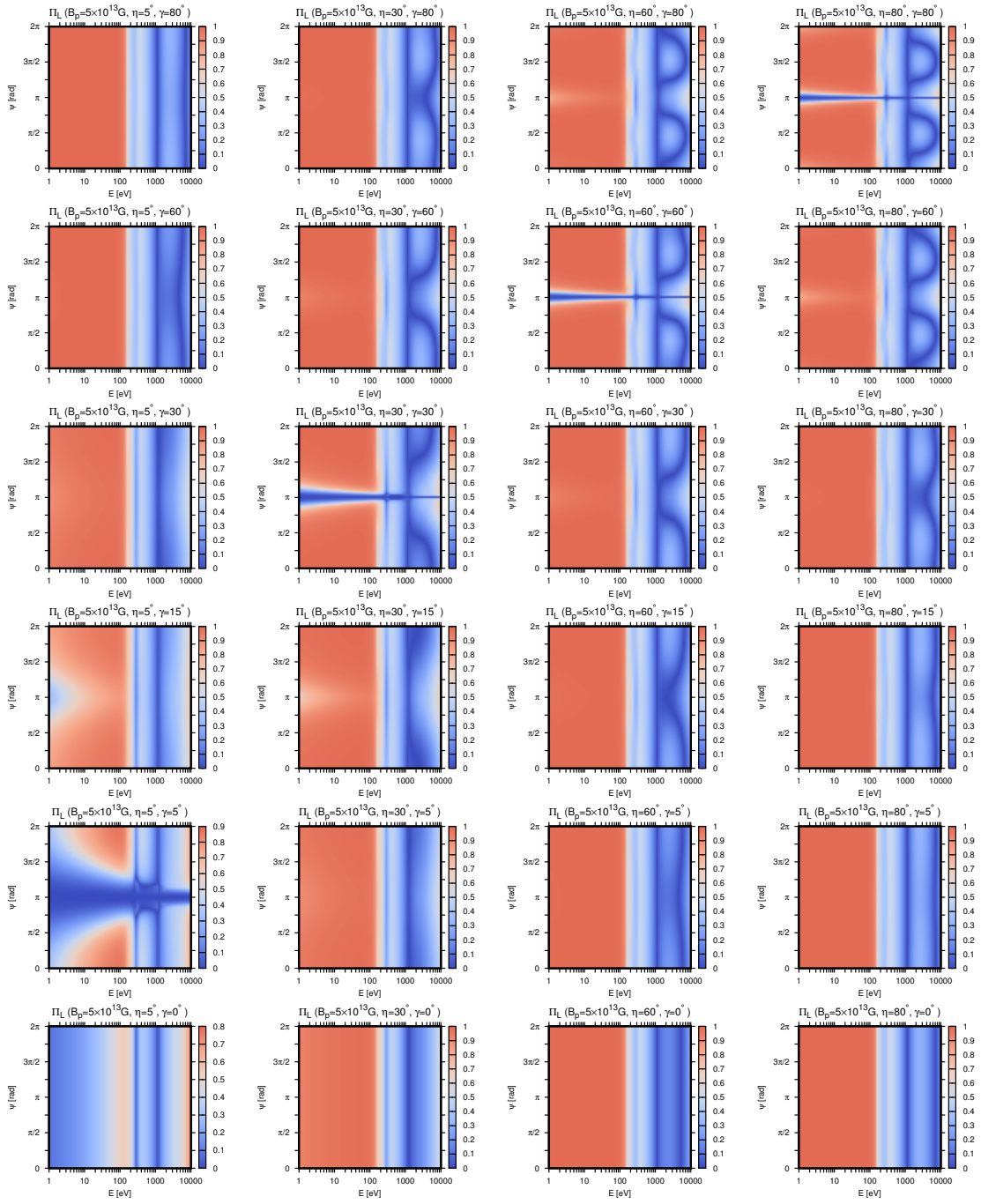

Figure 3.14: Same as Figure 3.12 but for $B_p = 5 \times 10^{13}$G.

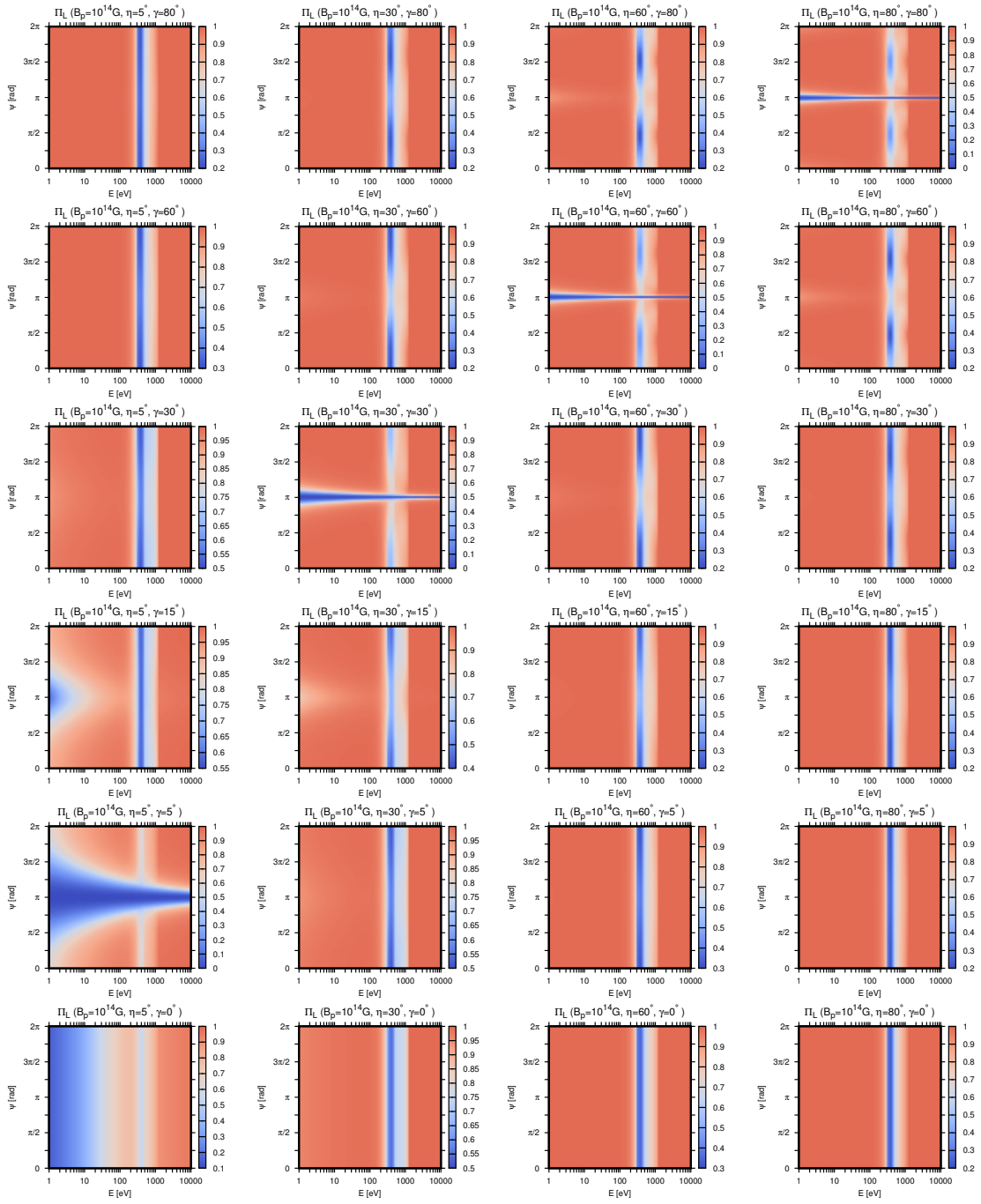

Figure 3.15: Same as Figure 3.12 but for $B_p = 10^{14}$G.

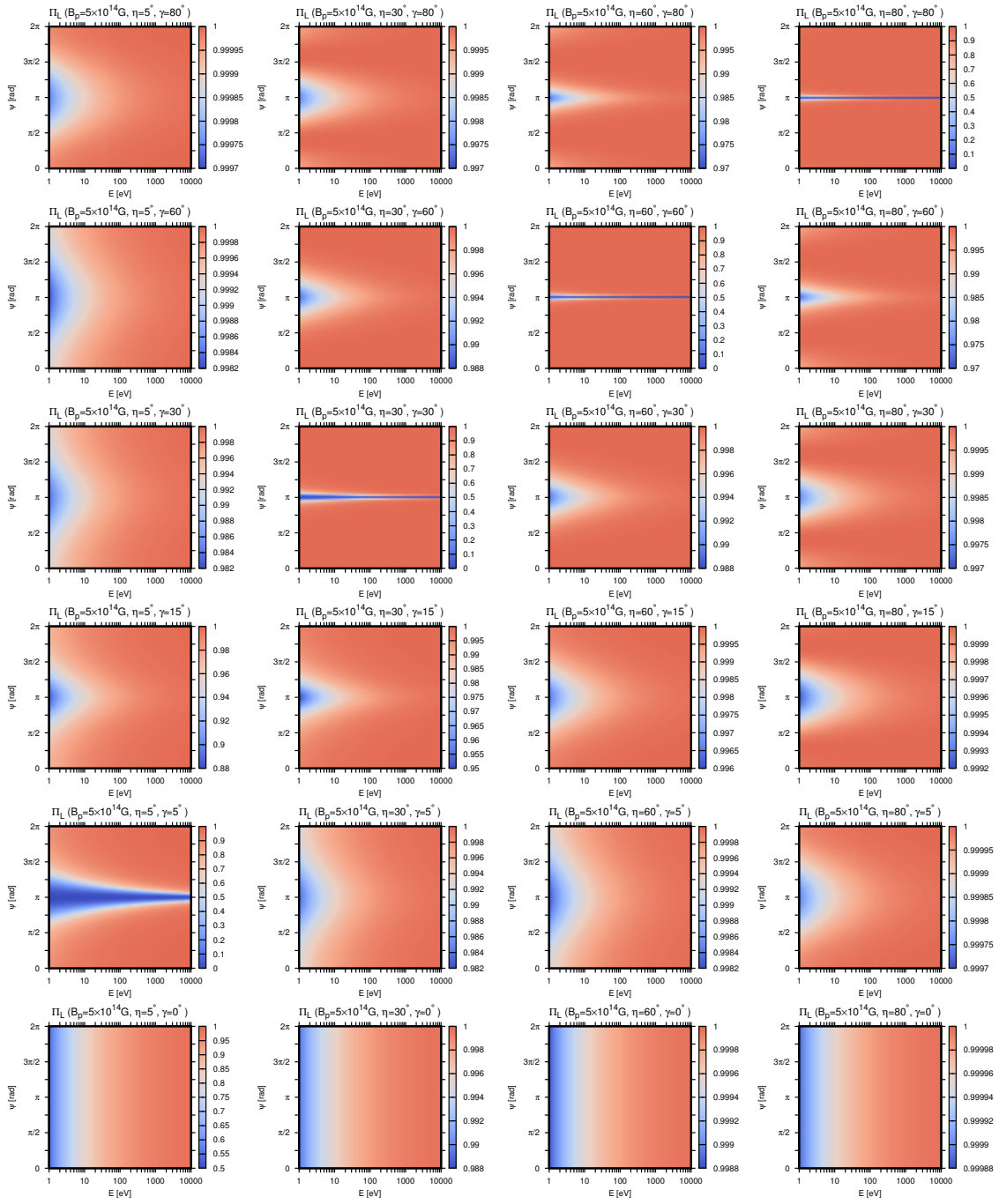

Figure 3.16: Same as Figure 3.12 but for $B_p = 5 \times 10^{14}$G.

of the rotational phase without the mode conversion, I now look into how the mode conversion modifies them. In so doing, I also change the magnetic field strength. The results are exhibited for $B_p = 10^{13}, 5 \times 10^{13}, 10^{14}$, and 5×10^{14}G in Figures 3.11-3.16, which I consider in turn in the following.

The phase-resolved polarization angles and fractions shown for $B_p = 10^{13}$G in Figures 3.11 and 3.12 are the mode-conversion counterparts of those given in Figures 3.9 and 3.10 without the mode conversion (note that the color scales are different between Figures 3.10 and 3.12). At $E \gtrsim E_{\rm ad} \simeq 1$keV, the mode conversion occurs adiabatically, and the O-mode photon becomes dominant. Then the polarization angle changes by 90°. Note again that $\chi_p = 0°$ and $\chi_p = 180°$ are the same from the mod(π) nature of the polarization angle. In the case of $\eta = \gamma$, the 90° change of the polarization angle occurs at much lower energies ($E \ll 1$keV) for $\psi \sim \pi$, which is particularly true of $\eta = \gamma = 5°$. This is because the magnetic field is nearly aligned with the propagation direction of photons ($\theta_B \sim 0$), and $E_{\rm ad}$ becomes smaller (see Equation (3.1)). Note also that the influences of the cyclotron energies of the protons are also apparent at $\lesssim 100$eV.

The polarization fraction is reduced by the mode conversion in general if it occurs at $E \sim E_{\rm ad} \sim 1$keV and both the original E- and converted O-modes exist in some proportion, leading to partial cancellations. Note, however, that $E_{\rm ad}$ is in fact a function of the photon energy and is lowered remarkably at some energies. This is particularly the case for the cyclotron energies of the protons, as already mentioned earlier (see Figure 3.17 (a)). At these energies, the photon is adiabatically converted from E-mode to O-mode completely. Since the cyclotron energy depends on the magnetic field strength, it is not constant on the neutron star surface. As a result, only those photons that have energies close to the local cyclotron energy and are propagating in certain directions are mode-converted and mixed with unconverted photons originating from different portions of the observed patch, which leads to the reduction of the polarization fraction as strips at $E \lesssim 100$eV. This issue will be considered more in detail in the following.

The mode conversion occurs adiabatically when $E \gtrsim E_{\rm ad} \propto (\tan\theta_B |1 - u_i|)^{2/3}$, with $u_i = (E_{ci}/E)^2 \propto (B/E)^2$ (see Equation (3.1)) and θ_B being the angle between the photon momentum and the magnetic field. Panel (a) schematically shows the dependence of $E_{\rm ad}$ on the magnetic field strength B (green and blue dashed lines). It is seen that there is a region $B_{\rm MIN} < B < B_{\rm MAX}$, in which $E > E_{\rm ad}$ is satisfied and the mode conversion occurs for a given θ_B. Note that θ_B is fixed to a certain nonzero value in drawing the dashed lines in the panel. Here $B_{\rm ci}$ is the magnetic field strength at which the cyclotron energy is equal to the photon energy E and the adiabatic energy vanishes. This range is in fact dependent on θ_B, the angle between the photon momentum and the magnetic field, through the adiabatic energy. It is found from the companion of the two dashed lines that the range gets wider as the θ_B becomes smaller. The adiabatic mode conversion occurs in wider ranges in B, as the magnetic field tends to be aligned with the Z-axis.

The polarization fraction can be then understood from panels (b) and (c) in Figure 3.17, in which I show the areas where the mode-converted O-mode photons are emitted for different photon energies: 32eV $\le E \le$ 34eV (red), 39eV $\le E \le$ 41eV (green), 49eV $\le E \le$ 51eV (blue), and 59eV $\le E \le$ 61eV (purple). It should

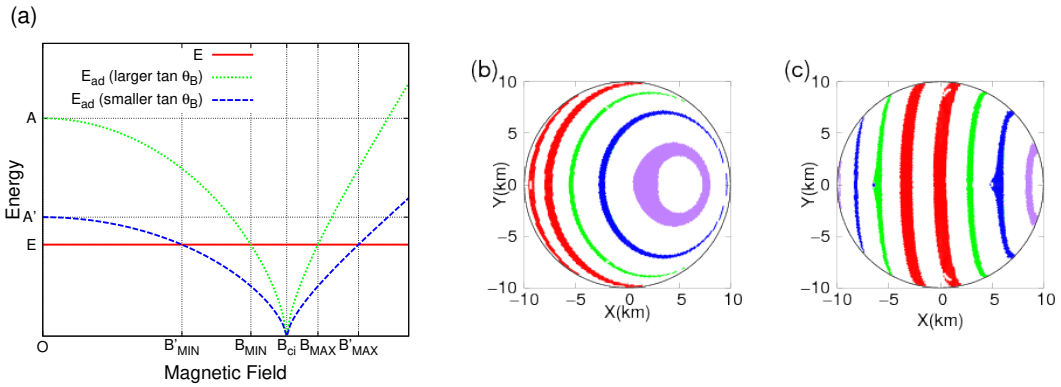

Figure 3.17: (a) Schematic figure of the adiabatic energy $E_{\rm ad}$ as a function of the magnetic field strength B for a given photon energy E. The green and blue dashed lines correspond to larger and smaller values of the angle between the photon momentum and the magnetic field, θ_B. In the panel, A and A' are the corresponding y-intercepts. Note that θ_B is fixed in drawing these lines. The mode conversion occurs adiabatically when $B_{\rm MIN} < B < B_{\rm MAX}$ is satisfied, the condition corresponding to $E > E_{\rm ad}$. The adiabatic energy $E_{\rm ad}$ vanishes at B_{ci}. Panels (b) and (c) exhibit the regions where the mode conversion occurs for the photon energies of $E \simeq 33$eV (red), 40eV (green), 50eV (blue), and 60eV (purple), with different colors on the neutron star surface toward the observer, which is projected onto the X-Y plane. In the two panels, the configurations of the neutron star are different: (b) $\eta = 0°,\ \gamma = 30°$ and (c) $\eta = 0°,\ \gamma = 80°$.

be mentioned here that there appear to be multiple strips with the same color in some cases; in fact, it may change with the rotational phase. In the two panels, I assume different configurations of the neutron star: (b) $\eta = 0°,\ \gamma = 30°$ and (c) $\eta = 0°,\ \gamma = 80°$. The dipole magnetic field strength is set to $B_p = 10^{13}$G for both cases.

The case in panel (b) is representative of the configurations in which the (projected) magnetic pole is near the origin of the X-Y plane. It is found that the red and purple areas are larger on the projected surface than the green and blue ones. This leads to the fact that the polarization fraction is lower for $E \simeq 30$ and 60 eV than for other photon energies, and two distinct strips appear in the corresponding panel in Figure 3.12. In contrast, panel (c) is a representative case, in which the magnetic pole is far from the origin and shows that each colored region has roughly the same area. As a result, the polarization fraction decreases almost uniformly for these photon energies, producing a single broad strip in the plot of the polarization fraction.

In Figures 3.13 and 3.14, I present the results for one of the higher field strengths, $B_p = 5\times10^{13}$G. It is apparent from Figure 3.13 that the behaviors of the polarization angle are qualitatively different in some configurations from those for $B_p = 10^{13}$G given in Figure 3.11. In fact, in addition to the familiar result obtained for $\eta = 80°$ and $\gamma = 5°$, I find a case, e.g., with $\eta = 5°$ and $\gamma = 15°$, in which nothing occurs at all. For $\eta = 60°$ and $\gamma = 30°$ or $\eta = \gamma = 80°$, the polarization angle changes only at some rotational phases; the result for $\eta = \gamma = 5°$ has yet another pattern

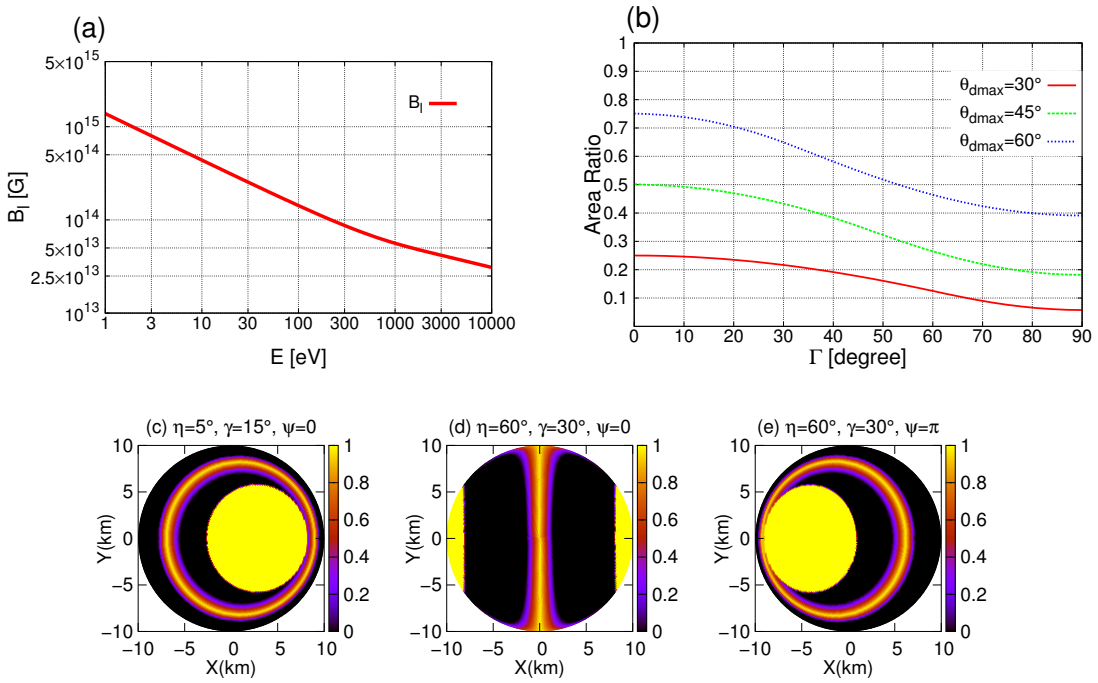

Figure 3.18: (a) Plot of B_l as a function of the photon energy E. (b) Fraction of the projected area with $B > B_l$ as a function of Γ, the angle between the line of sight and the magnetic axis for three values of $\theta_{d\max}$: $\theta_{d\max} = 30°$ (red solid line), $\theta_{d\max} = 45°$ (green dashed line), and $\theta_{d\max} = 60°$ (blue dotted line). (c)-(e) Snapshots of the fraction of the E-mode photon at $E = 2$keV for three configurations: (c) $\eta = 5°$, $\gamma = 15°$, $\psi = 0$, (d) $\eta = 30°$, $\gamma = 60°$, $\psi = 0$; and (e) $\eta = 30°$, $\gamma = 60°$, $\psi = \pi$.

different from those in the above cases. The reason for all these phenomena is that the condition given in Equation (3.9) is no longer satisfied at all rotational phases, and instead the condition in Equation (3.10) holds at some phases. In the latter case, the mode conversion occurs inside the O-mode photosphere, and its effect is mainly to shift the photosphere of the E-mode photons outward.

The above explanations are substantiated in the following. I plot the values of B_l as a function of the photon energy in panel (a) of Figure 3.18, where the surface temperature is set to $kT = 0.4$keV and $f = 1$ is assumed. Here B_l decreases monotonically and the condition $B < B_l$ is satisfied everywhere on the neutron star surface at $E \lesssim 1$keV for $B_p = 5 \times 10^{13}$G. At higher photon energies, this is no longer the case. In fact, since $B_l < B_p$, the condition is violated near the magnetic pole, and the mode conversion occurs inside the O-mode photosphere. If the area with $B > B_l$ near the magnetic pole projected on the X-Y plane is larger than the region with $B < B_l$, the E-mode is dominant and the polarization angle is unchanged from those of low-energy photons.

In the case of the dipole magnetic field, the condition of $B > B_l$ is equivalent to $\theta_d < \theta_{d\max}$ for the magnetic colatitude θ_d. Then, the ratio between the (projected) area of the region satisfying $B > B_l$ and the (projected) star surface is a function of $\theta_{d\max}$ and Γ, the angle between the magnetic axis and the Z-axis. It is plotted as a function of the latter, with the former being fixed in panel (b) of Figure 3.18. I

choose three different values of $\theta_{d\max}$: $\theta_{d\max} = 30°$ (red), 45° (green), and 60° (blue). Note that $\theta_{d\max}$ is a function of the photon energy and is larger for higher energies, as can be understood from panel (a) in Figure 3.18.

I now revisit the results in Figure 3.13. In the case of $\eta = 5°$ and $\gamma = 15°$, the north pole, which has the strongest magnetic field and violates the condition given in Equation (3.9) for $E \gtrsim 2$keV, stays close to the origin of the X-Y plane: Γ varies between 10° and 20°. At $E = 2$keV, for example, the region, in which Equation (3.9) is violated, corresponds to $\theta_{d\max} = 26°$. This area alone is not sufficient to make the E-mode photons dominant, though. There is another region that predominantly emits the E-mode photons (the bright ring in panel (c) of Figure 3.18). This happens not because of the violation of the condition in Equation (3.9) but because of large values of $\tan\theta_B$, which narrows the region of $E > E_{\rm ad}$, where the mode conversion occurs adiabatically. The projected areas of both regions do not change much during the rotational period. As a result, the original E-mode is dominant at all rotational phases.

For $\eta = 60°$ and $\gamma = 30°$, in contrast, the rotational phase is important. The angle between the magnetic and Z-axis, Γ, ranges from 30° to 90°, and the north pole comes close to the origin only at $\psi \sim \pi$ (see panels (d) and (e) in the same figure). Then, the E-mode photon is dominant at $30° \leq \Gamma \lesssim 42°$ or, equivalently, at $3\pi/4 < \psi < 5\pi/4$ (panel (e)).

In the case of $\eta = \gamma = 80°$, the condition $B < B_l$ is not fulfilled at $\psi \sim 0$ and 2π ($\Gamma \sim 20°$), where the south pole is located near the origin, as well as at $\psi \sim \pi$ ($\Gamma \sim 0°$), where the north pole faces the observer. At these phases, the mode conversion occurs inside the O-mode photosphere, and the polarization angle is unchanged.

In all of the above cases, Equation (3.9) tends to be violated in wider regions on the neutron star surface for higher photon energies: $\theta_{d\max} = 39°$ ($E = 3$keV), $\theta_{d\max} = 52°$ ($E = 5$keV), and $\theta_{d\max} = 65°$ ($E = 10$keV). Then, the values of $\tan\theta_B$ become smaller for the higher photon energies, narrowing the range of $E < E_{\rm ad}$ (see Figure 3.17 (a)). This leads to narrower bright rings in panels (c)-(e) of Figure 3.18.

Finally, I shift my attention to the case of $\eta = \gamma = 5°$, which yields a distinct pattern in the polarization angle given in Figure 3.13. In fact, the jump of the polarization angle occurs at $\psi \sim \pi$ in the range of $100 \lesssim E \lesssim 1000$eV. This energy range corresponds to the vicinity of the cyclotron energy again. In contrast, the rotational phase $\psi \sim \pi$ is the phase at which $\tan\theta_B$ takes small values. At $E \gtrsim 2$keV, Equation (3.9) is violated near the magnetic pole, which always faces the observer in this case, and the mode conversion occurs inside the O-mode photosphere.

The polarization fractions for $B_p = 5 \times 10^{13}$G are displayed in Figure 3.14, with the mode conversion being taken into account. This should be compared with Figure 3.12. Since the polarization-limiting radius is larger than that for $B_p = 10^{13}$G (see Equation (3.12)), the magnetic north or south pole tends to be located outside the observed patch, and, as a result, the polarization fraction should be higher as long as the mode conversion is ignored. This is true at low energies, $E \lesssim 100$eV, where no conversion is expected from the beginning. The polarization fraction is lowered either when the partial conversion occurs nonadiabatically or when the observer sees not only the region in which the mode conversion occurs outside the photospheres

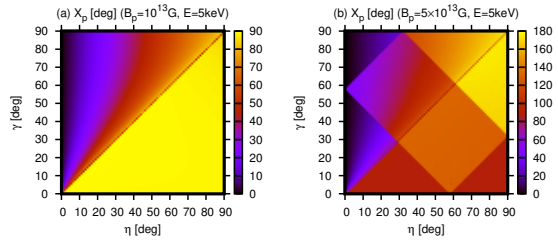

Figure 3.19: Semi-amplitudes of the polarization angle for two magnetic field strengths: (a) $B_p = 10^{13}$G and (b) $B_p = 5 \times 10^{13}$G. The photon energy is set to $E = 5$keV.

of the two modes but also the region in which the mode conversion takes place between the two photospheres. The former occurs at $E \sim E_{\rm ad}$, while the latter is evident near the boundary between the 90° change and the unchanging regimes of the polarization angle. The cyclotron energy of the proton in this case varies continuously from ~ 300eV at the magnetic pole down to ~ 150eV on the equator. In most cases, its effect is visible at $E \sim 300$eV. This is because for higher cyclotron energies, the adiabatic condition Equation (3.1) is satisfied for wider ranges of θ_B, the angle between the magnetic field and photon momentum. This leads to the single vertical blue strip at $E \sim 300$eV in Figure 3.14.

The polarization fractions for $B_p = 10^{14}$G are presented in Figure 3.15. Although not shown, the polarization angles are essentially the same as those given in Figure 3.9, with the mode conversion being ignored entirely. This is because the condition given in Equation (3.9) is not satisfied at $E \gtrsim E_{\rm ad} \sim 1$keV in this case. This does not imply that the mode conversion occurs outside the O-mode photosphere in any region. In fact, the polarization fraction is reduced at the cyclotron energies of the proton, which range from ~ 300eV on the equator to 600eV at the pole in the current case. It is added that the polarization fraction is increased as a whole owing to the larger polarization-limiting radius.

As shown in Figure 3.16, if I raise the field strength further to $B_p = 5 \times 10^{14}$G, then there remains no region that satisfies both $E \gtrsim E_{\rm ad}$ and Equation (3.9) simultaneously, and the mode conversion occurs inside the O-mode photosphere even at the cyclotron energies of the proton. As a result, the polarization angle and fraction are identical to those in Figures 3.9 and 3.10 except for an overall increase due to the larger size of the polarization-limiting surface. Note again that the E-mode photons emerging from the E-mode photosphere are affected by the mode conversion in the cases where $B > B_l$ is satisfied.

I now consider the semi-amplitude defined in Equation (3.20) for the three magnetic fields: $B_p = 10^{13}$, 5×10^{13} and 10^{14}G. The results are shown in Figure 3.19 for the first two cases: (a) $B_p = 10^{13}$G and (b) $B_p = 5 \times 10^{13}$G. The photon energy is set to $E = 5$keV for both. In the first case, the features in the semi-amplitude are almost the same as those in Figure 3.6 (a), in which the mode conversion is neglected. This is because the mode conversion occurs for all combinations of η and γ at this photon energy, and, as a result, the O-mode is always dominant. In the case of $B_p = 10^{14}$G, in contrast, the mode conversion occurs inside the O-mode photosphere

and the E-mode always prevails, since Equation (3.9) is not satisfied. Although the polarization angles are different by 90°, the semi-amplitude for $B_p = 10^{14}$G is almost identical to that for $B_p = 10^{13}$G and hence is not shown in the figure.

In contrast, the right panel for case (b) exhibits qualitatively different features with some discontinuous changes in the parameter space of η and γ. The reason for these discontinuities is, of course, the mode conversion. In fact, the polarization angle changes by 90° when the dominant mode is changed from E-mode to O-mode or vice versa. Such a change takes place twice or four times during a single rotation, as is understood from Figure 3.13. The semi-amplitude, which is the total variation of the polarization angle divided by four, may hence change by 45° or 90° at the discontinuities.

3.3.3 Phase-averaged Quantities for Different configurations, Field Strengths and Photon Energies

Turning to the phase-averaged quantities, I show in Figure 3.20 the four representative patterns of the polarization angle and fraction in the $\eta - \gamma$ plane: (a) $B_p = 10^{13}$G, $E = 5$keV with no mode conversion; (b) $B_p = 10^{13}$G, $E = 5$keV; (c) $B_p = 5 \times 10^{13}$G, $E = 5$keV; and (d) $B_p = 10^{14}$G, $E = 5$keV. Note again that the phase-averaged quantities are calculated not as the averages of the corresponding phase-resolved quantities but from the integral of the Stokes parameters over the entire rotational phase.

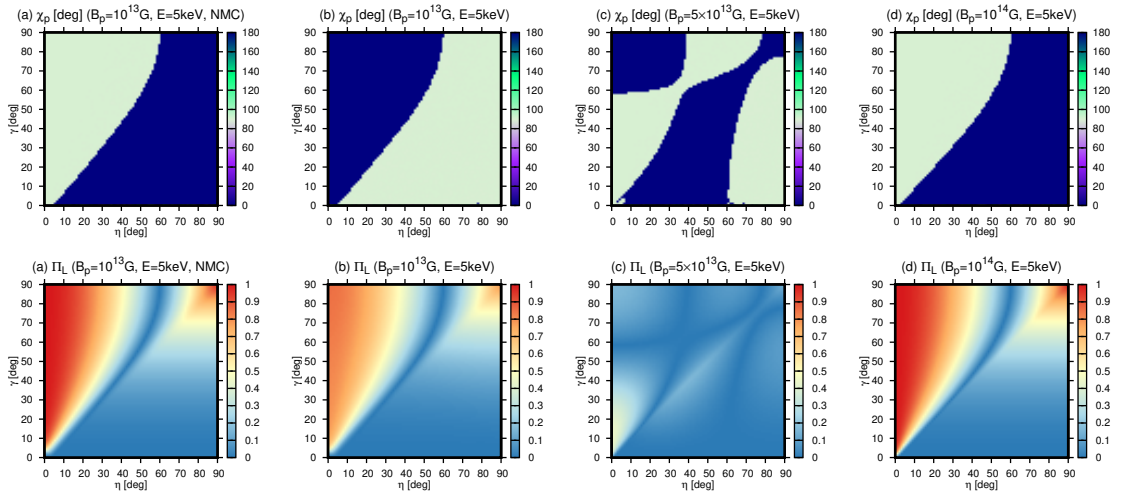

Figure 3.20: Phase-averaged polarization angles χ_p (upper panels) and fractions Π_L (lower panels) for four different cases. The photon energy is fixed to $E = 5$keV. The magnetic field strengths are assumed to be $B_p = 10^{13}$G in (a) and (b) and $B_p = 5 \times 10^{13}$ and 10^{14}G for (c) and (d), respectively. The mode conversion is considered for all cases except case (a).

It is seen from the upper panels that the phase-averaged polarization angle is either $\chi_p \simeq 0°$, 90°, or 180°, shown in dark violet, light green, or dark violet, respectively, and that the parameter space is divided into the regions either with

$\chi_p \approx 90^\circ$ or with $\chi_p \approx 0,\ 180^\circ$. Note that the values of $\chi_p \simeq 0^\circ$ and 180° are equal to each other because of the mod(π) nature of the polarization angle and that they are shown in the same color.

If the mode conversion is neglected (case (a)), the phase-averaged polarization angle can be understood from Figure 3.8 (b). In regions (1) and (3) in the figure, the polarization is roughly directed toward the X-axis at each rotational period, and $\chi_p \simeq 90^\circ$ is hence obtained. In regions (5)-(10), the average magnetic fields are oriented in the Y-axis more often than not, and, as a result, the polarization angle changes by 90°. In the boundary layer, i.e., regions (2) and (4), the polarization angle is still $\chi_p \approx 0^\circ$ or 180°, but the polarization itself is suppressed. See the corresponding bottom panel.

It is apparent from Figure 3.20 that case (d), with the highest magnetic field strength, $B_p = 10^{14}$G, is quite similar to case (a). This is the case not only for the polarization angle but also for the polarization fraction and is simply because the mode conversion occurs in the O-mode photosphere in case (d), either, which is understood from Figures 3.15 and 3.18. For the lower magnetic fields, $B_p = 10^{13}$ and 5×10^{13}G, assumed in cases (b) and (c), the mode conversion is important. In case (b), photons are mostly in the O-mode at $E = 5$keV, as seen in Figures 3.11 and 3.12. As a consequence, the phase-averaged polarization angles are changed by 90° from those of case (a). There are some E-mode photons emitted, though, from the region that satisfies $E < E_{\rm ad}$ because of large values of $\tan\theta_B$ in Equation (3.1). The polarization is partially canceled then, and the phase-averaged polarization fraction is lowered a bit in regions (1), (3), (5), (7), and (10).

In case (c) with $B_p = 5 \times 10^{13}$G, in contrast, the observer will see not only the region in which the mode conversion occurs outside the photospheres of the two modes but also the region in which the mode conversion takes place between the two photospheres. The E-mode photons come from the latter region, at which Equation (3.9) is not satisfied. It extends from the magnetic pole and covers approximately half the neutron star surface. The O-mode photons are originated at low magnetic latitudes, in contrast. As a result, the numbers of E-mode and O-mode photons are nearly equal in this case, and the phase-averaged polarization fractions are severely reduced. The phase-averaged polarization angles have different features in this case. In some parameter regions, the polarization angle is seen to change by 90° because of the mode conversion.

I have so far considered a single photon energy. I expect, however, that the results depend strongly on the photon energy. This is confirmed in Figure 3.21, in which I show the phase-averaged polarization angle and fraction for $B_p = 5 \times 10^{13}$G but at $E = 1$keV and $E = 10$keV this time. It is indeed found that the phase-averaged polarization fraction is smaller at $E = 1$keV than at $E = 5$keV. This is because $E = 1$keV is much closer to the adiabatic energy $E_{\rm ad}$, nearly half the E-mode photons are converted to O-mode, and the polarization is almost canceled.

At $E = 10$keV, in contrast, the mode conversion occurs inside the O-mode photosphere in some regions because of the violation of Equation (3.9) in this case (see Figures 3.13 and 3.18 (a)). The cancellation between the two modes is less severe than at $E = 5$keV, though. The phase-averaged polarization angles for different photon energies change by 90° at different combinations of η and γ. Such

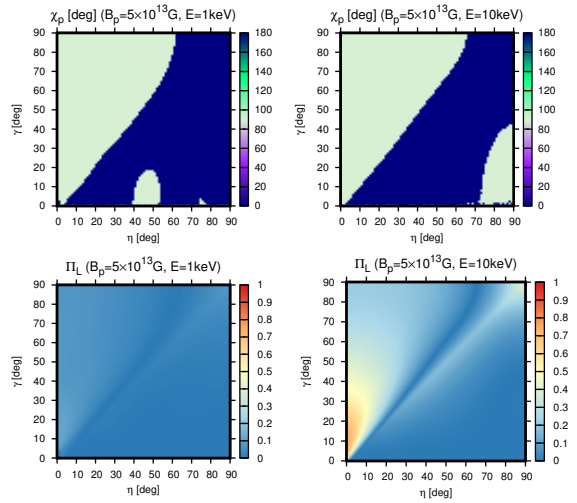

Figure 3.21: Phase-averaged polarization angles χ_p (upper panels) and fractions Π_L (lower panels) for the photon energies of $E = 1$keV (left) and $E = 10$keV (right). The magnetic field strength is set to $B_p = 5 \times 10^{13}$G.

energy dependence of the mode conversion will be useful to distinguish the effects of the mode conversion from those of the configuration of the neutron star if they are observed at multiple energy bands in the future.

3.3.4 Hot Spot

So far I have assumed that the temperature is uniform on the neutron star surface, but this may not be true. In fact, the observed energy spectra of the magnetar emissions are normally fitted with the composition of a blackbody radiation and a power-law emission and give us an estimate of the temperature and size of the region that produces the thermal emission as $T \sim 0.4$keV and $R_{\rm Th} \sim 5$km for anomalous X-ray pulsars (AXPs) and $T \sim 0.7$keV and $R_{\rm Th} \sim 1$km for soft gamma-ray repeaters (SGRs). These results suggest that the thermal-emission region does not cover the entire surface and may be associated with a hot spot.

I hence consider the possible effects of the existence of such a hot spot on the phase-averaged polarization angle and fraction. I actually assume that two hot spots of the same size cover both the magnetic polar regions. I set the magnetic field strength to $B_p = 5 \times 10^{14}$G so that the mode conversion should occur inside the O-mode photosphere. The results are shown in Figure 3.22. The photon energy is again fixed to $E = 5$keV. The phase-averaged polarization angles and fractions are presented in the upper and lower panels, respectively, for the hot spot radii of $R_{\rm Th} = 10,\ 5$, and 1km. As for the polarization fraction, it is immediately apparent from the figure that the red region, where the polarization fraction is large, is not changed much by the variation in the spot size; it is the vicinity of $\eta = \gamma = 45°$ that is most affected. The increase of the polarization fraction is also seen in the region near $\eta = 90°$, $\gamma = 20°$. The polarization angle also changes by 90° in these parameter regions. As expected, the parameter regions with low polarization fractions tend to be affected (González Caniulef et al., 2016).

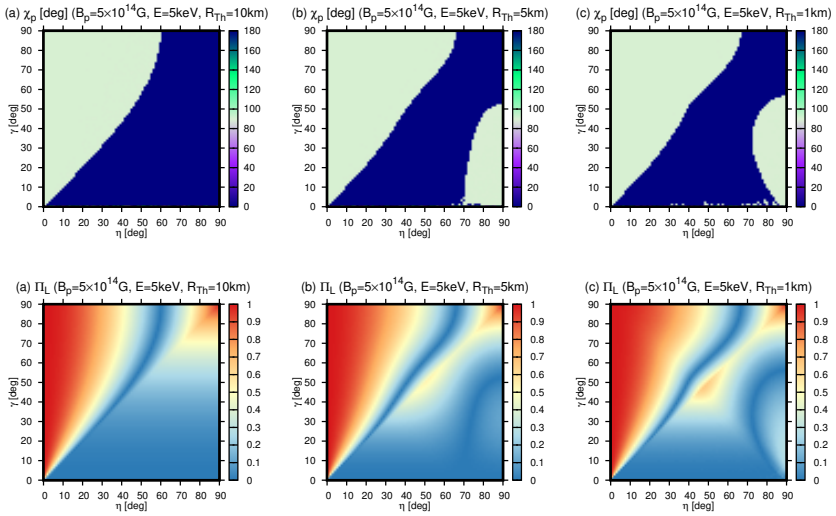

Figure 3.22: Phase-averaged polarization angles (upper panels) and fractions (lower panels) of a neutron star with hot spots. The dipole magnetic field strength is set to $B_p = 5 \times 10^{14}$G. The spot size is assumed to be $R_{\rm Th} = 10,\ 5$, and 1km from left to right.

In general, the polarization fraction tends to increase as the emission is limited to a smaller region, since the magnetic field becomes more uniform in this region. There is another reason, however, for the increases of the polarization fraction in the parameter regions mentioned above. This is understood from Figures 3.23 and 3.24, in which the snapshots of the polarization directions in the observed patch on the polarization-limiting surface are shown at different rotational phases for the spot radii of $R_{\rm Th} = 10$km and $R_{\rm Th} = 5$km, respectively. The magnetic field strength is fixed to $B_p = 5 \times 10^{14}$G, and $\eta = \gamma = 45^\circ$ is chosen. The localization of the emission region to the hot spot is evident in the latter case. At $\psi = 0$, hot spots at both the north and south poles are barely visible at the left and right edges of the observed patch, while at $\psi = \pi$, the hot spot at the north pole comes at the center. In the former case, the radiation is polarized in the Y-direction, whereas in the latter, the net polarization vanishes. At $\psi = \pi/2$ and $3\pi/2$, in contrast, the polarization directions are tilted by about 45° to the Y-axis. It is easily understood, then, that as the spot size gets smaller, the cancellation between the radiation at $\psi = 0$ and that at $\psi = \pi/2$ and $3\pi/2$ becomes weaker, since the hot spots at $\psi = 0$ are less visible. This is the reason for the increase in the polarization fraction around $\eta = \gamma = 45^\circ$ with the decrease in the spot size exhibited in panels (a)-(c) of Figure 3.22. The change in the neighborhood of $\eta = 90^\circ,\ \gamma = 20^\circ$ is also understood in the same way (see Figure 3.25).

The behaviors of the phase-averaged polarization angle should now be apparent. In the vicinity of $\eta = 45^\circ,\ \gamma = 45^\circ$, the contributions from the rotational phases around $\psi = 0$ are reduced as the spot radius gets smaller. Then, the phase-averaged polarization angle tends to be $\chi_p \simeq 0^\circ$, or 180° for small spot sizes. In the case of $\eta \simeq 90^\circ, \gamma \simeq 20^\circ$, in contrast, it is evident from Figure 3.25 that the polarization angle tends to be $\chi_p \simeq 90^\circ$.

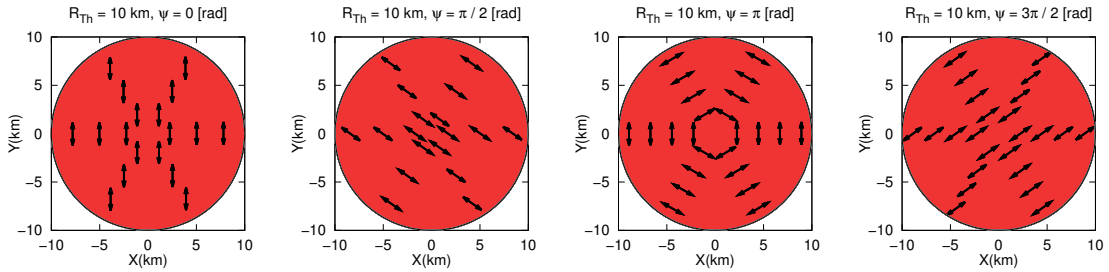

Figure 3.23: Polarizations of photons at different rotational phases ($\psi = 0, \pi/2, \pi, 3\pi/2$) for the spot radius $R_{\rm Th} = 10$km. The magnetic field strength is $B_p = 5 \times 10^{14}$G and $\eta = 45°$, $\gamma = 45°$. The black circles indicate the observed patch on the polarization-limiting surface. The red areas indicate the hot spot, which covers the whole surface in this case.

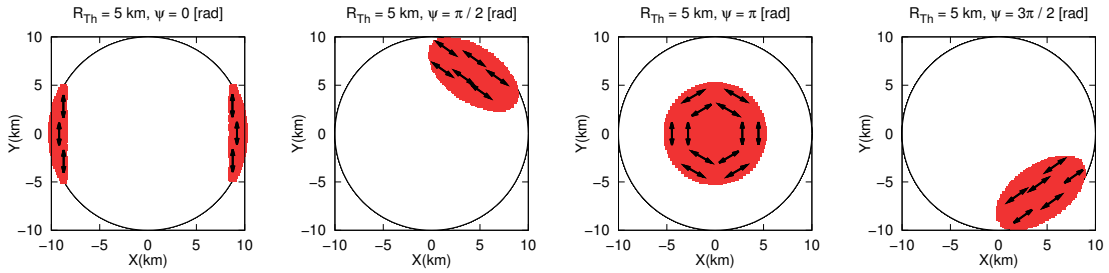

Figure 3.24: Same as Figure 3.23 but for the spot radius of $R_{\rm Th} = 5$km.

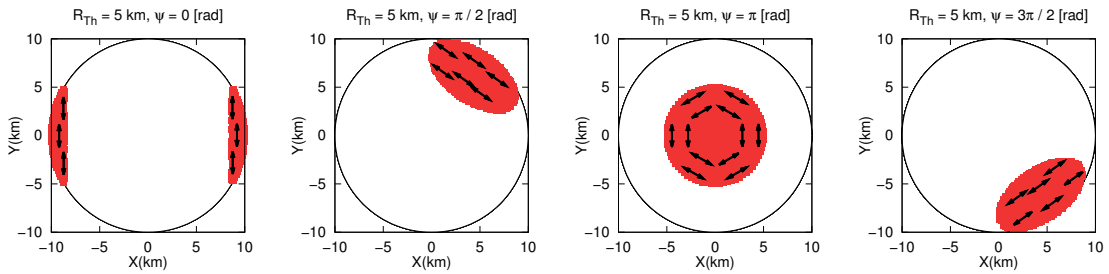

Figure 3.25: Same as Figure 3.24 but for $\eta = 90°$, $\gamma = 20°$.

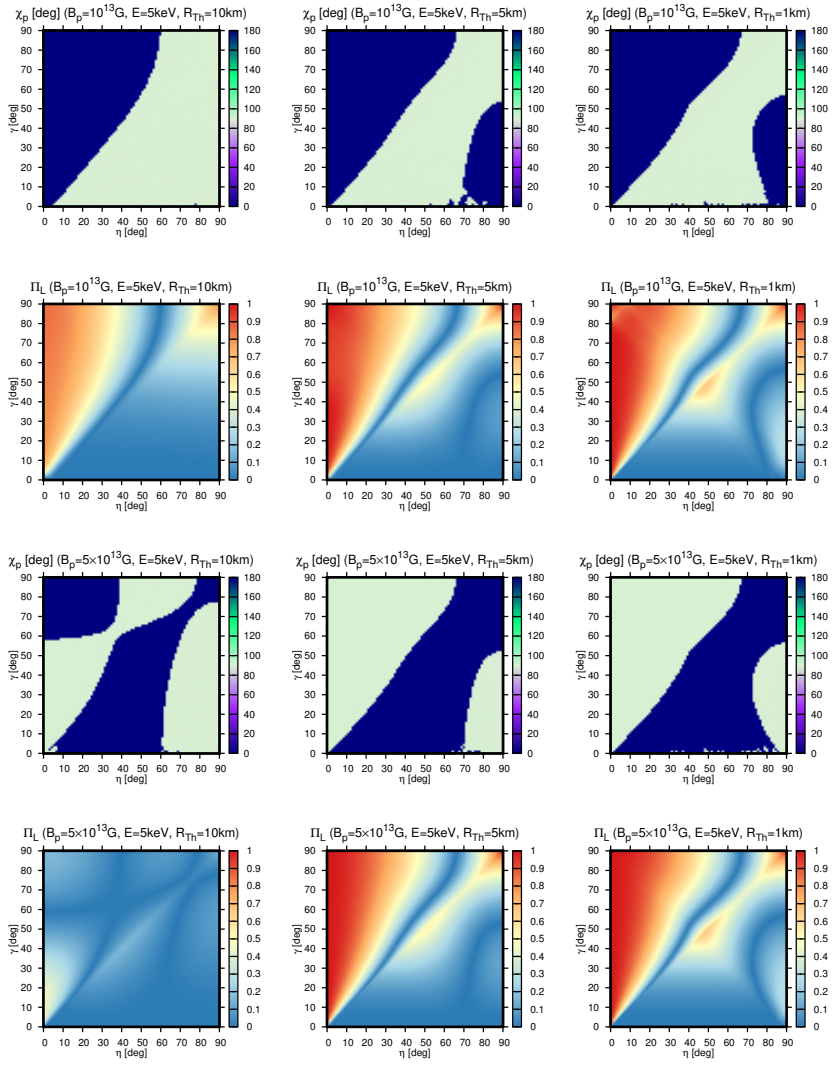

Figure 3.26: Phase-averaged polarization angles and fractions for different hot-spot sizes. The magnetic field strength is set to $B_p = 10^{13}$G (top two rows) and 5×10^{13}G (bottom two rows). The left, middle, and right panels correspond to the spot sizes of $R_{\rm Th} = 10,\ 5$, and 1km, respectively.

The mode conversion still occurs inside the O-mode photosphere on any part of the neutron star surface for $B_p = 10^{14}$G at $E = 5$keV, since the condition $B > B_l$ is satisfied everywhere (see Figure 3.18 (a)). The phase-averaged polarization properties are hence essentially the same as those for $B_p = 5 \times 10^{14}$G, irrespective of the hot spot. As the magnetic field strength becomes even lower, the mode conversion starts to the place at low magnetic latitudes and lowers the polarization fractions in general if photons are emitted from the entire neutron star surface, as was demonstrated in the previous section. This is particularly the case for $B_p = 5 \times 10^{13}$G (see the two bottom left panels of Figure 3.26), since the surface is almost equally divided into the region where the mode conversion occurs inside the O-mode photosphere, near the pole, and the region where the mode conversion occurs outside the two photospheres, extended from the magnetic equator. In the case of $B_p = 10^{13}$G, the mode conversion always occurs, and photons are mostly in the O-modes, except in the region where $E < E_{\rm ad}$ is satisfied because of large values of $\tan\theta_B$. The latter effect is the reason why the phase-averaged polarization fractions are still somewhat reduced from those for the corresponding no mode conversion.

In Figure 3.26, I show how the existence of hot spots modified the phase-averaged polarization angles and fraction for $B_p = 10^{13}$ and 5×10^{13}G. The left, middle, and right columns correspond to the spot sizes of $R_{\rm Th} = 10,\ 5$ and 1km, respectively. Note that the left four panels are essentially the same as those presented in Figure 3.20. The top two rows show the results for $B_p = 10^{13}$G. In the case of $R_{\rm Th} = 10$km, as mentioned above, the polarization fractions decrease a little from those for no mode conversion, particularly in the region where it is high. The polarization angles are also changed by 90°.

As the size of the hot spot becomes smaller, the phase-averaged polarization fractions return to the higher values for no mode conversion. This is because the region with $E < E_{\rm ad}$ rarely enters the hot spot. The exceptional cases are limited to the configurations with $\gamma \sim \eta + 80°$ for $R_{\rm Th} = 1$km. In these cases, $E < E_{\rm ad}$ is satisfied at some rotational phases, and the cancellation between the two modes lowers the phase-averaged polarization fractions slightly, as observed. In contrast, the O-mode is dominant for this magnetic field strength irrespective of the spot size, and the behavior of the polarization angles in the $\eta - \gamma$ plane is essentially the same as that for $B_p = 5 \times 10^{14}$G, except for the overall difference by 90° because of the mode conversion.

In the case of $B_p = 5 \times 10^{13}$G, the effect of the hot spot is drastic, as can be immediately seen in the bottom two rows in Figure 3.26. In fact, the reduction of the phase-averaged polarization fraction by the mode conversion is nearly nullified when the spot size becomes as small as 5km. This is easily understood as follows. Since the mode conversion occurs outside the two photospheres in the region near the equator, it is not included in the hot spot if its size is small. Then, the photons are mostly in the E-mode, just as in the case neglecting the mode conversion and the phase-averaged polarization fractions for $R_{\rm Th} = 1,\ 5$km are almost the same as those for $B_p = 5 \times 10^{14}$G. Since the dominant mode is the E-mode for all combinations of η and γ for these small hot-spot sizes, the polarization angles are identical to those for $B_p = 5 \times 10^{14}$G in Figure 3.22.

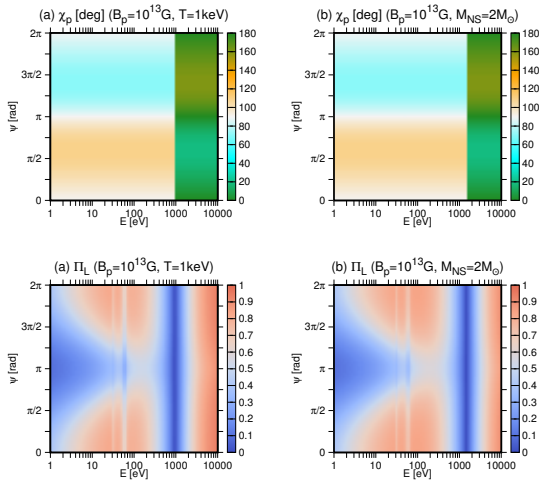

Figure 3.27: Same as for the case of $\eta = 5°$ and $\gamma = 15°$ in Figures 3.11 and 3.12 but (a) for a different temperature $T = 1$keV or (b) for a different mass of neutron star $M_{\rm NS} = 2M_\odot$.

3.3.5 Other Parameters

I next discuss the dependence on the surface temperature T, neutron star mass $M_{\rm NS}$, and radius $R_{\rm NS}$. They affect the results mainly through the adiabatic energy for the vacuum resonance $E_{\rm ad}$, which depends on the scale height of the atmosphere H_ρ in Equation (3.1). The latter is proportional to the temperature and the inverse of the surface gravity, $g = GM_{\rm NS}/R_{\rm NS}^2$. Recall that the adiabatic energy $E_{\rm ad}$ is the energy above which the mode conversion occurs adiabatically and the polarization angle changes by 90°, and near which the polarization fraction tends to be reduced.

The phase-resolved polarization angle χ_p and fraction Π_L for $\eta = 5°$ and $\gamma = 15°$ are recalculated either with a higher temperature of $T = 1$keV or with a larger neutron star mass of $M_{\rm NS} = 2M_\odot$. They are $T = 0.4$keV and $M_{\rm NS} = 1.4M_\odot$, respectively, in the fiducial model. Note that it is the increase or decrease in the scale height that matters, and one can equally change the neutron star radius instead of the temperature or the neutron star mass, since the scale height is a function of the combination $T/(M_{\rm NS}/R_{\rm NS}^2)$. The magnetic field strength is set to $B_p = 10^{13}$G. The results are shown in Figure 3.27. One can see that the difference between the models is almost indiscernible. This is just as expected, since the adiabatic energy depends on the scale height only weakly: $E_{\rm ad} \propto H_\rho^{-1/3}$. I hence conclude that the results obtained so far are robust.

3.3.6 Applications to Real Magnetars

I finally apply the theory developed thus far to real magnetars. My intention here is not to make a strong claim on the possibility to detect polarizations as envisaged in this chapter from these magnetars, which would be impossible if one considers various uncertainties in theoretical interpretations and modelings of observations as explained below. Instead, I would like to get a rough idea of what the polarization

Table 3.1: Observationally inferred magnetic field strengths, surface temperatures and the radii of hot spots for four of the known magnetars.

Magnetar [1]	B_p (10^{14} G)	T (keV)	$R_{\rm Th}$ (km)
2259+58	0.59	0.37	5.0
0142+61	1.3	0.36	9.4
0501+45	1.9	0.70	1.4
1708-40	4.7	0.48	4.5

angles and fractions would be like if my models were true. Here I deal with the four magnetars 1E 2259+586, 4U 0142+61, SGR 0501+4516, and 1RXS J17089.0-400910, since thermal radiation is identified observationally in the soft X-ray band (Enoto et al., 2010).

I employ the values of the dipole magnetic field strength B_p, the temperature T, and the radius of the emission region $R_{\rm Th}$ obtained from the spectral fittings by two blackbody components with different temperatures and radii by Nakagawa et al. (2009). They are summarized in Table 3.1. Since the radius of the emission region for the high-temperature component is only about a tenth of that for the low-temperature component, and the former component gives a rather poor fit to the high-energy part of the spectrum, I assume in this chapter that the low-temperature component is originated from the hot spot on the magnetar surface and do not consider the high-temperature component. In fact, the magnetars other than SGR 0501+4516 do not reproduce the apparent excesses at > 7keV in their spectral fit (Nakagawa et al., 2009). It should also be mentioned that the spectra of persistent emissions from these magnetars may be better fit by the superposition of a blackbody component plus a power-law tail (Rea et al., 2007b,a, 2009; Vogel et al., 2014). The power-law tails become important already $\sim 3-4$keV in some cases. It is important here, regardless of which model is better, that both of them indicate the existence of the thermal component and that the temperatures and radii of the emission regions inferred from the observed blackbody components are not much different between the two cases. Note, however, that Comptonization effects, which are supposed to be responsible for the formation of the high-energy tails in the spectra, are normally associated with flows of charged particles along magnetic field lines (Thompson et al., 2002), which will hit the magnetar surfaces intensely (Thompson et al., 2002; Nobili et al., 2008). As a result, the atmospheric state may be different from what I have considered in this chapter. As I know nothing of the mass and radius for these magnetars, I simply adopt the canonical values, $M = 1.4M_\odot$ and $R_{\rm NS} = 10$km, for all of them.

With all of these caveats in mind, I present the phase-averaged polarization angles and fractions for 5keV photons in Figure 3.28. As expected, the existence of the hot spot is recognized from the increase in the polarization fraction around $\eta = \gamma = 45^\circ$ for all of the cases except 4U 0142+61, in which the spot size is comparable to the neutron star radius. In fact, the smaller the spot is, the larger the enhancement becomes. These pictures are not changed qualitatively as long as

[1]The obvious abbreviations are employed for 1E 2259+586, 4U 0142+61, SGR 0501+4516, and 1RXS J17089.0-400910. The values are taken from Nakagawa et al. (2009).

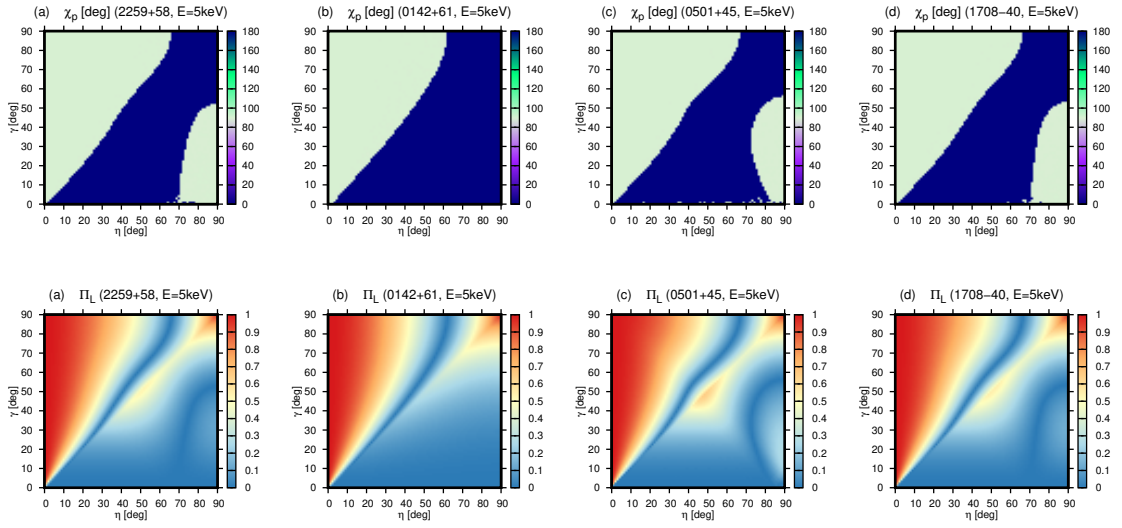

Figure 3.28: Phase-averaged polarization angles (upper panels) and fractions (lower panels) at $E = 5$keV for the four magnetars: (a) 1E 2259+586, (b) 4U 0142+61, (c) SGR 0501+4516, and (d) 1RXS J17089.0-400910.

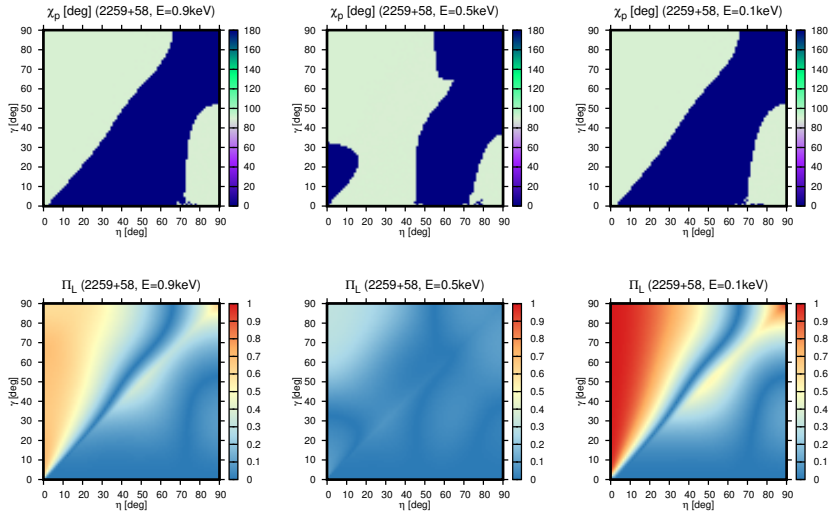

Figure 3.29: Phase-averaged polarization angles (upper panels) and fractions (lower panels) for magnetar 1E 2259+586 at $E = 0.9$keV (left column), $E = 0.5$keV (middle column), and $E = 0.1$keV (right column).

the photon energy is higher than $\sim$ 1keV. The effects of the small spot radii are also seen in the polarization angles in the parameter regions of $\eta \simeq 90°$, $\gamma \simeq 20°$, except for the case for 4U 0142+61.

At lower energies, $E \lesssim 1$keV, the phase-averaged polarization fraction may be reduced as a consequence of the partial mode conversion at $E \sim E_{\rm ad}$, and the polarization angle is also affected. This is demonstrated in Figure 3.29 for magnetar 1E 2259+586 at the photon energies of $E = 0.5$ and 0.9keV. It is evident that at $E = 0.9$keV (left column) the reduction of the polarization fraction is already substantial, though the polarization angle is not so much affected. In contrast, at $E = 0.5$keV (middle column), the polarization angle is also modified in some region of η and γ, and, as a matter of fact, the photons are essentially unpolarized for all configurations at this photon energy. At much smaller energies $E \sim 0.1$keV (right column), however, the mode conversion is frozen, and the polarization angles and fractions return to those for nonconversion.

3.4 Summary

In this chapter, I have systematically computed the phase-resolved polarization angles and fractions, which are one of the most important observables in future observations, for different photon energies and various configurations of the rotation axis and the dipole magnetic field to facilitate the interpretation of observational data. In so doing, I have accounted for the mode conversion, which was neglected in the previous study (Taverna et al., 2015).

I have started with the reproduction of the previous results for $B_p = 10^{13}$G (Taverna et al., 2015). For that purpose, I have neglected the mode conversion intentionally. I have found a good agreement, although the bending of photon trajectories and modifications of the dipole magnetic field by general relativity are not considered in my calculations. This suggests that these effects are rather minor. I have then included the mode conversion and studied in detail how the results are modified.

I have found that the adiabatic mode conversion occurs for high-energy photons with $E \gtrsim E_{\rm ad} \sim 2$keV and the polarization angle changes by 90°. At $E \simeq E_{\rm ad}$, the mode conversion occurs nonadiabatically and the E- and O-modes are mixed, resulting in lower polarization fractions in general. At lower energies, the mode conversion is frozen, the photons are all in the original E-mode, and the polarization fraction returns to high values. The adiabatic energy $E_{\rm ad}$ is actually a function of photon energy, though, and vanishes at the cyclotron frequencies of the proton, $\sim 30 - 60$eV. The polarization fraction is somewhat reduced at these energies again, although the polarization angle is not affected. At very low energies, the polarization fraction is lowered again, since the polarization-limiting surface gets much closer to the neutron star and the polarizations are largely canceled among photons coming from different parts of the neutron star surface.

I have also presented the semi-amplitude, i.e., the total variation of the polarization angle (divided by a factor of 4) and the phase-averaged polarization fraction following Taverna et al. (2015). I have divided the η-γ plane into 10 regions and discussed the features in each region in detail. I have observed that high polarization

fractions are obtained when $\eta \ll \gamma$. The semi-amplitude is small in that case. The mode conversion tends to reduce the phase-averaged polarization fractions.

I have then conducted more comprehensive investigations of both the phase-resolved and averaged quantities, varying not only the configuration of the rotation and magnetic axes but also the magnetic field strength and photon energy. I have also considered the effect of the possible existence of a hot spot on the neutron star surface. Although the dependence of the results on other parameters that specify the properties of the neutron star, i.e., the mass, radius, and surface temperature, has also been studied, I have found it minor, since they appear only in the adiabatic energy through the density scale height of the atmosphere of the neutron star.

I have shown that in the absence of the mode conversion, the behavior of the phase-resolved polarization angle in the E-ψ (rotational phase) plane can be divided into three cases with $\eta < \gamma$, $\eta = \gamma$, and $\eta > \gamma$. In the first case, the polarization angle oscillates around $\chi_p = 90^\circ$. In the second case, it changes by 180°, whereas in the third case, it changes more than 180° during a single rotation of the neutron star. Without the mode conversion, the phase-resolved polarization fraction is large at high photon energies, as in the previous case. As the photon energy is lowered, the polarization-limiting surface comes closer to the neutron star, and the cancellation among photons originated from different parts of the neutron star surface tends to decrease the polarization fraction. This is particularly the case at the rotational phase of $\psi = \pi/2$.

Taking into account the mode conversion, I have demonstrated that the polarization angle is changed by 90° at high photon energies $E \gtrsim E_{\rm ad}$. In the case of $\eta = \gamma$, $E_{\rm ad}$ becomes small at $\psi = \pi/2$, and the jump of the polarization angle occurs accordingly at much lower energies at this rotational phase. The phase-resolved polarization fraction is reduced by the mode conversion at $E \simeq E_{\rm ad}$, since it occurs nonadiabatically at these energies and the E- and O-modes are mixed in some proportions. At much lower energies, the mode conversion is frozen, and the results are essentially the same as those without the mode conversion except at the cyclotron energies of the proton $\sim 30 - 60$eV for $B_p = 10^{13}$G, where $E_{\rm ad}$ vanishes and the resultant adiabatic mode conversion lowers the polarization fraction a bit.

For a bit stronger magnetic field, $B_p = 5 \times 10^{13}$G, I have found that the 90° change of the polarization angle can occur twice or four times at $E \gtrsim E_{\rm ad}$ during a single rotation of the neutron star. This happens because the neutron star surface is dominated at some rotational phases by the region that violates the condition given in Equation (3.9), where the mode conversion occurs inside the O-mode photosphere, in addition to the region that has a large value of $\tan\theta_B$ and the effect of the mode conversion is suppressed. The phase-resolved polarization fraction is modified in two ways: since the polarization-limiting radius is larger, the polarization fraction tends to be higher as a whole; the cyclotron energy is raised to $\sim 150 - 300$eV, and the slight reductions of the polarization fraction have been observed at these photon energies. I have also seen some variations with the rotational phase at $E \gtrsim E_{\rm ad}$. I have found, in contrast, that the semi-amplitudes have an interesting pattern in the η-γ plane according to the number of 90° changes in the polarization angle during a single rotation of the neutron star.

For even stronger magnetic fields, the mode conversion tends to occur inside the

O-mode photosphere. Although the reductions of the polarization fraction are still visible at the cyclotron energies of the proton for $B_p = 10^{14}$G, even they are gone at $B_p = 5 \times 10^{14}$G, and the results are completely the same as those neglecting the mode conversion.

The phase-averaged polarization angles and fractions have been calculated for $B_p = 10^{13}$, 5×10^{13}, and 10^{14}G. The mode conversion is important at $E = 5$keV in the first two cases. For $B_p = 10^{13}$G, the polarization fraction is reduced, and the polarization angle changes by 90° by the mode conversion. For $B_p = 5 \times 10^{13}$G, in contrast, the polarization fraction is lowered, because the observer sees not only the region in which the mode conversion takes place outside the photospheres of the two modes but also the region in which the mode conversion occurs between the two photospheres. A complicated pattern of the polarization angles in the η-γ plane is also produced in this case. I have also demonstrated that the polarization angles and fractions depend strongly on the photon energy.

I have discussed the modifications that nonuniformities in the surface temperature may make in the polarization. In fact, I have considered the situation in which the thermal emissions are limited to the hot spots located at the magnetic poles. I have shown for $B_p = 5 \times 10^{14}$G, at which the mode conversion occurs inside the O-mode photosphere, that the cancellation is somewhat relaxed, and the phase-averaged polarization fraction is increased in the vicinity of $\eta = \gamma = 45°$ and $\eta = 90°$, $\gamma = 20°$. The smaller the spot is, the larger this effect becomes. The phase-averaged polarization angle also changes by 90° in these parameter regions.

For $B_p = 10^{13}$G and 5×10^{13}G, the mode conversion again becomes important. In fact, in the former case, the condition given in Equation (3.9) is always satisfied at $E = 5$keV, and the mode conversion occurs except when $E < E_{\rm ad}$ holds because of large values of $\tan\theta_B$. I have found that as the hot-spot size becomes smaller, the latter condition is met only at some limited configurations, and the polarization fractions are raised in general. The phase-averaged polarization angle is further changed by the mode conversion in these cases.

At $B_p = 5 \times 10^{13}$G, the neutron star surface is divided into two regions: the polar region, where the mode conversion occurs inside the O-mode photosphere and the E-mode photons are emitted, and the equatorial region, in which the mode conversion produces the O-mode photons. Since the two regions have nearly equal areas, the polarizations are canceled almost completely if the entire surface radiates these photons. In the presence of the hot spot, in contrast, I have demonstrated that the polarization fractions are increased, since the radiation is limited to the polar region and the cancellations tend to be suppressed. I have also shown that the polarization angles are little affected by the mode conversion.

I have finally considered four of the existing magnetars for which the magnetic field strength, surface temperature, and hot-spot size are estimated from observations. Realizing the possible caveats in my interpretation of the observations and modeling of the atmospheres of these magnetars, I have applied the theory to calculate the phase-averaged polarization angles and fractions for these objects. It is found that, under the assumption that my models are indeed applicable, the imprints of the mode conversion will manifest themselves only at low energies, $E \lesssim 1$keV, in magnetar 1E 2259+586, which has the lowest magnetic field strength,

$B_p \sim 5 \times 10^{13}$G, among the four, and that they will not be observed with the gas pixel detectors aboard *IXPE* Weisskopf et al. (2013), *XIPE* Soffitta et al. (2016) and *eXTP* Zhang et al. (2016), which are all based on the photoelectric effect and of which operational energy is above 2keV. I will have to wait for polarimeters employing the Bragg reflections Marshall et al. (2013).

In this chapter, I ignore general relativistic effects such as ray bendings and possible modifications of dipole magnetic fields. Although they are likely to be minor, they have to be accounted for in the quantitative comparison with observations and the determination of the configuration of the neutron star thereby. I have also assumed for simplicity that the photons are all in the E-mode initially. In reality, there are some O-mode photons as well. In order to handle them properly, I need to solve the transport equations in the atmosphere of the neutron star. Circular polarizations that are entirely neglected in this chapter are produced in principle (Heyl and Shaviv, 2002; Lai and Ho, 2003a), in addition to the linear polarizations considered in this chapter. Hence, they have to be investigated quantitatively in the future. Although I have focused on the thermal emissions in this chapter, nonthermal components are also known to exist at $E \lesssim 10$keV in the magnetar radiation (Rea et al., 2007b,a, 2009; Enoto et al., 2010; Vogel et al., 2014). Then, scatterings in the magnetosphere should be taken into account in considering these emissions (Nobili et al., 2008; Fernández and Davis, 2011; Taverna et al., 2014). This is even more true at higher energies, $E \gtrsim 10$keV, where these nonthermal emissions are supposed to be dominant.

3.5 Derivations of Equations (3.2) and (3.3)

This section gives the supplementary explanation to derive Equations (3.2) and (3.3). I start with the Euler-Heisenberg Lagrangian

$$\mathcal{L} = -\frac{I}{4} + \frac{e^2}{8\pi^2}\int_0^\infty \frac{d\eta}{\eta^3} e^{-\eta}\left[i\eta^2 \frac{\sqrt{-K}}{4}\frac{\cos(X_+)+\cos(X_-)}{\cos(X_+)-\cos(X_-)} + B_Q^2 + \frac{\eta^2}{6}I\right], \quad (3.21)$$

in which $X_\pm$ are given as

$$X_+ = \frac{\eta}{B_Q}\sqrt{-\frac{I}{2} + i\frac{\sqrt{-K}}{2}}, \quad X_- = \frac{\eta}{B_Q}\sqrt{-\frac{I}{2} - i\frac{\sqrt{-K}}{2}}, \quad (3.22)$$

with two Lorentz invariants: $I = 2(|\boldsymbol{B}|^2 - |\boldsymbol{E}|^2)$, $K = -(4\boldsymbol{E}\cdot\boldsymbol{B})^2$. It contains the one-loop level of the quantum correction to the classical Lagrangian of electrodynamics.

Normalizing these invariants as $I_{\rm N} = I/B_Q^2$ and $K_{\rm N} = K/B_Q^4$, I can rewrite the Euler-Heisenberg Lagrangian as

$$\begin{aligned}\mathcal{L} &= -\frac{I_{\rm N}B_Q^2}{4} + \frac{e^2}{8\pi^2}\int_0^\infty \frac{d\eta}{\eta^3} e^{-\eta} B_Q^2 \\ &\quad \times \left[i\eta^2 \frac{\sqrt{-K_{\rm N}}}{4}\frac{\cos(X_{+{\rm N}})+\cos(X_{-{\rm N}})}{\cos(X_{+{\rm N}})-\cos(X_{-{\rm N}})} + 1 + \frac{\eta^2}{6}I_{\rm N}\right], \end{aligned} \quad (3.23)$$

where $X_{+\mathrm{N}}$ and $X_{-\mathrm{N}}$ are X_+ and X_- expressed in terms of I_N and K_N, respectively. Then, the parameters q and m are derived from this form of the Lagrangian as

$$q = -\frac{32}{B_Q^4}\left.\frac{\partial \mathcal{L}}{\partial K_\mathrm{N}}\right|_{K_\mathrm{N}=0},\ m = -\frac{16}{B_Q^4}\left.\frac{\partial^2 \mathcal{L}}{\partial I_\mathrm{N}^2}\right|_{K_\mathrm{N}=0}. \tag{3.24}$$

Note that there is an alternative expression that appears different but is actually equivalent:

$$m = \int_0^\infty d\eta \frac{e^2 e^{-\eta}}{8b\pi^2\eta^2}\left\{2b^2\eta^2\frac{1}{\tanh^3(b\eta)} - b\eta\frac{1}{\sinh^2(b\eta)} - (1+2b^2\eta^2)\frac{1}{\tanh(b\eta)}\right\}. \tag{3.25}$$

This can be obtained by using some formulae for the hyperbolic functions.

4
Conclusion

In this thesis, I considered the vacuum polarization which is one of the fundamental processes in nonlinear QED. In Chapter 2, I investigated the vacuum polarization itself in the external electromagnetic plane waves. I derived the induced electromagnetic current, which is proportional to the vacuum polarization tensor, by Schwinger's proper-time method. The refractive index of the probe photon was computed by solving the modified Maxwell equation. I take into account the variations of the external field by utilizing the gradient expansion. I assumed that the vacuum polarization tensor has three tensor components, two of which correspond to the real polarization modes of the electromagnetic wave and the other is gauge-dependent.

The refractive index of each polarization was first computed for the case of the crossed field, which is the long wavelength limit of the plane wave. In this case, the refractive indices are different for the two eigenmodes, which is the birefringence of the vacuum. It was found that the expressions of the eigenmode vectors are the same as those in the weak-field limit of the crossed field. The refractive index depends on the external field strength and the energy of the probe photon. Although the refractive index of the crossed field has been computed for the arbitrary probe photon energy in the previous studies, it is not the case for the external field strength. The refractive index has been investigated in the case that the external field strength is not much stronger than the critical field strength and the case that a special limit of the external field strength and the probe photon energy. In my study, the refractive index of the crossed field can be computed without such limitations on the field strength and the photon energy.

I then computed the refractive index for the case that the crossed field has the gradient of the field strength. It was found that the field variation mainly changes the imaginary part of the refractive index. The imaginary part of the refractive index means the damping of the electromagnetic wave, which may correspond to the creation of the electron-positron pair. Such situations would be realized in laser

facilities that emit high energy photons, e.g., X-ray laser.

In Chapter 3, I considered the influence of the vacuum polarization to the polarization of the surface radiation from the isolated neutron star. It is known that neutron stars are endowed with strong dipole magnetic fields and the vacuum in the magnetosphere around the neutron star becomes birefringent. The polarization of the emission further evolves in the magnetosphere according to the direction of the magnetic field. If the gas atmosphere consisting of plasma exists on the neutron star surface, the conversion of the polarization modes may occur because of the balance between the dielectric properties by the plasma and the vacuum. This mode conversion is thought to occur adiabatically when the energy of the photon propagating therein is higher than a few keV. The point of the mode conversion moves to the inward of the atmosphere, where the plasma density is higher, as the strength of the magnetic field increases. It may be inside the photosphere for the strongly magnetized neutron stars such as magnetars. In such cases, I assumed that the effect of the mode conversion is not manifested. I estimated the polarization angle and fraction, which are the observable quantities in the polarimetry, with considering these effects.

I first calculated the polarization for the case that the radiation is emitted from the entire surface of the neutron star. To see the effects of the configuration of the dipole magnetic field, I ignored the mode conversion. Then I took into account it for some different magnetic field strengths. Both the phase-resolved and the phase-averaged polarization properties were computed. It is found that the strongly polarized emission is generally observed when the magnetic field is strong. When the magnetic field is not so strong ($B_p \lesssim 10^{13}$G), the polarization angle differs by 90° between in the low energy regime ($\lesssim$ 1keV) and in the high energy regime ($\gtrsim$ 2keV). This is because the E-mode is dominant in the low energy regime, on the other hand, most of the radiation is O-mode. In the energy between them, the polarization fraction is low because the polarizations of the O-mode and the E-mode photons cancel each other.

I next investigated the case that the emission area is limited to the hot spot, which covers a part of the surface around the magnetic pole. In this case, it was found that the emission area of the surface seen by the observer decreases in some rotational phase and that the phase-averaged polarization fraction in some configurations increases. The effect of the mode conversion tends to be hidden in the photosphere near the magnetic pole, where the magnetic field is strong. Finally, I computed the cases assuming four real magnetars with taking into account the dipole magnetic field and emission radius. The effect of the mode conversion cannot be seen in the energy range of $1 - 10$keV because of magnetars' strong magnetic fields. Therefore, the strongly polarized emission from a magnetar is expected in the next-generation polarimetry satellites. In contrast, one of the four magnetars, which has the weakest magnetic field among them, shows the cancellation of the polarization in the energy below 1keV. Thus, the strongly polarized emission is expected in the radiation of magnetars with the magnetic field of $B_p \gtrsim 10^{14}$G and the effect of mode conversion would be observed in the emission of the not-so-strongly magnetized ($B_p \lesssim 10^{13}$G) neutron stars in the near future.

A

Units of Electrodynamics

I use the Heaviside-Lorentz units in treating the vacuum polarization itself, and the cgs Gauss units are utilized in the application to the polarimetry. There are the multiple cgs units in electrodynamics, which is confusing. So I explain the units of the electrodynamics here. The explanation is mainly based on the explanation in the famous textbook by Jackson (Jackson, 1975). The basic units in the physical quantities in the electrodynamics are the mass (M), the length (L) and the time (T). I show the dimension of a unit with a bracket, e.g., the dimension of the force f is shown as $[f] = [ML^2T^{-2}]$. The unit is defined by the fundamental laws of electrodynamics.

First fundamental law is the Coulomb law. This gives the force between two particles separated by a distance r with electric charges q and q', which is expressed with the proportional constant k_1 as

$$f_{\text{Coulomb}} = k_1 \frac{qq'}{r^2}. \tag{A.1}$$

It is necessary to fix the dimension of k_1 to determine the dimension of the charge.

Next fundamental law is the Ampère law. It describes the force per the unit length of electrical leads $df_{\text{Ampèere}}/dl$ as

$$\frac{df_{\text{Ampère}}}{dl} = 2k_2 \frac{II'}{d}, \tag{A.2}$$

where the current of I and I' flows in the two electrical leads, respectively, and the distance between them is d. k_2 is the proportional constant. The current is generally defined as the change of the charge with time and it is known that the dimension of k_1/k_2 is $[k_1/k_2] = L^2T^{-2}$ at this stage. The value of k_1/k_2 is also known to be given as

$$\frac{k_1}{k_2} = c^2. \tag{A.3}$$

Now one can connect the dimension of the electric charge and current with that of the force.

The dimension of the magnetic flux density B, which is called the "magnetic field" in the other part of this thesis, is defined by the Biot-Savart law. The magnetic flux density is defined as the force per unit current. The strength of the magnetic flux density at the point separated from an infinitely long lead through which the current I flows by the distance d is expressed as

$$B = 2k_2\alpha\frac{I}{d}, \tag{A.4}$$

where α is again the proportional constant. From this expression, the ratio of the electric field E and the magnetic flux density B is found to be $[E/B] = [LT^{-1}\alpha^{-1}]$.

Finally, the Faraday law of electromagnetic induction is considered. This law describes that the electromotive force induced by the current circuit is proportional to the change rate of the magnetic flux penetrating the circuit, which is expressed as

$$\nabla \times \boldsymbol{E} + k_3\frac{\partial \boldsymbol{B}}{\partial t} = 0, \tag{A.5}$$

where k_3 is the proportional constant. The dimension of k_3 is given as $[k_3] = [\alpha^{-1}]$ because the two terms in the left hand side have the same dimension.

These laws described above are summarized into the Maxwell equations

$$\nabla \cdot \boldsymbol{E} = 4\pi k_1\rho, \tag{A.6}$$

$$\nabla \times \boldsymbol{B} = 4\pi k_2\alpha\boldsymbol{J} + \frac{k_2\alpha}{k_1}\frac{\partial \boldsymbol{E}}{\partial t}, \tag{A.7}$$

$$\nabla \times \boldsymbol{E} + k_3\frac{\partial \boldsymbol{B}}{\partial t} = 0, \tag{A.8}$$

$$\nabla \cdot \boldsymbol{B} = 0. \tag{A.9}$$

From these equations, the relation $k_3 = 1/\alpha$ is found. The evolution of the transverse plane electromagnetic wave is described as

$$\frac{\partial^2 \boldsymbol{B}}{\partial t^2} = \frac{k_1}{k_2k_3\alpha}\frac{\partial^2 \boldsymbol{B}}{\partial \boldsymbol{x}^2}. \tag{A.10}$$

We know that the electromagnetic wave propagates at the speed of light and

$$\frac{k_1}{k_2k_3\alpha} = c^2 \tag{A.11}$$

is obtained. Then, from Equation (A.3),

$$k_3 = \frac{1}{\alpha} \tag{A.12}$$

is known.

There are four quantities $\boldsymbol{E}$, $\boldsymbol{D}$, $\boldsymbol{B}$ and $\boldsymbol{H}$ in the Maxwell equation and the relation between $\boldsymbol{E}$, $\boldsymbol{D}$ and that between $\boldsymbol{B}$, $\boldsymbol{H}$ are necessary. They are defined as

$$\boldsymbol{D} = \varepsilon_0 \boldsymbol{E}, \tag{A.13}$$

$$\boldsymbol{H} = \frac{1}{\mu_0} \boldsymbol{B}, \tag{A.14}$$

in the (normal) vacuum so that the Maxwell equations are easy. First I explain the emu (electromagnetic) units. In the cgs emu unit, k_2 is defined to be unity. Therefore, k_1 is fixed as $k_1 = c^2$. The Gauss law (A.6) is given as

$$\nabla \cdot \boldsymbol{D} = 4\pi c^2 \rho. \tag{A.15}$$

The electric flux density is determined as

$$\boldsymbol{D} = \frac{1}{c^2} \boldsymbol{E}, \tag{A.16}$$

so that the Gauss law take the form of

$$\nabla \cdot \boldsymbol{D} = 4\pi \rho. \tag{A.17}$$

The coefficient α in the Ampère-Maxwell law

$$\nabla \times \boldsymbol{B} = 4\pi\alpha \boldsymbol{J} + \frac{\alpha}{c^2} \frac{\partial \boldsymbol{E}}{\partial t} \tag{A.18}$$

is fixed to be unity and this law is expressed as

$$\nabla \times \boldsymbol{B} = 4\pi \boldsymbol{J} + \frac{\partial \boldsymbol{D}}{\partial t}. \tag{A.19}$$

The left hand side contains the magnetic flux $\boldsymbol{H}$. The relation between the magnetic flux $\boldsymbol{H}$ and the magnetic flux density $\boldsymbol{B}$ is defined as

$$\boldsymbol{H} = \boldsymbol{B}, \tag{A.20}$$

so that the equation is simple. Then, k_3 is determined to be unity and the other Maxwell equations are

$$\begin{aligned} &\nabla \times \boldsymbol{E} + \frac{\partial \boldsymbol{B}}{\partial t} = 0, \\ &\nabla \cdot \boldsymbol{B} = 0. \end{aligned} \tag{A.21}$$

On the other hand, k_1 equals unity in the cgs esu (electrostatic) units. Then, $k_2 = 1/c^2$ is satisfied. α and k_3 are defined to be unity as in the cgs emu units. $\boldsymbol{D}$ and $\boldsymbol{H}$ are

$$\boldsymbol{D} = \boldsymbol{E}, \quad \boldsymbol{H} = c^2 \boldsymbol{B}. \tag{A.22}$$

In the cgs Gauss units, k_1 is determined to be unity as the esu units, however, $\boldsymbol{H} = \boldsymbol{B}$ is satisfied. To satisfy this relation, α is fixed as $\alpha = c$. Although the

Heaviside-Lorentz units are similar to the Gauss units, the Maxwell equations do not contain 4π in the Heaviside-Lorentz units. From this, the Heaviside-Lorentz units are called rationalized. In contrast, the units which contain 4π in the Maxwell equations are called non-rationalized. In the Heaviside-Lorentz units, k_1 and α are defined as $k_1 = 1/4\pi$ and $\alpha = c$. The Maxwell equations in the cgs units are summarized in Table A.1.

In the medium, the dielectric polarization $\boldsymbol{P}$ and the magnetic polarization $\boldsymbol{M}$ are taken into account in the Maxwell equations. The relations between $\boldsymbol{D}$, $\boldsymbol{H}$ and these are given as

$$\boldsymbol{D} = \varepsilon_0 \boldsymbol{E} + \chi_P \boldsymbol{P}, \tag{A.23}$$

$$\boldsymbol{H} = \mu_0 \boldsymbol{B} + \chi_M \boldsymbol{M}, \tag{A.24}$$

where χ_P and χ_M are the dimensionless quantities. They are defined as $\chi_P = \chi_M = 1$ in the rationalized units and defined as $\chi_P = \chi_M = 4\pi$ in the non-rationalized units.

Table A.1: Summary of the Maxwell equations in the cgs units.

	cgs emu units	cgs esu units	cgs Gauss units	Heaviside-Lorentz units
ϵ_0	$\frac{1}{c^2}$	1	1	1
μ_0	1	$\frac{1}{c^2}$	1	1
Maxwell Equations	$\nabla \cdot \boldsymbol{D} = 4\pi\rho$	$\nabla \cdot \boldsymbol{D} = 4\pi\rho$	$\nabla \cdot \boldsymbol{D} = 4\pi\rho$	$\nabla \cdot \boldsymbol{D} = \rho$
	$\nabla \times \boldsymbol{H} = 4\pi\boldsymbol{J} + \frac{\partial \boldsymbol{D}}{\partial t}$	$\nabla \times \boldsymbol{H} = 4\pi\boldsymbol{J} + \frac{\partial \boldsymbol{D}}{\partial t}$	$\nabla \times \boldsymbol{H} = \frac{4\pi}{c}\boldsymbol{J} + \frac{1}{c}\frac{\partial \boldsymbol{D}}{\partial t}$	$\nabla \times \boldsymbol{H} = \frac{1}{c}\left(\boldsymbol{J} + \frac{\partial \boldsymbol{D}}{\partial t}\right)$
	$\nabla \times \boldsymbol{E} + \frac{\partial \boldsymbol{B}}{\partial t} = 0$	$\nabla \times \boldsymbol{E} + \frac{\partial \boldsymbol{B}}{\partial t} = 0$	$\nabla \times \boldsymbol{E} + \frac{1}{c}\frac{\partial \boldsymbol{B}}{\partial t} = 0$	$\nabla \times \boldsymbol{E} + \frac{1}{c}\frac{\partial \boldsymbol{B}}{\partial t} = 0$
	$\nabla \cdot \boldsymbol{B} = 0$	$\nabla \cdot \boldsymbol{B} = 0$	$\nabla \cdot \boldsymbol{B} = 0$	$\nabla \cdot \boldsymbol{B} = 0$
Dimension of Charge $[q]$	$[M^{1/2}\,L^{1/2}]$	$[M^{1/2}\,L^{3/2}\,T^{-1}]$	$[M^{1/2}\,L^{3/2}\,T^{-1}]$	$[M^{1/2}\,L^{3/2}\,T^{-1}]$
Dimension of Electric Field $[E]$	$[M^{1/2}\,L^{1/2}\,T^{-2}]$	$[M^{1/2}\,L^{-1/2}\,T^{-1}]$	$[M^{1/2}\,L^{-1/2}\,T^{-1}]$	$[M^{1/2}\,L^{-1/2}\,T^{-1}]$
Dimension of Magnetic Flux Density $[B]$	$[M^{1/2}\,L^{-1/2}\,T^{-1}]$	$[M^{1/2}\,L^{-3/2}]$	$[M^{1/2}\,L^{-1/2}\,T^{-1}]$	$[M^{1/2}\,L^{-1/2}\,T^{-1}]$

Acknowlegments

First of all, I would like to express my profound gratitude to my supervisor Prof. Shoichi Yamada. He has educated me for six years without forsaking. It has been invaluable learning experiences to discuss with him and to see his way to do research. He has been supported me financially to participate in many workshops and I have learned a lot about the high-field lasers and X-ray astronomy as well as theoretical astrophysics. Also, I have been always encouraged by his enthusiasm to complete the research. Thanks to him, I have continued my research.

I also appreciate Dr. Kotaro Fujisawa for giving me the research topic about polarimetry and attending my research discussions. Thanks to his network, I attended many workshops about neutron stars and broaden my network. He supported me when I was in a difficult period and I was able to overcome it. His extensive knowledge and objective viewpoint are useful not only in research but in daily life.

I am also very grateful to my senior colleagues in Yamada laboratory, Dr. Hidetomo Sawai, Dr. Hiroki Nagakura, Dr. Shun Furusawa, Dr. Kazuya Takahashi, Dr. Yu Yamamoto, Dr. Ryosuke Hirai, Dr. Motoyuki Saijo, Dr. Ko Nakamura, Dr. Wakana Iwakami and Dr. Hirotada Okawa for teaching me the posture on research and the insight into physics. I thank my junior colleagues and the members of Maeda laboratory, too. The discussion in seminars was very useful in my research.

Finally, I thank all my family and friends for all their support in my daily life.

Bibliography

Adler, S. L.: 1971, *Annals of Physics* **67**, 599

Affleck, I.: 1988, *Journal of Physics A* **21**, 693

Affleck, I. and Kruglyak, L.: 1987, *Physical Review Letters* **59**, 1065

Archibald, R. F., Kaspi, V. M., Tendulkar, S. P., and Scholz, P.: 2016, *The Astrophysical Journal Letters* **829**, L21

Artimovich, G. K.: 1990, *Soviet Physics-JETP* **70**, 787

Baade, W. and Zwicky, F.: 1934, *Physical Review* **46**, 76

Baier, R. and Breitenlohner, P.: 1967a, *Acta Physica Austriaca* **25**, 212

Baier, R. and Breitenlohner, P.: 1967b, *Il Nuovo Cimento B* **47**, 117

Batalin, I. A. and Shabad, A. E.: 1971, *Soviet Physics-JETP* **33**, 483

Baĭer, V. N., Mil'shteĭn, A. I., and Strakhovenko, V. M.: 1975, *Soviet Physics-JETP* **42**, 961

Becker, W. and Mitter, H.: 1975, *Journal of Physics A* **8**, 1638

Berestetskii, V. B., Lifshitz, E. M., and Pitaevskiĭ, *Quantum electrodynamics*

Bialynicka-Birula, Z. and Bialynicki-Birula, I.: 1970, *Physical Review D* **2**, 2341

Bialynicki-Birula, I.: 1983, in B. Jancewicz and J. Lukierski (eds.), *Quantum Theory Of Particles and Fields*, pp 31–48, World Scientific

Brezin, E. and Itzykson, C.: 1971, *Physical Review D* **3**, 618

Brodin, G., Marklund, M., and Stenflo, L.: 2001, *Physical Review Letters* **87**, 171801

Chauvin, M., Florén, H.-G., Friis, M., Jackson, M., Kamae, T., Kataoka, J., Kawano, T., Kiss, M., Mikhalev, V., and Mizuno, T. *et al.*.: 2017, *Scientific Report* **7**, 7816

Chauvin, M., Florén, H.-G., Jackson, M., Kamae, T., Kawano, T., Kiss, M., Kole, M., Mikhalev, V., Moretti, E., and Olofsson, G. *et al.*.: 2016, *Monthly Notices of the Royal Astronomical Society* **456**, L84

Dean, A. J., Clark, D. J., Stephen, J. B., McBride, V. A., Bassani, L., Bazzano, A., Bird, A. J., Hill, A. B., Shaw, S. E., and Ubertini, P.: 2008, *Science* **321**, 1183

di Piazza, A., Hatsagortsyan, K. Z., and Keitel, C. H.: 2006, *Physical Review Letters* **97**, 083603

Di Piazza, A., Hatsagortsyan, K. Z., and Keitel, C. H.: 2007, *Physics of Plasmas* **14**, 032102

Di Piazza, A., Müller, C., Hatsagortsyan, K. Z., and Keitel, C. H.: 2012, *Reviews of Modern Physics* **84**, 1177

Dinu, V., Heinzl, T., Ilderton, A., Marklund, M., and Torgrimsson, G.: 2014a, *Physical Review D* **90**, 045025

Dinu, V., Heinzl, T., Ilderton, A., Marklund, M., and Torgrimsson, G.: 2014b, *Physical Review D* **89**, 125003

Dittrich, W. and Gies, H.: 2000, *Probing the Quantum Vacuum*, No. 166 in Springer Tracts in Modern Physics, Springer

Dittrich, W. and Gies, H.: 2000, *Probing the Quantum Vacuum*

Enoto, T., Nakazawa, K., Makishima, K., Rea, N., Hurley, K., and Shibata, S.: 2010, *The Astrophysical Journal Letters* **722**, L162

Fernández, R. and Davis, S. W.: 2011, *The Astrophysical Journal* **730**, 131

Forot, M., Laurent, P., Grenier, I. A., Gouiffès, C., and Lebrun, F.: 2008, *The Astrophysical Journal Letters* **688**, L29

Franken, P. A., Hill, A. E., Peters, C. W., and Weinreich, G.: 1961, *Physical Review Letters* **7**, 118

González Caniulef, D., Zane, S., Taverna, R., Turolla, R., and Wu, K.: 2016, *Monthly Notices of the Royal Astronomical Society* **459**, 3585

Greenstein, G. and Hartke, G. J.: 1983, *The Astrophysical Journal* **271**, 283

Gusynin, V. and Shovkovy, I.: 1999, *Journal of Mathematical Physics* **40**, 5406

Haroche, S.: 2008, *Physical Review Letters* **101**, 160001

Hattori, K. and Itakura, K.: 2013a, *Annals of Physics* **330**, 23

Hattori, K. and Itakura, K.: 2013b, *Annals of Physics* **334**, 58

Heinzl, T., Liesfeld, B., Amthor, K.-U., Schwoerer, H., Sauerbrey, R., and Wipf, A.: 2006, *Optics Communications* **267**, 318

Heinzl, T. and Schröder, O.: 2006, *Journal of Physics A* **39**, 11623

Heisenberg, W. and Euler, H.: 1936, *Zeitschrift für Physik* **98**, 714, Translated edition is arXiv:physics/0605038

Hewish, A., Bell, S. J., Pilkington, J. D. H., Scott, P. F., and Collins, R. A.: 1968, *Nature* **217**, 709

Heyl, J. S. and Hernquist, L.: 1997a, *Physical Review D* **55**, 2449

Heyl, J. S. and Hernquist, L.: 1997b, *Journal of Physics A* **30**, 6485

Heyl, J. S. and Hernquist, L.: 1998, *Physical Review D* **58**, 043005

Heyl, J. S. and Hernquist, L.: 1999, *Physical Review D* **59**, 045005

Heyl, J. S. and Hernquist, L.: 2005, *The Astrophysical Journal* **618**, 463

Heyl, J. S. and Shaviv, N. J.: 2002, *Physical Review D* **66**, 023002

Heyl, J. S., Shaviv, N. J., and Lloyd, D.: 2003, *Monthly Notices of the Royal Astronomical Society* **342**, 134

Ho, W. C. G. and Lai, D.: 2003, *Monthly Notices of the Royal Astronomical Society* **338**, 233

Ishikawa, K., Kimura, D., Shigaki, K., and Tsujii, A.: 2013, *International Journal of Modern Physics A* **28**, 1350100

Jackson, J. D.: 1975, *Classical electrodynamics*

Karbstein, F.: 2013, *Physical Review D* **88**, 085033

Karbstein, F. and Shaisultanov, R.: 2015, *Physical Review D* **91**, 085027

King, B. and Heinzl, T.: 2016, *High Power Laser Science and Engineering* **4**, e5

Kogut, J. B. and Soper, D. E.: 1970, *Physical Review D* **1**, 2901

Kohri, K. and Yamada, S.: 2002, *Physical Review D* **65**, 043006

Lai, D. and Ho, W. C.: 2003a, *Physical Review Letters* **91**, 071101

Lai, D. and Ho, W. C. G.: 2002, *The Astrophysical Journal* **566**, 373

Lai, D. and Ho, W. C. G.: 2003b, *The Astrophysical Journal* **588**, 962

Lodenquai, J., Canuto, V., Ruderman, M., and Tsuruta, S.: 1974, *The Astrophysical Journal* **190**, 141

Maiman, T. H.: 1960, *Nature* **187**, 493

Makishima, K., Enoto, T., Hiraga, J. S., Nakano, T., Nakazawa, K., Sakurai, S., Sasano, M., and Murakami, H.: 2014, *Physical Review Letters* **112**, 171102

Manchester, R. N., Hobbs, G. B., Teoh, A., and Hobbs, M.: 2005, *The Astronomical Journal* **129**, 1993

Marshall, H. L., Schulz, N. S., Remlinger, B., Gentry, E. S., Windt, D. L., and Gullikson, E. M.: 2013, in *Optics for EUV, X-Ray, and Gamma-Ray Astronomy VI*, Vol. 8861 of *Proceedings of SPIE*, p. 88611D

Maruyama, H., Matsuoka, F., Kobayashi, K., and Yamazaki, H.: 1995, *Journal of magnetism and magnetic materials* **140**, 43

Mereghetti, S.: 2008, *The Astronomy and Astrophysics Review* **15**, 225

Mészáros, P.: 1992, *High-energy radiation from magnetized neutron stars.*

Mészáros, P. and Ventura, J.: 1979, *Physical Review D* **19**, 3565

Meuren, S., Keitel, C. H., and Piazza, A. D.: 2013, *Physical Review D* **88**, 013007

Mignani, R. P., Testa, V., González Caniulef, D., Taverna, R., Turolla, R., Zane, S., and Wu, K.: 2017, *Monthly Notices of the Royal Astronomical Society* **465**, 492

Mitter, H.: 1975, *Acta Physica Austriaca Supplementum* **14**, 397

Monden, Y. and Kodama, R.: 2011, *Physical Review Letters* **107**, 073602

Mourou, G. and Tajima, T.: 2012, *SPIE Newsroom*

Nakagawa, Y. E., Yoshida, A., Yamaoka, K., and Shibazaki, N.: 2009, *Publications of the Astronomical Society of Japan* **61**, 109

Narozhnyĭ, N. B.: 1969, *Soviet Physics-JETP* **28**, 371

Neville, R. and Rohrlich, F.: 1971, *Physical Review D* **3**, 1692

Nobili, L., Turolla, R., and Zane, S.: 2008, *Monthly Notices of the Royal Astronomical Society* **386**, 1527

Olausen, S. A. and Kaspi, V. M.: 2014, *The Astrophysical Journal Supplement Series* **212**, 6

Page, D.: 1995, *The Astrophysical Journal* **442**, 273

Pavlov, G. G. and Zavlin, V. E.: 2000, *The Astrophysical Journal* **529**, 1011

Potekhin, A. Y.: 2014, *Physics Uspekhi* **57**, 735

Potekhin, A. Y., Suleimanov, V. F., van Adelsberg, M., and Werner, K.: 2012, *Astronomy & Astrophysics* **546**, A121

Rea, N., Borghese, A., Esposito, P., Coti Zelati, F., Bachetti, M., Israel, G. L., and De Luca, A.: 2016, *The Astrophysical Journal Letters* **828**, L13

Rea, N., Israel, G. L., Oosterbroek, T., Campana, S., Zane, S., Turolla, R., Testa, V., Méndez, M., and Stella, L.: 2007a, *Astrophysics and Space Science* **308**, 505

Rea, N., Israel, G. L., Turolla, R., Esposito, P., Mereghetti, S., Götz, D., Zane, S., Tiengo, A., Hurley, K., and Feroci, M. *et al.*.: 2009, *Monthly Notices of the Royal Astronomical Society* **396**, 2419

Rea, N., Nichelli, E., Israel, G. L., Perna, R., Oosterbroek, T., Parmar, A. N., Turolla, R., Campana, S., Stella, L., and Zane, S. *et al.*.: 2007b, *Monthly Notices of the Royal Astronomical Society* **381**, 293

Ritus, V. I.: 1972, *Annals of Physics* **69**, 555

Schubert, C.: 2000, *Nuclear Physics B* **585**, 407

Schwinger, J.: 1951, *Physical Review* **82**, 664

Shore, G. M.: 2007, *Nuclear Physics B* **778**, 219

Silver, E. H., Kestenbaum, H. L., Long, K. S., Novick, R., Wolff, R. S., and Weisskopf, M. C.: 1978, *The Astrophysical Journal* **225**, 221

Soffitta, P., Bellazzini, R., Bozzo, E., Burwitz, V., Castro-Tirado, A., Costa, E., Courvoisier, T., Feng, H., Gburek, S., and Goosmann, R. *et al.*.: 2016, in *Space Telescopes and Instrumentation 2016: Ultraviolet to Gamma Ray*, Vol. 9905 of *Proceedings of SPIE*, p. 990515

Strickland, D. and Mourou, G.: 1985, *Optics Communications* **56**, 219

Suzuki, M., Inubushi, Y., Yabashi, M., and Ishikawa, T.: 2014, *Journal of synchrotron radiation* **21**, 466

Tajima, T. and Mourou, G.: 2002, *Physical Review Special Topics-Accelerators and Beams* **5**, 031301

Taverna, R., Muleri, F., Turolla, R., Soffitta, P., Fabiani, S., and Nobili, L.: 2014, *Monthly Notices of the Royal Astronomical Society* **438**, 1686

Taverna, R. and Turolla, R.: 2017, *Monthly Notices of the Royal Astronomical Society* **469**, 3610

Taverna, R., Turolla, R., Gonzalez Caniulef, D., Zane, S., Muleri, F., and Soffitta, P.: 2015, *Monthly Notices of the Royal Astronomical Society* **454**, 3254

Thompson, C., Lyutikov, M., and Kulkarni, S. R.: 2002, *The Astrophysical Journal* **574**, 332

Tiengo, A., Esposito, P., Mereghetti, S., Turolla, R., Nobili, L., Gastaldello, F., Götz, D., Israel, G. L., Rea, N., Stella, L., Zane, S., and Bignami, G. F.: 2013, *Nature* **500**, 312

Toll, J. S.: 1952, *Ph.D. thesis*, PRINCETON UNIVERSITY.

Tsai, W. and Erber, T.: 1974, *Physical Review D* **10**, 492

Tsai, W. and Erber, T.: 1975, *Physical Review D* **12**, 1132

Turolla, R., Zane, S., and Drake, J. J.: 2004, *The Astrophysical Journal* **603**, 265

Urrutia, L. F.: 1978, *Physical Review D* **17**, 1977

Vadawale, S., Chattopadhyay, T., Mithun, N., Rao, A., Bhattacharya, D., Vibhute, A., Bhalerao, V., Dewangan, G., Misra, R., Paul, B., et al.: 2017, *Nature Astronomy* p. 1

van Adelsberg, M. and Lai, D.: 2006, *Monthly Notices of the Royal Astronomical Society* **373**, 1495

van Putten, T., Watts, A. L., Baring, M. G., and Wijers, R. A. M. J.: 2016, *Monthly Notices of the Royal Astronomical Society* **461**, 877

Varfolomeev, A. A.: 1966, *Soviet Physics-JETP* **23**, 681

Vogel, J. K., Hascoët, R., Kaspi, V. M., An, H., Archibald, R., Beloborodov, A. M., Boggs, S. E., Christensen, F. E., Craig, W. W., and Gotthelf, E. V. *et al.*: 2014, *The Astrophysical Journal* **789**, 75

Volkov, D. M.: 1935, *Zeitschrift für Physik* **94**, 250

Weisskopf, M. C., Baldini, L., Bellazini, R., Brez, A., Costa, E., Dissly, R., Elsner, R. F., Fabiani, S., Matt, G., and Minuti, M. *et al.*: 2013, in *UV, X-Ray, and Gamma-Ray Space Instrumentation for Astronomy XVIII*, Vol. 8859 of *Proceedings of SPIE*, p. 885908

Weisskopf, M. C., Silver, E. H., Kestenbaum, H. L., Long, K. S., and Novick, R.: 1978, *The Astrophysical Journal Letters* **220**, L117

Yang, Y.-P. and Zhang, B.: 2015, *The Astrophysical Journal* **815**, 45

Yanovsky, V., Chvykov, V., Kalinchenko, G., Rousseau, P., Planchon, T., Matsuoka, T., Maksimchuk, A., Nees, J., Cheriaux, G., Mourou, G., et al.: 2008, *Optics Express* **16**, 2109

Zavattini, E., Zavattini, G., Ruoso, G., Polacco, E., Milotti, E., Karuza, M., Gastaldi, U., di Domenico, G., Della Valle, F., and Cimino, R. *et al.*: 2007, *Physical Review Letters* **99**, 129901

Zavattini, E., Zavattini, G., Ruoso, G., Polacco, E., Milotti, E., Karuza, M., Gastaldi, U., di Domenico, G., Della Valle, F., and *et al.*, C.: 2006, *Physical Review Letters* **96**, 110406

Zel'Dovich, Y. B.: 1967, *Soviet Physics-JETP* **24**, 1006

Zhang, S. N., Feroci, M., Santangelo, A., Dong, Y. W., Feng, H., Lu, F. J., Nandra, K., Wang, Z. S., Zhang, S., and Bozzo, E. *et al.*: 2016, in *Space Telescopes and Instrumentation 2016: Ultraviolet to Gamma Ray*, Vol. 9905 of *Proceedings of SPIE*, p. 99051Q

早稲田大学　博士（理学）　学位申請　研究業績書

（2018 年　2 月　現在）

種 類 別	題名、　発表・発行掲載誌名、　発表・発行年月、　連名者（申請者含む）
論文	Title: ○Vacuum Polarization and Photon Propagation in an Electromagnetic Plane Wave Journal: Progress of Theoretical and Experimental Physics, accepted Authors: Akihiro Yatabe & Shoichi Yamada Title: ○Systematic Analysis of the Effects of Mode Conversion on Thermal Radiation From Neutron Stars Journal: The Astrophysical Journal, Volume 850, article id. 185, 28 pp. Publication date: December, 2017 Authors: Akihiro Yatabe & Shoichi Yamada
講演 (口頭)	Title: マグネターの熱的放射の偏光の系統的な予想 Conference: 第 30 回 理論懇シンポジウム「星の物理の新地平」 Date: December, 2017 Authors: Akihiro Yatabe Title: 中性子星の表面放射における偏光の体系的予想 Conference: 第 6 回「中性子星核物質」研究会 Date: December, 2017 Authors: Akihiro Yatabe Title: マグネターの熱的放射に関する偏光予想 Conference: ～中性子星の観測と理論～　研究活性化ワークショップ 2017 Date: November, 2017 Authors: Akihiro Yatabe Title: 中性子星の配置による軟 X 線偏光に対する効果 Conference: 日本天文学会　2017 年秋季年会 Date: September, 2017 Authors: Akihiro Yatabe & Shoichi Yamada Title: Systematic analysis of polarization for thermal radiation of neutron star focusing on mode conversion Conference: 2nd CORE-U International Conference: Cosmic Polarimetry from Micro to Macro Scales Date: March, 2017 Authors: Akihiro Yatabe & Shoichi Yamada Title: 中性子星の X 線偏光に関する体系的な予想 Conference: 日本天文学会　2017 年春季年会 Date: March, 2017 Authors: Akihiro Yatabe & Shoichi Yamada Title: マグネターの X 線偏光 Conference: 中性子星勉強会　～中性子星の多様性に迫る～　@蔵王温泉 Date: September, 2016 Authors: Akihiro Yatabe

早稲田大学　博士（理学）　学位申請　研究業績書

種 類 別	題名、　発表・発行掲載誌名、　発表・発行年月、　連名者（申請者含む）
	Title: 強い電磁場の量子効果による真空の屈折率の変化 Conference: X 線ガンマ線偏光観測 RG ミーティング Date: March, 2016 Authors: Akihiro Yatabe & Shoichi Yamada Title: 高強度レーザーとプローブ光子の非線形相互作用による屈折率の変化と対生成 Conference: 日本物理学会　第 71 回年次大会 Date: March, 2016 Authors: Akihiro Yatabe & Shoichi Yamada Title: 強い電磁場の量子効果による真空の屈折率 Conference: 日本天文学会　2016 年春季大会 Date: March, 2016 Authors: Akihiro Yatabe & Shoichi Yamada Title: QED Vacuum Polarization and Photon Propagation in an Electromagnetic Plane Wave Conference: 1st CORE-U International Conference: Intense Fields and Extreme Universe Date: March, 2016 Authors: Akihiro Yatabe & Shoichi Yamada Title: マグネターの放射における量子電気力学的な効果 Conference: ～中性子星の観測と理論～研究活性化ワークショップ Date: December, 2015 Authors: Akihiro Yatabe & Shoichi Yamada Title: 高強度レーザーによる平面電磁波中を進行する電磁波 Conference: Plasma Conference 2014 Date: November, 2014 Authors: Akihiro Yatabe & Shoichi Yamada Title: レーザー実験の電磁場における光子の複屈折と対生成 Conference: 第 2 回 DTA シンポジウム Date: October, 2014 Authors: Akihiro Yatabe & Shoichi Yamada Title: マグネターのバースト現象とレーザー実験に実現する強い電磁場の非一様性に関する基礎的研究 Conference: 第 44 回　天文・天体物理若手　夏の学校 Date: July, 2014 Authors: Akihiro Yatabe

早稲田大学　博士（理学）　学位申請　研究業績書

種 類 別	題名、　発表・発行掲載誌名、　発表・発行年月、　連名者（申請者含む）
講演 (ポスター)	Title: Systematic analysis about the polarization in thermal radiations of magnetars Conference: IAUS 337: Pulsar Astrophysics -- The Next 50 Years Date: September, 2017 Authors: Akihiro Yatabe & Shoichi Yamada Title: マグネター磁気圏における X 線放射の偏光 Conference: 日本天文学会　2016 年秋季年会 Date: September, 2016 Authors: Akihiro Yatabe & Shoichi Yamada Title: 中性子星放射の偏光に対する磁気圏の効果 Conference: 第 46 回　天文・天体物理若手　夏の学校 Date: July, 2016 Authors: Akihiro Yatabe Title: 強い平面電磁波中の屈折率の変化 Conference: 第 28 回理論懇シンポジウム Date: December, 2015 Authors: Akihiro Yatabe & Shoichi Yamada Title: レーザー実験の電磁場における光子の複屈折と対生成 Conference: ～中性子星の観測と理論～研究活性化ワークショップ Date: December, 2015 Authors: Akihiro Yatabe & Shoichi Yamada Title: 平面電磁波における真空偏極 Conference: 第 45 回　天文・天体物理若手　夏の学校 Date: July, 2015 Authors: Akihiro Yatabe & Shoichi Yamada Title: Vacuum Polarization of Plane-Wave Fields Conference: OPIC 2015 Date: April, 2015 Authors: Akihiro Yatabe & Shoichi Yamada Title: 強磁場における電子プロパゲータの様々な表式 Conference: 第 43 回　天文・天体物理若手　夏の学校 Date: July, 2013 Authors: Akihiro Yatabe & Shoichi Yamada
その他 (セミナー)	Title: 強い磁場を伴う中性子星の放射に対する QED 効果 Seminar: 理化学研究所玉川研究室セミナー Date: May, 2016 Authors: Akihiro Yatabe